Development and application of Eulerian and Particle-in-Cell gyrokinetic codes for studying the effect of non-adiabatic passing electron dynamics on microturbulence

THÈSE N^{O} 7286 (2016)

PRÉSENTÉE LE 25 NOVEMBRE 2016

À LA FACULTÉ DES SCIENCES DE BASE
SPC - THÉORIE
PROGRAMME DOCTORAL EN PHYSIQUE

ÉCOLE POLYTECHNIQUE FÉDÉRALE DE LAUSANNE

POUR L'OBTENTION DU GRADE DE DOCTEUR ÈS SCIENCES

PAR

Julien Stanislas Pierre DOMINSKI

acceptée sur proposition du jury:

Prof. V. Savona, président du jury
Prof. L. Villard, Dr S. Brunner, directeurs de thèse
Prof. B. F. McMillan, rapporteur
Dr Y. Camenen, rapporteur
Dr J. Decker, rapporteur

ÉCOLE POLYTECHNIQUE
FÉDÉRALE DE LAUSANNE

Suisse
2016

“You must put your head into the lion’s mouth if the performance is to be a success.”
Wiston Churchill

À Andrea…

Abstract

In tokamak fusion plasmas, micro-turbulence transport is known to be the cause of large losses of heat and particles. The present work deals with the study of electrostatic micro-turbulence transport driven by instabilities of essentially two types: the ion temperature gradient (ITG) modes and the trapped electron modes (TEM). The plasma is described within the gyrokinetic framework, which permits to save computational resources compared to the classical Vlasov kinetic description. In gyrokinetic simulations of fusion plasmas, the passing electrons are often assumed fast enough so that they respond instantaneously to the electrostatic perturbations. In this case, their response is computed adiabatically instead of kinetically. The main advantage is that this simplified model for the electron response is less demanding in computational resources. This assumption is nonetheless incorrect, in particular near mode rational surfaces where the non-adiabatic response of passing electrons cannot be neglected. This thesis work focuses on the study of this passing electron non-adiabatic response, whose influence on microturbulence is studied by means of numerical simulations carried out with the gyrokinetic codes GENE and ORB5.

In the first part of this thesis work, the response of passing electrons in ITG and TEM microturbulence regimes is studied by making use of the flux-tube version of the GENE code. Results are obtained using two different electron models, fully kinetic and hybrid. In the hybrid model, passing particles are forced to respond adiabatically while trapped are handled kinetically. Comparing linear eigenmodes obtained with these two models enables one to systematically isolate fine radial structures located at corresponding mode rational surfaces, clearly resulting from the non-adiabatic passing-electron response. Nonlinear simulations show that these fine structures on the non-axisymmetric modes survive in the turbulent phase. Furthermore, through nonlinear coupling to axisymmetric modes, they induce radial modulations in the effective profiles of density, ion and electron temperature and zonal flows $E \times B$ shearing rate. Finally, the passing-electron channel is shown to significantly contribute to the transport levels, at least in our ITG case. Also shown is that the passing electrons significantly influence the $E \times B$ saturation mechanism of turbulent fluxes.

Following this study in flux tube geometry, the influence of the non-adiabatic passing electron response near mode rational surfaces is further studied in global geometry with the global gyrokinetic code ORB5, in which a new field solver is implemented for the gyrokinetic quasi-neutrality equation valid at arbitrary wavelength, overcoming the former long wavelength approximation made in the original version of the code. A benchmark is conducted against the global version of the gyrokinetic code GENE, showing very good agreement. Nonlinear simulations are carried out with the new solver in conditions relevant to the TCV tokamak, with the physical deuterium to electron mass ratio ($m_i/m_e = 3672$) and are compared to simulations carried out with heavy electrons ($m_i/m_e = 400$). The particular spectral organization of the passing electron turbulent flux and its dependence on the radial profile of the safety factor are revealed. In particular, the formation of short-scale transport barriers is studied near low-order mode rational surfaces. Results show that quantitatively correct nonlinear fully-kinetic simulations of tokamak transport must be carried out in a full torus and with the physical mass ratio.

Key words: Tokamaks, plasma, microturbulence, turbulence, non-adiabatic response, passing electrons, mode rational surfaces, field solver, finite elements.

Résumé

Dans les plasmas de fusion des tokamaks, le transport micro-turbulent est connu pour être la cause de grandes pertes de chaleur et de particules. Le travail présenté ici concerne l'étude de la micro-turbulence électrostatique produite par des instabilitées de deux types : les modes de gradient de température ionique (ITG) et les modes dus aux électrons piégés (TEM). Le plasma turbulent est modélisé dans le cadre de la théorie gyrocinétique qui permet de simuler la turbulence en utilisant moins de resources numériques que l'approche Vlasov classique. Dans ces simulations gyrocinétiques des plasmas de fusion, les électrons passants sont souvent supposés suffisamment rapides pour répondre de manière instantanée aux perturbations électrostatiques. L'avantage principal est que ce modèle simplifié pour les électrons est moins exigeant en resources computationelles. Cette supposition est cependant fausse, en particulier à proximité des surfaces rationelles, où la réponse non-adiabatique des électrons ne peut pas être négligée. Ce travail de thèse concerne l'étude de cette réponse non-adiabatique des électrons passants aux surfaces rationelles par le moyen de simulations numériques réalisées avec les code gyrocinétiques GENE et ORB5.

La première partie de ce travail de thèse a porté sur l'étude de la réponse non-adiabatique des électrons passants dans les régimes turbulents ITG et TEM via l'utilisation de la version “flux-tube” du code GENE. Deux modèles ont été utilisés pour produire les résultats : pleinement cinétique et hybride. Dans le modèle hybride, les particules passantes sont forcées de répondre de manière adiabatique alors que les piégées sont traitées cinétiquement. La comparaison des modes propres linéaires obtenus avec ces deux modèles a permis de systématiquement mettre en évidence les fines structures radiales localisées aux surfaces rationnelles correspondantes, fine structures qui résultent clairement de la réponse non-adiabatique des électrons passants. Les simulations non-linéaires montrent que ces structures fines sur les modes non-axisymétriques persistent dans la phase turbulente. De plus, à travers le couplage non-linéaire aux modes axisymétriques, elles induisent des modulations radiales dans les profils effectifs de densité, de température ionique et électronique, et du taux de cisaillement des écoulements zonaux $E \times B$. Finalement, il est montré que le canal des électrons passants contribue de manière significative au transport, au moins dans le cas de test ITG. Il est aussi montré que les électrons passants influencent significativement le mécanisme de saturation des flux turbulents par les écoulements zonaux.

À la suite de cette étude en géométrie flux tube, l'influence de la réponse non-adiabatique des électrons passants proche des surfaces rationelles a été éxaminée en géométrie globale avec le code gyrocinétique ORB5, dans lequel un nouveau solveur de champ a été implémenté pour l'équation de quasi-neutralité dans une version valide pour les longueurs d'ondes arbitraires, afin de ne plus être limité par l'approximation des grandes longueurs d'ondes faite dans la version originale du code. Un benchmark a été réalisé avec la version globale du code gyrocinétique GENE, démontrant un très bon accord entre les résultats. Les premières simulations non-linéaires utilisant ce nouveau solveur sont réalisées dans des conditions pertinentes pour le tokamak TCV avec le rapport de masse deuterium/électron ($m_i/m_e = 3672$) et sont comparées à des simulations réalisées avec des électrons lourds ($m_i/m_e = 400$). L'organisation spectrale propre aux flux turbulents portés par la dynamique des électrons passants, ainsi que leur couplage avec le profil radial du facteur de sécurité sont révélés. En particulier, la formation de fines barrières de transport aux surfaces rationelles est étudiée. Les résultats montrent que les simulations non-linéaires quantitativement correctes utilisant le modèle pleinement cinétique doivent être réalisées avec un tore complet et le rapport de masse réel.

Mots clefs : Tokamaks, plasma, micro-turbulence, turbulence, réponse non-adiabatique, électrons passants, surface rationelle, solveur de champ, éléments finis.

List of symbols

(R, Z, φ)	magnetic coordinates
R	major radius (horizontal)
Z	vertical direction
φ	toroidal angle
$(\psi, \theta^\star, \varphi)$	straight field line magnetic coordinates
ψ	poloidal magnetic flux
$\theta^\star$	straight field line angle
(x, y, z)	field aligned coordinate system
x	radial direction (any function of ψ)
y	binormal direction
z	parallel direction ($z \equiv \theta^\star$)
$\mathcal{J}^{xyz}$	Jacobian ($\lvert\partial(x, y, z)/\partial \mathbf{x}\rvert$)
t	time
t_w	time window
Δt	time step
$\mathbf{x}$	particle position
$\mathbf{X}$	guiding-center
$\boldsymbol{\rho}$	Larmor vector
α	gyroangle (or gyrophase)
$\mathbf{v}$	velocity
$v_\perp$	perpendicular velocity
$v_\parallel$	parallel velocity
μ	magnetic moment
s	radial coordinate ($\sqrt{\psi/\psi_{edge}}$)
ρ_{vol}	radial coordinate ($\sqrt{V/V_{edge}}$)
V	volume contained in a magnetic surface
R_0	major radius on axis
a	minor radius
ϵ_A	inverse aspect ratio (a/R_0)
$\rho^\star$	rho star parameter (ρ_s/a)

$\mathbf{E}$	electric field
ϕ	electrostatic potential
$\mathbf{B}$	magnetic field ($\mathbf{B} = B\mathbf{b}$)
$\mathbf{b}$	magnetic field unit vector
B	magnetic field amplitude
$\mathbf{A}$	vector potential
$\mathbf{A}^\star$	$\mathbf{A} + (mv_\parallel/q)\mathbf{b}$
$\mathbf{B}^\star$	$\nabla \times \mathbf{A}^\star$
$B_\parallel^\star$	$\mathbf{B}^\star \cdot \mathbf{b}$
$\mathbf{J}$	current
q_s	safety factor
$\hat{s}$	magnetic shear
σ	labels the species quantity
	$\sigma = e$ for electrons
	$\sigma = i$ for ions
q	electric charge
	$q_e = -e$ for electrons
	$q_i = Z_i e$ for ions
m	particle mass
	(or poloidal mode number)
α_t	fraction of trapped particles
Ω	cyclotron frequency
N	density
T	temperature
P	pressure
v_{th}	thermal velocity ($\sqrt{T/m}$)
c_s	sound speed ($\simeq \sqrt{T_e/m_i}$)
ρ	Larmor radius
ρ_s	sonic Larmor radius (c_s/Ω_0)
ρ_{th}	thermal Larmor radius (v_{th}/Ω_0)
τ	temperature ratio (T_e/T_i)

List of symbols

ϵ	small (gyrokinetic) parameter
ϵ_B	small magnetic parameter (ρ/R)
∇	gradient
$\nabla\times$	rotational
$\nabla\cdot$	divergence
∂	partial derivative
d	total derivative
$\int$	integral
$\oint$	integral over the periodic direction
$\equiv$	equivalent
$\simeq$	approximately equal to
$\propto$	proportional to
$\bullet$	optionaly used in operator notation to represent an operated quantity example: $\nabla \times \bullet$ (rotational)
$\dot{\bullet}$	time derivative ($\dot{\mathcal{A}} = d\mathcal{A}/dt$)
$\langle\bullet\rangle$	averaging operation
$\langle\bullet\rangle_{FS}$	flux surface average
$\langle\bullet\rangle_{\mathcal{S}}$	surface average
$\langle\bullet\rangle_\alpha$	gyroaverage
$\langle\bullet\rangle_s$	average over the radial direction s
$\langle\bullet\rangle_x$	average over the radial direction x
$\langle\bullet\rangle_y$	average over the binormal direction y
$\langle\bullet\rangle_z$	average over the parallel direction z
$\langle\bullet\rangle_{yz}$	average over both y and z
$\langle\bullet\rangle_t$	time average
$\widetilde{\bullet}$	deviation from gyroaverage example: $\widetilde{\mathcal{A}} = \mathcal{A} - \langle\mathcal{A}\rangle_\alpha$
J_0	0th order Bessel function
I_0	modified Bessel function
Γ_0	scaled modified Bessel function
Λ	finite element
$\widehat{\bullet}$	Fourier transformed qtty example: $f(\varphi_l) = \sum_n \widehat{f}_n e^{\imath 2\pi nl}$
δx	radial width

$_0$	labels the equilibrium quantities
δ	prefix the prerturbation quantities example: $B = B_0 + \delta B$
ω	frequency (of the perturbation)
ω_r	real frequency
γ	growth rate
$\mathbf{k}$	wave vector (of the perturbation)
ω_*	diamagnetic drift frequency
ω_N	density gradient contribution to ω^*
ω_T	temperature gradient contribution to ω^*
ω_D	gc drift frequency
$\langle\omega_D\rangle$	gc drift frequency averaged over the Maxwellian
$\omega_{E\times B}$	$E \times B$ zonal flow shearing rate
$\mathbf{v}_{E\times B}$	$E \times B$ (or electric) drift
$\mathbf{v}_\mathbf{E}$	same as $\mathbf{v}_{E\times B}$
$\mathbf{v}_{\mathrm{curv}}$	curvature drift ($\mathbf{v}_{\mathrm{curv}} = \mathbf{v}_\kappa + \mathbf{v}_{\nabla P}$)
$\mathbf{v}_\kappa$	kappa drift
$\mathbf{v}_{\nabla P}$	∇P drift
$\mathbf{v}_{\nabla B}$	∇B drift
$\mathbf{v}_{gc}$	unperturbed perpendicular drift $\mathbf{v}_{gc} = \mathbf{v}_\kappa + \mathbf{v}_{\nabla B}$ ($+\mathbf{v}_{\nabla P}$)
Γ	particle flux
Q_{kin}	kinetic energy flux
q_H	heat flux
f	distribution function
f_M	Maxwellian distribution function
f_{can}	Canonical distribution function
f_0	background distribution function
δf	perturbation distribution function
δh	$\delta h = \delta f + q\delta\phi N_0/T_0$
δg	$\delta g = \delta f - (q/m)\delta A_\parallel \partial f_0/\partial v_\parallel$
$\mathcal{E}_k$	gyrocenter kinetic energy
$\mathcal{E}_f$	gyrocenter potential energy
$\langle\mathcal{E}_k\rangle$	plasma kinetic energy
$\langle\mathcal{E}_f\rangle$	plasma potential energy

List of acronyms

3D	3 dimensional
5D	5 dimensional
BC	Boundary Condition
CBC	Cyclone Based Case
DFT	Discrete Fourier Transform
ETG	Electron Temperature Gradient
FLR	Finite Larmor Radius
FS	Flux Surface
FWHM	Full Width at Half Maximum
GB	Gyro Bohm
GC (or gc)	Guiding-Center
ITG	Ion Temperature Gradient
LHS	Left-Hand-Side
LMRS	Lowest order Mode Rational Surface
MHD	Magneto Hydro Dynamic
MRS	Mode Rational Surface
PIC	Particle-In-Cell
RHS	Right-Hand-Side
QNE	Quasi-Neutrality Equation
TCV	Tokamak à Configuration Variable
TEM	Trapped Electron Mode
ZF	Zonal Flow

CHEASE	name of a MHD equilibrium code
GENE	name of an Eulerian gyrokinetic code
GLOGYSTO	name of a gyrokinetic code
ORB5	name of a PIC gyrokinetic code

ad	adiabatic
hyb	hybrid
kin	kinetic
pas	passing
trp	trapped

Contents

Abstract **i**

List of symbols **v**

List of acronyms **vii**

1 Introduction **1**

2 Physical model for simulating core plasma turbulence **7**
- 2.1 Magnetic equilibrium 7
- 2.2 Particle orbits 10
- 2.3 Vlasov-Maxwell system 13
- 2.4 Diamagnetic drift 14
- 2.5 The gyrokinetic framework 14
- 2.6 The electron models 24
- 2.7 Micro-instabilities 27
- 2.8 The gyrokinetic codes GENE and ORB5 31

3 How non-adiabatic passing-electron layers of linear microinstabilities affect turbulent transport **41**
- 3.1 Introduction 41
- 3.2 Test cases of reference 42
- 3.3 Fine structures at low order MRS, in linear regimes 44
  - 3.3.1 Analytical estimate of the radial width of fine structures 44
  - 3.3.2 Fine structures near MRS in linear GENE simulations 45
  - 3.3.3 Local dispersion relation 48
  - 3.3.4 Systematic scan of physical parameters and comparison of the radial width estimates 56
- 3.4 Fine structures in nonlinear simulations and their effect on transport . . . 57
  - 3.4.1 ITG and TEM test cases 57
  - 3.4.2 Fine structures at MRSs 60
  - 3.4.3 Turbulent fluxes 65
- 3.5 Conclusion 74

4 An arbitrary wavelength solver for resolving fine layers of nonadiabatic passing electron response in the gyrokinetic code ORB5 77
4.1 Introduction 77
4.2 Quasi-neutrality equation 78
4.3 Discretized QNE with finite elements 81
4.4 Matrix assembly in discrete Fourier representation 83
4.5 Gyroaveraging in magnetic coordinates 90
4.6 Structure of the polarization matrix 91
4.7 Linear benchmark ORB5 versus GENE 95
4.8 Conclusion 97

5 The passing electron channel of turbulent transport in global gyrokinetic simulations relevant for TCV 101
5.1 Introduction 101
5.2 Test case description 102
5.3 Arbitrary wavelength and Padé solvers in the *half-torus* test case with heavy electrons 104
5.4 Full-torus versus half-torus simulations 108
5.5 Half-torus simulation with the physical Deuterium to electron mass ratio . 110
5.5.1 Linear destabilization 112
5.5.2 Non-adiabatic electron responses 113
5.5.3 Local flux estimate 116
5.5.4 Particle electron flux in the linear growing phase of the nonlinear simulation 119
5.5.5 Particle and heat electron fluxes in the turbulent saturated regime 122
5.5.6 Organization of zonal flows 128
5.6 Conclusion 129

6 Conclusion and outlook 131

A Matrix assembly in discrete Fourier representation 135

B ORB5 moments and fluxes diagnostics 139

C Influence of the magnetic shear on the turbulence organization 143

Bibliography 154

Acknowledgements 155

Curriculum Vitae 157

1 Introduction

Today, the energy supply is mainly based on fossil fuels whose non-renewable stocks are limited and non-homogeneously distributed on the earth surface. To sustain the human society development in a fair way, it is of prime interest to develop new concepts of energy production based on reasonably abundant and accessible resources. The research related to the achievement of a magnetic fusion reactor aims at providing a clean, sustainable, and on-demand source of energy based on the fusion of light atoms. For example, these fusion reactors can be fueled by a combination of deuterium, D, and tritium, T, which fusion reaction produces an atom of Helium, He, and a neutron, n, and releases 17.6 MeV of energy. This release of energy coming essentially from the mass defect, $\Delta m = m_D + m_T - m_{H_e} - m_n$ between the D-T system and the He-n system, as predicted by the Einstein's equation $E = \Delta m\, c^2$. This D-T fusion reaction is described by the equation

$$D[10\,\mathrm{keV}] + \mathrm{T}[10\,\mathrm{keV}] \rightarrow \mathrm{He}[3.5\,\mathrm{MeV}] + \mathrm{n}[14.1\,\mathrm{MeV}].$$

In terms of fuel resources, deuterium is particularly abundant in the ocean, but tritium, which is a radioactive element with a half-life time of 12 years, is a rare resource. Tritium can be produced from lithium by fusion reaction with a neutron and lithium is an abundant resource. The breeding of tritium from lithium in the blanket of the reactor during operation is one of the challenges on the path to achieve magnetic fusion as a new source of energy.

As addressed in [Lawson, 1957], the plasma of an efficient fusion reactor must provide at least as much electric power as it consumes. In this break-even scenario, the net output power P_{out} is converted, with an efficiency η, to electric power $P_E = \eta P_{\mathrm{out}}$ of the same level as the heating power P_{aux} used for sustaining the plasma operation. This heating power is necessary for compensating the losses due to the radiation P_{Br} and heat transport W/τ_E, where W is the kinetic energy content of the plasma and τ_E is the energy confinement time. The output power is composed of the power losses and of the power produced by fusion reactions P_α. Therefore, one has $P_{aux} = P_{Br} + W/\tau_E$ and $P_{out} = P_\alpha + P_{Br} + W/\tau_E$. To reach the break-even with a power transfer efficiency of $\eta = 1/3$, the Lawson criteria stipulates a necessary condition on the triple product

$$N_e T \tau_E \geq 10^{21} \text{ [keV s/m}^3\text{]},$$

with T the plasma temperature and N_e the electron density. A more constraining scenario would also take into account the efficiency, $\epsilon \simeq 1/2$, for converting the electric power into heating power, such that in this more constraining scenario $P_{aux} = \epsilon P_E = \epsilon\eta P_{\text{out}}$. In general, for an industrial reactor, *i.e.* when considering all the processes of energy transformation so that the power plant net output is economically profitable, the relation $P_{aux} = P_{out}/30$ is more appropriate and leads to the condition on the triple product $N_e T \tau_E \geq 2 \times 10^{22}$ [keV s/m^3], see [Lister, 2011]. One of the key challenge of magnetic fusion research is the optimization of the confinement time τ_E of fusion reactor prototypes.

The *tokamak* is one of the most promising concept of magnetic fusion reactor. Among the different existing tokamak experiments, let us mention that JET (United Kingdom, Culham) is the one that operated in the closest conditions to break-even with 16 MW of fusion power from 24MW of input power ($Q = 16/24 \simeq 0.67$), and that ITER (France, Cadarache) is designed to operate a long-pulsed plasma with 500 MW of fusion power from 50 MW of input power ($Q = 10$), numbers taken from www.iter.org. The *stellarator* concept, first proposed by [Spitzer, 1951], is an alternate toroidal device prototype whose periodic magnetic field is solely produced by coils of complex geometry. The most advanced stellarator experiment is Wendelstein 7-X (Germany, Greifswald). Its first Helium plasma has been succesfully produced in December 2015. A recent comparison between these two toroidal devices has been carried out in [Helander et al., 2012]. The main known advantages of the stellarator over the tokamak is that it operates in steady state because its poloidal field is not generated by induction and that it is not subject to disruptions. Disadvantages are that its neoclassical transport is bigger than in tokamaks. Note that this thesis work concerns essentially the study of the tokamak turbulent transport in the core of the reactor.

Micro-turbulence occurring in the core of tokamak magnetic confinement experiments is known to be responsible for large losses of heat and particles. These losses are essentially due to the turbulent transport driven by instabilities of various types, as for example the ion temperature gradient (ITG) modes, the trapped electron modes (TEM), or the electron temperature gradient (ETG) modes. The dynamics of these regimes have different characteristic length and time scales and, because these modes can coexist in a fusion plasma, plasma turbulence is a multi-scale problem [Görler, 2009, Howard et al., 2014, Maeyama et al., 2015, Howard et al., 2016].

When studying microinstabilities and associated turbulence at the ion time scale, as in the cases of ion temperature gradient (ITG) and trapped electron mode (TEM), it is often assumed that the real frequencies ω_r of these modes are sufficiently low such that the highly mobile passing electrons are responding adiabatically. The reduced adiabatic (Boltzmann) response [Horton, 1999] for passing electrons has thus been extensively applied in gyrokinetic codes with the purpose of studying turbulent transport in the ITG and TEM regimes, for example in ORB5 [Tran et al., 1999, Jolliet et al., 2007], GT5D [Idomura et al., 2008], and GYSELA [Grandgirard et al., 2007]. This approximation is practical due to the large time scale separation between the ion and electron dynamics, especially that of passing electrons. Resolving the full kinetic evolution of all species corresponds to a multi-scale computation which therefore remains a significant numerical challenge.

The assumption of an adiabatic response for the passing electrons is based on the argument that these particles are sufficiently mobile along the magnetic field line to remain in thermal equilibrium even in the presence of field fluctuations [Horton, 1999]. This adiabatic response is justified as long as $|\omega_r/k_\parallel| \ll v_{the}$, *i.e.* the parallel phase velocity $\omega_r/k_\parallel$ of ITG/TEM microinstabilities is small compared to the electron thermal velocity $v_{the} = \sqrt{T_{e0}/m_e}$, where $k_\parallel$ is the component parallel to the magnetic field of a given mode wave vector $\mathbf{k}$, T_{e0} the equilibrium temperature of the electrons, and m_e their mass. Near mode rational surfaces (MRSs) of low order, *i.e.* magnetic surfaces where the safety factor q_s is a low order rational number, $q_s = -m/n$ with m, n integer, the adiabatic assumption is in fact not justified. Indeed, near such a MRS, resonant Fourier modes with poloidal and toroidal mode numbers (m, n) align with the magnetic field line, $k_\parallel \approx (nq_s + m)/Rq_s = 0$ when $q_s = -m/n$. It results that the associated parallel phase velocity $|\omega_r/k_\parallel|$ becomes larger than the electron thermal velocity v_{the} within a certain radial width δx around this surface. The condition for adiabatic response is thus clearly violated within this interval.

Thesis contribution

This thesis work addresses the physics of passing electrons near mode rational surfaces where their response to the electrostatic perturbation is non-adiabatic. This study has been carried out with the gyrokinetic codes GENE and ORB5 which are briefly described in chapter 2.

The importance of accounting for the non-adiabatic response of passing electrons when simulating ITG or TEM micro-turbulence is shown with the flux-tube version of the GENE code. To pursue this study in global geometry with the ORB5 code, a new field solver valid for arbitrary wavelegnth in $k_\perp \rho_i$ is implemented. This new solver enables the study of the non-adiabatic passing electron response which is associated to the presence of fine radial structures on the perturbation fields near mode rational surfaces. This new solver implementation is benchmarked with the global version of the gyrokinetic Eulerian code GENE, which includes an arbitrary wavelength solver. To study the passing electron channel of turbulent transport with this new solver, new $3D$ diagnostics and associated post-processings have been implemented in the ORB5 code. The radial organization of the turbulence spectra is thus studied in a global nonlinear simulation relevant for the TCV tokamak. The differing roles of the sub- and supra-thermal electrons within the electron channel of transport are furthermore studied.

The main numerical contribution of this thesis work is thus the implementation of a new arbitrary wavelength solver in the ORB5 code, see chapter 4. This upgrade was realized in order to overcome the former long wavelength approximation made in the original version of the code. During the testing of this new arbitrary wavelength solver, side contributions have been made: the possibility to run a manufactured problem for the field equation, the cubic finite elements of ORB5 have been modified to be exactly the Bsplines defined in [de Boor, 1978]; and; because the new arbitrary solver is much more sensitive to small numerical errors, its verification resulted in the detection and correction of already existing minor bugs, among which the numerical implementation of the boundary conditions. The collaboration with Ben McMillan was fruitful during all phases of the implementation of this new solver. A benchmark effort has been carried out for validating this new functionnality of the ORB5 code, in collaboration with Gabriele Merlo.

To permit the study of the global micro-turbulence organization, and more particularly to permit the study of the radial organization of the turbulence spectra, new diagnostics associated to new post processings have thus been implemented for the ORB5 code. These new diagnostics are based on the $3D$ finite-element representation of the turbulence and take advantage of the field-aligned organization of the turbulence to only store the essentially field-aligned part of the species distribution function moments. This filtering results in a significant reduction of the output file size (factor 100 for medium size tokamaks). Associated post-processings have been implemented which allow us to reveal the organization of the turbulence in simulations relevant for the TCV tokamak, see chapter 5.

During the study of the non-adiabatic response of passing-electrons with the GENE code, many post-processing analysis have been implemented in Matlab. The low level data access post-processings have been benchmarked with the original GENE post-processing written in IDL. A panel of these diagnostics have been used in chapter 3.

Outline

In chapter 2, the gyrokinetic models and codes used for simulating micro-instabilities and micro-turbulence in the frame of this thesis work are introduced. The flux-tube version of the Eulerian gyrokinetic code GENE and the global gyrokinetic PIC code ORB5 are presented.

Chapter 3 is a study of the influence of the non-adiabatic response of passing electrons on the ITG and TEM unstable modes, in linear and nonlinear simulations carried out with the flux-tube version of the GENE code. The presence of fine structures due to the non-adiabatic response of passing electrons near MRSs is shown. The influence of these fine structures on microturbulence is studied.

In chapter 4, the implementation of a new generalized field solver in the ORB5 code is described in detail. This new field solver, which is valid for arbitrary wavelength in $k_\perp \rho_i$, is necessary to the ORB5 code for pursuing the study of the fine layers of non-adiabatic passing-electron response near MRSs in global geometry. The former long wavelength approximation made in the code precludes the study of fine radial structures on the perturbation field. A benchmark between the global version of the GENE code and the ORB5 code is carried out for both the ITG and TEM parts of the spectra, using ideal MHD equilibria. Benchmarks are carried out for the three electron models: adiabatic, hybrid, and kinetic; and for the three different versions of the new ORB5 field solver: long wavelength, arbitrary wavelength, and Padé approximation.

In chapter 5, global nonlinear simulations relevant for TCV are carried out using the physical deuterium to electron mass ratio and compared to heavy electron simulations. The electron channel of turbulent transport is studied focusing on the radial organization of the turbulence spectra and on the subgroups of subthermal and suprathermal particles.

Finally, main results are summarized in the last chapter and an outlook of possible follow-up studies is drawn.

2 Physical model for simulating core plasma turbulence

The core plasma turbulence and associated micro-instabilities are modeled within the gyrokinetic framework. This framework describes the plasma dynamics in a reduced 5d phase-space which is independent of the fast gyromotion of particles. This reduction is possible because of the adiabatic invariance of the magnetic moment of particles evolving in typical tokamak equilibrium.

The remainder of this chapter is organized as follow. In Sec.2.1, the tokamak ideal MHD equilibrium is described. In Sec. 2.2, one briefly describes single particle orbits in electromagnetic fields. In Sec. 2.3 the Vlasov-Maxwell system is introduced. In Sec. 2.4, the diamagnetic drift is described. In Sec. 2.5, the reduced gyrokinetic framework is introduced. In Sec. 2.6, the different electron models used in this thesis are described. In Sec. 2.7, the ion temperature gradient (ITG) and trapped electron mode (TEM) instabilities are introduced by means of local dispersion relations. Finally, in Sec. 2.8, the gyrokinetic codes GENE and ORB5 are briefly presented.

2.1 Magnetic equilibrium

In magneto-hydro-dynamics (MHD), the plasma equilibrium is described by its pressure P, current $\mathbf{J}$, and magnetic field $\mathbf{B}$. At equilibrium these quantities must obey the following system of equations

$$\begin{cases} \nabla P = \mathbf{J} \times \mathbf{B}, & \text{(Force balance)} \\ \nabla \times \mathbf{B} = \mu_0 \mathbf{J}, & \text{(Ampère)} \\ \nabla \cdot \mathbf{B} = 0. & \text{(Divergence free)} \end{cases} \tag{2.1}$$

The divergence-free magnetic field can be written $\mathbf{B} = \nabla \times \mathbf{A}$ with $\mathbf{A}$ the potential vector.

A tokamak being axisymmetric, its equilibrium is conveniently described with cylindrical coordinates (R, φ, Z) with R the major radius, Z the vertical direction, and φ the toroidal

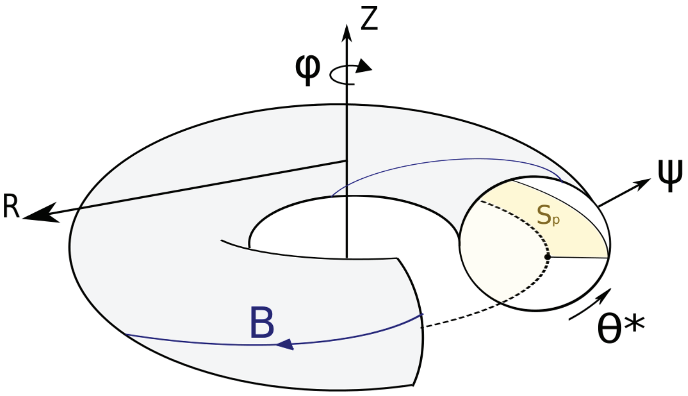

Figure 2.1 – Cartoon of a truncated magnetic flux surface (grey). The system is axisymmetric in the φ direction. The axis-of symmetry is the Z axis, which is located at $R = 0$. The magnetic axis located at major radius R_0 is represented with a black dashed line. A fraction of a twisted magnetic field line is represented with a blue line. Two poloidal coordinate systems are illustrated: (R, Z) Cartesian and $(\psi, \theta^\star)$ polar-like. A poloidal surface S_p with a ribbon topology is represented in yellow.

angle in the direction of the symmetry, see figure 2.1. One neglects the fact that in reality the toroidal component of the tokamak magnetic field is constructed with a discrete number of coils so that the system is not exactly axisymmetric.

Grad-Shafranov equation

The equilibrium magnetic field of a tokamak is both divergence free, $\mathbf{B} = \nabla \times \mathbf{A}$, and axisymmetric, $\partial \mathbf{B}/\partial \varphi = 0$. Therefore its general solution takes on the form

$$\mathbf{B}(R, Z) = \nabla \varphi \times \nabla \psi(R, Z) + I\left(\psi\right) \nabla \varphi, \tag{2.2}$$

where $\psi = RA^\varphi$, $I = R\left(\partial A^R/\partial Z - \partial A^R/\partial Z\right) = RB^\varphi$, $\mathbf{A} = A_R \nabla R + A_Z \nabla Z + A_\varphi \nabla \varphi = A^R \hat{e}_R + A^Z \hat{e}_Z + A^\varphi \hat{e}_\varphi$, and $(\hat{e}_R, \hat{e}_Z, \hat{e}_\varphi) = (\nabla R, \nabla Z, R\nabla \varphi)$. Note that $2\pi\psi$ corresponds to the *poloidal magnetic flux*

$$\psi_P = 2\pi\psi = \int_{S_p} d\boldsymbol{\sigma} \cdot \mathbf{B} = \int_{S_p} d\boldsymbol{\sigma} \cdot \nabla \times \mathbf{A} = \oint_{\partial S_p} d\mathbf{l} \cdot \mathbf{A} = 2\pi R A^\varphi,$$

where the poloidal surface S_p has the topology of a ribbon enclosed by two toroidal lines, one of which is on the magnetic surface ψ and the second is chosen to be the magnetic axis. The magnetic axis is the curve $C_{\text{axis}} := \{R = R_0, Z = 0, \varphi \in [0, 2\pi]\}$ with R_0 the major radius. The magnetic field amplitude on the axis is B_{axis} and the magnetic flux on axis is $\psi_{\text{axis}} = 0$.

The divergence of Ampere's law also leads to a similar form for the axisymmetric current

$$\mathbf{J}(R,Z) = \mu_0^{-1}\nabla\varphi \times \nabla I\,(\psi) + J_\varphi(R,Z)\,\nabla\varphi. \tag{2.3}$$

To obtain the Grad-Shafranov equation, one injects equation (2.2) and (2.3) in Euler's equation, giving

$$\nabla P(\psi) = -R^{-2}J_\varphi\nabla\psi - (\mu_0 R^2)^{-1}I\nabla I \tag{2.4}$$

with

$$\mu_0 R^{-2}J_\varphi = (\nabla\times\mathbf{B})\cdot\nabla\varphi = \nabla\cdot(\mathbf{B}\times\nabla\varphi) = \nabla\cdot(\nabla\varphi\times\nabla\psi\times\nabla\varphi) = \nabla\cdot(R^{-2}\nabla\psi) = R^{-2}\Delta^*\psi.$$

Finally projecting equation (2.4) in the direction normal to the magnetic surface, $\nabla P(\psi)\cdot\nabla\psi$, one obtains the Grad-Shafranov equation

$$\Delta^*\psi = R^2\nabla\cdot(R^{-2}\nabla\psi) = R\frac{\partial}{\partial R}\frac{1}{R}\frac{\partial\psi}{\partial R} + \frac{\partial^2\psi}{\partial Z^2} = -\mu_0 R^2\frac{\partial P}{\partial\psi} - I\frac{\partial I}{\partial\psi} = \mu_0 J_\varphi. \tag{2.5}$$

One can then compute the solution to this equation for any given profiles of pressure $P = P(\psi)$ and poloidal plasma current flux $I = I(\psi)$.

The circular ad-hoc geometry

The circular ad-hoc geometry is an approximation of a solution to the Grad-Shafranov equation (2.5), but is not a true solution to the Grad-Shafranov equation. In this circular ad-hoc geometry, the nested magnetic surfaces, $\psi = \psi(r)$, have circular poloidal cross-sections and they respect the relation $d\psi/dr = B_0\,r/\bar{q}(r)$ with $\bar{q}(r)$ the pseudo safety factor and r the minor radius. In this ad-hoc geometry, the magnetic field is

$$\mathbf{B}(r,\theta) = \frac{B_0(r,\theta)R_0}{R(r,\theta)}\left(\hat{e}_\varphi + \frac{r}{R_0\bar{q}(r)}\hat{e}_\theta\right), \tag{2.6}$$

where (r,θ,φ) are the toroidal coordinates, and r and θ are the geometric radius and angle. The pseudo safety factor, $\bar{q}$, can be related to the safety factor

$$q_s(r) = \frac{1}{2\pi}\oint d\theta\frac{\mathbf{B}\cdot\nabla\varphi}{\mathbf{B}\cdot\nabla\theta} \simeq \frac{rB_\varphi}{RB_\theta},$$

by the relation $\bar{q}(r) = q_s(r)\sqrt{1-\epsilon_A^2}$ with $\epsilon_A = a/R_0$ the inverse aspect ratio, a the minor radius of reference, and R_0 the major radius of reference.

The straight field line coordinate system

A common set of coordinates used in tokamak geometry are the magnetic coordinates $(\psi, \theta^\star, \varphi)$ with ψ the poloidal magnetic flux, φ the toroidal angle, and $\theta^\star$ the straight field line poloidal angle defined by

$$\theta^\star(r,\theta) = \frac{1}{q_s}\int_0^\theta d\theta' \frac{\mathbf{B}\cdot\nabla\varphi}{\mathbf{B}\cdot\nabla\theta'},$$

such that

$$q_s(\psi) = \frac{\mathbf{B}\cdot\nabla\varphi}{\mathbf{B}\cdot\nabla\theta^\star}. \tag{2.7}$$

The corresponding poloidal plane coordinates system $(\psi, \theta^\star)$ is a polar like coordinate system which is singular on axis. Any bijective function of ψ can be chosen for the radial coordinate, as for example $s = \sqrt{\psi/\psi_{edge}}$. The *Jacobian* in magnetic coordinates is written $\mathcal{J}^{\psi\theta^\star\varphi} = [(\nabla\psi \times \nabla\theta^\star)\cdot\nabla\varphi]^{-1}$.

More details on the system of coordinates are given by [D'haeseleer et al., 1991] and a convention system has been defined in [Sauter and Medvedev, 2013].

The field-aligned coordinate system

Another set of coordinates, which is used in the GENE code, is the field-aligned coordinate system (x, y, z) where $x = f(\psi)$ labels the flux surfaces, $y = C_y[q_s(\psi)\theta^\star - \varphi]$ labels the field lines on a surface, and $z = \theta^\star$ is the parallel coordinate. The equilibrium magnetic field, equation (2.2), expressed with these field aligned variables takes on the Clebsh form $\mathbf{B} = \mathcal{C}(x)\nabla x \times \nabla y$ with $\mathcal{C}(x)$ a flux-surface quantity [Lapillonne, 2010]. This notation reveals the topology of the magnetic field which is organized in nested magnetic flux surfaces, labeled x, themselves covered by magnetic field lines, labeled y. The angular nature of the coordinates y is due to the periodicity of the dimension: a same line is distant to itself within a finite length in the direction y. Note that the angle y acquires units of length because of the multiplicative constant $C_y = r_0/q_0$.

2.2 Particle orbits

The motion of a non-relativistic electrically charged particle in an electromagnetic field, $(\mathbf{E}, \mathbf{B}) = (-\nabla\phi - \partial\mathbf{A}/\partial t, \nabla\times\mathbf{A})$ with $\nabla\cdot\mathbf{A} = 0$ the Coulomb gauge, can be described by the equation of motion

$$m\dot{\mathbf{v}} = q(\mathbf{E} + \mathbf{v}\times\mathbf{B}) = q(-\nabla\phi - \partial\mathbf{A}/\partial t) + q\mathbf{v}\times(\nabla\times\mathbf{A}) = \nabla(-q\phi + q\mathbf{v}\cdot\mathbf{A}) - q\dot{\mathbf{A}}.$$

Its Lagrangian reads $L = m\dot{\mathbf{x}}^2/2 + q\dot{\mathbf{x}} \cdot \mathbf{A}(\mathbf{x};t) - q\phi(\mathbf{x};t)$ with m the particle mass and q the particle electric charge.

The velocity of a single charged particle evolving in a magnetic field can be decomposed in two components, respectively, parallel and perpendicular to the magnetic field line, such that $\mathbf{v} = v_\parallel \mathbf{b} + \mathbf{v}_\perp$ with $\mathbf{b} = \mathbf{B}/B$.

In the case of a uniform magnetic field, $\mathbf{B} = \vec{const}$, with no electric field, $\mathbf{E} = 0$, the particle motion consists of a parallel translation along the magnetic field line, $\mathbf{v}_\parallel = v_\parallel \mathbf{B}/B$, associated to a gyration around this magnetic field line, $\mathbf{v}_\perp = \mathbf{v}_c = q\boldsymbol{\rho} \times \mathbf{B}/m$. The gyration also called "gyromotion" is a circular trajectory of radius equal to the Larmor radius $\rho = v_\perp/\Omega$ and of angular frequency $\Omega = qB/m$. The center of rotation, which is moving at constant $v_\parallel$, in this particular case, is called the guiding center.

In the case that the particle experiences an external force $\mathbf{F}$ its trajectory drifts by a *drift* velocity $\mathbf{v}_D = \mathbf{F} \times \mathbf{B}/qB^2$. Such a force can be the consequence of the magnetic field line curvature, a change of magnetic field amplitude along the line, or the existence of an electric field perturbation. The perpendicular velocity is now composed of two components: $\mathbf{v}_\perp = \mathbf{v}_c + \mathbf{v}_D$. In the frame of this thesis work, these drifts are considered slow compared to the gyromotion, $v_D < \rho\Omega$. The computation of these drifts in arbitrary geometry will be discussed in section 2.5 when introducing the gyrokinetic framework.

An adiabatic invariant can be deduced from the cyclic gyromotion of particles. In the case of a *smooth* magnetic field slowly varying in space and time, *i.e.*, $\rho_{\mathrm{th}} \nabla \ln \mathbf{B} \ll 1$ and $dB/dt \ll B\Omega$ with $\rho_{\mathrm{th}} = \sqrt{Tm}/qB$, the gyromotion of the particle around the guiding center can be approximated to be a closed circular orbit. This closed orbit describes an elementary current loop of intensity $i = q\Omega/2\pi$ and magnetic moment $\mu = (q\Omega/2\pi)(\pi\rho_\perp^2)$ with $S = \pi\rho_\perp^2$ the surface enclosed by the closed orbits. If in addition the perturbed electric field varies slowly in time, $dE/dt \ll E\Omega$, the magnetic moment $\mu = iS = mv_\perp^2/2B$ is an adiabatic invariant. This adiabatic invariant can be obtained by computing the action associated to the gyroangle

$$\mathfrak{J}_\mu = \oint_{C_\alpha} dl_\rho \cdot \mathbf{p}_\perp = \oint_{C_\alpha} dl_\rho \cdot (m\mathbf{v}_\perp + q\mathbf{A}) = m \oint_{C_\alpha} dl_\rho \cdot \boldsymbol{\rho} \times \boldsymbol{\Omega} + q \int_{S_\alpha} d\mathbf{S} \cdot \nabla \times \mathbf{A} = \frac{2\pi m}{-q}\,\mu,$$

with $dl_\rho \equiv \rho d\alpha$ the elementary displacement along the closed gyro orbit C_α and S_α a surface contained in this closed orbit. The electric field fluctuations need to be slow enough so that the work done on the particle cancels over a gyroperiod

$$q \int_0^{2\pi/\Omega} dt\, \mathbf{v}_c \cdot \mathbf{E} = v_c \oint_{\mathcal{C}} d\mathbf{l} \cdot \mathbf{E} = \oint_S d\mathbf{S} \nabla \times \mathbf{E} = -\oint_S d\mathbf{S} \nabla \times \nabla\phi = 0.$$

For a particle evolving in a curved magnetic field of varying amplitude along the magnetic field lines, the invariance of μ might preclude the particle to reach the region where the

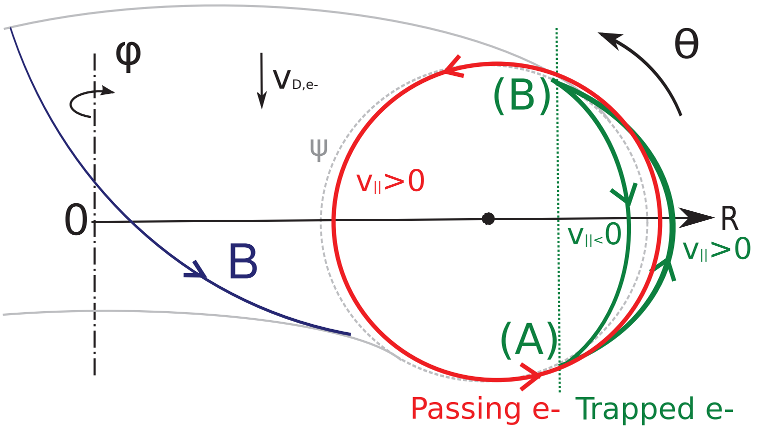

Figure 2.2 – Cartoon of the orbits a passing electron (red) and trapped electron (green) with $v_{\parallel} > 0$, in case of a vertical drift $\mathbf{v}_{D,e-} = -|v_D|\hat{e}_Z$. These orbits are actually projected on a poloidal plane. The gray dashed line symbolizes the magnetic surface on which the particle evolves at leading order.

magnetic field amplitude is maximum. For example in a tokamak, the magnetic field lines are twisted on torus-shaped magnetic surfaces and the magnetic field strength, B, which is roughly proportional to $1/R$, varies along field lines. Therefore, the particle guiding-center, which follows these lines at leading order, evolves from region of low field toward region of strong field with a parallel velocity $v_{\parallel} = \sqrt{2(\mathcal{E}_k - \mu B)/m}$ where $\mathcal{E}_k = mv_{\parallel}^2/2 + \mu B_0$. There might thus exist points on the magnetic field line where $\mathcal{E}_k = \mu B_0$ such that $v_{\parallel} = 0$ and the particle bounces back. Such bouncing particles are called trapped and are identified anywhere in the plasma by the condition on the parallel velocity $v_{\parallel} < v_{\parallel c}$ with

$$v_{\parallel c}(\mathbf{x}, \mu) = \sqrt{2\mu[B_{0,\max}(\psi) - B(\mathbf{x})]/m},$$

where $B_{0,\max}(\psi)$ is the maximum amplitude of the magnetic field on the surface ψ where the particle lies, $\psi = \psi(\mathbf{x})$. The particle which are not trapped are called passing ($v_{\parallel} > v_{\parallel,c}$), see cartoon in figure 2.2.

The passing and trapped particles are actually not exactly lying on a magnetic surface. Their orbits are rather slightly shifted from the surface, because of the existence of velocity drifts and of the twisted nature of the magnetic field lines. A simple way of picturing the origin of this excursion consists in looking at the projection of the guiding-center orbits on a poloidal plane where its vertical velocity is $v_Z = (v_{\parallel}\mathbf{b} + \mathbf{v}_d) \cdot \hat{e}_Z = v_{\parallel,Z} + v_{d,Z}$ and its radial velocity is $v_R = (v_{\parallel}\mathbf{b} + \mathbf{v}_d) \cdot \hat{e}_R = v_{\parallel,R} + v_{d,R}$ (along the horizontal major radius direction). In case that there is no drift, one has $v_Z(v_{\parallel}) = -v_Z(-v_{\parallel})$, $v_R(v_{\parallel}) = -v_R(-v_{\parallel})$, and the particle sticks to a magnetic surface with no excursion. In case that there is a vertical drift such that $sgn(q)v_{d,Z} > 0$ and $v_{d,R} = 0$, the vertical velocity of the particle will change with the sign of $v_{\parallel}$, because $|v_{\parallel,Z} + v_{d,Z}| \neq | - v_{\parallel,Z} + v_{d,Z}|$. In the cartoon of figure 2.2, the influence of the vertical drift on a trapped electron is illustrated with a green curve. Its banana orbit is composed of a trajectory $A \to B$ outside the volume delimited by ψ when $v_{\|} > 0$, and one trajectory $B \to A$ inside the volume delimited by ψ when $v_{\|} < 0$. As illustrated by the variation of safety factor, the particle experiences different curvatures on these two trajectories such that the particle drifts toroidaly after each bounce orbit $(A) \to (B) \to (A)$. A *passing electron* has a parallel velocity of constant sign, such that, compared to the magnetic surface of reference, its orbits is shifted in the horizontal direction. This shift is outward or inward depending on the sign of the parallel velocity. An example of passing electron orbit projection on the poloidal plane is plotted in figure 2.2.

2.3 Vlasov-Maxwell system

Now that the motion of a single particle in an electromagnetic field has been introduced, one is interested to briefly introduce the Vlasov-Maxwell system of equations used for describing the dynamics of a plasma.

The plasma evolution can be described with species particle distribution functions f_σ which obey the Vlasov equation

$$\frac{df_\sigma}{dt} = \frac{\partial f_\sigma}{\partial t} + \dot{\mathbf{x}} \cdot \frac{\partial f_\sigma}{\partial \mathbf{x}} + \dot{\mathbf{v}} \cdot \frac{\partial f_\sigma}{\partial \mathbf{v}} = 0, \tag{2.8}$$

and the self-consistent fields are obtained from the associated Maxwell equations

$$\begin{cases} \nabla \cdot \mathbf{E} = \varrho/\varepsilon_0, & \nabla \times \mathbf{E} + \partial \mathbf{B}/\partial t = 0, \\ \nabla \cdot \mathbf{B} = 0, & \nabla \times \mathbf{B} - \mu_0 \varepsilon_0 \, \partial \mathbf{E}/\partial t = \mu_0 \mathbf{J}, \end{cases} \tag{2.9}$$

where the source terms are obtained from the species contributions

$$\begin{cases} \varrho(\mathbf{x}; t) = \sum_\sigma q_\sigma \int d\mathbf{v} \;\, f_\sigma(\mathbf{x}, \mathbf{v}; t), \\ \mathbf{J}(\mathbf{x}; t) = \sum_\sigma q_\sigma \int d\mathbf{v} \;\, \mathbf{v} f_\sigma(\mathbf{x}, \mathbf{v}; t). \end{cases} \tag{2.10}$$

Note that σ labels the species.

The reversible nature of the Vlasov equation does not allow the distribution function to relax towards an equilibrium. To avoid an endless filamentation of the phase space, nonlinear kinetic simulations require finite dissipation, see reference [Garbet et al., 2010] and references therein. Examples of numerical implementation of dissipation are discussed in section 2.8 on gyrokinetic codes.

2.4 Diamagnetic drift

When considering the plasma as an ensemble of particles, which is the case when using the Vlasov-Maxwell description previously introduced, the diamagnetic nature of particle motion evolving in an inhomogeneous plasma leads to the existence of diamagnetic drifts.

These diamagnetic drifts which result from plasma inhomogeneities, can be illustrated in the case of a simple slab geometry, see thesis [Brunner, 1997]. The slab system consists of: a straight magnetic field of constant amplitude in the direction $\mathbf{b} = \hat{e}_3$, density and temperature gradients in the direction $\hat{e}_1$, and a perturbation in the direction $\hat{e}_2$. The basis $(\hat{e}_1, \hat{e}_2, \mathbf{b})$ is taken orthogonal. In this system, the particle distribution function is entirely defined by its constants of unperturbed motion: $X = \hat{e}_1 \cdot (\mathbf{x} - \boldsymbol{\rho})$ the guiding-center "radial" position and $\mathcal{E}_k$ the particle kinetic energy, such that, at the phase-space position $(\mathbf{x}, \mathbf{v}) = (\mathbf{X} + \boldsymbol{\rho}, v_\parallel \mathbf{b} + \mathbf{v}_\perp)$, the equilibrium distribution function reads $f_0(X, \mathcal{E}_k) \equiv f_0(x + v_y/\Omega, m v_\parallel^2/2 + \mu B_0)$. Taking a guiding-center Maxwellian distribution function for the equilibrium

$$f_M(X, \mathcal{E}_k) = \frac{N(X)}{[2\pi T(X)/m]^{3/2}} \exp\left[-\mathcal{E}_k/T(X)\right],$$

one obtains $f_0(x, \mathcal{E}_k) = f_M(x, \mathcal{E}_k) + \mathcal{O}(\rho/L_c)$ at leading order with $L_c \simeq L_n \simeq L_T$, $1/L_N = -\nabla \ln N$, and $1/L_T = -\nabla \ln T$. At first order in ρ/L_c, the equilibrium particle distribution function in particle variables reads

$$f_0(x, \mathcal{E}_k) = \left[1 + \frac{v_y}{\Omega}\left(\frac{d \ln N}{dx} + \frac{1}{T}\frac{d \ln T}{dx}\frac{\partial}{\partial T}\right)\right] f_M(x, \mathcal{E}_k) + \mathcal{O}(\rho/L_c)^2.$$

From this equilibrium particle distribution function, one can compute the diamagnetic velocity

$$\mathbf{v}^* = \frac{1}{N}\int d\mathbf{v}\, \mathbf{v} f_0(\mathbf{x}, \mathbf{v}) \simeq \frac{1}{N}\left(\frac{d \ln N}{dx} + \frac{1}{T}\frac{d \ln T}{dx}\frac{\partial}{\partial T}\right)\int dv_y \frac{v_y^2}{\Omega} f_M(x, \mathcal{E}_k)\, \hat{e}_y = \frac{-\nabla P \times \mathbf{B}}{q B^2 N}.$$

Note that the direcion of this drift depends on the sign of the species electric charge.

2.5 The gyrokinetic framework

Resolving the 6D Vlasov-Mawell system of equations for studying the tokamak plasma turbulence is beyond today numerical capacities. Nonetheless the core plasma turbulence respects spatial and temporal ordering, *i.e.* the so-called gyrokinetic ordering, and conserves the magnetic moment of particles. The gyrokinetic framework thus uses these features for modeling tokamak turbulence with a reduced 5D Vlasov-Maxwell system of equations by averaging out the fast gyromotion. This reduced system is much less demanding in computational resources for simulating the turbulent transport.

In the following, the equations of motions are obtained in this reduced phase-space, from a variational principle $\delta \int \gamma = 0$ with $\gamma = \mathcal{L}dt$ the Poincaré-Cartan one-form and $\mathcal{L}$ the phase-space Lagrangian expressed in canonical variables $(\mathbf{q}, \mathbf{p})$.

This discussion is based on several references among which references are [Littlejohn, 1983], [Hahm, 1988], [Brizard and Hahm, 2007], [Cary and Brizard, 2009], [Brizard, 2009], and [Abel et al., 2013].

Gyrokinetic ordering

The gyrokinetic ordering, which is valid in the core of the tokamak, is usually summarized by the relation

$$\frac{\omega}{\Omega} \simeq \frac{k_\parallel}{k_\perp} \simeq |k_\perp|\rho_i \frac{e\delta\phi}{T_{0e}} \simeq \frac{\rho_i}{L_N} = \mathcal{O}(\epsilon), \tag{2.11}$$

where $L_N = |\nabla \ln_0|^{-1}$ is the characteristic length scale of the background density.

The turbulence fluctuates at a frequency of the order of the diamagnetic drift frequency, roughly equal to $\omega \simeq \omega^\star \simeq Tk_\perp/qB_0L_N$, which is much smaller than the cyclotron motion of the particles, $\omega/\Omega_0 = \mathcal{O}(\epsilon)$.

The turbulence perturbation, in the core of the fusion reactor, is essentially field aligned $k_\parallel/k_\perp \simeq \mathcal{O}(\epsilon)$.

Electrostatic fluctuations follow the ordering $|k_\perp|\rho_i q\phi/T_0 \simeq \mathcal{O}(\epsilon)$, see [Dimits et al., 1992]. Note that in general one considers regimes for which $|k_\perp\rho_i| \simeq \mathcal{O}(1)$.

The typical turbulence length scale $\lambda_{\text{turb}} \simeq \rho_L$ is small compared to the inverse gradient length of the magnetic field amplitude, $L_B \simeq \nabla \ln B$, such that $\rho_L/L_B = \mathcal{O}(\epsilon_B)$.

The species density and temperature profiles of equilibrium vary smoothly over a distance of about a Larmor radius such that $\rho_L/L_{N,T} = \mathcal{O}(\epsilon)$ where $L_N = |\nabla \ln N_0|^{-1}$ and $L_T = |\nabla \ln T_0|^{-1}$ with N_0 the background density and T_0 the background temperature.

The amplitude of the perturbation is small compared to the background: $\delta N/N_0 \simeq \mathcal{O}(\epsilon)$, $\delta T/T_0 \simeq \mathcal{O}(\epsilon)$, as well as $\delta f/f_0 \simeq \mathcal{O}(\epsilon)$.

The one-form in gyrocenter variables

The dynamics of a particle in an electromagnetic field $(\phi, \mathbf{A})$ can be described by the canonical single particle Hamiltonian: $H = [\mathbf{p} - q\mathbf{A}(\mathbf{q})]^2/2m + q\phi(\mathbf{q}, t)$ where $(\mathbf{q}, \mathbf{p})$ are the canonical coordinates, *i.e.*, $\dot{q} = \partial_{\mathbf{p}}H$ and $\dot{p} = -\partial_{\mathbf{q}}H$. The corresponding Lagrangian is obtained from a Legendre transform, leading to $L = \mathbf{p} \cdot \dot{\mathbf{q}} - H$, and the one-form in non-canonical coordinates, $(\mathbf{x},\mathbf{v}) = (\mathbf{q},\mathbf{p}-q\mathbf{A})$, reads

$$\gamma(\mathbf{x},\mathbf{v}) = \underbrace{[q\mathbf{A}_0(\mathbf{x}) + m\mathbf{v}]\cdot d\mathbf{x} - \frac{mv^2}{2}dt}_{\gamma_0} + \underbrace{-q\delta\phi(\mathbf{x},t)dt + q\delta\mathbf{A}(\mathbf{x},t)\cdot d\mathbf{x}}_{\gamma_1}, \tag{2.12}$$

where $\phi(\mathbf{x};t) = \delta\phi(\mathbf{x};t)$ is a pure perturbation, $\mathbf{A}(\mathbf{x};t) = \mathbf{A}_0(\mathbf{x}) + \delta\mathbf{A}(\mathbf{x};t)$ is decomposed in a background component $\mathbf{A}_0$ and a fluctuating component $\delta\mathbf{A}$, and γ_0 and γ_1 are the respective zero and first order terms of the one-form.

Prior to obtaining the one-form in gyrocenter variables, the one-form is expressed in guiding-center variables $(\mathbf{X}, v_\parallel, \mu, \alpha)$. These guiding-center coordinates are defined by

$$\begin{cases} \mathbf{X} = \mathbf{x} - \boldsymbol{\rho}(\mathbf{X},\mu,\alpha) = \mathbf{x} - [v_\perp(\mathbf{X},\mu)/\Omega_0(\mathbf{X})]\mathbf{a}(\mathbf{X},\alpha) & \text{(guiding center)} \\ \mu = mv_\perp^2/2B_0(\mathbf{X}) & \text{(magnetic moment)} \\ v_\parallel = \mathbf{v}\cdot\mathbf{b} & \text{(parallel velocity)} \\ \alpha = \arctan\left(\mathbf{v}\cdot\hat{e}_1/\mathbf{v}\cdot\hat{e}_2\right), & \text{(gyro angle)} \end{cases} \tag{2.13}$$

where $(\hat{e}_1, \hat{e}_2)$ is an orthonormal basis vector in the plane perpendicular to the magnetic field line at the guiding-center position, $\mathbf{a} = \hat{e}_1\cos\alpha - \hat{e}_2\sin\alpha$, $\mathbf{b} = \mathbf{B}_0/B_0$, $\mathbf{c} = \mathbf{a}\times\mathbf{b} = \partial\mathbf{a}/\partial\alpha = -\hat{e}_1\sin\alpha - \hat{e}_2\cos\alpha$, $\Omega_0(\mathbf{X}) = qB_0(\mathbf{X})/m$, and $\mathbf{v}_\perp = v_\perp\mathbf{c} = \mathbf{v} - v_\parallel\mathbf{b}$. The Jacobian of this change of coordinates is $J_{gc} = |\partial(\mathbf{x},\mathbf{v})/\partial(\mathbf{X},v_\parallel,\mu,\alpha)| = B_{0\parallel}^\star/m$ with $B_{0\parallel}^\star = \mathbf{B}_0^\star\cdot\mathbf{b}$ and $\mathbf{B}_0^\star = \mathbf{B}_0 + (mv_\parallel/q)\nabla\times\mathbf{b}$.

Applying the change of variables from particle to guiding-centers $(\mathbf{x},\mathbf{v}) \mapsto (\mathbf{X}, v_\parallel, \mu, \alpha)$, leads to

$$\gamma_0 = \left[mv_\parallel\mathbf{b} + mv_\perp\mathbf{c} + q\mathbf{A}_0(\mathbf{X}+\boldsymbol{\rho})\right]\cdot d[\mathbf{X}+\boldsymbol{\rho}(\mathbf{X},\mu,\alpha)] - \left[\frac{mv_\parallel^2}{2} + \mu B_0(\mathbf{X})\right]dt, \tag{2.14}$$

where by definition of the guiding center, equation (2.13), one has

$$d\boldsymbol{\rho} = \frac{v_\perp}{\Omega_0(\mathbf{X})}\left[\nabla\mathbf{a}(\mathbf{X},\alpha) - \mathbf{a}(\mathbf{X},\alpha)\nabla\ln B_0(\mathbf{X})\right]\cdot d\mathbf{X} + \frac{\mathbf{a}(\mathbf{X},\alpha)}{qv_\perp}d\mu + \rho(\mathbf{X},\mu)\mathbf{c}(\mathbf{X},\alpha)d\alpha. \tag{2.15}$$

By using the first order expansion $\mathbf{A}_0(\mathbf{X}+\boldsymbol{\rho}) \simeq \mathbf{A}_0(\mathbf{X}) + \boldsymbol{\rho}\cdot\nabla\mathbf{A}_0|_\mathbf{X}$ and keeping the terms at leading (gyrokinetic) order for this change of variable, one obtains the zeroth order (gyro-averaged) one-form in guiding-center variables

$$\Gamma_{gc,0}(\mathbf{X},v_\parallel,\mu) = \underbrace{\left[mv_\parallel\mathbf{b} + q\mathbf{A}_0(\mathbf{X})\right]}_{q\mathbf{A}_0^\star(\mathbf{X},v_\parallel)}\cdot d\mathbf{X} + \frac{m}{q}\mu\, d\alpha - \left[\frac{mv_\parallel^2}{2} + \mu B_0(\mathbf{X})\right]dt. \tag{2.16}$$

The first order component of the guiding-center one-form follows in a straightforward manner

$$\Gamma_{gc,1}(\mathbf{X}, v_\parallel, \mu, \alpha) = -q\delta\phi(\mathbf{X}+\boldsymbol{\rho}, t)dt + q\delta A_\parallel(\mathbf{X}+\boldsymbol{\rho})\mathbf{b}\cdot d\mathbf{X},$$

where $\boldsymbol{\rho} = \boldsymbol{\rho}(\mathbf{X}, \mu, \alpha)$ and only the parallel component of the vector potential is kept, *i.e.*, $\delta\mathbf{A} \simeq \delta A_\parallel \mathbf{b}$.

The perturbed guiding-center one-form depending on the gyroangle, the reduction consists in finding the gyrocenter coordinates for which the one-form is gyrophase-independent. For this purpose, the one-form in gyrocenter coordinates, Γ, is obtained thanks to the transformation $\Gamma = T^{-1}\Gamma_{gc} + dS$ where T^{-1} is the push-forward operator and dS is a phase-space gauge. The inverse of this push-forward operator, namely the pull-back operator, T, is composed of individual Lie transforms, such that $T = ...T_3T_2T_1$ with $T_n = \exp(\epsilon^n \pounds_n)$. Under a Lie derivative, a scalar, s, and a one-form, γ, transform, respectively, as

$$\pounds_n s = \sum_i g_n^i \frac{\partial s}{\partial z^i} \qquad \text{and} \qquad (\pounds_n\gamma)_j = \sum_i g_n^i \left(\frac{\partial \gamma_j}{\partial z^i} - \frac{\partial \gamma_i}{\partial z^j}\right), \tag{2.17}$$

where $g_n^i = \partial Z^i/\partial\epsilon^n$ are the generators of the Lie transformations, Z^i the new coordinates, z^i the original coordinates, and $\gamma = \sum_i \gamma_i dz^i$. The one-form Γ_{gc} is pushed forward up to first order, giving

$$\Gamma = T_1^{-1}(\Gamma_{gc,0} + \Gamma_{gc,1}) + dS_1 + \mathcal{O}(\epsilon^2) = \underbrace{\Gamma_{gc,0}}_{\Gamma_0} \underbrace{-\pounds_1\Gamma_{gc,0} + \Gamma_{gc,1} + dS_1}_{\Gamma_1} + \mathcal{O}(\epsilon^2), \tag{2.18}$$

with $dS_0 = 0$, $g_n^t = 0$ as time in not transformed, and dS_1 is a phase-space gauge. The term Γ_0 is directly identified by noting $\Gamma_0 = \Gamma_{gc,0} + \mathcal{O}(\epsilon)$ which is expected from a near identity transformation. The gauge and generator functions are, at this point, a set of tools which can be used to manufacture the new one-form. It then suffices to take out the gyroangle dependency from the one-form by choosing

$$\Gamma_1 = -q\langle\delta\phi\rangle_\alpha\, dt + q\langle\delta A_\parallel\rangle_\alpha\, \mathbf{b}\cdot d\mathbf{X}, \tag{2.19}$$

so that the generator functions are defined by

$$\begin{cases} g_1^{\mathbf{X}} = \frac{1}{qB_{0\parallel}^\star}\left(\nabla S_1 \times \mathbf{b} - \frac{qB_0^\star}{m}\frac{\partial S_1}{\partial v_\parallel}\right), \\ g_1^\parallel = \frac{1}{mB_{0\parallel}^\star}\nabla S_1\cdot\mathbf{B}_0^\star + \frac{q}{m}\left[A_\parallel(\mathbf{X}+\boldsymbol{\rho}) - \langle A_\parallel\rangle_\alpha(\mathbf{X},\mu)\right], \\ g_1^\mu = \frac{q}{m}\frac{\partial S_1}{\partial\alpha}, \\ g_1^\alpha = -\frac{q}{m}\frac{\partial S_1}{\partial\mu}. \end{cases} \tag{2.20}$$

The operation $\langle\ \rangle_\alpha$ is the gyro-averaging operation. The gyro-averaged electrostatic potential is

$$\langle\delta\phi\rangle_\alpha(\mathbf{X},\mu) = \oint \frac{d\alpha'}{2\pi}\delta\phi(\mathbf{X}+\boldsymbol{\rho}(\mathbf{X},\mu,\alpha')). \tag{2.21}$$

From the definition of the phase-space gauge, one can compute the first-order phase-space gauge

$$S_1(\mathbf{X},\mu,\alpha) = \frac{q}{\Omega_0}\int_0^\alpha d\alpha' \left[\widetilde{\delta\phi}(\mathbf{X},\mu,\alpha') - v_\parallel \widetilde{\delta A_\parallel}(\mathbf{X},\mu,\alpha')\right], \tag{2.22}$$

which contains the non gyro-averaged fields and where the operator $\widetilde{\bullet}$ is the deviation from the gyro-averaged field

$$\widetilde{\delta\phi}(\mathbf{X},\mu,\alpha) = \delta\phi(\mathbf{X}+\boldsymbol{\rho}) - \langle\delta\phi\rangle_\alpha(\mathbf{X},\mu). \tag{2.23}$$

Stopping the derivation at first order (as no higher order terms are implemented in the gyrokinetic codes used in the frame of this thesis work), one obtains an expression for the gyrocenter one-form

$$\begin{aligned}\Gamma(\mathbf{X},v_\parallel,\mu) = q\left[\mathbf{A}_0^\star(\mathbf{X},v_\parallel) + \langle\delta A_\parallel\rangle_\alpha(\mathbf{X},\mu)\,\mathbf{b}\right]\cdot d\mathbf{X} + \frac{m}{q}\mu\,d\alpha \\ - \left[\frac{mv_\parallel^2}{2} + \mu B_0(\mathbf{X}) + q\langle\delta\phi\rangle_\alpha(\mathbf{X},\mu)\right]dt.\end{aligned} \tag{2.24}$$

Equations of motion

The equations of motion are obtained from the variational principle

$$\delta\int dz^i\gamma_i = \delta\int dZ^j\frac{\partial z^i}{\partial Z^j}\gamma_i = \delta\int dZ^j\Gamma_j = 0,$$

which leads to the Euler-Lagrange equations

$$\sum_{j\in\{\mathbf{X},v_\parallel,\mu,\alpha\}}\hat{\omega}_{ij}\frac{dZ^j}{dt} = \left(\frac{\partial\Gamma_i}{\partial t} - \frac{\partial\Gamma_t}{\partial Z_i}\right), \qquad \text{with} \quad \hat{\omega}_{ij} = \left(\frac{\partial\Gamma_i}{\partial Z_j} - \frac{\partial\Gamma_j}{\partial Z_i}\right). \tag{2.25}$$

Therefore using the one-form described in equation (2.24), one obtains

$$\begin{align}
\dot{\mu} &= 0, \tag{2.26}\\
\dot{\alpha} &= \Omega_0 + \Omega_0 \frac{q}{B_0}\frac{\partial}{\partial \mu}\left(\langle \delta\phi\rangle_\alpha - v_\parallel \langle \delta A_\parallel\rangle_\alpha\right), \tag{2.27}\\
\dot{\mathbf{X}} &= \frac{1}{B^\star_{0\parallel}}\left(v_\parallel \mathbf{B}^\star_0 - \frac{\mu}{q}\nabla B_0 \times \mathbf{b} - \nabla\langle \delta\phi\rangle_\alpha \times \mathbf{b} + v_\parallel \nabla \langle \delta A_\parallel\rangle_\alpha \times \mathbf{b}\right), \tag{2.28}\\
\dot{v}_\parallel &= -\frac{\dot{\mathbf{X}}}{m v_\parallel}\cdot\left(\mu\nabla B_0 + q\nabla\langle \delta\phi\rangle_\alpha + q\partial_t \langle \delta A_\parallel\rangle_\alpha \mathbf{b}\right) = -\frac{\dot{\mathbf{X}}}{m v_\parallel}\cdot\left(\mu\nabla B_0 - q\mathbf{E}^\star\right), \tag{2.29}
\end{align}$$

with $\nabla \times (\langle \delta A_\parallel\rangle_\alpha \mathbf{b}) \simeq \nabla\langle \delta A_\parallel\rangle_\alpha \times \mathbf{b}$, $\Omega_0 = \Omega_0(\mathbf{X})$, $\langle\delta\phi\rangle_\alpha = \langle\delta\phi\rangle_\alpha(\mathbf{X},\mu)$, $\langle \delta A_\parallel\rangle_\alpha = \langle \delta A_\parallel\rangle_\alpha(\mathbf{X},\mu)$, $\mathbf{B}^\star_0 = \mathbf{B}^\star_0(\mathbf{X}, v_\parallel) = \nabla \times \mathbf{A}^\star_0$, $\mathbf{A}^\star_0 = \mathbf{A}_0 + (m/q)v_\parallel \mathbf{b}$, $\mathbf{E}^\star = -\nabla\langle\delta\phi\rangle_\alpha - \partial_t\langle \delta A_\parallel \mathbf{b}\rangle_\alpha \mathbf{b}$, $B_0 = B_0(\mathbf{X})$, and $\partial_t \bullet = \partial \bullet / \partial t$ is the partial time derivative.

Equation (2.26), $\dot{\mu} = 0$, proves that the gyrocenter magnetic moment is an exact adiabatic invariant.

Equation (2.27) describes the gyrophase evolution. The first term on the right-hand-side is the cyclotron frequency (zero-th order), the second term is the first order correction related to the perturbation fields. The gyroangle is not evolved in a 5D gyrokinetic code. It is nonetheless interesting to see that the deviation from the cyclotron frequency is related to the perturbations. Indeed, in the limit of vanishing perturbation, the dynamics of guiding centers and gyrocenters are identical.

Equation (2.28) contains the different drift contributions

$$\dot{\mathbf{X}} = v_\parallel \mathbf{b} + \mathbf{v}_\kappa + \mathbf{v}_{\nabla P} + \mathbf{v}_{\nabla B} + \mathbf{v}_{\bar{\mathbf{E}}},$$

with $v_\parallel \mathbf{b}$ the parallel motion, $\mathbf{v}_\kappa$ the kappa drift, $\mathbf{v}_{\nabla P}$ the (kinetic) pressure gradient drift, and $\mathbf{v}_{\bar{\mathbf{E}}}$ the electric drift. The parallel velocity, $v_\parallel \mathbf{b}$, and both drifts $\mathbf{v}_\kappa$ and $\mathbf{v}_{\nabla P}$ are obtained from the decomposition

$$\frac{1}{B^\star_{0\parallel}} v_\parallel \mathbf{B}^\star_0 = v_\parallel \mathbf{b} + \underbrace{\frac{v_\parallel^2}{\Omega_\sigma B^\star_{0\parallel}}\mathbf{b}\times\nabla B_0}_{v_\kappa} + \underbrace{\frac{v_\parallel^2}{\Omega_\sigma B^\star_{0\parallel}}\frac{\mu_0}{B_0}\mathbf{b}\times\nabla P_0}_{v_{\nabla P}}, \tag{2.30}$$

where one employed the relation $B_0 \nabla \times \mathbf{b} = \nabla \times \mathbf{B}_0 \cdot \mathbf{b}\mathbf{b} - \nabla \times \mathbf{B}_0 \times \mathbf{b} \times \mathbf{b} - \nabla B_0 \times \mathbf{b}$ and the ideal MHD equilibrium MHD equation (2.1). The curvature drift is defined by

$$\mathbf{v}_{\text{curv}} = \mathbf{v}_\kappa + \mathbf{v}_{\nabla P} = \frac{v_\parallel^2}{\Omega_\sigma B_0 B^\star_{0\parallel}}\mathbf{b}\times\nabla(B_0^2/2 + \mu_0 P_0),$$

where the pressure gradient contribution is typically small in electrostatic simulations. The plasma pressure is often normalized to the magnetic one, and referred to as the quantity $\beta = P_0/2\mu_0 B_0^2$. The second term of the right-hand-side of equation (2.28) is the "grad B" drift, $\mathbf{v}_{\nabla B} = (\mu/qB^\star_{0\|})\mathbf{b}\times\nabla B_0$, which can be associated with the kappa drift to give

$$\mathbf{v}_\kappa + \mathbf{v}_{\nabla B} = \frac{1}{\Omega_0 B^\star_{0\|}}(v_\|^2 + v_\perp^2/2)\mathbf{b}\times\nabla B_0.$$

The third and fourth terms of equation (2.28) can be regrouped in a perturbation drift

$$\mathbf{v}_{\bar{\mathbf{E}}} = \bar{\mathbf{E}}\times\mathbf{b}\,/B^\star_{0\|} = -\nabla\langle\delta\phi - v_\|\delta A_\|\rangle_\alpha \times \mathbf{b}\,/B^\star_{0\|},$$

with $\bar{\mathbf{E}} = -\nabla\langle\delta\phi - v_\|\delta A_\|\rangle_\alpha$. The quantity $\langle\delta\phi - v_\|\delta A_\|\rangle_\alpha$ is sometimes referred to as the gyrokinetic potential [Merz, 2009, Lapillonne, 2010].

The equation (2.29) describes the evolution of the parallel velocity. The first term of the RHS, which is proportional to $\mu\nabla B_0$, is related to the diamagnetic force acting on the particle, it is the term which can cancel the parallel velocity of trapped particles along the unperturbed trajectories. The other terms of the RHS correspond to the particle interaction with the perturbation which take the form of an electric force $q\mathbf{E}^\star = -q(\nabla\langle\delta\phi\rangle_\alpha + \partial_t\langle\delta A_\|\rangle_\alpha\mathbf{b})$.

Note that in case of purely electrostatic perturbations ($\delta A_\| = 0$), the equations simplify with $\bar{\mathbf{E}} = \mathbf{E}$ and $\mathbf{E}^\star = \mathbf{E}$.

The gyrokinetic equation

The gyrokinetic equation is a 5D reduced Vlasov equation, expressed in gyrocenter variables:

$$\frac{df_\sigma}{dt} = \frac{\partial f_\sigma}{\partial t} + \dot{\mathbf{X}}\cdot\frac{\partial f_\sigma}{\partial\mathbf{X}} + \dot{v}_\|\cdot\frac{\partial f_\sigma}{\partial v_\|} = 0, \tag{2.31}$$

having taken into account $\dot{\mu} = 0$ and $\partial f_\sigma/\partial\alpha = 0$.

The particle distribution function is split into a stationary background term $f_{\sigma 0}$ and a time-dependent perturbation term δf_σ, such that $f_\sigma = f_{\sigma 0} + \delta f_\sigma$. The subscript σ labels the plasma particle species.

The stationary background particle distribution function is usually taken as a near equilibrium solution to the unperturbed gyrokinetic equation

$$\left.\frac{df_{\sigma 0}}{dt}\right|_{u.t.} = \frac{1}{B^\star_{0\|}}\left(v_\|\mathbf{B}_0^\star + \mathbf{b}\times\nabla B_0\right)\cdot\left(\frac{\partial f_{\sigma 0}}{\partial\mathbf{X}} - \frac{1}{v_\| m_\sigma}\mu\nabla B_0\frac{\partial f_{\sigma 0}}{\partial v_\|}\right) = 0, \tag{2.32}$$

where $d/dt|_{u.t.}$ is the total time derivative along unperturbed trajectories. This choice leads to the following gyrokinetic equation

$$
\begin{aligned}
0 \;=\;& \frac{\partial \delta f_\sigma}{\partial t} + \frac{1}{B^\star_{0\parallel}} \bar{\mathbf{E}} \times \mathbf{b} \cdot \left(\frac{\partial f_{\sigma 0}}{\partial \mathbf{X}} - \frac{1}{v_\parallel m_\sigma} \mu \nabla B_0 \frac{\partial f_{\sigma 0}}{\partial v_\parallel} \right) \\
+\;& \frac{1}{B^\star_{0\parallel}} \left(v_\parallel \mathbf{B}^\star_0 - \frac{\mu}{q} \nabla B_0 \times \mathbf{b} + \bar{\mathbf{E}} \times \mathbf{b} \right) \cdot \left(\frac{\partial \delta f_\sigma}{\partial \mathbf{X}} + \frac{1}{v_\parallel m_\sigma} q \mathbf{E}^\star \frac{\partial f_{\sigma 0}}{\partial v_\parallel} \right) \\
-\;& \frac{1}{v_\parallel m_\sigma B^\star_{0\parallel}} \left(v_\parallel \mathbf{B}^\star_0 - \frac{\mu}{q} \nabla B_0 \times \mathbf{b} + \bar{\mathbf{E}} \times \mathbf{b} \right) \cdot \left(\mu \nabla B_0 - q \mathbf{E}^\star \right) \frac{\partial \delta f_\sigma}{\partial v_\parallel}.
\end{aligned}
\tag{2.33}
$$

Gyrokinetic field equations

The self consistent perturbation fields can be computed from the perturbation source terms. These sources are defined as moments of the particle distribution functions. The particle distribution functions are recovered from the gyrocenter distribution functions by means of the pull-back operator $T_\epsilon = T_{gc} T$

$$
f(\mathbf{x}, \mathbf{v}) = T_{gc} f_{gc}(T_{gc}^{-1} \mathbf{Z}_{gc}) = T_\varepsilon \bar{f}(T_\varepsilon^{-1} \bar{\mathbf{Z}}),
$$

with T_{gc} the pull-back from guiding-center to particles, which is implicitly defined by the system of equations (2.13), and T the pull-back from gyrocenter to guiding-center, which is defined by the generator transformations (2.20). Note that, in this subsection, we use a bar over the gyrocenter distribution function, for clarity. In other part of the thesis, such a distinction is not made .

In the frame of this thesis work, the pull-back transformation involves only terms which are linear in the perturbation, such that

$$
f_{\sigma,gc} = \bar{f}_{\sigma 0} + \delta \bar{f}_\sigma + \frac{q_\sigma}{B_0} \widetilde{\delta\phi} \frac{\partial \bar{f}_{\sigma 0}}{\partial \mu} + \frac{q_\sigma}{m_\sigma} \widetilde{\delta A_\parallel} \frac{\partial \bar{f}_{\sigma 0}}{\partial v_\parallel} - \frac{q_\sigma}{B_0} v_\parallel \widetilde{\delta A_\parallel} \frac{\partial \bar{f}_{\sigma 0}}{\partial \mu} + \mathcal{O}(\epsilon^2),
$$

having neglected higher order terms. Higher order terms are mentioned when discussing equation (4.1). In case of a Maxwellian distribution function, $\bar{f}_{\sigma 0}(v_\parallel, \mu) \propto \exp -(m_\sigma v_\parallel^2 / 2T_\sigma + \mu B_0 / T_\sigma)$, this equation simplifies into

$$
f_{\sigma,gc} = \bar{f}_{\sigma 0} + \delta \bar{f}_\sigma + \frac{q_\sigma}{B_0} \widetilde{\delta\phi} \frac{\partial \bar{f}_{\sigma 0}}{\partial \mu} + \mathcal{O}(\epsilon^2),
$$

because in this case $(q_\sigma / m_\sigma) \widetilde{\delta A_\parallel} \partial \bar{f}_{\sigma 0} / \partial v_\parallel - (q_\sigma / B_0) v_\parallel \widetilde{\delta A_\parallel} \partial \bar{f}_{\sigma 0} / \partial \mu = 0$.

The *Poisson equation*, $-\nabla^2 \delta\phi = \sum_\sigma \varrho_\sigma$, for solving the electrostatic field consistently is replaced by the quasi-neutrality equation, $\sum_\sigma \varrho_\sigma{=}0$, where ϱ_σ symbolizes the species charge density $\varrho_\sigma = q_\sigma N_\sigma = q_\sigma \int d^3v f_\sigma$. This approximation is valid because, in the core of the tokamak, the deviation from quasi-neutrality is small compared to the charge density contributions, *i.e.*, $|\nabla^2\phi/\varrho_\sigma| \ll 1$. In case of a Maxwellian gyrocenter distribution function, the particle density is

$$\begin{aligned} N_\sigma(\mathbf{x}) &= \int d\mathbf{Z}\,\delta(\mathbf{X}+\rho-\mathbf{x})\,T\bar{f}_\sigma(\mathbf{X},v_\parallel,\mu) \\ &= N_0(\mathbf{x}) + \int d\mathbf{Z}\,\delta(\mathbf{X}+\rho-\mathbf{x})\left[\delta\bar{f}_\sigma + \frac{q_\sigma}{B_0}\widetilde{\delta\phi}\frac{\partial\bar{f}_{\sigma0}}{\partial\mu}\right] + \mathcal{O}(\epsilon^2), \end{aligned}$$

and one obtains the gyrokinetic quasi-neutrality equation for the self-consistent field

$$\delta\phi = \left\{\sum_\sigma \int d\mathbf{Z}\,\delta(\mathbf{X}+\rho-\mathbf{x})\frac{q_\sigma}{B_0}\frac{\partial\bar{f}_{\sigma0}}{\partial\mu}\,\widetilde{\bullet}\right\}^{-1} \sum_\sigma \int d\mathbf{Z}\,\delta(\mathbf{X}+\rho-\mathbf{x})\delta\bar{f}_\sigma. \tag{2.34}$$

In the frame of this thesis work, this integral equation for solving the self consistent electrostatic field has been implemented in the ORB5 code, see chapter 4.

The *Ampère equation*, $\nabla\times\nabla\times\mathbf{A} = \mu_0\sum_\sigma \mathbf{J}_\sigma$, for solving the potential vector consistently is replaced by the parallel Ampère law $\nabla_\perp^2\delta A_\parallel = \mu_0\sum_\sigma \delta J_{\parallel\sigma}$. In case of a Maxwellian gyrocenter distribution function, the parallel current perturbation is

$$\delta J_{\parallel,\sigma}(\mathbf{x}) = q_\sigma \int d\mathbf{Z}\,\delta(\mathbf{X}+\rho-\mathbf{x})v_\parallel\delta\bar{f}_\sigma + \mathcal{O}(\epsilon^2),$$

and one recovers the gyrokinetic parallel Ampere equation

$$\delta A_\parallel = \left\{\nabla_\perp^2\right\}^{-1}\sum_\sigma q_\sigma \int d\mathbf{Z}\,\delta(\mathbf{X}+\rho-\mathbf{x})v_\parallel\delta\bar{f}_\sigma + \mathcal{O}(\epsilon^2). \tag{2.35}$$

This equation is in general not solved in this form but, for example, in the form

$$\begin{aligned} \delta A_\parallel = &\left\{\nabla_\perp^2 + \sum_\sigma \int d\mathbf{Z}\,\delta(\mathbf{X}+\rho-\mathbf{x})v_\parallel\frac{q}{m}\langle\bullet\rangle_\alpha\frac{\partial\bar{f}_{\sigma0}}{\partial v_\parallel}\right\}^{-1} \\ &\times\left[\sum_\sigma q_\sigma \int d\mathbf{Z}\,\delta(\mathbf{X}+\rho-\mathbf{x})v_\parallel\delta g_\sigma\right] + \mathcal{O}(\epsilon^2), \end{aligned} \tag{2.36}$$

with $\delta g_\sigma = \delta\bar{f}_\sigma - (q/m)\langle\delta A_\parallel\rangle_\alpha\partial\bar{f}_{\sigma0}/\partial v_\parallel$, see reference [Told, 2012]. Other form can be considered [Bottino et al., 2010, Biancalani et al., 2016] by using $p_\parallel = mv_\parallel + q\langle\delta\mathbf{A}_\parallel\rangle_\alpha$ instead of $v_\parallel$.

Background particle distribution function

The splitting of the particle distribution function into a background and a perturbation, $f = f_0 + \delta f$, is preferably made such that f_0 is a solution to the unperturbed gyrokinetic equation, $df_0/dt|_{u.t.} = 0$. This choice is practical for obtaining linearized Vlasov-Maxwell equations when doing basic stability analysis, as well as for optimizing the signal to noise ratio in numerical simulations based on a Particle-in-Cell (PIC) representation of the phase space such as in the ORB5 code, see section 2.8 on gyrokinetic codes.

Any function of the unperturbed constants of motion is a solution of the unperturbed gyrokinetic equation. Usually, a Maxwellian distribution is assumed, which we call here "canonical" Maxwellian. This canonical Maxwellian distribution function which is solution to the unperturbed gyrokinetic equation reads

$$f_{0,can}(\mathcal{E}_k, \mu, \Psi) = \frac{N_{eq}(\Psi)}{[2\pi T_0(\Psi)/m]^{3/2}} \exp\left[-\mathcal{E}_k/T_0(\Psi)\right],$$

where $\mathcal{E}_k = mv_\parallel^2/2 + \mu B_0$ is the kinetic energy and $\Psi = \Psi(\psi_0, \mathcal{E}_k, \mu)$. We define $\Psi(\psi_0, \mathcal{E}_k, \mu) = \psi_0 + \psi_{0\mathrm{corr}}$ with $\psi_0 = q^{-1}\partial L/\partial\dot{\varphi} = \psi + v_\parallel\, mRB_\varphi/B$ the toroidal canonical momentum and

$$\psi_{0\mathrm{corr}} = -sign(v_\parallel)(q/m)R_0\sqrt{2(\mathcal{E}_k - \mu B_{\max})}\ \mathcal{H}(\mathcal{E}_k - \mu B_{\max}),$$

see reference [Angelino et al., 2006] .

A local Maxwellian which is not an exact solution to the unperturbed gyrokinetic equation can also be used. It reads

$$f_{0,loc}(\mathcal{E}_k, \mu, \psi) = \frac{N_{eq}(\psi)}{[2\pi T_0(\psi)/m]^{3/2}} \exp\left[-\mathcal{E}_k/T_0(\psi)\right],$$

which is function of the magnetic flux ψ.

Let us specify that one makes the difference in between N_0 and N_{eq}, so that the background quasi neutrality ($q_i N_{0i} - q_e N_{0e} = 0$) is ensured. For example, in ORB5, the electron background profile is computed numerically from the ion gyrodensity, *i.e.*, $N_{0e} = N_{0i}^{\mathrm{gy}} = \int d\mathbf{Z}\delta(\mathbf{X} + \boldsymbol{\rho} - \mathbf{x}) f_{i0}$, see reference [Angelino et al., 2006].

Gyrokinetic moments and fluxes

For each species, we are interested in observing macroscopic quantities which are moments of the species distribution functions. These observables should be obtained from the pulled back gyrocenter distribution function

$$\mathcal{A}_\sigma = \langle a \rangle_{Tf_\sigma}(\mathbf{x}) = \int d\mathbf{X} \int_V d\mu dv_\parallel \oint d\alpha \frac{B^\star_{0\parallel}}{m_\sigma} \delta(\mathbf{X}+\boldsymbol{\rho}-\mathbf{x}) a(\mathbf{X}, v_\parallel, \mu)\, Tf_\sigma(\mathbf{X}, v_\parallel, \mu), \quad (2.37)$$

where $\mathcal{A}_\sigma$ is a moment of the distribution Tf_σ weighted by $a(\mathbf{X}, v_\parallel, \mu)$. At leading order in $\delta f_\sigma / f_{\sigma 0}$ these moments are obtained from the background distribution function. One thus has $\mathcal{A} = \mathcal{A}_0 + \delta\mathcal{A} \simeq \langle a \rangle_{f_{\sigma 0}} + \langle a \rangle_{\delta f_\sigma} + \langle a \rangle_{\pounds_1 f_{\sigma 0}}$, according to the definition of the pull-back T. In electrostatic simulations the moment computed from $\pounds_1 f_0$ is a polarization correction and requires only the knowledge of $\delta\phi$.

The main quantities of interest for a species σ are:

- The gyro density: $\delta N_\sigma = \langle 1 \rangle_{\delta f_\sigma + \pounds_1 f_{\sigma 0}}$.
- The parallel fluid velocity: $\delta u_{\parallel,\sigma} = \langle v_\parallel \rangle_{\delta f_\sigma + \pounds_1 f_{\sigma 0}} / N_{\sigma 0}$.
- The parallel temperature: $\delta T_{\parallel,\sigma} = \langle (v_\parallel - \delta u_{\parallel,\sigma})^2 \rangle_{\delta f_\sigma + \pounds_1 f_{\sigma 0}} - T_{\sigma 0} \delta N_\sigma / N_{\sigma 0}$.
- The perpendicular temperature: $\delta T_{\perp,\sigma} = \langle v_\perp^2 \rangle_{\delta f_\sigma + \pounds_1 f_{\sigma 0}} - T_{\sigma 0} \delta N_\sigma / N_{\sigma 0}$.
- The particle flux: $\mathbf{\Gamma}_\sigma = \langle \mathbf{v}_{\bar{E}} \rangle_{\delta f_\sigma + \pounds_1 f_{\sigma 0}} \simeq \mathbf{v}_E\, \delta N_\sigma$.
- The kinetic energy flux: $\mathbf{Q}_\sigma = \langle \mathbf{v}_{\bar{E}}\, m_\sigma v^2/2 \rangle_{\delta f_\sigma + \pounds_1 f_{\sigma 0}} \simeq \mathbf{v}_E\, \langle m_\sigma v^2/2 \rangle_{\delta f_\sigma + \pounds_1 f_{\sigma 0}}$.
- The parallel momentum transport: $\mathbf{\Pi}_\sigma = \langle \mathbf{v}_{\bar{E}}\, m_\sigma v_\parallel \rangle_{\delta f_\sigma + \pounds_1 f_{\sigma 0}} \simeq \mathbf{v}_E\, m_\sigma \delta u_{\parallel,\sigma}$.

Note that these species diagnostics can be furthermore split into subgroups: *e.g.* passing/trapped and subthermal/suprathermal. This can be done by splitting the velocity phase-space volume V, used for integrating equation (2.37), into subgroups g of volume V_g, such that $V = \sum_g V_g$.

Diagnostics implemented for GENE in the chapter 3 of this thesis work are based on these definitions. New 3D diagnostics have been implemented in ORB5, see chapter 5. In these new diagnostics the moments are split into these species subgroups: passing/trapped and subthermal/suprathermal.

2.6 The electron models

The electrostatic ($\delta\phi$) plasma turbulence which is driven by the ions or by the bounce-averaged motion of the trapped electrons is typically evolving at a velocity of the order of the sound speed $c_s \simeq \sqrt{T_{e0}/m_i}$. This turbulence motion is slow in comparison with the fast parallel motion of the electrons which is of the order of the thermal velocity, $v_{the} = \sqrt{T_{e0}/m_e}$. It is therefore a good approximation to assume that these electrons respond instantaneously to the electrostatic turbulence, as long as the following ordering holds

$$|\omega/k_\parallel| \ll v_{\mathrm{th,e}} \qquad \text{“Adiabatic electron condition”.}$$

The *adiabatic* electron response to the electrostatic perturbation $\delta\phi$ can be obtained from the fluid description of the parallel force balance in which the electron mass is neglected $m_e = 0$ and the electron population is assumed isothermal on a magnetic surface $T_{e0} = T_{e0}(\psi)$, leading to

$$m_e \frac{dv_e}{dt} = \nabla_\parallel P_e + eN_e \nabla_\parallel \delta\phi \qquad \rightarrow \qquad 0 = T_{0e}\nabla_\parallel N_e + eN_{0e}\nabla_\parallel \delta\phi.$$

The solution of this equation is $N_e = N_{0e} \exp\left(e\delta\phi/T_{0e}\right) + cst$ with cst a constant. In a tokamak, this constant is chosen such as to have a constant density over the magnetic surfaces, giving an expression for the density perturbation

$$\delta N_e^{ad} = \frac{eN_{0e}}{T_{0e}} \left(\delta\phi - \langle\delta\phi\rangle_{FS}\right). \tag{2.38}$$

This expression for the electron density perturbation can substitute the gyrokinetic electron response in the quasi-neutrality equation. This model is referred to as the adiabatic electron model. Numerically, one does not need to evolve the electron distribution function when using this model.

A *hybrid electron* model is also used for approximating the electron response. In this case the passing electrons are also adiabatic but the trapped electrons are kinetic. Indeed, the kinetic description of the trapped electron dynamics is required for describing their precessional drift motion which is at the origin of the trapped electron mode (TEM) instability, see section 2.7. The hybrid electron response to the electrostatic perturbation is thus computed from equation

$$\delta N_e^{\mathrm{hyb}} = (1-\alpha_t)\frac{eN_{e0}}{T_{e0}}(\delta\phi - \langle\delta\phi\rangle_{\mathrm{FS}}) + \int_{\mathrm{trp}} d\mathbf{Z}\, \delta(\mathbf{X}+\rho_e-\mathbf{x}) \left(\delta f_e + \frac{q}{B_0}\widetilde{\delta\phi}\frac{\partial f_{e0}}{\partial\mu}\right), \tag{2.39}$$

where α_t is the trapped electron fraction

$$\alpha_t = \int_{\mathrm{V=trap}} d^3v\, \frac{f_{e0}}{N_{e0}} = \sqrt{1 - \frac{B_0}{B_{0,\mathrm{max}}(x)}}. \tag{2.40}$$

For the case of a Maxwellian distribution function f_{e0} with constant background quantities, such as in flux tube geometry, this equation can be approximated by

$$\delta N_e^{\mathrm{hyb}} \simeq (1-\alpha_t)\frac{eN_{e0}}{T_{e0}}(\delta\phi - \langle\delta\phi\rangle_{\mathrm{FS}}) + 2\pi\int_0^{+\infty} d\mu \int_{-v_{\parallel c}}^{+v_{\parallel c}} dv_\parallel \frac{B_{0\parallel}^\star}{m_e}\langle\delta f_e\rangle_\alpha$$
$$+ \quad \alpha_t\frac{eN_{e0}}{T_{e0}}\delta\phi - \frac{eN_{e0}B_0}{T_{e0}^2}\mathrm{erf}\left(\frac{v_{\parallel c}}{2v_{the}}\right)\int_0^{+\infty} d\mu\langle\langle\delta\phi\rangle\rangle_\alpha \exp\left(-\frac{\mu B_0}{T_{e0}}\right), \quad (2.41)$$

where in the first line the fluctuating component of the electron charge density on the right hand side yields two contributions: the first term from the passing particles, handled adiabatically, and the other terms from the trapped particles, handled kinetically. The trapped electron contribution, at a position $\mathbf{x}$, is obtained by integrating the kinetic estimate over the velocity phase-space volume of trapped particles $\int_{V=\mathrm{trp}} d\mu dv_\parallel = \int_0^{+\infty} d\mu \int_{-v_{\parallel c}}^{+v_{\parallel c}} dv_\parallel$. In equation (2.39) the presence of the error function, $\mathrm{erf}(x) = (2/\sqrt{\pi})\int_0^x dt\, e^{-t^2}$, results from the analytical integration of the background Maxwellian distribution appearing in the polarization drift term over the parallel velocity phase-space of trapped electrons. Note that in the limit of $\alpha_t \to 0$ ($v_{\parallel c} \to 0$), one recovers the adiabatic model of equation (2.38) from equation (2.39).

In a gyrokinetic code, when using this hybrid model, the distribution for both trapped and passing electrons must be evolved, because the microturbulence perturbation of the particle trajectories can lead to passing particles becoming trapped and *vice versa*.

The gyro *kinetic model* is also used. In this case both trapped and passing are evolved kinetically, and the electron density perturbation reads

$$\delta N_e^{kin} = \int d\mathbf{Z}\,\delta(\mathbf{X} + \rho_e - \mathbf{x})\left(\delta f_e + \frac{q}{B_0}\widetilde{\delta\phi}\frac{\partial f_{e0}}{\partial\mu}\right). \quad (2.42)$$

In case of a Maxwellian distribution function f_{e0} with constant background quantities, such as it is the case in flux tube geometry, this equation can be approximated by

$$\delta N_e^{kin} \simeq 2\pi\int_0^{+\infty} d\mu \int_{-\infty}^{+\infty} dv_\parallel \frac{B_{0\parallel}^\star}{m_e}\langle\delta f_e\rangle_\alpha$$
$$+ \frac{eN_{e0}}{T_{e0}}\left[\delta\phi - \frac{B_0}{T_{e0}}\int_0^{+\infty} d\mu\langle\langle\delta\phi\rangle\rangle_\alpha \exp\left(-\frac{\mu B_0}{T_{e0}}\right)\right].$$

In the second line, the background Maxwellian distribution function appearing in the polarization-drift term has been analytically integrated over the $v_\parallel$ variable. This response corresponds to the hybrid electron response in the limit $v_{\parallel c} \to \infty$ ($\alpha_t \to 1$) where all electrons are handled kinetically. The operator $\langle\langle\phi\rangle\rangle_\alpha$ is computed from

$$\langle\langle\phi\rangle\rangle_\alpha = \oint\frac{d\alpha}{2\pi}\oint\frac{d\alpha'}{2\pi}\,\delta\phi\left(\mathbf{X} + \boldsymbol{\rho}(\mathbf{X},\mu,\alpha) - \boldsymbol{\rho}'(\mathbf{X}+\boldsymbol{\rho},\mu,\alpha')\right).$$

A *drift kinetic* model for electrons can also be used. This model is equivalent to the gyro kinetic model in the limit of small electron mass such that the gyrocenter polarization is neglected, $\widetilde{\delta\phi} \simeq 0$. This approximation is valid in the turbulent regimes of interest for this thesis work. It gives

$$\delta N_e^{kin} \;=\; \int d\mathbf{Z}\,\delta(\mathbf{X}+\rho_e-\mathbf{x})\,\delta f_e = 2\pi\int_0^{+\infty} d\mu \int_{-\infty}^{+\infty} dv_\parallel\,\frac{B^\star_{0\parallel}}{m_e}\,\langle\delta f_e\rangle_\alpha. \qquad (2.43)$$

2.7 Micro-instabilities

The ion temperature gradient (ITG) and the trapped electron mode (TEM) are turbulent electrostatic regimes studied in the frame of this thesis work. The electron temperature gradient (ETG) electrostatic regime and other electromagnetic turbulence have not been studied in the frame of this thesis work.

The ITG and TEM unstable modes are illustrated in the following subsections with local dispersion relations. Such local studies were introduced in reference [Catto, 1978] and furthermore studied in references [Romanelli and Briguglio, 1990, Brunner, 1997] (non exhaustive list). The influence of the kinetic response of the passing electrons will be introduced and studied in more detail in chapter 3.

Ion temperature gradient (ITG)

See figure 2.3 and caption for a qualitative description of the toroidal ITG destabilizing mechanism.

The linearized version of the gyrokinetic equation (2.33) for the ion gyrokinetic non-adiabatic response is $\delta h_i = \delta f_i - q_i\langle\delta\phi\rangle_\alpha f_{i0}/T_{i0}$

$$\left.\frac{d}{dt}\right|_{u.t}\delta h_i = \frac{\nabla\langle\delta\phi\rangle_\alpha\times\mathbf{b}}{B^\star_{0\parallel}}\cdot\nabla\psi\left[\partial_\psi \ln N_{i0} + \partial_\psi \ln T_{i0}\left(\frac{\mathcal{E}_k}{T_{i0}}-\frac{3}{2}\right)\right] f_{i0} + \frac{q f_{i0}}{T_{i0}}\frac{\partial\langle\delta\phi\rangle_\alpha}{\partial t},$$

with $d/dt|_{u.t.}$ the total derivative along the unperturbed trajectories defined by equation (2.32), $f_{i0}(\psi,\mu,\epsilon)$ a local Maxwellian, $\mathcal{E}_k = m_i v_\parallel^2/2 + \mu B_0$ the ion kinetic energy, and neglecting the term propotionnal to $\partial\delta h_i/\partial v_\parallel$.

The non-adiabatic ion response is thus given by equation

$$\widehat{\delta h}_i(\omega,\mathbf{k}) = \frac{q_i}{T_{i0}}\widehat{\delta\phi} J_0(k_\perp v_\perp/\Omega_i)\frac{\omega-\omega_i^*}{\omega - k_\parallel v_\parallel - \omega_{Di}} f_{i0},$$

with $\omega_i^* = \omega_{Ni}(1+\eta_i T_i\partial_{T_i})$, $\omega_{Ni} = -k_y T_i/q_i B_0 L_N$, $1/L_N = |\nabla \ln N_{i0}|$, $1/L_{Ti} = |\nabla \ln T_{i0}|$,

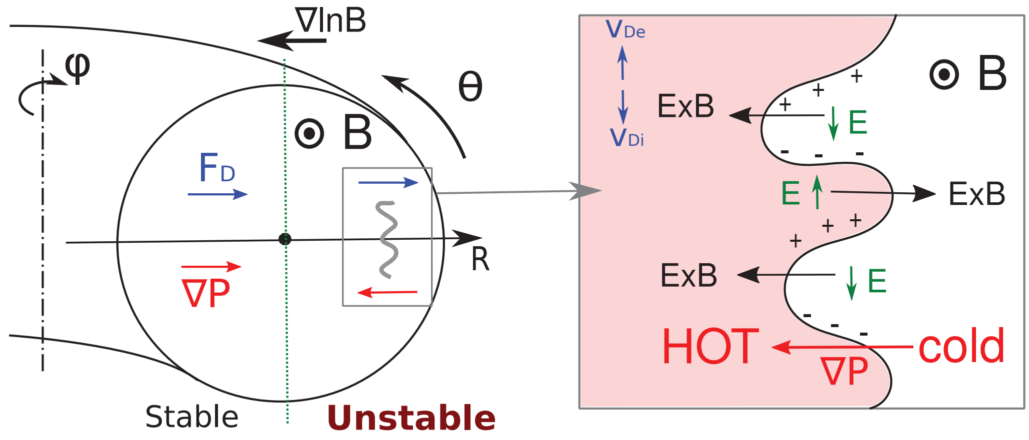

Figure 2.3 – Cartoon of the ITG destabilization. The ion and electrons species experience vertical averaged drifts $\langle v_{D\sigma}\rangle = \langle v_{\text{curv}} + v_{\nabla B}\rangle = 2N_\sigma T_\sigma \mathbf{b} \times \nabla \ln B_0/q_\sigma$ in opposite directions which causes a charge separation and thus an electric drift. This electric drift furthermore amplify the perturbation on the unfavorable side of the tokamak.

$\eta_i = L_N/L_{Ti}$, $\omega_{Di} = -k_y(v_\parallel^2 + v_\perp^2/2)/\Omega_0 B_0 L_B$, k_y is the wave vector in the binormal direction $\mathbf{y} = \mathbf{b} \times \nabla\psi/|\nabla\psi|$, J_0 is the Bessel function, $\delta h = \sum_{\omega,\mathbf{k}} \widehat{\delta h}(\omega, \mathbf{k}) e^{-\imath(\omega t - \mathbf{k}.\mathbf{X})}$, and $\delta\phi = \sum_{\omega,\mathbf{k}} \widehat{\delta\phi}(\omega, \mathbf{k}) e^{-\imath(\omega t - \mathbf{k}.\mathbf{X})}$.

Finally, the adiabatic electron dispersion relation, $\epsilon(\omega, \mathbf{k}) = 0$, is obtained from the quasi-neutrality equation when considering kinetic ions (δf_i), adiabatic electrons, and a quasi neutral background $N_{e0} = Z_i N_{i0}$, thus leading to

$$0 = \frac{T_{i0}}{T_{e0}} + Z_i \left[1 - \int d^3v \, J_0^2\left(\frac{k_\perp v_\perp}{\Omega_i}\right) \frac{\omega - \omega_i^*}{\omega - k_\parallel v_\parallel - \omega_{Di}} \frac{f_{i0}}{N_{i0}}\right], \tag{2.44}$$

where there is an additional J_0 term in the ion kinetic response because of the guiding-center to particle transformation ($\oint d\alpha e^{\boldsymbol{\rho}\cdot\mathbf{k}}$), and $q_i = Z_i e$.

This dispersion relation can be simplified in a fluid limit $|\omega/k_\parallel v_{thi}| \gg 1$, with slow guiding-center drifts $|\omega_{Di}/\omega| \simeq |\omega_{Di}/\omega^*| \ll 1$ and by keeping finite Larmor radius effect at low order $J_0^2(\xi) \simeq 1 - \xi^2/2$. These approximations lead to

$$0 = \frac{T_{i0}}{T_{e0} Z_i} + \frac{\omega_{Ni}}{\omega} + \left[1 - \frac{\omega_N}{\omega}(1 + \eta_i)\right] \left(k_\perp^2 \rho_\perp^2 - \frac{\langle\omega_{Di}\rangle}{\omega} - \frac{k_\parallel^2 v_{thi}^2}{\omega^2}\right),$$

where $\langle\omega_{Di}\rangle = \int dv \, \omega_{Di} f_{i0}/N_{i0} = -2T_{i0}k_\perp/q_i B_0 L_B$ is the drift frequency moment of the Maxwellian distribution function. A first solution can be obtained for the case of a homogeneous equilibrium with no diamagnetic drift $\omega^* = 0$ and no force drift $\omega_{Di} = 0$. In this case, the dispersion relation $\omega^2 = k_\parallel^2 c_s^2/(1 + k_\perp^2 \rho_s^2)$ keeps FLR effects. A second solution, illustrating the interchange nature of the toroidal ITG, can be found in the particular case of $k_\parallel \simeq 0$ (field aligned), $\omega_{Ni}(1 + \eta_i) \simeq \omega_{T_i}$ (ITG), and keeping $\omega_{Di} \neq 0$

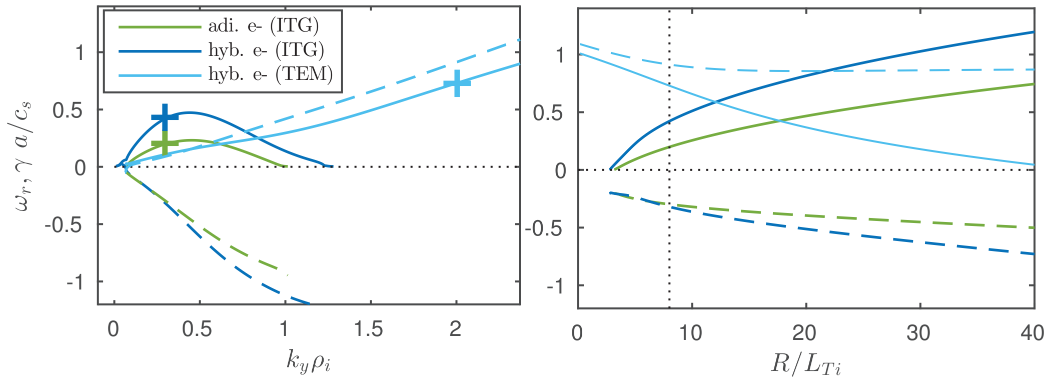

Figure 2.4 – Local dispersion relation obtained with the adiabatic electron model (green) and with the hybrid electron model (light blue and dark blue). The growth rates are plotted with full lines and the real frequencies are plotted with dashed lines. The crosses in subplot (a) indicates the point from which the scan with respect to R/L_{Ti} is carried out in subplot (b).

(toroidal). In this particular case the dispersion relation simplifies into

$$0 = \omega^2 \left(1 + \frac{T_{i0}}{T_{e0} Z_i}\right) - \omega \left(\omega_{Ti} k_\perp^2 \rho_\perp^2 - \langle\omega_{Di}\rangle\right) + \omega_{Ti}\omega_{Di},$$

which has unstable branches for $\Delta = \left(\omega_{Ti} k_\perp^2 \rho_\perp^2 - \langle\omega_{Di}\rangle\right)^2 - 4\left(1 + \frac{T_{i0}}{T_{e0} Z_i}\right)\omega_{Ti}\langle\omega_{Di}\rangle < 0$. This condition, only possible if $\omega_{Ti}\langle\omega_{Di}\rangle > 0$, thus illustrates the interchange nature of the toroidal ITG instability. In our approximation $|\langle\omega_{Di}\rangle/\omega_{Ti}| \ll 1$ so that increasing $k_\perp^2\rho_\perp^2$, when keeping both $\langle\omega_{Di}\rangle$ and ω_{Ti} constant, stabilizes the mode (Δ becomes positive).

Numerical application: Fig. 2.4 shows an example of ITG branch (green) obtained with the local dispersion relation (2.44). The ITG is shown to be unstable for long wavelengths compared to the ion Larmor radius with a maximum of the growth rate near $k_y\rho_i \simeq 0.4$. The destabilizing influence of the ion temperature gradient is illustrated in subplot (b). In dark blue the same ITG branch is obtained when using the hybrid electron model instead of the adiabatic model.

Trapped electron mode (TEM)

The precessional motion of the trapped electrons is slow enough compared to their bounce motion along the magnetic field line, such that there exists an adiabatic invariant associated to this bounced motion which permits to reduce these trapped electron orbits to the one of their bounce center, see [Brunner, 1997]. As a consequence, the trapped electrons have a slow toroidal precessional motion which could resonate with the perturbation thus leading to the so-called trapped electron mode (TEM). A kinetic description of

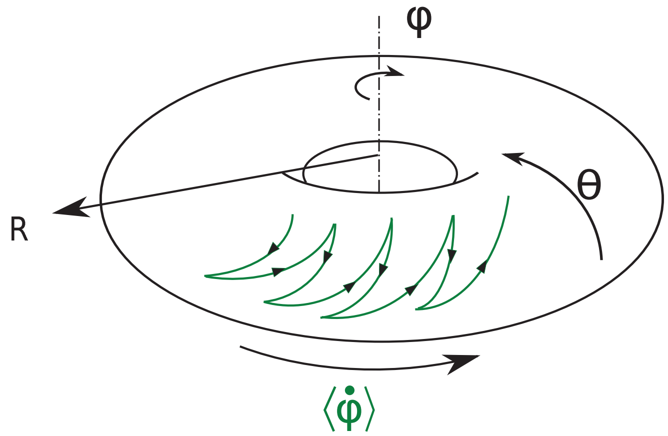

Figure 2.5 – Cartoon of the TEM destabilization. The green trajectory represents the bounce motion of a trapped electron. This trajectory is composed of a bounce motion in the region of low field and of a toroidal precessional drift $\langle\dot{\varphi}\rangle$.

the trapped electron orbits is necessary for characterizing this resonance. For the local dispersion relation, one thus uses the bounce-averaged kinetic description for the trapped electrons and the adiabatic response for the passing electrons, see [Brunner, 1997],

$$\frac{\delta N_{e,trp}}{N_{e0}} = \alpha_t \frac{e\phi}{T_{e0}} \left(1 - 4\pi \int_0^{+\infty} d\varepsilon \sqrt{2\varepsilon} \frac{\omega - \omega_e^\star}{\omega - n\langle\dot{\varphi}\rangle} \frac{f_{e0}}{N_{e0}} \right), \tag{2.45}$$

where $\varepsilon = (v_\perp^2 + v_\parallel^2)/2$ is the kinetic energy divided by the mass and $n\langle\dot{\varphi}\rangle$ is the toroidal precessional drift frequency of the trapped electrons. Introducing the dispersion function $W(z) = (2\pi)^{-1/2} \int_\Upsilon dx\, e^{-x^2/2}\, x/(x-z)$, this last equation reduces, see [Brunner, 1997], to

$$\frac{\delta N_{e,\mathrm{trp}}}{N_{e0}} = \alpha_t \frac{e\phi}{T_{e0}} \left\{ 1 + \left(1 - \frac{\omega_e^\star}{\omega} \right) \left[z_{be}^2 W(z_{be}) \right] \right\}, \tag{2.46}$$

where $\omega_{\varphi e} = n\langle\dot{\varphi}\rangle v_{the}^2/\varepsilon = \omega_{Ne} G L_N/R$, $G \simeq 1$ and $z_{be} = \mathrm{sgn}(\omega_{\varphi e})\sqrt{2\omega/\omega_{\varphi e}}$ has been chosen in order to respect causality over the Landau contour Υ of the integral defining $W(z)$.

The local dispersion relation, when considering kinetic ions and hybrid electrons, is finally obtained from the quasi-neutrality equation

$$0 = Z\tau - Z\tau \int d^3v\, J_0^2 \frac{\omega - \omega_i^\star}{\omega - k_\parallel v_\parallel - \omega_{Di}} \frac{f_{i0}}{N_{i0}} + 1 + \left(1 - \frac{\omega_e^\star}{\omega} \right) \left[\alpha_t z_{be}^2 W(z_{be}) \right]. \tag{2.47}$$

Numerical application: Fig. 2.4 shows two unstable branches: an ITG (dark blue) and a TEM (light blue). These unstable branches are obtained with the hybrid electron local dispersion relation (2.47). The ITG is the most unstable mode at long wavelength and the TEM is the most unstable mode at shorter wavelength. It is noticeable that the ITG branch is furthermore destabilized by the non-adiabatic trapped electron response.

2.8 The gyrokinetic codes GENE and ORB5

The gyrokinetic codes GENE and ORB5 evolve electromagnetic turbulence in ideal MHD equilibrium background by solving the gyrokinetic equation (2.31) together with the self-consistent field equations (2.34) and (2.35). In these codes, the plasma phase space is represented with an Eulerian grid in GENE and by marker particles in ORB5. To reduce the cost of numerical simulations both codes take advantage of a "delta f" representation of the plasma such that each species, σ, gyrocenter distribution function $f_\sigma = f_{\sigma 0} + \delta f_\sigma$ is decomposed into a background $f_{\sigma 0}$ and perturbation component δf_σ.

Regarding the magnetic geometry, both GENE and ORB5 can handle generalized axisymmetric equilibria with triangularity, elongation, Shafranov shift,... The ORB5 code has the particularity of including the magnetic axis, and it exists only in a global version. The GENE code exists in both flux tube and global versions. The flux tube version of the GENE code has been extensively used in chapter 3. The global version of these codes are used in chapters 4 and 5.

The global Lagrangian gyrokinetic code ORB5

The gyrokinetic code ORB5, orginally presented in reference [Tran et al., 1999] is today a multi-scale, multi-species, collisional, electromagnetic, and global gyrokinetic PIC code, in which the statistical numerical noise is controlled using Krook operators or coarse graining procedures. The main steps which led to the current state of the code are: the inclusion of zonal flows [Angelino et al., 2006], the inclusion of straight-field-line coordinates and a field-aligned Fourier filter [Jolliet et al., 2007], the inclusion of new sources and noise control [McMillan et al., 2008], an electromagnetic version [Bottino et al., 2010] sometimes referred to as NEMORB, a field-aligned Fourier field solver [McMillan et al., 2010], inter- and intra-species collisions [Vernay et al., 2010], and the effect of strong flows [Collier, 2015].

To enable carrying out multi-scale simulations in global geometries with the gyrokinetic code ORB5, a new arbitrary-wavelength (compared to the ion Larmor radius) electrostatic field solver has been implemented, see chapter 4. This new feature of the ORB5 code overcomes the limitations of the former long-wavelength approximation made in the original version of the code.

Lagrangian representation of the phase space

In the *Lagrangian* code ORB5, the phase space is represented by numerical particles or markers, such that

$$\delta f(\mathbf{X}, v_\parallel, \mu; t) \equiv \frac{N_{ph}}{N} \sum_{p=1}^{N} \frac{m_p w_p(t)}{2\pi B_\parallel^\star(\mathbf{X})} \delta(\mathbf{X}_p(t) - \mathbf{X}) \delta(\mathbf{v}_{\parallel p}(t) - \mathbf{v}_\parallel) \delta(\mu_p - \mu), \tag{2.48}$$

where N_{ph} is the physical number of particles and N is the number of numerical particles, p indexes the marker particles located at phase-space position $(\mathbf{X}_p, v_{\parallel p}, \mu_p)$ and w_p is a marker weight. Each numerical particle represents a phase-space volume $\Omega_p = (B_\parallel^\star/m_p) d\mathbf{X} dv_\parallel d\mu d\alpha/dN$ with dN the number of markers in an infinitesimal phase-space volume. The numerical marker position $\mathbf{X}(t)$ and $v_\parallel(t)$ are obtained by integrating numerically the equations of motion (2.28) and (2.29), respectively. See thesis [Jolliet, 2010] for the implementation of these equations. Note that when solving electromagnetic perturbations, the phase-space variable $v_\parallel$ is replaced by the variable $p_\parallel = mv_\parallel + q\langle \delta A_\parallel \rangle_\alpha$ and the equation for $\dot{v}_\parallel$ is replaced with an equation for $\dot{p}_\parallel$, see references [Bottino et al., 2010, Biancalani et al., 2016] for more details concerning the electromagnetic feature of ORB5. The weights must be evolved consistently with the fact that for the collisionless Vlasov equation one has $df/dt = 0$, such that $d\delta f/dt = -df_0/dt$. Two techniques can be employed for computing the weights. One can evolve the weight according to equation

$$\frac{1}{\Omega_p} \frac{dw_p}{dt} = \frac{N}{N_{ph}} \tau\Big(\langle \mathbf{E} \rangle_\alpha (\mathbf{X}_p, \mu_p) \Big),$$

where $\tau(\mathbf{E}) = -\frac{df_0}{dt}$ can be estimated with

$$\tau(\mathbf{E}) = -f_0(\Upsilon)\, \frac{\partial \ln f_0}{\partial \Upsilon} \left. \frac{d\Upsilon}{dt} \right|_1 + \frac{q f_0}{T_0(\Upsilon)} \langle \mathbf{E} \rangle_\alpha \cdot (v_\parallel \mathbf{b} + \mathbf{v}_\kappa + \mathbf{v}_{\nabla P} + \mathbf{v}_{\nabla B})$$

with $d\Upsilon(\mathbf{X}, v_\parallel)/dt|_1$ the perturbation component of the total time derivative $\dot{\Upsilon}$, see thesis [Jolliet, 2010]. Indeed, $d/dt = d/dt|_0 + d/dt|_1$ is the total time derivative used in the equation of motion (2.28) and (2.29), *i.e.*, $\dot{\mathbf{X}} = d\mathbf{X}/dt|_0 + d\mathbf{X}/dt|_1$ and $\dot{v}_\parallel = dv_\parallel/dt|_0 + dv_\parallel/dt|_1$, where $d/dt|_0$ represent the component independent of the perturbations and $d/dt|_1$ the evolution due to the perturbed fields. For example, $d\mathbf{X}/dt|_0 = v_\parallel \mathbf{b} + \mathbf{v}_\kappa + \mathbf{v}_{\nabla P} + \mathbf{v}_{\nabla B}$ and $d\mathbf{X}/dt|_1 = \mathbf{v}_{\bar{\mathbf{E}}}$. Alternatively, these weights can be computed directly

$$\frac{w_p(t)}{\Omega_p} = \Bigg[\underbrace{f_0(\mathbf{X}_p(0), v_{\parallel p}(0), \mu_p) + w_p(0)/\Omega_p}_{f_p} - f_0(\mathbf{X}_p(t), v_{\parallel p}(t), \mu_p) \Bigg],$$

which is obtained from the fact the f_p is conserved along characteristics, see thesis [Vernay, 2013] and references therein. Evolving the particles requires the knowledge of the self-consistent fields which are, in ORB5, represented with finite elements

$$\delta\phi(\mathbf{x}) = \sum_\nu \delta\phi_\nu\, \Lambda_\nu(\mathbf{x}) \qquad \text{and} \qquad \delta A_\parallel(\mathbf{x}) = \sum_\nu \delta A_{\parallel,\nu}\, \Lambda_\nu(\mathbf{x}),$$

with $\Lambda_\nu(\mathbf{x})$ a 3D finite element basis. These perturbation fields are solved self-consistently by using a weak variational formulation of the quasi-neutrality and Ampère's equations. For example, the weak formulation for the fully kinetic quasi-neutrality equation is

$$\int d\mathbf{x}\Lambda_\nu(\mathbf{x}) \sum_\sigma \int d\mathbf{Z}\delta(\mathbf{X}+\boldsymbol{\rho}-\mathbf{x}) \frac{q_\sigma^2}{B_0(\mathbf{X})} \sum_{\nu'} \delta\phi_{\nu'}[\Lambda_{\nu'}(\mathbf{x}) - \langle\Lambda_{\nu'}\rangle_\alpha(\mathbf{X},\mu)] \frac{\partial f_{\sigma 0}}{\partial\mu}$$
$$= \int d\mathbf{x}\Lambda_\nu(\mathbf{x}) \sum_\sigma q_\sigma \int d\mathbf{Z}\delta(\mathbf{X}+\boldsymbol{\rho}-\mathbf{x})\delta f_\sigma(\mathbf{X}, v_\parallel, \mu) \quad (2.49)$$

which can be written in the matrix form $L_{\nu\nu'}\delta\phi_{\nu'} = S_\nu$ and the source term is computed using a Galerkin projection of the weighted markers

$$S_\nu = \sum_p q_p w_p \langle\Lambda_\nu\rangle_\alpha(\mathbf{X}_p, \mu_p).$$

In the frame of this thesis work, this solver has been entirely rewritten and upgraded in order to account for the ion polarization drift contribution to the quasi-neutrality equation in its integral form. See chapter 4 for a complete description of the equation and discretization. Ampère's law is discretized following the same technique based on a finite-element representation of the perturbation fields, see [Bottino et al., 2010].

One of the consequences of using a PIC representation of the phase space is the inevitable presence of statistical noise. The level of noise present in a PIC simulation can be decreased by: increasing the number of numerical particles, decreasing the grid resolution, or using an optimized loading of the marker particles to reduce the weight variance. In ORB5, the perturbation fields are represented by their nearly field-aligned Fourier components. Therefore, it is not the resolution of the grid which matters, but rather the number of Fourier modes used for representing the perturbation. See thesis [Jolliet, 2010] and references therein for more details. The ORB5 code is also equipped with noise reduction techniques: a modified Krook operator presented in [McMillan et al., 2008] and a coarse graining procedure presented in [Vernay, 2013] and references therein. These techniques also ensure dissipation at short scales which is necessary for obtaining quasi-steady state as discussed in [Garbet et al., 2010]. The modified Krook operator has been used in the frame of this thesis work for global nonlinear simulations of the TCV tokamak. The modified Krook operator permits a weight spreading reduction. This modified Krook operator acts as a right-hand-side for the gyrokinetic equation (2.31)

$$\frac{d}{dt}f = -\gamma_k \delta f(\mathbf{X}, v_\parallel, \mu; t) + S_{corr}(\mathbf{X}, v_\parallel, \mu; t),$$

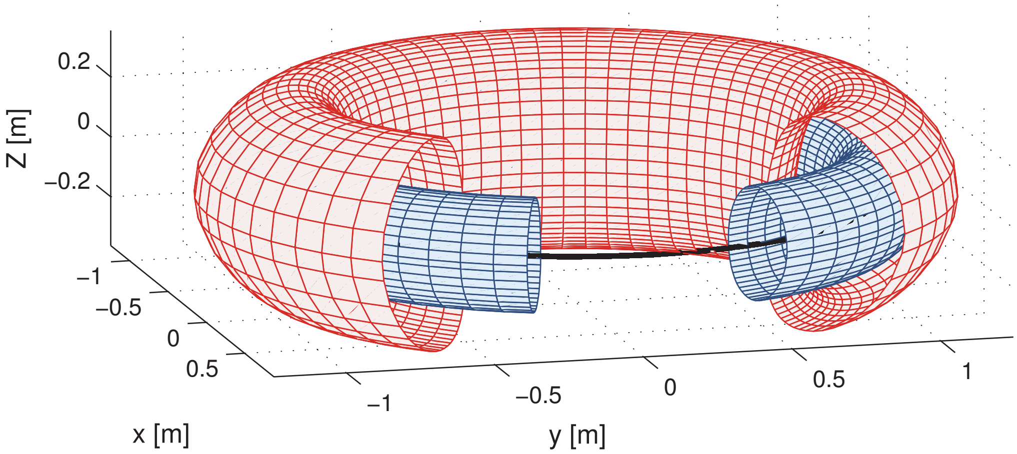

Figure 2.6 – Magnetic surfaces of the TCV tokamak. Data taken from simulations carried out in chapter 4. In black the magnetic axis, in red the edge surface ψ_{edge}, and in blue a surface ψ. The mesh is in $\{s, \theta^\star, \varphi\}$ coordinates.

where γ_k is the Krook damping rate usually taken to be a tenth of the maximum linear growth rate, and S_{corr} is a correction term which ensures conservation properties. This term is constructed such as to optionally conserve any of the following flux-surface averaged quantities: zonal flow component, density, temperature, and parallel momentum.

Global geometry

In ORB5, the global geometry equilibrium is described in straight-field-line magnetic coordinates $\{s, \theta^\star, \varphi\}$ with $s = \sqrt{\psi/\psi_{edge}}$. This equilibrium can be a circular ad-hoc geometry or an ideal MHD equillibirum, see section 2.1. Results presented in chapter 4 are obtained from simulations carried out with an ideal MHD equilibrium relevant for the TCV tokamak, see figure 2.6. These magnetic equilibria are obtained from the ideal MHD code CHEASE [Lütjens et al., 1996]. Density and temperature profiles can either be chosen consistently with the ideal MHD equilibrium or independently by user-defined specifications.

The ORB5 simulation volume has the topology of a torus with either the full domain $s \in [0, s_{max}]$ or an annulus with $s \in [s_{min}, s_{max}]$ and $0 < s_{min} < s_{max} \leq 1$. For the case of a torus including the magnetic axis, unicity and regularity boundary conditions are applied on the perturbed field on axis, because the polar-like coordinates are singular at this position. For the case of an annular domain, the same boundary conditions are applied on both edges. For the differential long wavelength operator, Dirichlet boundary conditions are applied. For the new arbitrary wavelength solver, boundary conditions are not imposed but rather natural. More details are given in chapter 4.

The Eulerian gyrokinetic code GENE

The flux tube version of the GENE code has been initially presented by [Jenko et al., 2000]. Collisions and a multi-species feature have been added by [Merz and Jenko, 2008]. The flux tube version has been extended to a global version by [Görler, 2009, Lapillonne, 2010].

The GENE basic description and main references are provided on http://genecode.org/.

The Eulerian representation of the phase space

In the *Eulerian* code GENE, the plasma phase-space is represented on a grid

$$\delta f_\sigma \equiv \delta f_\sigma(\mathbf{X}_\mathfrak{g}, \mathbf{v}_{\|\mathfrak{g}}, \mu_\mathfrak{g}) \qquad \text{and} \qquad f_{\sigma 0} \equiv f_{\sigma 0}(\mathbf{X}_\mathfrak{g}, \mathbf{v}_{\|\mathfrak{g}}, \mu_\mathfrak{g}),$$

where $\mathfrak{g}$ indexes the points of the 5D grid. The associated species density and temperatures, as well as the fields are defined on the corresponding position grid $\mathbf{x}_\mathfrak{g} \equiv \mathbf{X}_\mathfrak{g}$. The plasma perturbation is evolved with the gyrokinetic equations (2.33) which is furthermore simplified in GENE:

$$\begin{aligned} \frac{\partial \delta g_\sigma}{\partial t} &= -\mathbf{v}_{\bar{\mathbf{E}}} \cdot \left(\frac{\partial f_{\sigma 0}}{\partial \mathbf{X}} - \frac{\mu}{v_\| m_\sigma} \nabla B_0 \frac{\partial f_{\sigma 0}}{\partial v_\|} \right) \\ &- \left(v_\| \mathbf{b} + \mathbf{v}_\kappa + \mathbf{v}_{\nabla P} + \mathbf{v}_{\nabla B} + \mathbf{v}_{\bar{\mathbf{E}}} \right) \cdot \left(\frac{\partial \delta f_\sigma}{\partial \mathbf{X}} - \frac{q_\sigma}{m_\sigma v_\|} \nabla \langle \delta\phi \rangle_\alpha \frac{\partial f_{\sigma 0}}{\partial v_\|} \right) \\ &+ \frac{\mu}{m_\sigma v_\|} \left(v_\| \mathbf{b} + \mathbf{v}_\kappa + \mathbf{v}_{\nabla P} \right) \cdot \nabla B_0 \frac{\partial \delta f_\sigma}{\partial v_\|}, \end{aligned} \tag{2.50}$$

thus evolving $\delta g_\sigma = \delta f_\sigma - (q_\sigma/m_\sigma)\langle \delta A_\| \rangle_\alpha \partial_{v_\|} f_{\sigma 0}$ instead of δf_σ. The only nonlinear term which is kept is $\mathbf{v}_{\bar{\mathbf{E}}} \cdot \nabla_\mathbf{X} \delta f_\sigma$. The parallel non linearity is neglected, see [Lapillonne, 2010]. This approximation is not made in ORB5 [Jolliet et al., 2009, Garbet et al., 2010]. In GENE, the linearized gyrokinetic equation can be solved with an eigenmode solver or with a time integrator. The time integrator is a $4th$ order Runge-Kutta with an adaptive time step. The fields are consistently solved on the grid from the discretized version of the field equations (2.34) and (2.35). For example, in a flux tube, the electrostatic potential is obtained from

$$\widehat{\delta\phi} = \frac{\sum_\sigma N_{0\sigma} \pi B_0 q_\sigma \int_{-\infty}^{+\infty} dv_\| \int_0^{+\infty} d\mu J_0(k_\perp \rho_\sigma) \widehat{\delta g_\sigma}}{\cancel{k_\perp^2 \lambda_D^2} + \sum_\sigma (q_\sigma^2 N_{\sigma 0}/T_{\sigma 0})[1 - \Gamma_0(k_\perp \rho_{th}^2/2)]}, \tag{2.51}$$

where the deviation from quasi-neutrality $k_\perp^2 \lambda_D^2$ is neglected and having used a Fourier representation of the phase-space quantities and fields $\widehat{\delta\phi} = \widehat{\delta\phi}(k_x, k_y, z, v_\|, \mu)$. Indeed, one anticipated the fact that the radial direction x is handled in Fourier space in a flux tube, see discussion in next section. In such a Fourier representation, the integral equation for the polarization drift contribution to the density becomes an algebraic relation

$$\int dv_{\parallel} d\mu \frac{q_\sigma}{B_0} \frac{\partial f_{\sigma 0}}{\partial \mu} [\widehat{\delta\phi} - \langle\langle \widehat{\delta\phi} \rangle\rangle_\alpha] \simeq \frac{q_\sigma N_{\sigma 0}}{T_{\sigma 0}} \left[1 - \Gamma_0(k_\perp^2 \rho_{th,\sigma}^2/2)\right] \widehat{\delta\phi},$$

with $\Gamma_0(\xi) = e^{-\xi} I_0(\xi)$ the scaled modified Bessel function. The QNE (2.51) has been expressed with the gyrokinetic model for the electrons but one can trivially replace this gyrokinetic electron response with the adiabatic or hybrid electron response introduced in section 2.6.

Compared to Lagrangian codes, Eulerian codes do not suffer from sampling noise, but the associated Eulerian numerical schemes have low dissipation effects due to finite difference discretization. Finally, additional hyper diffusivity is necessary to control the phase-space filamentation. This hyper diffusive term is added on the RHS of the GKE. It reads

$$D^n_{\mathrm{hyp}}\, \widehat{\delta g} = \left(h_\parallel \frac{\partial^n}{\partial v_\parallel} + h_z \frac{\partial^n}{\partial z} + h_x k_x^n + h_y k_y^n \right) \widehat{\delta g},$$

where $n = 4$ typically. The hyper-diffusion has been used in nonlinear simulations presented in chapter 3.

The flux tube

In GENE, the configuration space is described with field-aligned coordinates (x, y, z), see Sec. 2.1. These coordinates are a natural choice for representing the fluctuating fields of microturbulence, as they are themselves aligned with the equilibrium magnetic field $\mathbf{B}_0$ ($\mathbf{B}_0 \parallel \nabla x \times \nabla y$). In GENE, the simulation box is centered on a flux surface of reference ψ_0. The radial coordinate is arbitrarily chosen to be zero on this surface $x = r - r_0$, where r is a function of ψ with units of length and $r_0 = r(\psi_0)$.

In flux-tube geometry, see Fig. 2.7, the plasma is described in the limit of $\rho^\star \to 0$ with $\rho^\star = \rho_s/a$ the "rho star" parameter, ρ_s the ion sound Larmor radius, and a the tokamak minor radius. This $\rho^\star$ parameter symbolizes the scale separation in between the turbulence and the background quantities. In this limit, the *background* and *magnetic* equilibrium quantities are assumed independent of the radial coordinates x. The only exception is the radial profile of safety factor which is linearized [Beer et al., 1995]

$$q_s(x) = q_s(r_0) + x \left.\frac{dq_s}{dr}\right|_{r=r_0} = q_0 \left(1 + \hat{s}\frac{x}{r_0}\right), \tag{2.52}$$

where $\hat{s} = (r_0/q_0) dq_s/dr|_{r=r_0}$ stands for the magnetic shear and one has furthermore defined $q_0 = q_s(r_0)$. This linearized radial profile is taken into account when applying the pseudo-periodic boundary conditions. The *background* quantities and their radial gradients are assumed constant and evaluated at the flux-surface of minor radius r_0: $N_{\sigma j0} = N_{\sigma 0}(r_0)$,

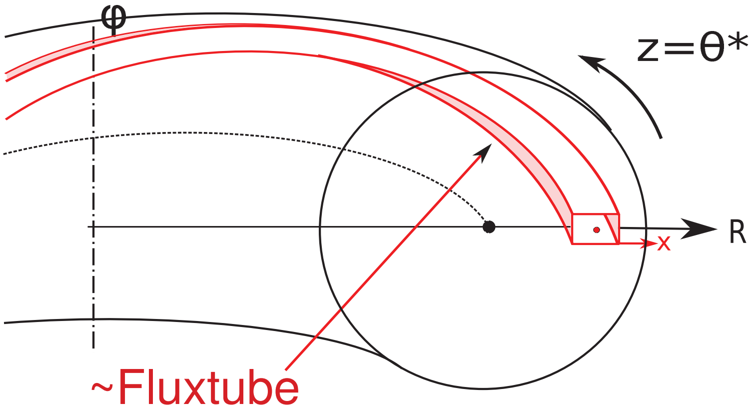

Figure 2.7 – Cartoon of a flux tube.

$T_{\sigma 0} = T_{\sigma 0}(r_0)$, $1/L_{N_\sigma} = -d \log T_{\sigma 0}/dr|_{r=r_0}$, and $1/L_{T_\sigma} = -d \log T_{\sigma 0}/dr|_{r=r_0}$. The essential *magnetic equilibrium* quantities only depend on the parallel coordinate: the magnetic field amplitude $B_0 = B_0(z)$, its gradient components $\frac{\partial B_0}{\partial x} = \frac{\partial B_0}{\partial x}(z)$ and $\frac{\partial B_0}{\partial z} = \frac{\partial B_0}{\partial z}(z)$, the Jacobian $\mathcal{J}^{xyz} = \mathcal{J}^{xyz}(z)$, and the metric coefficients $g^{\nu\mu}(z) = \nabla\nu \cdot \nabla\mu$ with ν and μ the flux-tube coordinates (x, y, z).

Boundary conditions in a flux tube

According to the standard flux-tube model, periodic boundary conditions are imposed in both the radial direction x and binormal direction y. The *periodicity in* x is justified by the spatial scale separation between the correlation length of turbulent eddies, $\sim \rho_s$, and the characteristic equilibrium length $L_c \sim L_N$, and $L_T \sim a$. This scale separation is usually appreciated with the rho star parameter $\rho^\star \ll 1$. The *periodicity in* y reflects the 2π-periodicity of any physical field $\mathcal{A}$ with respect to the toroidal angle φ. In the limit where the flux tube covers the full magnetic surface, the y periodicity corresponds exatcly to $\mathcal{A}(\psi, \chi, \varphi) = \mathcal{A}(\psi, \chi, \varphi + 2\pi)$. These *periodic boundary conditions* in x and y are naturally accounted for by considering a Fourier representation in both these directions

$$\mathcal{A}(x, y, z) = \sum_{k,l=-\infty}^{+\infty} \hat{\mathcal{A}}(k_x, k_y, z) \exp\left(\imath k_x x + \imath k_y y\right), \tag{2.53}$$

having defined $k_x = k\, k_{x,\min}$, $k_y = l\, k_{y,\min}$, $k_{x,\min} = 2\pi/L_x$, $k_{y,\min} = 2\pi/L_y$, as well as L_x and L_y denoting the width of the flux tube in the x and y directions, respectively.

In field-aligned coordinates, pseudo-periodic boundary conditions are applied in the z direction

$$\mathcal{A}(x, y, z + 2\pi) = \mathcal{A}(x, y - C_y q_s(x) 2\pi, z), \tag{2.54}$$

as a consequence of the poloidal periodicity of the fields $\mathcal{A}(\psi, \chi, \varphi) = \mathcal{A}(\psi, \chi + 2\pi, \varphi)$, see references [Beer et al., 1995, Scott, 1998, Merz, 2009]. In the Fourier representation, equation (2.53), these pseudo-periodic boundary conditions translate into

$$\sum_{k,l=-\infty}^{+\infty} \hat{\mathcal{A}}(k_x, k_y, z + 2\pi) \exp\left(\imath k_x x + \imath k_y y\right) =$$

$$\sum_{k,l=-\infty}^{+\infty} \hat{\mathcal{A}}(k_x, k_y, z) \exp\left(\imath k_x x + \imath k_y y\right) \exp\left\{-\imath 2\pi k_y C_y\, q_0(1 + \hat{s}x/r_0)\right\}, \quad (2.55)$$

having used the linearized profile of safety factor, equation (2.52). Accounting for this radial variation of $q_s(x)$ in the boundary conditions with respect to z provides the essential magnetic topology required for studying the particular particle dynamics that may develop in the vicinity of low order MRSs. For a given k_y mode, equation (2.55) leads to a coupling between different k_x Fourier modes:

$$\hat{\mathcal{A}}(k_x + 2\pi\hat{s}k_y, k_y, z - \pi) = \underbrace{e^{\imath\, 2\pi k_y C_y\, q_0}}_{=1} \hat{\mathcal{A}}(k_x, k_y, z + \pi). \quad (2.56)$$

This relation illustrates how a given k_y mode followed along a magnetic field line generates finer and finer radial structures after each poloidal turn, as a result of the magnetic shear. In GENE, the phase factor $\exp\left(\imath\, 2\pi k_y C_y\, q_0\right)$ in equation (2.56) is set to 1 for all k_y modes, following the standard flux-tube model convention. One can show that this corresponds to a simple shift of the origin of the x coordinate to the position of the nearest considered lowest-order mode rational surface. This explains why $x = 0$ always coincides with a MRS for all k_y modes. The linearization of the safety factor profile naturally implies that the MRSs related to a given $k_y = l\, k_{y,min}$ mode are equidistant and located at the radial positions $x = \Delta m L_{\text{MRS}} = \Delta m L_{\text{LMRS}}/l$, with p, l integers, $L_{\text{MRS}}(k_y) = 1/\hat{s}k_y$ standing for the distance between mode rational surfaces (MRSs) related to any k_y, and $L_{\text{LMRS}} = L_{\text{MRS}}(k_{y,min})$ the distance between lowest-order mode rational surface (LMRS), i.e. related to $k_{y,min}$.

In a tokamak, a linear eigenmode has a fixed k_y mode number as a result of the axisymmetry of the considered equilibrium, but in general is a superposition of an infinite number of coupled k_x modes given by $k_x = k_{x,0} + p\, 2\pi\hat{s}k_y$, $p \in \mathbb{Z}$, as described in equation (2.56). Such a linear eigenmode thus reads:

$$\mathcal{A}_{k_y}(x, y, z) = \exp\left(\imath k_y y\right) \exp\left(\imath k_{x,0} x\right)$$

$$\times \sum_{p=-\infty}^{+\infty} \hat{\mathcal{A}}(k_{x,0} + p 2\pi\hat{s}k_y, k_y, z) \exp\left(\imath p 2\pi\hat{s}k_y\, x\right). \quad (2.57)$$

From the coupled z-dependent coefficients $\hat{\mathcal{A}}(k_{x,0} + p2\pi\hat{s}, k_y, z)$ appearing in equation (2.57), one may construct the so-called ballooning envelope, denoted $\hat{\mathcal{A}}_b(z)$ and defined over the infinite space $z \in [-\infty, +\infty]$. This envelope, consistent with the standard ballooning representation [Connor et al., 1978, Hazeltine and Newcomb, 1990], is defined as follows:

$$\hat{\mathcal{A}}_b(z + p2\pi) = \hat{\mathcal{A}}(k_{x,0} + p2\pi k_y \hat{s}, k_y, z), \quad z \in [-\pi, \pi], \; p \in \mathbb{Z}. \tag{2.58}$$

Note that $\hat{\mathcal{A}}_b(z)$ is a continuous function, in particular at the connection points $z = \pi + p2\pi$, $p \in \mathbb{Z}$, as a consequence of equation (2.56). One can furthermore show that $k_{x,0}$ is related to the so-called ballooning angle χ_0 according to the relation $k_{x,0} = -k_y \hat{s} \chi_0$.

GENE flux-tube phase-space grid

In GENE, the $5D$ particle distribution function δf and the $3D$ self-consistent fields are represented with grids in coordinates $(k_x, k_y, z, v_\parallel, \mu)$ and (k_x, k_y, z), respectively. The phase-space simulation volume is thus discretized with $n_{k_x} \times n_{k_y} \times n_z \times n_\parallel \times n_\mu$ grid points and represents a volume $L_{k_x} \times L_{k_y} \times L_z \times L_\parallel \times L_\mu$.

The simulation box in respectively the radial and binormal directions is composed of $n_{k_x} = n_x$ and $n_{k_y} = n_y/2$ complex Fourier modes. Only positive k_y modes, $k_y \geq 0$, are considered in the binormal direction by invoking the reality condition. The simulation box lengths in these spectral directions are $L_{k_x} = n_{k_x} k_{x,min}$ and $L_{k_y} = n_{k_y} k_{y,min}$. The box size in the z direction L_z must be equal to $L_z = 2\pi$, *i.e.* one poloidal turn, for consistency between flux-tube and global geometries as demonstrated in reference [Scott, 1998]. This direction is discretized using n_z grid points.

The considered gyrocenter velocity space variables are $(v_\parallel, \mu)$. The numerical representation of these directions are restricted to $-v_{\text{max}} < v_\parallel < +v_{\text{max}}$ and $0 < \mu < \mu_{\text{max}} = m v_{\text{max}}^2 / 2B_0$ where typically $v_{\text{max}} = 4 - 5\, v_{\text{th}\sigma}$. This species-dependent velocity phase space is discretized with $n_{v_\parallel}$ equidistant mesh points in the $v_\parallel$ direction and with n_μ points, either equidistant or given by Gauss-Legendre integration points, in the μ direction.

3 How non-adiabatic passing-electron layers of linear microinstabilities affect turbulent transport

3.1 Introduction

The non-adiabatic response of passing electrons in ion temperature gradient (ITG) and trapped electron mode (TEM) microturbulence regimes is investigated in tokamak plasmas making use of the flux-tube version of the gyrokinetic code GENE [Jenko et al., 2000]. The presence of fine structures near MRSs due to this non-adiabatic electron response was observed in linear simulations [Chowdhury et al., 2008], as well as in nonlinear simulations [Waltz et al., 2005, Candy, 2005, Waltz et al., 2006]. The quasi-linear estimate of the particle flux was shown to be altered by the passing electrons in references [Hallatschek and Dorland, 2005, Angioni et al., 2007] and turbulence simulations including full passing electrons dynamics have also been discussed in [Scott, 2006]. This chapter contains a systematic study of the non-adiabatic response of passing electrons in the vicinity of MRSs in both ITG and TEM dominated regimes. Results are obtained using three different electron models, adiabatic, hybrid, and fully kinetic. See the description of these electron models in section 2.6. Comparing linear eigenmodes obtained with the hybrid and the fully kinetic electron models enables to systematically isolate fine radial structures located at corresponding mode rational surfaces, clearly resulting from the non-adiabatic passing-electron response. Nonlinear simulations show that these fine structures on the non-axisymmetric modes survive in the turbulent phase. Furthermore, through nonlinear coupling to axisymmetric modes, they induce radial modulations in the effective profiles of density, ion and electron temperatures, and $E \times B$ shearing rate. Finally, the passing-electron channel is shown to significantly contribute to the transport levels, at least in our ITG case. Also shown is that the passing electrons significantly influence the $E \times B$ saturation mechanism of turbulent fluxes.

The chapter is organized as follows. In Sec. 3.2, the ITG and TEM test cases of reference are presented. In Sec. 3.3, the impact of the non-adiabatic response of passing electrons on the linear mode destabilization is addressed. Systematically comparing eigenmodes obtained from GENE linear simulations where the electron response is fully kinetic, with eigenmodes obtained from simulations where the electron response is hybrid, one clearly identifies a fine structure near MRSs resulting from the non-adiabatic response of passing electrons [Dominski et al., 2012]. The underlying mechanisms of the destabilization near MRSs due to the non-adiabatic response of passing electrons are revealed by the derivation of a local dispersion relation to which GENE results are confronted. A systematic comparison based on the estimate of the fine radial structure width, within which the electrons respond non-adiabatically, is carried out by scanning physical parameters: the magnetic shear $\hat{s}$, the safety factor q_0, the electron to ion temperature ratio $\tau = T_{e0}/T_{i0}$, the ion to electron mass ratio $\mu = m_i/m_e$ and the wave vector in the binormal direction $k_y\rho_i$ (normalized to the ion Larmor radius). The interplay between the non-adiabatic response of passing electrons and the nonlinear turbulence is analyzed in Sec. 3.4. The persistence in the turbulent regime of these fine structures on the considered $k_y \neq 0$ modes is first addressed. The resulting radial modulation of the axisymmetric mode ($k_y = 0$) due to the nonlinear coupling with the $k_y \neq 0$ modes is shown. In particular, the development of corrugations in the flux-surface-and-time-averaged profiles is pointed out as already observed [Waltz et al., 2005, Candy, 2005, Waltz et al., 2006]. The importance of the passing electron contribution to the different turbulent fluxes is quantified as well as their influence on the $E \times B$ saturation mechanism. Conclusions are finally drawn in Sec. 5.6

3.2 Test cases of reference

Differences between three electron models are briefly illustrated by looking at the linear spectra obtained with the GENE code when using alternatively the fully kinetic, adiabatic, and hybrid electron models. The physical parameters of these test cases are summarized in table 3.1. The real frequencies ω_r and growth rates γ of the most unstable mode at each wave number k_y are presented in figure 3.1 subplots (a,b,c,d). This figure shows the results obtained for two different instability regimes: an ITG and a TEM. These two cases are the reference cases considered in this entire work. The ITG is close to the cyclone base case (CBC), whose characteristic gradients lengths of density and ion/electron temperatures have been slightly modified to avoid the presence of secondary TEM or ETG modes. The TEM case is inspired by reference [Merz and Jenko, 2008] but considering the temperature ratio $\tau = 1$ instead of 3, this change is made to obtain a TEM case whose turbulent fluxes are significantly saturated by the zonal flows (ZFs). In the ITG case, figure 3.1 (a) and (c), for small wave numbers, $0 < k_y\rho_i \lesssim 0.7$, the fully kinetic electron model (blue) provides an ITG instability ($\omega_r < 0$), well reproduced by the hybrid (red) but not so well reproduced by the adiabatic model (green): there is indeed a $\sim 50\%$ lower γ with this latter model, resulting from the trapped electrons being forced to respond adiabatically, when in fact they are essentially passive for this ITG. Accounting for the fully kinetic electron response provides essentially the same spectra as when accounting for the hybrid electron response, in this ITG case where no unstable TEM or ETG are present.

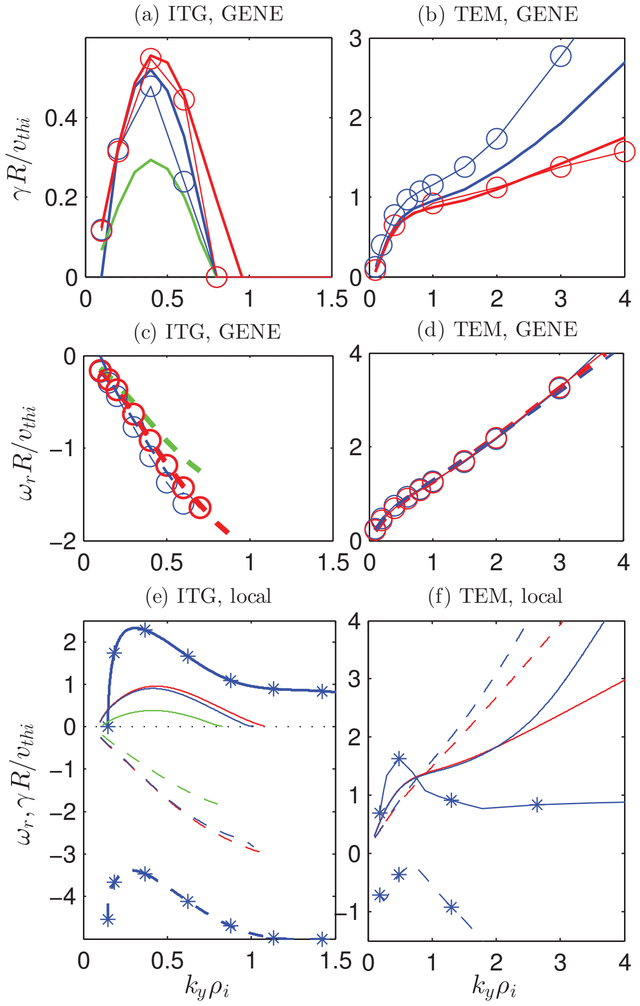

Figure 3.1 – Growth rates γ (full lines) and real frequencies ω_r (dashed lines) in units v_{thi}/R as a function of $k_y\rho_i$ for the test cases of reference described in table 3.1, and considering different electron models: adiabatic (green), hybrid (red), fully kinetic (blue). Both ITG (left column) and TEM (right column) cases shown. Results obtained with (a-d) GENE and (e-f) local dispersion relation. Also plotted are the results obtained with GENE when running simulation with the reduced mass ratio $\mu = 400$ (thin lines with circles). For the local dispersion relation, one considers $k_\parallel R q_0 = 0.2$ for all the electron models, and one considers the additional case with $k_\parallel R q_0 = 0$ (lines with asterisk) for the kinetic electron model.

For all cases: concentric circular geometry with $q_0 = 1.4$, $\hat{s} = 0.8$, $Z = 1$, $\tau = T_{e0}/T_{i0} = 1$. $\beta = 10^{-3}$ for fully-kinetic model.

Case	R/L_n	$R/L_{T_{e0}}$	$R/L_{T_{i0}}$	$k_{y,min}\rho_i$	$\mu = m_i/m_e$	$\epsilon = r_0/R$
ITG	2.0	2.0	6.0	0.3 (0.07)	1836 (400)	0.18
TEM	3.0	6.0	0.0	0.3 (0.04)	1836 (400)	0.16

Grid resolution:

$$\begin{aligned} n_x \times n_{k_y} \times n_z \times n_{v_\parallel} \times n_\mu &= 64 \times 1 \times 32 \times 64 \times 32 \quad \text{(linear)}, \\ &= 432 \times 64 \times 16 \times 64 \times 8 \quad \text{(nonlinear ITG)}, \\ &= 256 \times 64 \times 16 \times 64 \times 16 \quad \text{(nonlinear TEM)}. \end{aligned}$$

Table 3.1 – Physical parameters for the ITG and TEM reference cases, considered in GENE simulations and in the local dispersion relation. The parameters ϵ and R stand respectively for the inverse aspect ratio and the major radius. Parameter values in parenthesis correspond to the ones considered in the nonlinear simulations when different from the corresponding linear run values.

In the TEM case, figure 3.1 (b) and (d), the kinetic model (blue) provides a TEM instability ($\omega_r > 0$) well reproduced by the hybrid model (red) for small to intermediate wave numbers $0 < k_y\rho_i \lesssim 1.5$. At high wave numbers, $k_y\rho_i \gtrsim 1.5$, the fully kinetic spectra shows a progressive transition of the TEM mode towards an ETG instability, at which point the hybrid representation starts to fail. The adiabatic electron model does not give any TEM instability because this response cannot be used to reproduce the TEM destabilization mechanism which is caused by a resonance between the perturbation and the toroidal precessional drift of the trapped electrons.

3.3 Fine structures at low order MRS, in linear regimes

3.3.1 Analytical estimate of the radial width of fine structures

An analytical estimate of the radial width δx^{th} measuring the region centered around a MRS, within which the passing electron response is expected to be non-adiabatic, is derived. The considered MRS is assumed located at $x_0 = 0$ where $q_0 = -m/n$. The wave vector of the Fourier mode of poloidal-toroidal mode numbers (m, n) is given by $\mathbf{k} = m\nabla\chi + n\nabla\varphi$ and its component parallel to $\mathbf{B}_0$ reads:

$$k_\parallel = \mathbf{k} \cdot \frac{\mathbf{B}_0}{B_0} = \frac{\mathbf{B}_0 \cdot \nabla\chi}{B_0}[m + nq_s(x)] = \frac{\mathbf{B}_0 \cdot \nabla\varphi}{B_0 q_s}[m + nq_s(x)],$$

having used $q_s = \mathbf{B}_0 \cdot \nabla\varphi / \mathbf{B}_0 \cdot \nabla\chi$, constant on a magnetic surface for the straight field line poloidal angle χ. Near the MRS located at x_0, one clearly has $k_\parallel \to 0$ and the condition of validity for limiting the passing electron response to their adiabatic response, $|\omega_r/k_\parallel| \ll v_{the}$, breaks down. Note that the parallel component of the wave vector goes to zero as the mode aligns with the magnetic field at the position of the MRS.

To have an estimate of the parallel phase velocity $\omega_r/k_\parallel$ with respect to x, one Taylor expands the parallel component of the wave vector around x_0 with respect to the small deviation $x = x - x_0$, leading to:

$$k_\parallel(x) \simeq \frac{\hat{s}}{q_0}\frac{x}{R}k_y, \tag{3.1}$$

with q_s defined in equation (2.52), $k_y = -nq_0/r_0$, and $\mathbf{B}_0 \cdot \nabla\varphi \approx B_0/R$ with R the major radius. Then, assuming that the electrons respond non-adiabatically in the region where the phase velocity of the perturbation is larger than the electron thermal velocity, one estimates the boundaries of this region to be where $|\omega_r/k_\parallel(\pm\delta x^{\text{th}}/2)| = v_{the}$. Finally, the distance between these boundaries located on both sides of the MRS gives the so-called "theoretical" estimate of the fine structure

$$\frac{\delta x^{\text{th}}}{\rho_i} = 2\,\frac{|\omega_r|}{v_{thi}/R}\,\frac{q_0}{\hat{s}\,\sqrt{\tau\mu}\,k_y\rho_i}. \tag{3.2}$$

This theoretical estimate requires the knowledge of the real frequencies, ω_r, which we take here from GENE linear simulations. For example, to estimate the theoretical width of the $k_y\rho_i = 0.3$ mode of reference, the real frequencies of the ITG and TEM cases are taken from figure 3.1(c,d): $\omega_r \approx -0.7v_{thi}/R$ and $0.6v_{thi}/R$, respectively. Then considering appropriate physical parameters from table 3.1, one roughly estimates the respective radial widths to be $\delta x^{\text{th}} \approx 0.21\rho_i$ and $0.18\rho_i$. This narrow region of non-adiabatic electron response motivates the use of high radial resolution in GENE simulations.

3.3.2 Fine structures near MRS in linear GENE simulations

Linear flux-tube simulations of ITG and TEM eigenmodes have been carried out by using the spectral approach provided in the GENE code, which enables one to compute dominant as well as sub-dominant unstable eigenmodes with complex frequency $\omega = \omega_r + i\gamma$, as detailed in references [Kammerer et al., 2008, Roman et al., 2010, Merz et al., 2012]. In the GENE representation, an eigenmode of a field $\mathcal{A}$ thus takes on the functional form

$$\mathcal{A}(x, y, z; t) = \widehat{\mathcal{A}}(x, z)\exp[i(k_y y - \omega t)].$$

The eigenmode is therefore essentially characterized by the complex amplitude $\widehat{\mathcal{A}}(x, z)$, which represents the slow spatial variation, the fast phase variation being contained in the factor $\exp(ik_y y)$, see Sec.2.8. Typical eigenmode envelopes of fluctuating fields of interest (ϕ, δN, δT_e and δT_i which are weighted by the Jacobian $\mathcal{J}^{\text{xyz}}$) are shown in Figs. 3.2 and 3.3, for both the ITG and TEM test cases in respectively the left and right columns of these figures. Note that, as introduced in Sec. 2.8, in a linear flux-tube simulation, due to the imposed periodic boundary conditions in x, the system size L_x along this direction is taken as the distance between consecutive lowest-order MRSs for the considered k_y mode number such that all k_x modes are coupled and the ballooning

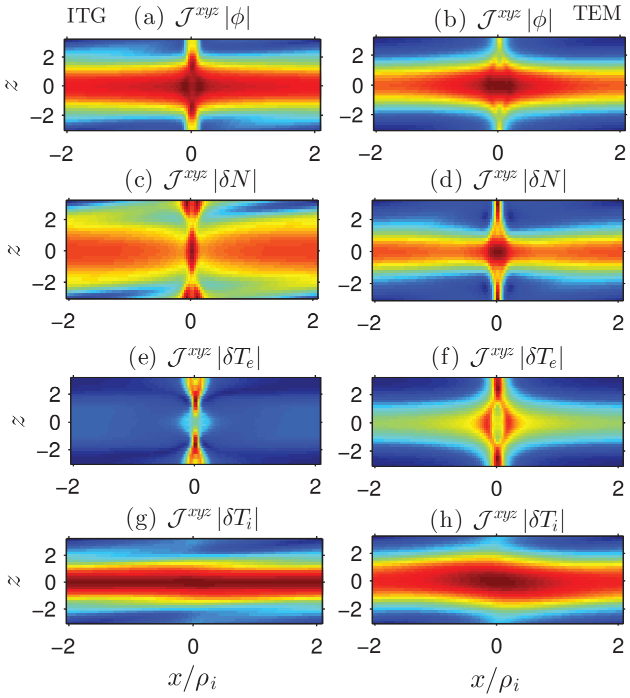

Figure 3.2 – (x, z)-envelopes of fluctuation fields ϕ, δN, δT_e, δT_i weighted by the Jacobian $\mathcal{J}^{\text{xyz}}$ and corresponding to the ITG (a,c,e,g) and to the TEM (b,d,f,h) reference cases whose parameters are given in Tab. 3.1. The fully kinetic model has been used and $k_y\rho_i = 0.3$. Color coding: dark blue = zero, dark red = maximum value.

angle range is maximized: $L_x = 1/(k_y\hat{s})$, and the origin of the x coordinates is always chosen to be located at MRS. For $k_y\rho_i = 0.3$ and $\hat{s} = 0.8$ considered here, one thus obtains $L_x = 4.17\,\rho_i$.

In figure 3.2, whose results are obtained with the fully kinetic electron model, the characteristic ballooned structures of ITG/TEM modes is recovered: the amplitude of the slow spatial envelope of the perturbation is systematically modulated in the $z \equiv \chi$ direction with a minimum located in the inner mid-plane at $z = \pm\pi$ and a maximum located in the outer mid-plane at $z = 0$. Indeed the maximum of amplitude is positioned in both cases at the outer mid-plane of the tokamak where the interchange is unfavorable in the ITG case and where the trapped electrons are resonating with the perturbation in the TEM case. Remarkable on all fields, except δT_i, is the presence of a fine radial structure centered on the MRS located, as previously mentioned above, at $x = 0$ where the non-adiabatic response of the passing electrons cannot be neglected.

To clearly identify the effect of the non-adiabatic response of passing electrons, the envelopes of the electrostatic potential $|\phi|$ obtained with the hybrid model and with the fully kinetic model, respectively, are compared in figure 3.3. Subplots (a,b) present results carried out with the fully kinetic model, while subplots (c,d) show results carried

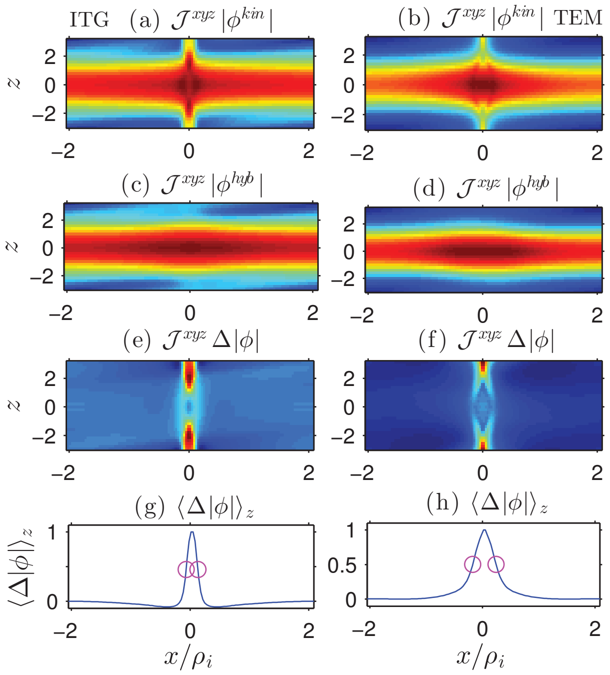

Figure 3.3 – Envelopes $\mathcal{J}^{\mathrm{xyz}}|\widehat{\phi}|(x,z)$ of linear eigenmodes for the same ITG and TEM cases as in figure 3.2. The first and second row of sub-plots respectively present the results from the fully kinetic and hybrid electron models. The difference $\Delta|\widehat{\phi}|$ is shown in the third row and its z-averaged profile in the fourth row, from which the numerical FWHM $\delta x_{\mathrm{lin}}^{\mathrm{sim}}$ (magenta circles) estimate for the fine structure width can be obtained. Color coding: dark blue = zero, dark red = maximum value.

out with the hybrid model. Note that the ballooned structure is recovered for the case of hybrid electron model. A notable difference, however, is the presence of the fine, almost slab-like, structure centered at the MRS ($x = 0$) in the eigenmodes from the fully kinetic model, which is absent in the hybrid model results, thus clearly identified as a feature resulting from the non-adiabatic response of passing electrons in the vicinity of the lowest-order MRS of the considered k_y mode number. The slab-like feature along z at $x = 0$ ensures $|k_\parallel| \approx |\partial \log \widehat{\phi}/\partial z| \approx 0$, essential for a non-adiabatic response of passing electrons. $\partial\widehat{\phi}/\partial z = 0$ is clearly only possible at MRS. By subtracting the mode envelopes obtained from the two different electron models, $\Delta|\widehat{\phi}|(x, z) = |\widehat{\phi}^{\mathrm{kin}}| - |\widehat{\phi}^{\mathrm{hyb}}|$, we are able to cleanly isolate the radial structure, see figure 3.3 (e,f). Note that prior to this subtraction, the field $\widehat{\phi}^{\mathrm{hyb}}$ has been normalized such that $\langle|\widehat{\phi}^{\mathrm{hyb}}|\rangle_z = \langle|\widehat{\phi}^{\mathrm{kin}}|\rangle_z$ at $x = \pm L_x/2$, *i.e.* at the most distant radial points from the MRSs where the fields provided by the fully kinetic and hybrid models are essentially identical. Furthermore z-averaging provides an average radial profile

$$\langle\Delta|\widehat{\phi}|\rangle_z(x) = \frac{\int dz \mathcal{J}^{\mathrm{xyz}} \Delta|\widehat{\phi}|(x, z)}{\int dz \mathcal{J}^{\mathrm{xyz}}}, \tag{3.3}$$

shown in subplots (g,h) of figure 3.3, from which a numerical estimate $\delta x^{\mathrm{sim}}_{\mathrm{lin}}$ of the structure width is measured as the full width at half maximum (FWHM): $\delta x^{\mathrm{sim}}_{\mathrm{lin}}/\rho_i \approx 0.27$ (ITG) and 0.48 (TEM). Numerical estimates are of the same order of magnitude than the theoretical ones, $\delta x^{\mathrm{th}}/\rho_i \approx 0.21$ (ITG) and 0.18 (TEM), with good agreement for ITG and a factor 2.5 larger for TEM.

These fine structures can be indirectly observed through the presence of so-called "Giant tails" [Hallatschek and Dorland, 2005] in the ballooning representation envelope [as defined by relation (2.58)] of the electrostatic potential. Indeed, giant tails in Fourier space correspond to a localized fine structure in direct space. Corresponding giant tails as illustrated in figure 3.4, for the ITG case, are present in the fully kinetic case, when no such big tails are present in the hybrid or adiabatic cases, thus confirming that the fine radial structures are due to the non-adiabatic response of the passing electrons. Nonetheless tails of lower amplitude (2 orders of magnitude smaller) are also present in the hybrid cases corresponding to much weaker radial modulation in direct space and visible in Fig 3.3(c-d). They are due to the trapped electrons response as there is no such tail of low amplitude in the adiabatic case. In the TEM case, not shown here, results are essentially the same.

3.3.3 Local dispersion relation

In this section, the local destabilization of the plasma is studied by the use of a local dispersion relation. This simple code is independent of the GENE code. The purpose is to address the basic mechanisms of destabilization and to have a model of comparison

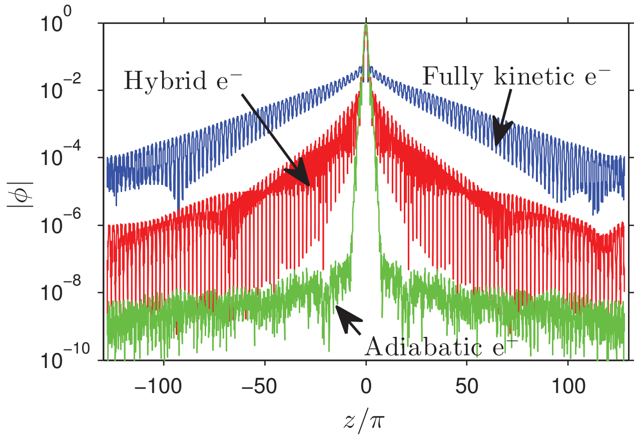

Figure 3.4 – Ballooning representation envelope of the electrostatic potential $|\phi|$ obtained in linear GENE simulations when using the different electron models. ITG test case with $n_x = 128$.

against the GENE linear results, such a comparison is addressed in the next section 3.3.4.

Model

In this section one introduces the local dispersion relation used to describe both ITG and TEM instabilities at the most unfavorable position ($\chi = 0$). In this local approach the field-aligned coordinate system is approximated by a local Cartesian system whose orthogonal directions are: the radial direction where the typical gradients are defined ($1/L_{N,T_i,T_e} = d\ln(N, T_i, T_e)/dx$), the binormal direction which is associated in this local approach to be the perpendicular direction ($k_\perp \equiv k_y$), and the parallel direction to the magnetic field ($k_\| \equiv k_z$). This dispersion relation is based on the gyrokinetic QNE. The perturbed density contribution of each species σ to the QNE is obtained from the gyrokinetic equation [Romanelli and Briguglio, 1990]:

$$\delta N_\sigma = -\frac{q_\sigma \phi}{T_{\sigma 0}} \int_V d^3v \left[1 - J_0^2(\vartheta_\sigma)\frac{\omega - \omega_\sigma^\star}{\omega - k_\| v_\| - \omega_{d\sigma}}\right] f_{\sigma 0}, \tag{3.4}$$

where the first term in the square brackets of the RHS gives the adiabatic response and the second term containing the Bessel function of the first kind J_0 gives the non-adiabatic response. Other parameters are: $\vartheta_\sigma = k_\perp v_\perp/\Omega_\sigma$, $\Omega_\sigma = q_\sigma B_0/m_\sigma$ the cyclotron frequency, $\omega_{d\sigma} = -(v_\|^2 + v_\perp^2/2)k_\perp/R\Omega_\sigma$ the drift frequency related to curvature and gradient of $\mathbf{B}_0$, $\omega_\sigma^\star = \omega_{N\sigma}(1 + \eta_\sigma T_{\sigma 0}\partial/\partial T_\sigma)$, $\omega_{N\sigma} = -T_{\sigma 0}k_\perp/q_j B_0 L_N$, and $\eta_\sigma = L_{N_\sigma}/L_{T_\sigma}$. The kinetic estimate of the ion perturbed density with charge $q_i = Ze$ is obtained from equation (3.4) where the domain of integration is the whole velocity space, giving:

$$\frac{\delta N_i}{N_{i0}} = -\frac{Ze\phi}{T_{i0}} \left[1 - \int_{-\infty}^{+\infty} d^3v\, J_0^2\left(\vartheta_i\right) \frac{\omega - \omega_i^\star}{\omega - k_\| v_\| - \omega_{Di}} \frac{f_{i0}}{N_{i0}}\right]. \tag{3.5}$$

In the frame of the hybrid electron model, the electron density is composed of two contributions: the adiabatic response of the passing electrons $\delta N_{e,pas}/N_{e0} = (1-\alpha_t)e\phi/T_{e0}$ and the bounce-averaged kinetic response of the trapped electrons

$$\frac{\delta N_{e,trp}}{N_{e0}} = \alpha_t \frac{e\phi}{T_{e0}} \left(1 - 4\pi \int_0^{+\infty} d\varepsilon \sqrt{2\varepsilon} \frac{\omega - \omega_e^\star}{\omega - n\langle\dot{\varphi}\rangle} \frac{f_{e0}}{N_{e0}}\right), \tag{3.6}$$

where $\varepsilon = (v_\perp^2 + v_\parallel^2)/2$ is the kinetic energy divided by the mass and $n\langle\dot{\varphi}\rangle$ is the toroidal precessional drift frequency of the trapped electrons. Introducing the dispersion function $W(z) = (2\pi)^{-1/2} \int_\Upsilon dx\, e^{-x^2/2}\, x/(x-z)$, this last equation reduces [Brunner, 1997] to

$$\frac{\delta N_{e,\mathrm{trp}}}{N_{e0}} = \alpha_t \frac{e\phi}{T_{e0}} \left\{1 + \left(1 - \frac{\omega_e^\star}{\omega}\right) \left[z_{be}^2 W(z_{be})\right]\right\}, \tag{3.7}$$

where $\omega_{\varphi e} = n\langle\dot{\varphi}\rangle v_{the}^2/\varepsilon = \omega_{Ne} G L_N/R$, $G \approx 1$ and $z_{be} = \mathrm{sgn}(\omega_{\varphi e})\sqrt{2\omega/\omega_{\varphi e}}$ has been chosen in order to respect causality over the Landau contour Υ of the integral defining $W(z)$.

In order to study the fully kinetic response of the plasma in this local approach, the previously ignored non-adiabatic response of the passing electrons is introduced. The passing electron drift frequency is averaged to zero $\omega_{de} = 0$ because these passing electrons circulate successively over the favorable and unfavorable sides of the poloidal plane with a much higher transit frequency ω_t than the typical ITG/TEM frequencies. The Larmor radius of electrons being small enough, $k_\perp \rho_e \ll 1$, the electron finite Larmor radius effects are neglected: $J_0(\vartheta_e) \approx 1$. The non-adiabatic response of passing electrons is then obtained by integrating equation (3.4) with $\omega_{de} = 0$ and $J_0 = 1$ over the passing velocity phase space $\int_{\mathrm{pas}} d^3v = 2\pi \int_{-\infty}^{+\infty} dv_\parallel \int_0^{v_{\perp c}} dv_\perp$, where $v_{\perp c} = v_\parallel \tan\theta_c$ is the critical perpendicular velocity above which the electrons are trapped. Finally, the fully kinetic response of the passing electrons reads:

$$\frac{\delta N_{e,\mathrm{pas}}}{N_{e0}} = (1-\alpha_t)\frac{e\phi}{T_{e0}} \left\{1 - \left(1 - \frac{\omega_e^\star}{\omega}\right)\left[1 - \frac{W(z_e) - \alpha_t W(z_e/\alpha_t)}{1-\alpha_t}\right]\right\}, \tag{3.8}$$

where $W(z)$ is the dispersion function and $z_e = \omega/k_\parallel v_{the}$. Finally, having a quasi-neutral background ($ZN_{i0} = N_{e0}$), the dispersion relation of the fully kinetic model is:

$$\begin{aligned} 0 &= Z\tau + 1 - Z\tau \int d^3v\, J_0^2(\vartheta_i) \frac{\omega - \omega_i^\star}{\omega - k_\parallel v_\parallel - \omega_{Di}} \frac{f_{i0}}{N_{i0}} \\ &+ \left(1 - \frac{\omega_e^\star}{\omega}\right)\left[\alpha_t z_{be}^2 W(z_{be})\right] \\ &+ \left(1 - \frac{\omega_e^\star}{\omega}\right)\left[-1 + \alpha_t + W(z_e) - \alpha_t W\left(\frac{z_e}{\alpha_t}\right)\right]. \end{aligned} \tag{3.9}$$

Removing both terms proportional to $(1-\omega_e^\star/\omega)$ which contain the non-adiabatic response of electrons gives the dispersion relation of the adiabatic model. Removing only the second term proportional to $(1-\omega_e^\star/\omega)$ gives the dispersion relation of the hybrid model.

Analytical solution at MRS

We are now interested in deriving an analytical solution at MRS, *i.e.* $k_\parallel = 0$, by keeping the essential terms of this local dispersion relation. Equation (3.9) is simplified by noting that $k_\parallel v_\parallel/\omega = 0$. For all cases, ion finite Larmor radius effects turn out to be essential in the destabilization mechanism at MRS, and they are kept at second order by employing the approximation $J_0^2(\vartheta_i) \approx 1 - \vartheta_i^2/2$. This seems to be a reasonable approximation for our reference cases as $k_\perp \rho_i = 0.3$. Also assuming $|\omega/\omega_{Di}| \gg 1$, the ion density response at MRS reads

$$\frac{\delta N_i}{N_{i0}} \approx -\frac{Ze\phi}{T_{i0}}\left\{1 - \frac{\omega-\omega_i^\star}{\omega}\left[1-\xi_i + (2-3\xi_i)\frac{\langle\omega_{Di}\rangle}{2\omega}\right]\right\}, \tag{3.10}$$

where $\xi_i = (k_\perp\rho_i)^2$ and $\langle\omega_{Di}\rangle = \int dv\,\omega_{Di} f_{i0}/N_{i0} = -2T_{i0}k_\perp/q_i B_0 R$ is the drift frequency moment of the Maxwellian distribution function. The kinetic response of the trapped electrons is assumed to be passive ($=0$) in the ITG case and to be the bounce-averaged one in the TEM case. The latter response is obtained by taking the asymptotic expansion $W(z_{be}) \simeq -z_{be}^{-2} - z_{be}^{-4}$ when assuming $|z_{be}| \gg 1$, thus giving [Brunner, 1997]

$$\frac{\delta N_{e,trp}}{N_{e0}} \simeq \alpha_t \frac{e\phi}{T_{e0}}\left[\frac{\omega_{Ne} - 3\omega_{\varphi e}/2}{\omega} + \frac{3}{2}(1+\eta_e)\frac{\omega_{Ne}\omega_{\varphi e}}{\omega^2}\right]. \tag{3.11}$$

The kinetic response of passing electrons is obtained by making use of the asymptotic expansion $W(z_e) \simeq -z_e^{-2}$ for $|z_e| \gg 1$ which in the limit $k_\parallel \to 0$ leads to

$$\frac{\delta N_{e,pas}}{N_{e0}} \underset{k_\parallel\to 0}{=} (1-\alpha_t)\frac{e\phi}{T_{e0}}\frac{\omega_{Ne}}{\omega}. \tag{3.12}$$

These approximations finally lead to the so-called asymptotic dispersion relation

$$\begin{aligned}
0 = {} & \omega^2\left(\xi_i + \frac{c_1}{Z\tau}\right) \\
& + \omega\left\{\omega_{Ni}\left[1 - c_2 - (1+\eta_i)\,\xi_i\right] - \langle\omega_{Di}\rangle\left(1 - \frac{3}{2}\xi_i\right)\right\} \\
& + \omega_{Ni}\langle\omega_{Di}\rangle\left[(1+\eta_i)\left(1-\frac{3}{2}\xi_i\right) - \frac{3}{2}\eta_i\xi_i\right] \\
& \qquad - c_3\,\omega_{Ni}\left\{\omega - \frac{3L_N G}{2R}\left[\omega + Z\tau\omega_{Ni}\,(1+\eta_e)\right]\right\},
\end{aligned} \tag{3.13}$$

where c_1 is the proportion of adiabatic electrons, c_2 is the proportion of kinetic passing electrons, and c_3 is the proportion of kinetic trapped electrons. In the ITG case for adiabatic electrons ($c_1 = 1, c_2 = 0, c_3 = 0$), for hybrid electrons ($c_1 = 1-\alpha_t, c_2 = 0, c_3 =$

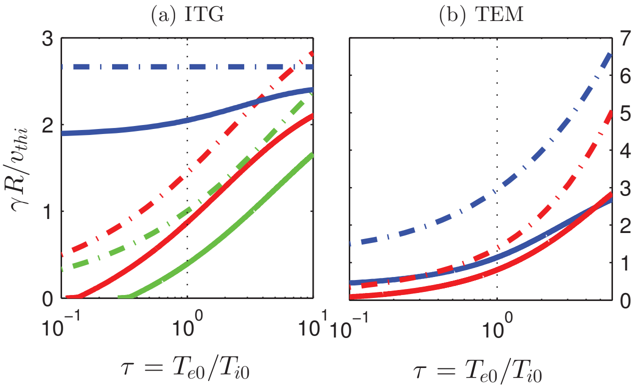

Figure 3.5 – Growth rate γ at the MRS ($k_{\parallel} = 0$) obtained with the local dispersion relation equation (3.9) (full line), and with the asymptotic dispersion relation equation (3.13) (dash-dotted line). ITG case (a) and TEM case (b). Electron models: kinetic (blue), hybrid (red) and adiabatic (green). The vertical dotted line indicates the reference temperature ratio $\tau = 1$.

0), and for fully kinetic electrons ($c_1 = 0, c_2 = 1 - \alpha_t, c_3 = 0$). In the TEM case for the hybrid electron model ($c_1 = 1 - \alpha_t, c_2 = 0, c_3 = \alpha_t$) and for the fully kinetic model ($c_1 = 0, c_2 = 1 - \alpha_t, c_3 = \alpha_t$). Note that in all cases $c_1 + c_2 + c_3 = 1$ except in the ITG case for hybrid and fully kinetic models where $c_1 + c_2 + c_3 = 1 - \alpha_t$ as trapped electrons are assumed to be passive.

The second order polynomial equation (3.13) of the form $A\omega^2 + B\omega + C = 0$ accounts for an instability if and only if the discriminant $\Delta = B^2 - 4AC$ is negative. Noting that $A > 0$, in all cases, a necessary condition for instability is thus $C > 0$ which in turns requires $\omega_{Ni}(1 + \eta_i)\langle\omega_{Di}\rangle > 0$ reflecting the interchange nature of the instability.

In order to appreciate the agreement between the local dispersion relation (3.9) and the asymptotic one (3.13), a scan in τ is carried out in figure 3.5. The destabilizing influence of the non-adiabatic electron response, near MRSs, is recovered with both dispersion relations: $\gamma^{\text{kin}} > \gamma^{\text{hyb}} > \gamma^{\text{ad}}$. The growth rates obtained from equation (3.13) are in a quite good agreement with those obtained from equation (3.9) in the ITG case but appear to be overestimated in the TEM case by a factor $\approx 2 - 3$: this may be due to the approximation $|z_{be}| \gg 1$ when in fact $|z_{be}| \gtrsim 1$ in this TEM case when $k_{\parallel} = 0$. Also for both local and asymptotic dispersion relations, increasing τ, which corresponds to decreasing the adiabatic response, has the effect of reducing the difference between the growth rates obtained with the different electron models.

We now discuss results obtained with the local dispersion relation equation (3.9).

Local destabilization near MRS, results

We first illustrate the destabilizing influence of the three electron models, in the frame of the local dispersion relation study, by carrying out a k_y scan of the most unstable branch using equation (3.9). Results are plotted in figure 3.1 subplots (e) and (f), for the ITG and TEM cases, respectively. The complex frequencies obtained with these local models (plain lines with no markers) are in a qualitative agreement with results obtained from GENE and plotted in subplots (a-d) but the local dispersion relation overestimates the real frequencies and growth rates up to a factor two. This difference can be explained by the fact that the local dispersion is located at the most unstable position, but the flux tube accounts for both unstable and stable sides of the magnetic surface. Note that these results were obtained with the $k_{\|}$ parameter set to: $k_{\|} R q_0 = 0.2$, such that $|\omega_r / k_{\|}| \ll v_{the}$. For the fully-kinetic electron model, also plotted (with asterisk) are the results obtained with a second value of the parallel wave vector: $k_{\|} R q_0 = 0$, such that $|\omega_r / k_{\|}| \gg v_{the}$. In this latter case, the unstable branch in both ITG and TEM cases is now an ion unstable branch ($\omega_r < 0$) which is unstable at very short scales. Notice that our previous analytical results pointed out the ion interchange nature of this destabilization when $k_{\|} = 0$.

The plasma stability study conducted with the local dispersion-relation, equation (3.9), demonstrates the destabilizing role of the non-adiabatic response of passing electrons near MRSs. Note that in this local description of the plasma, the distance from the MRS is adjusted with the parameter $k_{\|}$, by using the mapping $k_{\|} \mapsto x$ defined by equation (3.1). Results plotted in figure 3.6 (a,b) clearly show that when getting closer to the MRS, *i.e.* $k_{\|}$ going to zero, the kinetic model provides larger growth rates than the hybrid model. It thus reveals the destabilizing role of the non-adiabatic response of passing electrons near MRS. Moreover, as one can appreciate in figure 3.6 (c,d), this divergence between kinetic and hybrid results starts from a value of $k_{\|}$ where the parallel phase velocity of the wave is of the order of the electron thermal velocity ($|\omega_r / k_{\|} v_{the}| \approx 1$). It validates the choice of the criteria $|\omega / k_{\|}| = v_{the}$ used to derive the theoretical width estimate of the fine structures equation (3.2).

In order to compare these local results with GENE results, we define a “local” width estimate of the fine structure in which the unstable growth rate obtained with the fully kinetic model is significantly larger than the one obtained with the hybrid electron model. This local estimate of the fine structure width is defined as the FWHM of $\Delta\gamma = (\gamma^{\text{kin}} - \gamma^{\text{hyb}})$. For comparison purpose, $\Delta\gamma$, as well as the difference between kinetic and hybrid envelopes of the electrostatic potential, $\Delta|\phi| = |\phi^{\text{kin}}| - |\phi^{\text{hyb}}|$, obtained with GENE are plotted with respect to the radial distance to the MRS in figure 3.7. It is remarkable that the abrupt increase of the growth rate due to the non-adiabatic response of passing electrons near MRS occurs within a radial region where the radial fine structure is present over the perturbation fields of GENE results. The FWHM of $\Delta\gamma$ localizes the fine structure “boundary” to be at $x/\rho_i \approx 0.1$ (ITG) and 0.2 (TEM), in figure 3.6. At these respective positions one has $|\omega_r / k_{\|} v_{the}| \approx 1$ and 0.4.

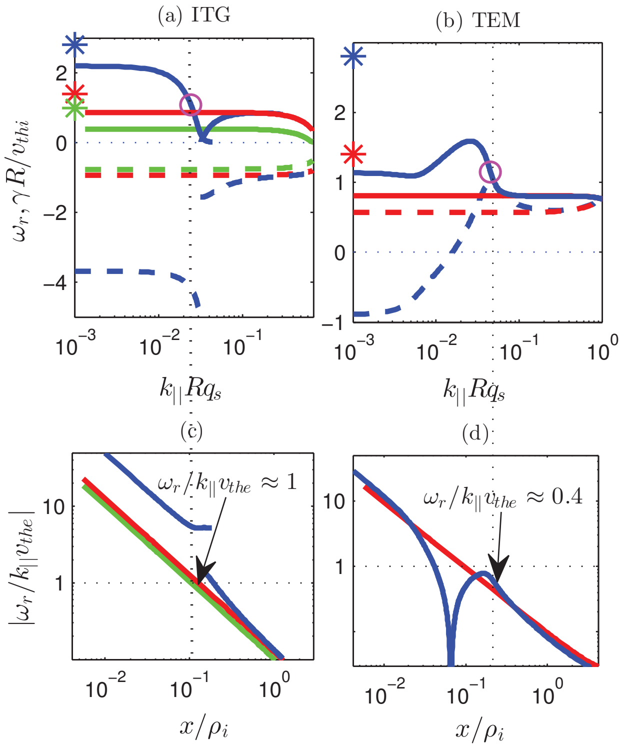

Figure 3.6 – Solution to the local dispersion relations equation (3.9) obtained when considering the different electron models: adiabatic (green), hybrid (red) and fully kinetic (blue), for both (a,c) ITG and (b,d) TEM test cases of reference described in Tab. 3.1. In the top subplots (a) and (b), the growth rate is plotted with full lines and the real frequency with dashed lines. In the bottom subplots (c) and (d), the phase velocity normalized with respect to the electron thermal one is shown as a function of the distance x to the MRS. The radial distance to the MRS x, in the x-axis of (a) and (b) is mapped to the value of $k_{||}$ in the x-axis of (c) and (d) by using equation (3.1). The FWHM which corresponds to the local width estimate of the fine structure δx^{loc} is plotted with magenta circles. Growth rates obtained with the asymptotic dispersion relation (3.13) are indicated with an asterisk in subplots (a) and (b).

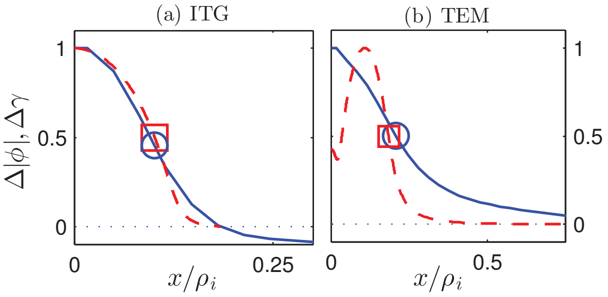

Figure 3.7 – Fine radial structure over the electrostatic potential $\Delta|\phi| = |\widetilde{\phi}^{\mathrm{kin}}| - |\widetilde{\phi}^{\mathrm{hyb}}|$ in linear GENE simulations (blue full lines) and of the growth rate $\Delta\gamma = (\gamma^{\mathrm{kin}} - \gamma^{\mathrm{hyb}})$ obtained from local dispersion relation (red dashed lines). Both curves are normalized to their maximum value as one is only interested in the radial localization of the structures. Estimates of the width $\delta x^{\mathrm{sim}}_{\mathrm{lin}}$ and δx^{loc} (FWHMs) are indicated with circles and squares, respectively.

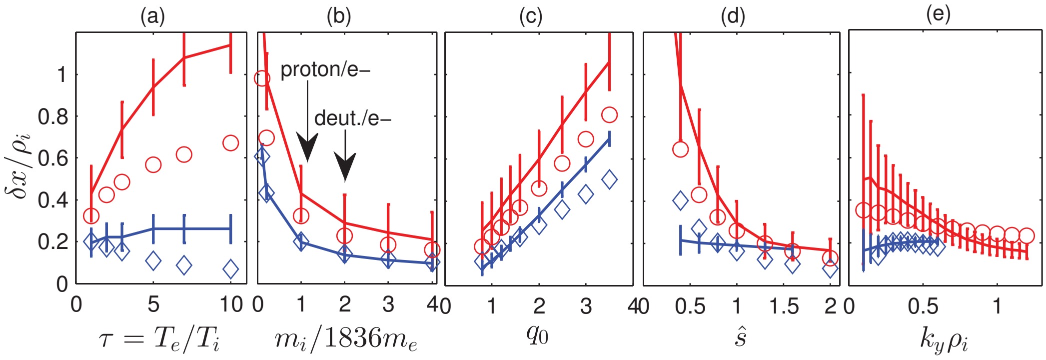

Figure 3.8 – Numerical estimates of the fine radial structure width with respect to different scanned parameters. Results obtained from GENE $\delta x^{\mathrm{sim}}_{\mathrm{lin}}$ are plotted in full line, with vertical error bars $\pm 2\Delta x$ and $\Delta x = L_x/n_x$ the radial resolution, ITG in blue and TEM in red. Results obtained from the local dispersion relation δx^{loc}: ITG in blue diamonds and TEM in red circles.

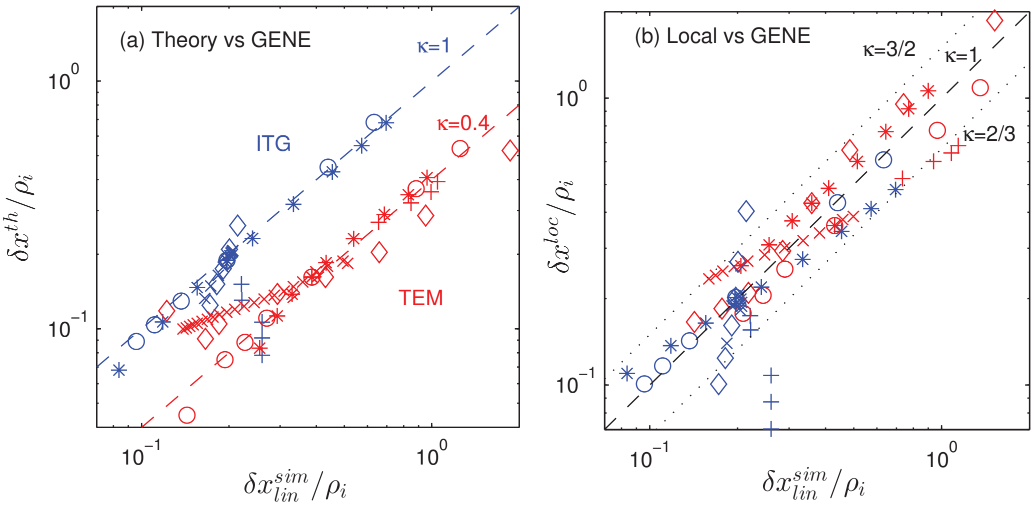

Figure 3.9 – Numerical width estimate $\delta x^{\mathrm{sim}}_{\mathrm{lin}}$ of the fine structures near MRSs obtained with the FWHM in GENE versus (a) the theoretical estimate δx^{th} using linear GENE frequencies and versus (b) the estimate $\delta x^{\mathrm{local}}$ computed from the local dispersion relation. For the different scans of figure 3.8: τ $(+)$, $\mu(\circ)$, $q_s(*)$, $\hat{s}(\diamond)$ and $k_y(\times)$. ITG in blue and TEM in red. Lines of constant slope have been plotted such that $\delta x = \kappa\, \delta x^{\mathrm{sim}}_{\mathrm{lin}}$.

3.3.4 Systematic scan of physical parameters and comparison of the radial width estimates

Numerical width estimates $\delta x^{\mathrm{sim}}_{\mathrm{lin}}$ plotted in figure 3.8 are obtained while scanning the aforementioned physical parameters of equation (3.2): τ, μ, q_0, $\hat{s}$, and k_y. It is remarkable that a fine structure is always present over the eigenmode of the electrostatic potential with a radial width systematically smaller than an ion Larmor radius or so, except for $\hat{s} \to 0$. It is also remarkable that the width estimate obtained from the local dispersion relation is in qualitative agreement with GENE simulation results, thus confirming that the radial fine structures are related to a local destabilization of the plasma due to the non-adiabatic response of passing electron near MRSs. The influence of the scanned physical parameters over the structure width can be obtained by fitting the results with power scaling laws: in the ITG case we obtain $\delta x^{\mathrm{sim}}_{\mathrm{lin,ITG}} \propto \mu^{-1/2} q_0$ and in the TEM case we obtain $\delta x^{\mathrm{sim}}_{\mathrm{lin,TEM}} \propto \tau^{1/2}\mu^{-1/2} q_0^{3/2} \hat{s}^{-1} k_y^{-1/2}$. The difference of these two relations with the theoretical relation given by equation (3.2) reflects the fact that ω_r is not constant and its value taken from GENE varies with the scanned parameters.

In figure 3.9, for each linear simulation carried out with GENE when scanning the physical parameters, the numerical width estimate $\delta x^{\mathrm{sim}}_{\mathrm{lin}}$ is compared to both theoretical estimate δx^{th} and local estimate δx^{loc} obtained with corresponding parameters. In subplot (a), the numerical estimates obtained from GENE simulations are in good agreement with the theoretical ones, as their ratio is of order unity. In the ITG case, for the majority

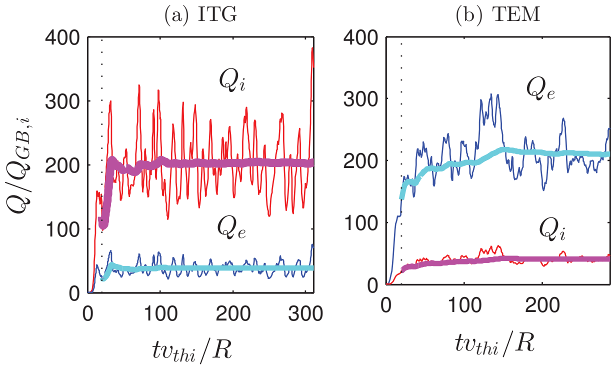

Figure 3.10 – Ion and electron kinetic energy fluxes, respectively Q_i (red) and Q_e (blue), for both the (a) ITG and (b) TEM cases. The thicker lines are the running averages, which start at $t_s = 20\, v_{thi}/R$ indicated with a vertical dotted line. Fluxes normalized in ion Gyro-Bohm units $Q_{\mathrm{GB,i}} = N_0 T_{i0} v_{thi} \rho_i^2/R^2$.

of scanned parameters one has $\kappa = \delta x^{\mathrm{th}}/\delta x^{\mathrm{sim}}_{\mathrm{lin}} \approx 1$. In the TEM case, this velocity ratio is of the order of, but smaller, than unity: $\kappa = \delta x^{\mathrm{th}}/\delta x^{\mathrm{sim}}_{\mathrm{lin}} \approx 0.4$ indicating that the destabilization occurs for slower parallel wave velocities in this case than for ITG modes. It thus validates the choice of using the criteria $|\omega_r/k_\parallel| \approx v_{the}$ to localize, at leading order, the boundaries of the non-adiabatic region when defining the theoretical estimate δx^{th} of the width, equation (3.2). In subplot (b), the numerical width estimates obtained from GENE $\delta x^{\mathrm{sim}}_{\mathrm{lin}}$ are in good agreement with the local ones δx^{loc} for all scanned parameters of both the ITG and TEM test cases. This good agreement between the results obtained with GENE and the results obtained with the local dispersion relation, also clearly appreciable in figure 3.8, shows that the fine structures near MRSs are related to the local destabilization due to the passing electrons dynamics.

3.4 Fine structures in nonlinear simulations and their effect on transport

3.4.1 ITG and TEM test cases

Nonlinear simulations with hybrid and fully kinetic electrons have been carried out considering the reduced mass ratio $\mu = 400$ (see table 3.1) over a sufficiently long time (up to $t \sim 300\, R/v_{thi}$) to ensure good statistics over the saturated turbulent phase, as illustrated in figure 3.10 showing the time traces of the ion and electron kinetic energy fluxes, Q_i and Q_e respectively, for both the ITG and TEM cases. Also reported in these plots are the running time averages, $Q_j^{\mathrm{run}}(t) = \int_{t_s}^{t} Q_j(t')dt'/(t-t_s)$, taken over the turbulent saturated regime, which has been estimated to start in both cases at $t_s = 20\, R/v_{thi}$. The final values of these running averages provide the time-averaged fluxes over the full saturated turbulent phase of the simulation. In the following, $\langle\cdot\rangle_t$

stands for the time average of different physical quantities taken over the so-defined saturated time window.

Turbulence simulations involve the evolution of a spectrum of nonlinearly coupled k_y modes which consists, in our simulations, of a set of 64 modes $k_y = i_y k_{y,min}$ ($i_y = 0, .., 63$), so that $k_{y,min}\,\rho_i = 0.07$ and 0.04, in ITG and TEM cases, respectively. The k_x spectrum consists of a set of $n_{k_x} = 432$ (resp. 256) modes $k_x = i_x k_{x,min}$ ($i_x = -n_{k_x}/2, .., 0, ..., n_{k_x}/2$), so that $k_{x,min}\,\rho_i = 0.032$ (resp. 0.056), in ITG (resp. TEM) case. A convergence study with respect to the number of k_x modes, $n_{k_x} = n_x$, is conducted in Sec. 3.4.3.

Shearing of turbulent eddies by turbulence-generated Zonal Flows (ZFs) is understood to be the dominant saturation mechanism of ITG-driven turbulence and therefore of the associated transport fluxes [Lin et al., 1998, Diamond et al., 2005, Itoh et al., 2006]. As various studies have shown [Lang et al., 2008, Merz and Jenko, 2008], the role played by ZFs in saturating TEM driven turbulence is more complex. In particular, in reference [Lang et al., 2008] the efficiency of turbulence saturation by ZFs is strongly dependent on the parameter range considered. It is to be noted that the physical parameters for the considered TEM case are essentially the same as the ones considered in Ref [Merz and Jenko, 2008], except for the temperature ratio $\tau = 1$ considered here instead of $\tau = 3$. According to Ref [Lang et al., 2008], going from $\tau = 3$ to $\tau = 1$ pushes the system from a regime where ZFs play a sub-dominant role in the saturation mechanism of the TEM turbulence towards a regime where ZFs play a dominant role. This has been confirmed in our simulations by artificially zeroing out the ZFs, which led to a 10-fold increase of the turbulent fluxes, clearly reflecting the essential role played by the ZFs in regulating the turbulence.

As already mentioned when discussing the linear results, the boundary conditions require the radial length L_x of the simulation to be an integer multiple of the distance between MRSs for each considered k_y mode. Note that it is sufficient for this condition to be verified by L_x for $k_{y,min}$ for it to be verified for all k_y. One thus needs to set $L_x = M\,L_{\text{LMRS}}$, with M an integer and $L_{\text{LMRS}} = 1/\hat{s}k_{y,min}$ the distance between lowest-order MRSs. For the ITG and TEM cases, $M = 8$ and 4 were chosen, giving respectively $L_x = 142.9\,\rho_i$ and $125.0\,\rho_i$, thus ensuring a large enough box ($> 100\,\rho_i$) compared to the typical radial turbulence correlation length of order $\sim 10\,\rho_i$. The number of radial grid points n_x is taken so as to resolve the fine structures in the corresponding *linear* eigenmodes of the k_y modes which dominate the turbulent flux spectra (see figure 3.15). The values $n_x = 432$ and 256 were thus chosen for the basic simulations, corresponding to radial grid spacings $\Delta x = L_x/n_x = 0.33\,\rho_i$ and $0.49\,\rho_i$ for the ITG and TEM cases, respectively. Figure 3.11 confirms that these resolutions are indeed sufficient according to this criteria. Note that the radial widths $\delta x_{\text{lin}}^{\text{sim}}$ of linear eigenmode structures as a function of $k_y\rho_i$ shown in figure 3.11 are very similar to the results shown in figure 3.8(e), these widths being however broadened as a result of the reduced mass ratio considered here. This is explained by the fact that $\delta x \propto \omega_r/\mu^{1/2}$ according to equation (3.2) with the real frequency ω_r

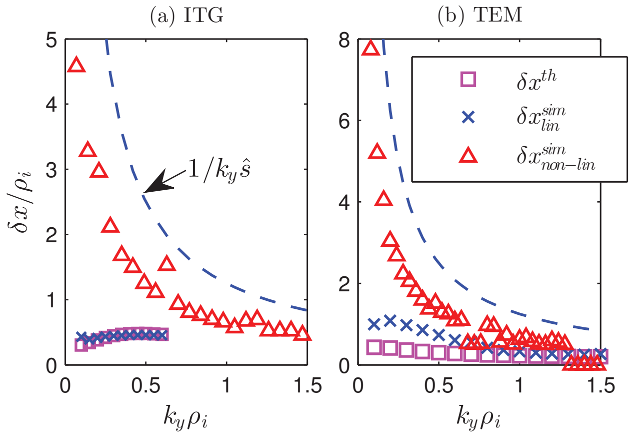

Figure 3.11 – Comparing fine structure widths as a function of k_y: linear theoretical estimate $\delta x^{\rm th}$ (equation (3.2), squares), linear GENE $\delta x^{\rm sim}_{\rm lin}$ ($=$ FWHM$[\Delta|\widehat{\phi}|]$, crosses), and nonlinear GENE ($\delta x^{\rm sim}_{\rm non-lin} =$ FWHM$[|\widehat{\phi}|]$, triangles) for both the (a) ITG and (b) TEM test cases. The distance $1/\hat{s}k_y$ between MRSs is indicated with a blue dashed line. $n_x = 432$.

being essentially unchanged when reducing μ from the physical value 1836 to the reduced value 400 as shown in figure 3.1. This has been confirmed with linear simulations when establishing the power scaling laws $\delta x^{\rm sim}_{\rm lin,ITG}$ and $\delta x^{\rm sim}_{\rm lin,TEM}$ both proportional to $\mu^{-1/2}$. Simulations with other values of n_x were carried out as well and are presented in Sec. 3.4.3 where the issue of radial resolution convergence of fine structures is discussed. The broadening of the radial structures are the main rationale for considering a reduced mass ratio for the nonlinear simulations, as it enables to more easily ensure sufficient radial resolution with a tractable number of grid points.

Concerning the grid resolutions in the other phase space directions, $n_z = 16$ points along z were chosen for both the ITG and TEM cases. Boundaries along the velocity space directions were set to $v_{\parallel,\rm max} = 4.2\,v_{th}$ and $\mu_{\rm max} = 9\,T/B_0$ for each species both in the ITG and TEM cases, with the corresponding resolutions $n_{v_\parallel} \times n_\mu = 64 \times 8$ and 64×16 respectively. Note the slightly higher velocity resolution for the latter case, to ensure an accurate description of the trapped/passing boundary, essential for TEM simulations. In GENE, the filamentation of the phase space in the $v_\parallel$ and z directions is either controlled by considering physically realistic collisions (inter- and intra-species linearized Landau collision operators) or thanks to fourth order hyper-diffusion terms. For the results presented in this paper, the latter approach is considered by using fourth order hyper-diffusion terms [Pueschel et al., 2010, Hatch et al., 2013] to the RHS of the gyrokinetic equation: $D/Dt = -\nu_\parallel \partial^4/\partial v_\parallel^4 - \nu_z \partial^4/\partial z^4$. In our ITG and TEM test cases, we set the numerical parameters equal to $\nu_\parallel/\Delta v_\parallel^4 = 0.5$ and 1, and $h_z = \nu_z/\Delta z^4 = 0.5$ and 1, respectively. No significant differences were observed when using lower v hyper

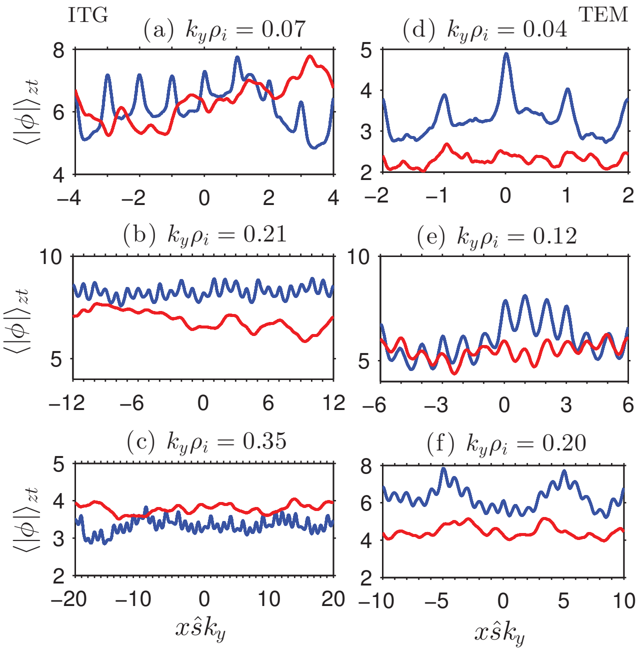

Figure 3.12 – Radial dependence of the z- and time- averaged electrostatic potential amplitude $\langle|\widehat{\phi}_{k_y}|\rangle_{zt}(x)$ for the nonlinear (a-c) ITG and (d-f) TEM cases. Comparing results from both the fully kinetic (blue) and hybrid (red) electron models for different values of $k_y\rho_i$. For each k_y, associated MRSs are pointed out with tick marks along the box edge of the corresponding figure.

diffusion: there is at maximum 1 to 4% of difference between the fluxes due to the effect of decreasing the hyper-diffusion at a value of $h_v = 0.2$, in both the ITG and TEM test cases with $n_x = 256$.

3.4.2 Fine structures at MRSs

Fine structure over $k_y \neq 0$ modes

The z- and time- averaged amplitudes of non-zero k_y Fourier modes obtained from the electrostatic potential, $\langle|\widehat{\phi}_{k_y}|\rangle_{zt}(x,z)$, are shown in figure 3.12. These plots clearly illustrate for each mode $k_y \neq 0$ the presence in the fully kinetic results of fine radial structures located at the associated MRSs, positioned at $x = \delta m/\hat{s}k_y$, δm integer and indicated with tick marks in the corresponding plots. Similar fine structures are essentially (see the next paragraph) absent in the hybrid simulations. This confirms that the fine structures related to the non-adiabatic passing electrons and originally identified in the linear simulations actually persist in the nonlinear turbulent regime. The systematic procedure applied in the linear study for measuring their radial width δx, based on subtracting the eigenmode envelope related to the hybrid computation from the one obtained with fully kinetic electrons, is however not applicable in any straightforward way for analyzing the nonlinear data. One can nonetheless estimate the widths δx by directly measuring on $\langle|\widehat{\phi}^{\rm kin}_{k_y}|\rangle_{zt}(x)$ the FWHM of fine structures appearing at corresponding MRSs. As the nonlinear simulation system contains multiple MRSs for each $k_y \neq 0$, one in fact estimates an *average* δx over all associated structures. Corresponding results in figure 3.11, labeled $\delta x^{\rm sim}_{\rm non-lin}$, show that structures, although persisting in the nonlinear regime, are significantly broadened compared to the linear widths $\delta x^{\rm sim}_{\rm lin}$ in both the ITG and TEM cases, by up to a factor ~ 9 for the lower k_y modes.

In the TEM nonlinear hybrid simulations, the particular case of the $k_y\rho_i = 0.12$ mode shows, in figure 3.12 (e), radial corrugations over the time-averaged envelope of $|\phi|^{\rm hyb}$. Indeed as shown with linear hybrid electron simulations in figure 3.3 (c) and (d), a large radial modulation of weak amplitude is already present on the linear mode envelope $|\phi^{\rm hyb}|$. This weak corrugation not exactly aligned with the MRS is even more visible on the small k_y modes in adiabatic electrons simulations ($k_y\rho_i < 0.15$) - not shown in this paper. We attribute this weak radial corrugation to the ion dynamics.

Fine radial corrugation of $k_y = 0$ modes

In nonlinear simulations, the axisymmetric Fourier modes ($k_y = 0$) are coupled to, and thus driven by, the unstable non-axisymmetric modes ($k_y \neq 0$). As a result, the radial structures located at MRSs of $k_y \neq 0$ modes lead to similar structures on the $k_y = 0$ modes in case of fully kinetic electron simulations. Such coupling is brought to the fore by studying time- and flux-surface- averages of various fluctuation field quantities, $\langle\cdot\rangle_{FS} = \langle\cdot\rangle_{yz}$ in flux-tube coordinates. Note that averaging over the y-direction provides the $k_y = 0$ Fourier component. This is clearly illustrated in figure 3.13(a-b) where the time-averaged shearing rate $\langle\omega_{E\times B}\rangle_t$ related to the zonal $E \times B$ flow has been plotted. This shearing rate is related to the zonal component $\langle\phi\rangle_{yz}(x,t) = \int \widehat{\phi}(x, k_y = 0, z, t)\mathcal{J}^{\rm xyz}dz / \int \mathcal{J}^{\rm xyz}dz$ by the relation $\omega_{E\times B}(x,t) \simeq (1/B_0)\partial^2\langle\phi\rangle_{yz}/\partial x^2$. As will appear even clearer in figure 3.14, radial structures can be identified not only at the position of lowest order MRSs (*i.e.* related to $k_y = k_{y,\rm min}$) but to the positions of next order MRSs (corresponding to $k_y = 2k_{y,\rm min}$ and $k_y = 3k_{y,\rm min}$) as well. This appearance of radial structures on the $k_y = 0$ Fourier modes through nonlinear coupling can be identified on essentially all fluctuation fields. As an example, the radial gradient profile $\nabla_x\langle\delta T_e\rangle_{yzt}$ of the time- and flux-surface- averaged electron temperature fluctuation (with δT_e computed using $\delta T_j = \int d^3v \delta f_j v^2/3N_0 - T_{\sigma 0}\delta N/N_{\sigma j0}$) is shown in figure 3.13(c-d). Note how corresponding simulation results obtained with the hybrid electron model provide profiles with radial structures which either present much weaker amplitudes and/or whose radial positions do not appear to be correlated to MRSs. It is important to point out that in the nonlinear turbulent simulations, the fine radial structures are fully revealed only after *time-averaging* the fluctuations. The standard deviation over time, $\sigma(x)$, of the flux-surface-averaged fluctuations have been reported in figure 3.13 as well. Note that σ appears to be only very weakly dependent on x. The fact that σ in the case of fully

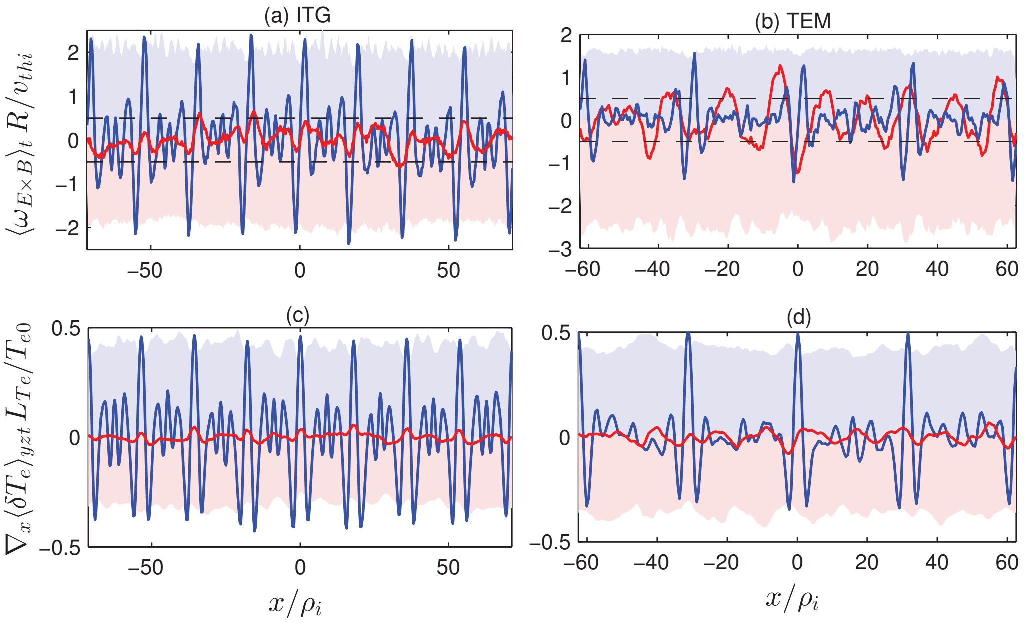

Figure 3.13 – (Color online) (a, b) Time-average of the $E \times B$ shearing rate $\langle\omega_{E\times B}\rangle_t$ related to the zonal component $\langle\phi\rangle_{yz}$, as well as (c, d) the radial gradient $\nabla_x\langle\delta T_e\rangle_{yzt}$ of the time- and flux-surface- averaged electron temperature fluctuation for hybrid (red) and kinetic (blue) electron response models. Showing results for both (a, c) the ITG and (b, d) the TEM cases. Shaded areas reflect the radially local standard deviation levels $\sigma(x)$ of corresponding fluctuation components (areas delimited by $-\sigma(x)$ and $+\sigma(x)$ for hybrid and kinetic models resp.). The maximum linear growth rate γ_{ref}, estimated as detailed in Sec. 3.4.3, is plotted with horizontal dashed lines.

kinetic electron simulations is of the same order as the radial modulation amplitude of the time averages (both for $\omega_{E\times B}$ and $\nabla_x\langle\delta T_e\rangle_{yzt}$) reflects that the time-averaged component of the fluctuations is at least partly "drowned" by the time-dependent component. This is all the more so in the case of the hybrid simulations, where the weak non-zero time-averaged component is significantly smaller than the time dependent component [*e.g.* $\max_x(|\omega_{E\times B}|) \sim \sigma/2$ and $\max_x(|\nabla_x\langle\delta T_e\rangle_{yzt}|) \sim \sigma/8$].

Characteristic profile modulation of flux-surface averaged fields and related gradients

Remarkable in figure 3.13 on both radial profiles $\langle\omega_{E\times B}\rangle_t$ and $\nabla_x\langle\delta T_e\rangle_{yzt}$ of the fully kinetic electron simulations are their periodicity with respect to the distance L_{LMRS} between lowest-order MRSs. This periodicity is emphasized in figure 3.14, where the time- and flux-surface- averaged profiles over the full radial simulation length $L_x = M\,L_{\text{LMRS}}$ of various fluctuation fields have been cut into M segments which were then superimposed, the lowest-order MRSs of each segment having been positioned at the center $x = 0$

of these plots. The nearly perfect alignment of profile segments for simulation results obtained with the fully kinetic electron model, both in the ITG and TEM case, thus clearly reflects the periodicity of radial structures, while the obvious misalignment in corresponding plots obtained with the hybrid model reflects that such periodicity of structures related to positions of MRSs is lacking or at least much weaker in these latter simulations. A hint of periodic structures aligned with the lowest-order mode rational surfaces is nonetheless apparent in the hybrid electron ITG simulation, Figs. 3.14(b) and 3.14(f). These structures must however be related to the particular resonant dynamics near MRSs of passing *ions* and corresponding widths are therefore much wider than in the simulations with fully kinetic electrons.

In particular, the radial gradient $\nabla_x \langle \delta\mathcal{A} \rangle_{yzt}$ of the time- and flux-surface- averaged fluctuations for different field quantities $\mathcal{A}$ normalized with respect to corresponding background gradients $|\nabla_x \mathcal{A}_0| = \mathcal{A}_0/L_\mathcal{A}$ are plotted in the first row of figure 3.14. Shown are profiles related to density, $\mathcal{A} = N$, as well as electron and ion temperatures, *i.e.* $\mathcal{A} = T_e$ and $\mathcal{A} = T_i$ respectively. The appearance of non-zero profiles $\nabla_x \langle \delta\mathcal{A} \rangle_{yzt}$ which converge in time during the saturated turbulent phase obviously correspond to a modification of the average profiles from the initial background profiles $\mathcal{A}_0$. The total time- and flux-surface-averaged radial gradient profile of a given field $\mathcal{A} = \mathcal{A}_0 + \delta\mathcal{A}$ can indeed be written:

$$\nabla_x \langle \mathcal{A} \rangle_{yzt} = \nabla_x \mathcal{A}_0 + \nabla_x \langle \delta\mathcal{A} \rangle_{yzt} = |\nabla_x \mathcal{A}_0|(-1 + \zeta_\mathcal{A}),$$

noting that $-\nabla_x \mathcal{A}_0 = |\nabla_x \mathcal{A}_0| = \mathcal{A}_0/L_\mathcal{A}$ and having used the notation

$$\zeta_\mathcal{A} = \nabla_x \langle \delta\mathcal{A} \rangle_{yzt} / (\mathcal{A}_0/L_\mathcal{A}),$$

for the normalized averaged fluctuation profiles as appearing in Figs. 3.14(a-d). Therefore where $\zeta_\mathcal{A} > 0$, respectively $\zeta_\mathcal{A} < 0$, the profile of $\mathcal{A}$ is locally flattened, respectively steepened, compared to the initial background $\mathcal{A}_0$. In particular, a value of $\zeta_\mathcal{A} = +1$ corresponds to a full (100%) flattening.

One observes that in the case of fully kinetic electron simulations, for both the ITG and TEM cases, all three gradients ratios ζ_N, ζ_{T_e}, and ζ_{T_i} present maxima at the low order mode rational surfaces. These maxima are most prominent for the electron temperature profile at the position $x = \delta m/\hat{s}k_{y,\text{min}}$ of the lowest-order mode rational surfaces, presenting values up to $\zeta_{T_e} = +0.5$ and thus reflecting a 50% flattening at these positions, in both the ITG and TEM cases. Somewhat lower local maxima are also clearly visible at the positions $x = \delta m/\hat{s}k_y$ of next order mode rational surfaces, *i.e.* at least for $k_y = 2\,k_{y,\text{min}}$ and $3\,k_{y,\text{min}}$. Between these lowest-order MRSs, $\zeta_\mathcal{A}$ of the different fields takes on negative values, reflecting steepening of corresponding profiles. Most prominent minimum values are again reached in case of the electron temperature, with values down to $\zeta_\mathcal{A} = -0.3$ corresponding to a 30% steepening. Due to the periodic radial boundaries in a flux-tube simulation, the radial average of the total profile gradient cannot be modified.

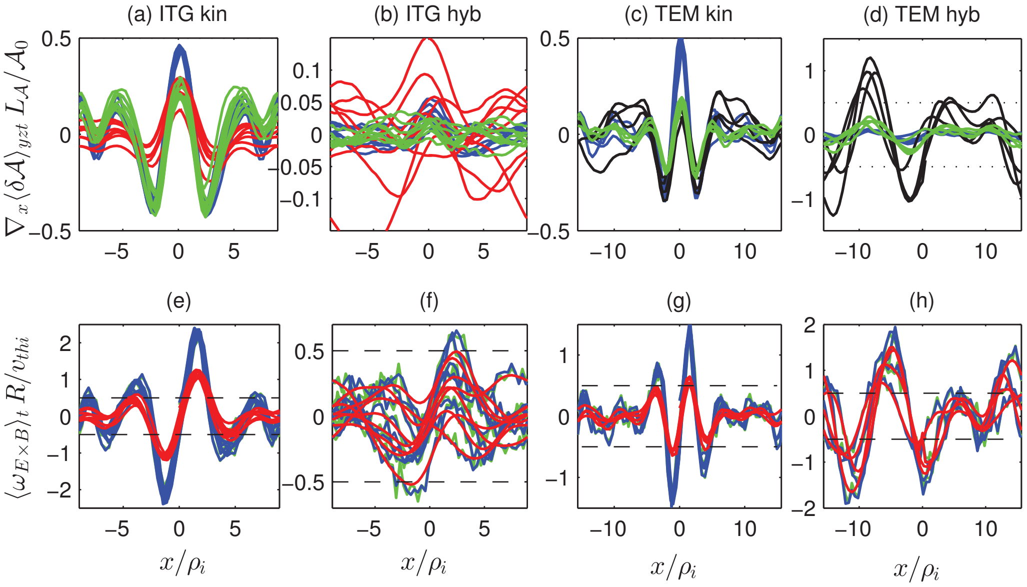

Figure 3.14 – (Color online). (a-d) Radial gradient $\nabla_x \langle \delta \mathcal{A} \rangle_{yzt}$ of the time- and flux-surface- averaged fluctuations for different field quantities $\mathcal{A}$ normalized with respect to corresponding background gradients $|\nabla_x \mathcal{A}_0| = \mathcal{A}_0 / L_{\mathcal{A}}$: density $\mathcal{A} = N$ (green), electron temperature $\mathcal{A} = T_{e0}$ (blue), and ion temperature $\mathcal{A} = T_{i0}$ (red). Profile sections of length L_{LMRS} have been superimposed (with lowest-order MRSs at $x = 0$), emphasizing periodicity in case of fully kinetic electron simulations. In the TEM case, $\nabla_x T_{i0} = 0$ so that $\nabla_x \langle \delta T_i \rangle_{yzt}$ is given in units of T_{i0}/ρ_i instead of $T_{i0}/L_{T,i}$ (black). (e-f) Time-averaged shearing rate $\langle \omega_{E\times B} \rangle_t$ estimated with $E = -\nabla_x \langle \phi \rangle_{yz}$ (green) and effective shearing rate $\langle \omega^{i,e}_{E\times B} \rangle_t$ felt by the ions and electrons estimated with gyroaveraged $\bar{E} = -\nabla_x \langle \bar{\phi} \rangle_{yz}$ (red and blue respectively). Horizontal dashed lines represent γ_{ref} of linear simulations. Shown are ITG results with (a,e) kinetic and (b,f) hybrid electrons, as well as TEM results with (c,g) kinetic and (d,h) hybrid electrons.

Locally flattened regions must therefore necessarily alternate with locally steepened ones: $\langle \zeta_{\mathcal{A}} \rangle_x = 0$.

Characteristic profile modulation of $\omega_{E\times B}$ and of its gyroaverage

In the second row of figure 3.14, the M segments of the shearing rate profile $\langle \omega_{E\times B} \rangle_t$ have been superimposed as well. In fact, the effective electric field felt by the particles is a gyroaveraged one. As the width δx of radial structures apparent on the $\langle \omega_{E\times B} \rangle_t$ shear profiles are comparable to the ion Larmor radius, an effective shearing rate $\langle \omega^j_{E\times B} \rangle_t$ should be computed separately for each species using the gyroaveraged zonal flow component of ϕ, *i.e.* $\omega^j_{E\times B} \simeq (1/B_0)\partial^2 \langle \bar{\phi} \rangle_{yz}/\partial x^2$, with $\bar{\phi} = \mathcal{G}_j \phi$ and the gyroaveraging operator $\mathcal{G}_j$, itself averaged over the Maxwellian background distribution, given in Fourier space by

$$\widehat{\mathcal{G}}_j = \frac{B_0}{T_{0,j}} \int_0^{+\infty} d\mu \exp\left(-\frac{\mu B_0}{T_{0,j}}\right) J_0\left(\frac{k_\perp v_\perp}{\Omega_j}\right) = e^{-\xi_j/2}, \tag{3.14}$$

recalling the notation $\xi_j = (k_\perp \rho_j)^2$. For ions, the so-obtained gyroaveraged shearing rate $\langle \omega^i_{E\times B} \rangle_t$ is reduced by nearly 50% in both the ITG and TEM simulations with fully kinetic electrons. For electrons, the corresponding effective shearing rate $\langle \omega^e_{E\times B} \rangle_t$ is essentially identical to the non-gyroaveraged profile $\langle \omega_{E\times B} \rangle_t$. This is to be expected as the radial structures remain large with respect to electron Larmor radii. In the hybrid simulations, the structures on the $\langle \omega_{E\times B} \rangle_t$ profile are less affected by the gyroaveraging effects, even for ions, as their widths are significantly larger than in the fully kinetic electron simulations.

Finally, comparing the gradients with the $E \times B$ shearing rate, in ITG and TEM cases with kinetic electrons, it appears that ζ_N, ζ_{T_i} and ζ_{T_e} have an extremum where the $\omega_{E\times B}$ shearing rate is zero. Conversely, ζ_N, ζ_{T_i} and ζ_{T_e} are zero when the $\omega_{E\times B}$ is extremum. In comparison, no such regular and well defined pattern seems to appear in the hybrid simulation cases. In figure 3.13, this basic pattern organization can be clearly recognized in the ITG case not only for the $k_{y,min}$ related MRSs but also for the $2\,k_{y,min}$ and $3\,k_{y,min}$ MRSs as already observed [Waltz et al., 2006] over the electron temperature profiles. The same structures related to $2\,k_{y,min}$ and $3\,k_{y,min}$ Fourier modes, although somewhat fainter, can be seen for the TEM case as well.

3.4.3 Turbulent fluxes

The turbulent radial fluxes result from the x-component of the $E \times B$ drift, given by $v_{E\times B,x} = -(1/B_0^2)(\nabla\phi \times \mathbf{B}_0)\cdot\nabla x/|\nabla x| \simeq -(1/B_0)\partial\phi/\partial y$, where ϕ is the scalar potential related to the essentially electrostatic fluctuations. One notes that although magnetic fluctuations have been accounted for in the fully kinetic simulations, their contribution to the turbulent fluxes represent less than 1% of the total fluxes and are not discussed here.

The electrostatic fluxes, specific to each species j and averaged over the flux-tube volume $V = \int d^3x = \int dxdydz\mathcal{J}^{\mathrm{xyz}}$, are essentially of the form:

$$\mathcal{F}_j[\bullet](t) = \frac{1}{V}\int d^3x\,\frac{1}{B_0}\left(-\frac{\partial\phi}{\partial y}\right)(\mathbf{x},t)\int d^3v\,\bullet\,\delta f_j(\mathbf{x},\mathbf{v},t). \tag{3.15}$$

In particular, the particle flux and kinetic energy flux are given by $\Gamma_j = \mathcal{F}_j[1]$ and $Q_j = \mathcal{F}_j[m_jv^2/2]$, and have been normalized to the following ion Gyro-Bohm units $\Gamma_{GB,i} = N_0 v_{thi}\rho_i^2/R^2$ and $Q_{GB,i} = N_0 T_{i0} v_{thi}\rho_i^2/R^2$, respectively. In our ITG and TEM reference cases $Z = 1$ and therefore $\Gamma_i = \Gamma_e = \Gamma$.

A fundamental issue, due to limited simulation statistics, is in providing error estimates of time-averaged fluxes $\langle\mathcal{F}\rangle_t$. The practical approach considered here consists in dividing the quasi-stationary turbulent phase of the simulation into N disjoint time intervals of equal span and computing the time averages $\langle\mathcal{F}\rangle_n$ over each of these sub-intervals. An estimate of the error $\langle v^2\rangle_t$ on the total time-average flux can then be provided by the root mean square deviation:

$$\mathrm{Err}[\mathcal{F}] = \left[\frac{1}{N}\sum_{n=1}^{N}\left(\langle\mathcal{F}\rangle_n - \langle\mathcal{F}\rangle_t\right)^2\right]^{1/2}. \tag{3.16}$$

The number of time intervals N one can consider is usually very limited (typically 3 for our simulations) as each must contain at least a few (~ 10) turbulent bursts. The rough error estimate on the time-averaged fluxes obtained in this way is less than 5% for nonlinear simulation results shown in Figs. 3.15, 3.16, and 3.17.

k_x and k_y Spectra

Flux *spectra* enable to study the contribution to transport from the different fluctuation scale lengths. Such spectra are derived by expressing relation (3.15) in terms of the Fourier representations of ϕ and δf_j with respect to x and y. In particular, the Fourier decomposition of ϕ reads:

$$\phi(x,y,z,t) = \sum_{k_x,k_y}\widehat{\phi}(k_x,k_y,z,t)\exp[i(k_xx + k_yy)].$$

In the case of particle flux, for example, equation (3.15) then becomes:

$$\Gamma_j(t) = \sum_{k_x,k_y}\frac{\int dz\mathcal{J}^{\mathrm{xyz}}B_0^{-1}ik_y\widehat{\phi}^{\star}\widehat{\delta N}_j}{\int dz\mathcal{J}^{\mathrm{xyz}}} = \sum_{k_x,k_y}\widetilde{\Gamma}_j(k_x,k_y,t),$$

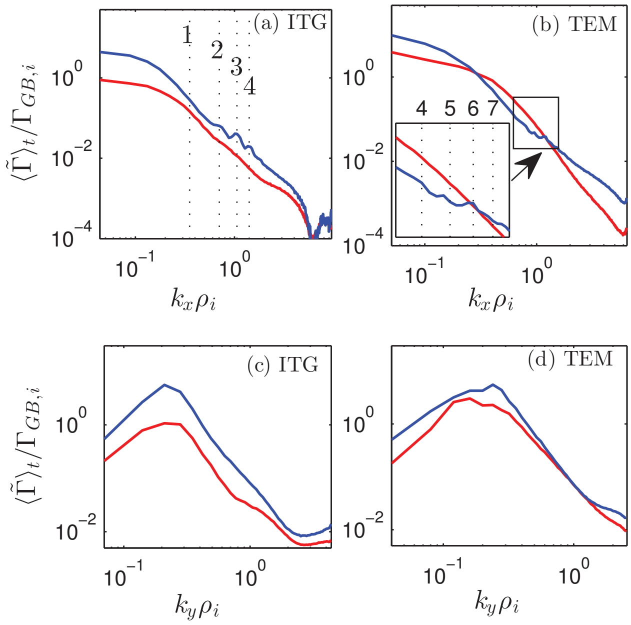

Figure 3.15 – Time-averaged, turbulent particle flux spectra $\langle\widetilde{\Gamma}\rangle_t$ in units of $\Gamma_{GB,i}$ with respect to (a and b) k_x and (c and d) k_y for the ITG (a and c, $n_x = 432$) and TEM (b and d, $n_x = 256$) test cases (log-log scale). Fully kinetic (blue) and hybrid (red) electron models. Peaks in the fully kinetic electron spectra at the harmonics $k_x = p\,2\pi/L_{\mathrm{LMRS}}$, $p = 1, 2, \ldots$, are related to the non-adiabatic response of passing electrons near lowest-order MRSs.

having identified the flux spectra as

$$\widetilde{\Gamma}_j(k_x, k_y, t) = \left\langle \frac{1}{B_0} i k_y \widehat{\phi}^\star \widehat{\delta N}_j \right\rangle_z ,$$

where $\widehat{\phi}^\star$ is the complex conjugate of $\widehat{\phi}$.

The time-averaged k_x- and k_y- particle flux spectra are plotted for both the ITG and TEM cases in figure 3.15, obtained by summing $\langle\widetilde{\Gamma}\rangle_t(k_x, k_y)$ over k_y and k_x, respectively. For comparison, the figure shows simulation results obtained with both the fully kinetic and hybrid electron models. All these spectra present a typical decay towards the shorter wavelengths, which is roughly algebraic, $\sim k^{-\alpha}$, corresponding to a straight line in log-log scale, often referred to as the “inertial range”. The contributions to the fluxes from the shortest considered wavelength modes are thus at least three orders of magnitude smaller than the one from the spectrum peak, typically located at $k_y\rho_i = 0.2 - 0.3$, which is a clear indication of a well-converged turbulent simulation in terms of the number of Fourier modes considered. The spectrum peak itself is well resolved, reflecting a good spectral resolution $\Delta k_{x,y} = k_{x,y,\text{min}} = 2\pi/L_{x,y}$, *i.e.* a sufficiently large simulation box. *In the ITG case*, at the very edge (Nyquist limit) of the spectra, one observes however a slight deviation from the algebraic decay, in the form of a flattening or even roll-over for the k_y-spectra. This is clearly not due to a linearly unstable mode at these scales, as shown in figure 3.1(a) (see results for $\mu = 400$ and $\tau = 1$), but is most probably related to a pile-up of energy cascading down toward small scales. *In the TEM case*, no roll-over is present at the very edge (Nyquist limit) of the spectra even if the curve’s decay slightly lessen for $k_y\rho_i \approx 1.5$. The absence of roll-over has also been confirmed for simulations with higher radial resolutions.

Remarkable on the k_x-spectra of fully kinetic electron simulations are peaks at harmonics $k_x^{(p)} = p\,2\pi/L_{\text{LMRS}} = pMk_{x,\text{min}}$. These peaks are most clearly visible in the particle flux spectra of the ITG case, and most prominent for $p = 2, 3$, and 4. These are clearly related to the Fourier mode components giving rise to the periodic structures located at the lowest-order MRSs and are thus absent from the hybrid simulation results. The origin of the peaks in the time-averaged k_x spectra $\langle\widetilde{\Gamma}\rangle_{t,k_y}(k_x) = \sum_{k_y}\langle\widetilde{\Gamma}\rangle_t(k_x, k_y)$ is shown to be due to the presence of peaks aligned along the line $k_y = k_x/2\pi\hat{s}$ in the time-averaged bi-dimensional *spectra* $\langle\widetilde{\Gamma}\rangle_t(k_x, k_y)$ which are plotted in figure 3.16. These modes correspond, for each k_y, to the first order coupling to the mode $(k_x, k_y) = (0, k_y)$ resulting from the pseudo periodicity boundary conditions described by equation (2.54). Very similar features are also observed on both electron and ion kinetic energy flux spectra (not shown).

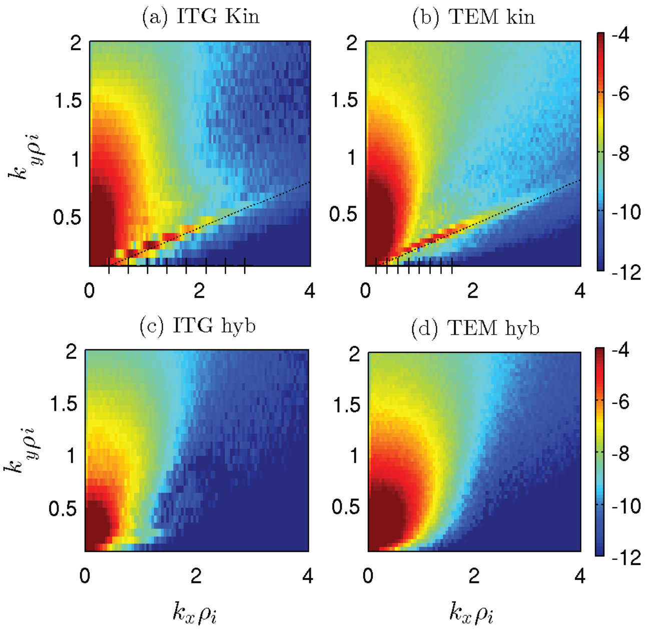

Figure 3.16 – Time-averaged, turbulent particle flux spectra $\langle\widetilde{\Gamma}\rangle_t(k_x, k_y)$ for same cases as in figure 3.15 (shown is $\log\langle\widetilde{\Gamma}\rangle_t(k_x, k_y)$). ITG (a and b) and TEM (c and d) cases with kinetic (a,b) and hybrid (c,d) electron models. For the kinetic results, a black dotted line is plotted at $k_y = k_x/2\pi\hat{s}$ to emphasize the (k_x, k_y) coupling due to pseudo-periodic boundary conditions equation (2.54) and positions of the harmonics $k_x^{(p)}$ with $p = 1..8$ are plotted with black tick marks along the x-axis. The $k_y = 0$ modes are not shown as they do not contribute to the transport in the ∇x direction: $\partial/\partial y \equiv -ik_y = 0$.

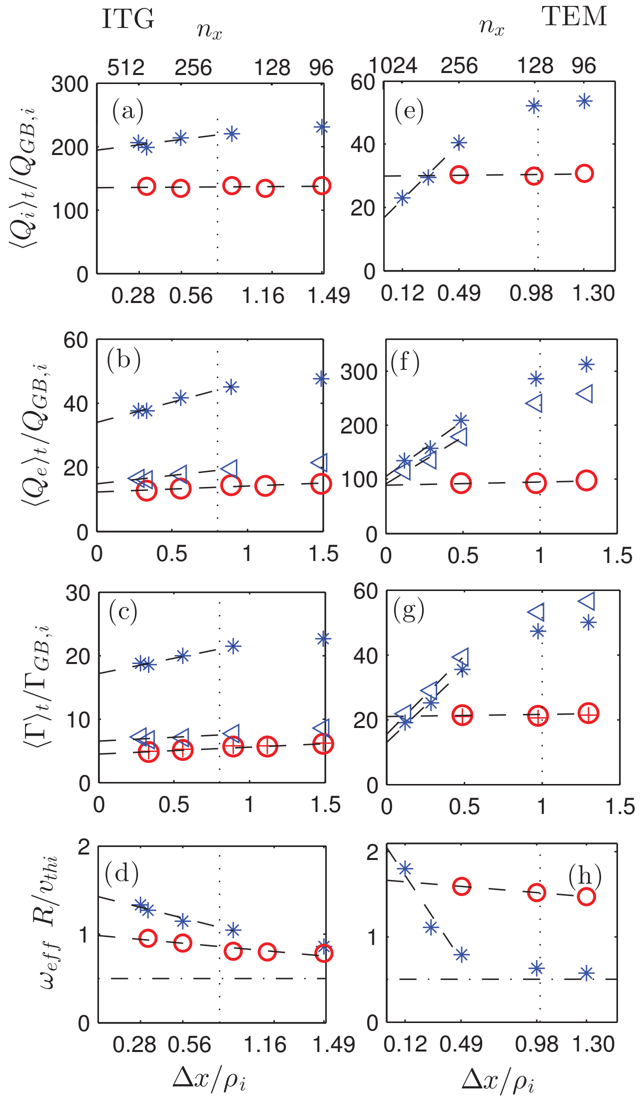

Figure 3.17 – Flux-surface and time averaged particle and kinetic energy fluxes plotted with respect to the radial resolution $\Delta x = L_x / n_x \rho_i$, and effective $E \times B$ shearing rate $\omega_{eff}(t_w = \gamma_{\text{ref}}^{-1})$ plotted with respect to the number of points in the radial direction n_x. In ITG (a,b,c,d) and TEM (e,f,g,h) regimes with hybrid (circles) and kinetic (asterisk) electrons. Also plotted are the fluxes solely due to the trapped electrons (triangle). In hybrid simulations particle flux is computed with ion (circles) and with trapped electrons (crosses). $\Gamma_{GB,i} = N_0 v_{thi} \rho_i^2 / R^2$; $Q_{GB,i} = N_0 T_{i0} v_{thi} \rho_i^2 / R^2$. Vertical dotted lines indicate the fine structure width of $k_y \rho_i \leq 1$ modes in linear simulations taken from figure 3.11.

Numerical radial resolution

As can be observed in figure 3.11, the widths of the fine structures roughly scale as half the distance between consecutive lowest-order MRSs for each k_y. Nonlinear simulation cases considered in this work are composed of 64 k_y modes; the biggest k_y mode has the highest number of MRSs ($64 \times M$) within the box boundaries: 512 (ITG) and 256 (TEM). As a result, if one wants for example a minimum of 10 points between the MRSs to resolve the fine radial structures of all modes, it respectively requires 5120 and 2560 points in x. Nonetheless, as discussed in Sec. 3.4.3, the turbulence spectra is dominated by low k_y modes ($k_y\rho_i < 0.3$) which have the largest radial structures at MRSs: $\delta x^{\mathrm{num}}_{\mathrm{non-lin}} \gtrsim 2\rho_i$. To have at least 10 points between these k_y's lowest-order MRSs, it requires to have $n_x > 340$ and 300. In our convergence study, we went beyond this resolution by taking $n_x = 512$ and 1024. Note that these two runs with very high radial resolutions have been carried out over a shorter time window $t_{end} \approx 200 v_{thi}/R$ compared to other simulations for which $t_{end} \approx 300 v_{thi}/R$.

In the convergence study (figure 3.17), we scanned a range of radial point numbers, n_x, for which the mesh size in units of the ion Larmor radius, $\Delta x/\rho_i = L_x/n_x\rho_i$, varies from 0.28 to 1.49 in the ITG case and from 0.12 to 1.30 in the TEM case. The highest resolutions provide more than 7 (ITG) and 16 (TEM) radial grid points over the fine structure widths, $\delta x^{\mathrm{sim}}_{\mathrm{non-lin}}$, of dominant k_y modes ($k_y\rho_i < 0.3$). In comparison, the lowest resolutions provide less than two grid points over the fine structure widths of almost all k_y modes. This low resolution is clearly not sufficient to describe the radial corrugations present near MRSs in kinetic electron simulations. In figure 3.17, we show with dashed lines the linear fits that have been extrapolated to obtain the converged values ($\Delta x \to 0$).

The particle and kinetic energy fluxes of ions and electrons, as well as the effective $E \times B$ shearing rate ω_{eff}, which are obtained from simulations running with the hybrid model, are essentially converged already for low resolutions (circles in figure 3.17). On the contrary, the fluxes and ω_{eff} obtained from simulations carried out with the kinetic electron model (asterisk in figure 3.17) are not converged at low resolutions. In subplot (h), the ω_{eff} does not appear clearly converged, even at the highest resolution. As we discuss now, the effective shearing rate ω_{eff} considered in this work includes a fluctuating contribution. The following results show that the strong increase of the effective shearing rate, occurring in the TEM case when $\Delta x \to 0$, is due to the contribution from the rapid fluctuations. The effective $E \times B$ shearing rate is defined by:

$$\omega_{eff}(t_w) = \left\langle \left| \frac{1}{t_w} \int_t^{t+t_w} dt' \, \omega_{E\times B}(x, t') \right| \right\rangle_{xt}, \tag{3.17}$$

which is a function of the time-window t_w. In the last row of figure 3.17, the effective shearing rate is plotted using a value of the time window equal to the the typical growth time of the turbulence: $t_w = \gamma_{ref}^{-1}$. This choice permits to filter out the $\omega_{E\times B}$ fluctuations assumed to oscillate too rapidly to be able to suppress turbulence [Hahm, 1994,

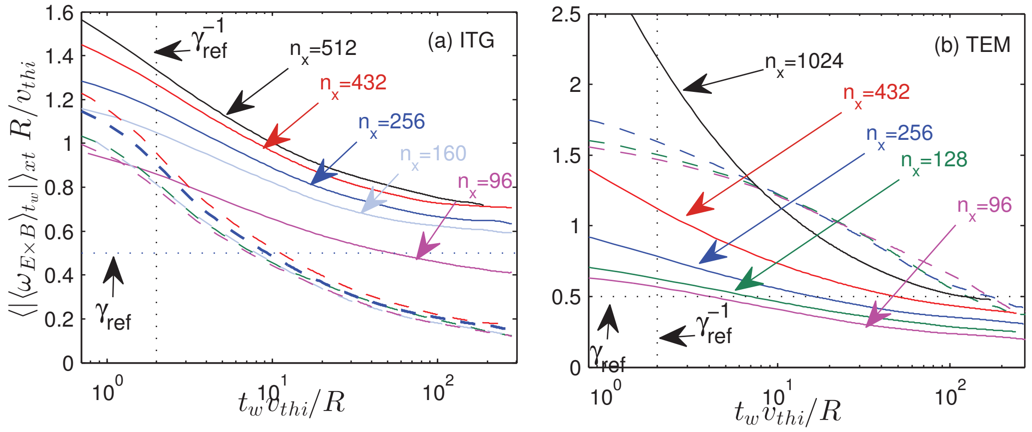

Figure 3.18 – Effective shearing rate $\omega_{eff} = \langle|\langle\omega_{E\times B}\rangle_{t_w}|\rangle_{xt}$ with respect to a time window t_w for different radial resolutions indicated for (a) ITG and (b) TEM test cases. Both hybrid (dashed) and kinetic (full line) electron models are considered here where each resolution respects the same color code as indicated in the plots. The linear growth rate of reference $\gamma_{\rm ref}$ is plotted with horizontal dotted line and its corresponding time $\gamma_{\rm ref}^{-1}$ is plotted with vertical dotted line.

Hahm et al., 1999] but to still account for the slower ones which should be effective in suppressing turbulence. In the ITG case, this particular time window is chosen as the inverse of the maximum linear growth rate of the dispersion relation in figure 3.1(a). In the TEM case, it is chosen as the maximum growth rate over the spectrum interval $0.1 < k_y\rho_i < 0.4$ of the dispersion relation in figure 3.1(b). This limited spectrum interval considered for the TEM case corresponds to modes which contribute the most to the turbulent fluxes (see 3.15(d)).

The fact that the ω_{eff} is essentially converged at lower resolution in hybrid electron simulations is clearer in figure 3.18 (dashed lines). In this figure, the effective shearing rate is plotted with respect to the time window width for different radial resolutions. In the TEM case (figure 3.18.b) with kinetic electrons (full line), the effective shearing rate strongly increases when the mesh size n_x increases, especially for small values of the time window t_w. This short scale effect is particularly important in the highest resolution simulation. Going back to figure 3.17 (f) and (h), we note that going to higher resolution has the effect of *increasing* ω_{eff} while *decreasing* the turbulent fluxes. This is in agreement with the drift wave-zonal flow paradigm for nonlinear saturation. Comparing the ω_{eff} between hybrid and kinetic simulations is not forcefully significant as the difference of the ZFs spatial organization is not taken into account by this indicator; but comparing the ω_{eff} between simulations with the same electron model and the same magnetic equilibrium, *i.e.* the same spatial organization of ZFs, one can expect that with a larger ω_{eff} the ZFs will be more effective for suppressing turbulence.

As a conclusion of this section, we emphasize the necessity to use a high radial resolution for converging the flux levels and associated $E \times B$ saturation mechanisms. Fully kinetic simulations carried out with too low radial resolution can lead to strong over-estimate of the fluxes correlated to a strong under-estimate of the $E \times B$ shearing rate.

Passing electrons contributions to the turbulent transport

In this section, we note $\langle \bullet \rangle_t$ the time-averaged level of transport extrapolated at $\Delta x = 0$ by linear fits indicated with dashed lines in figure 3.17.

In the ITG case, the particle and kinetic energy fluxes of ion and electron species are underestimated when running simulations using the hybrid electron model: $\langle \Gamma_e^{\mathrm{hyb}} \rangle_t \approx 27\% \langle \Gamma_e^{\mathrm{kin}} \rangle_t$, $\langle Q_e^{\mathrm{hyb}} \rangle_t \approx 36\% \langle Q_e^{\mathrm{kin}} \rangle_t$, and $\langle Q_i^{\mathrm{hyb}} \rangle_t \approx 69\% \langle Q_i^{\mathrm{kin}} \rangle_t$. The error due to the extrapolation method is small enough to be confident in these numbers.

The particle flux is composed of a passing electron flux and of a trapped electron flux: $\Gamma_e = \Gamma_{e,pas} + \Gamma_{e,trp}$. In simulations running with kinetic electrons, the main contribution to the flux comes from the passing electron channel of transport: $\langle \Gamma_{e,pas}^{\mathrm{kin}} \rangle_t \approx 63\% \langle \Gamma_e^{\mathrm{kin}} \rangle_t$. The passing electrons being adiabatic in the hybrid model, one obviously has $\Gamma_{e,pas}^{\mathrm{hyb}} = 0$. The trapped electron particle fluxes obtained from simulations running with hybrid or kinetic electron models are of same order: $\Gamma_{e,trp}^{\mathrm{hyb}} \approx \Gamma_{e,trp}^{\mathrm{kin}}$.

The kinetic energy flux is composed of a heat flux [Hinton and Hazeltine, 1976] and of an advective flux:

$$Q_j = q_{\mathrm{h},j} + \frac{5}{2} T_{0j} \Gamma_j, \tag{3.18}$$

where the heat flux [Hinton and Hazeltine, 1976] is defined by $q_{\mathrm{h},j} = \mathcal{F}_j[m_j(v^2 - 5v_{thj}^2)/2]$ and $\mathcal{F}_j[\bullet]$ is defined by equation (3.15). With the fully kinetic model, the advective contribution from the passing electrons dominates the electron kinetic energy flux: $(5/2) T_{e0} \langle \Gamma_{e,pas}^{\mathrm{kin}} \rangle_t \approx 78\% \langle Q_e^{\mathrm{kin}} \rangle_t$.

The ion kinetic energy flux, which is the most important for an ITG regime, is underestimated by simulations running with the hybrid model: $\langle Q_i^{\mathrm{hyb}} \rangle_t \approx 69\% \langle Q_i^{\mathrm{kin}} \rangle_t$. Having ambipolar fluxes, $\langle \Gamma_i \rangle_t = \langle \Gamma_e \rangle_t$, the hybrid model underestimation of the kinetic energy flux, *i.e.* $\langle Q_i^{\mathrm{hyb}} \rangle_t < \langle Q_i^{\mathrm{kin}} \rangle_t$, is significantly due to the missing passing electron channel of transport: $(5/2) T_{e0} \langle \Gamma_{e,pas}^{\mathrm{hyb}} \rangle_t = 0$.

In the TEM case, the extrapolated levels of transport obtained with the hybrid and kinetic models are: $\langle \Gamma_e^{\mathrm{hyb}} \rangle_t \approx 61\% \langle \Gamma_e^{\mathrm{kin}} \rangle_t$, $\langle Q_e^{\mathrm{hyb}} \rangle_t \approx 85\% \langle Q_e^{\mathrm{kin}} \rangle_t$, and $\langle Q_i^{\mathrm{hyb}} \rangle_t \approx 180\% \langle Q_i^{\mathrm{kin}} \rangle_t$. In absolute value, the differences between these hybrid and kinetic fluxes are of the order of the uncertainty on their amplitude due to the choice of extrapolation method.

The particle flux, in simulation with kinetic electrons, is mainly composed of the trapped electrons transport channel: $\langle \Gamma^{\mathrm{kin}}_{e,trp} \rangle_t \approx 119\% \langle \Gamma^{\mathrm{kin}}_{e} \rangle_t$, and the passing electron flux is inward. The trapped electron fluxes obtained from simulations carried out with hybrid and kinetic electron models are of comparable level: $\langle \Gamma^{\mathrm{hyb}}_{e,trp} \rangle_t \approx 134\% \langle \Gamma^{\mathrm{kin}}_{e,trp} \rangle_t$. The difference being of the order of the error due to the extrapolation method.

The electron kinetic energy flux is the major transport channel causing power loss in this TEM case, as expected of a TEM regime. In simulation with kinetic electrons, this flux is essentially due to the trapped electrons channel: $\langle Q^{\mathrm{kin}}_{e,trp} \rangle_t \approx 87\% \langle Q^{\mathrm{kin}}_{e} \rangle_t$, and it has a non negligible advective component (see equation (3.18)): $(5/2) T_{e0} \langle \Gamma^{\mathrm{kin}}_{e} \rangle_t \approx 37\% \langle Q^{\mathrm{kin}}_{e} \rangle_t$. Not shown here is the fact that, in both hybrid and kinetic simulations of the TEM case, the electron heat flux is solely due to the trapped electrons: $\langle q^{\mathrm{kin}}_{\mathrm{h},e} \rangle_t = \langle q^{\mathrm{kin}}_{\mathrm{h},e,trp} \rangle_t$ and $\langle q^{\mathrm{hyb}}_{\mathrm{h},e} \rangle_t = \langle q^{\mathrm{hyb}}_{\mathrm{h},e,trp} \rangle_t$. The transport levels obtained from hybrid and kinetic electron simulations are only different by $\approx 15\%$. This is not a significant difference regarding the error due to the extrapolation method.

The transport levels of ion kinetic energy obtained with the kinetic and hybrid electron models are different enough to at least say that this flux is decreased by the influence of the passing electron dynamics. But this ion kinetic energy flux remains much lower than the electron kinetic energy flux.

3.5 Conclusion

The non-adiabatic response of passing electrons near mode rational surfaces has been characterized in the flux-tube geometry by identifying its role in linear and nonlinear collisionless plasma, studying instabilities and turbulent saturated regimes of ITG and TEM dominated test cases. This characterization was achieved by systematically comparing results obtained when accounting for the fully kinetic response of the electrons with results obtained with a hybrid model in which the trapped electrons are handled kinetically and the passing electrons are forced to respond adiabatically.

In *linear simulations*, fine radial structures due to the non-adiabatic response of passing electrons are systematically present near MRSs. These fine structures develop in the vicinity of MRSs where $k_\parallel$ is small enough to have $|\omega_r / k_\parallel| \gtrsim v_{the}$. The condition $|\omega_r / k_\parallel| = v_{the}$ appears to be a good criteria to localize the boundaries of the region where passing electrons are non-adiabatic. The dependence on the main physical parameters of the fine structure radial width has been characterized.

For comparison, the underlying destabilization occurring near MRS and related to the passing electrons dynamics have been described with a local dispersion relation. It was shown that in the radial region where the fine structure related to the non-adiabatic response of passing electrons is present, the growth rate obtained with the local dispersion relation is significantly raised, by a factor two or more, when including the non-adiabatic response of passing electrons. The radial width estimate based on this local growth rate was found to be in good agreement with the one directly measured in the results from GENE numerical simulations.

This local dispersion relation has then been reduced to a second order polynomial equation, in order to compute an analytical solution. In this simple form, the finite ion Larmor radius effects cannot be neglected if one wants to correctly describe the destabilization mechanism due to the passing electrons near MRSs. Finally, with this analytical dispersion relation, an instability condition showing the interchange nature of the instability at MRSs has been found for both ITG and TEM cases.

In *nonlinear simulations* (carried out with the reduced mass ratio $m_i/m_e = 400$), fine structures due to the non-adiabatic response of passing electrons over $k_y \neq 0$ modes persist in the turbulent saturated regime, somewhat broadened compared to the linear case. By nonlinear coupling with the $k_y = 0$ mode, it leads to periodic radial corrugations over the flux-surface- and time- averaged gradients of temperature and density, as well as over the time-averaged $E \times B$ shearing rate. Consequently, dominant k_y modes which contribute the most to the fluxes, as illustrated in direct space and Fourier space, require to be finely resolved in the radial direction to properly account for the particular dynamics of passing electrons near MRSs. It has been necessary, with the fully kinetic model, to use a much higher radial resolution for converging the flux levels and associated $E \times B$ saturation mechanisms than with the hybrid model. Fully kinetic simulations carried out with too low radial resolution can lead to strong over-estimates of the fluxes correlated to a strong under-estimate of the $E \times B$ shearing rate.

In the ITG case, the hybrid model is shown to systematically underestimates the flux levels: $\langle \Gamma_e^{\text{hyb}} \rangle_t \approx 27\% \langle \Gamma_e^{\text{kin}} \rangle_t$, $\langle Q_e^{\text{hyb}} \rangle_t \approx 36\% \langle Q_e^{\text{kin}} \rangle_t$, and $\langle Q_i^{\text{hyb}} \rangle_t \approx 69\% \langle Q_i^{\text{kin}} \rangle_t$ (flux levels are extrapolated from the radial resolution convergence study). A first cause of this difference is related to the different radial organizations of the ZFs for simulations carried out with the hybrid model and simulations carried out with the fully kinetic model. These differences in the radial organization of the ZFs thus affect the turbulence saturation mechanism and associated transport levels. A second identified shortcoming of the hybrid model is directly related to the hypothesis of an adiabatic response of the passing electrons which consequently leads to ignore their contribution to the fluxes. The hybrid model then fails to reproduce the passing electrons channel of transport which represents, in the ITG case: 63% and 78% of particle and electron kinetic energy fluxes, respectively.

In the TEM case, the flux levels of hybrid and kinetic simulations, obtained in the radial resolution convergence study, are different but this difference is not significantly bigger than the uncertainty due to the extrapolation method. Nonetheless, for fully kinetic simulations, a much finer radial resolution was required to converge the fluxes than for the hybrid electron simulations. It shows that the turbulence dynamics and self regulation mechanisms are affected by the passing electron dynamics. Indeed, it could be interesting to carry out simulations of other TEM test cases to see if there are regimes for which the transport level obtained with the hybrid and kinetic electron models diverge more significantly. It should be recalled that not all the TEM cases are dominantly saturated by zonal flows, as mentioned when discussing the choice of temperature ratio for our TEM case. Therefore our results are relevant for particular TEM cases and do not contradict previous gyrokinetic studies.

4 An arbitrary wavelength solver for resolving fine layers of nonadiabatic passing electron response in the gyrokinetic code ORB5

4.1 Introduction

In the previous chapter, it has been shown that the non-adiabatic response of passing electrons significantly alters the level of turbulent transport, as well as the zonal flows organization. In particular, this non-adiabatic response is associated to the presence of fine radial structures (sub-ion Larmor radius scale) near low-order mode rational surfaces over the electrostatic potential, see references [Waltz et al., 2006, Chowdhury et al., 2008, Dominski et al., 2015]. Therefore, to enable the pursue of the study of the non-adiabatic passing-electron response in global geometries with the gyrokinetic code ORB5, a new arbitrary-wavelength (compared to the ion Larmor radius) electrostatic-field solver has been implemented. This new feature of the ORB5 code overcomes the former long-wavelength approximation made in the original version of the code, see references [Tran et al., 1999] and [Jolliet et al., 2007]. The gyrokinetic code ORB5 is today a multi-scale, multispecies, collisional, electromagnetic, and global gyrokinetic PIC code, in which the statistical numerical noise is controlled using modified Krook operators or coarse graining procedures. The main steps which led to the current state of the code are: the inclusion of new sources and noise control [McMillan et al., 2008], an electromagnetic version [Bottino et al., 2010] includes electromagnetic effects in the frame of a project called NEMORB, a field-aligned Fourier solver [McMillan et al., 2010], inter- and intra-species collisions [Vernay et al., 2010], and the effect of strong flows [Collier, 2015, Collier et al., 2016].

We present in this chapter first ORB5 results obtained with this new generalized field solver. In this solver, in which the field is represented with finite elements [Fivaz et al., 1998, Tran et al., 1999], the linearized polarization drift contribution to the quasi-neutrality equation (QNE) is accounted for in its integral form by following a similar method to [Lin and Lee, 1995, Mishchenko et al., 2005]. In this latter reference, the phase-space integral necessary for computing the polarization drift contribution to the quasi-neutrality equation is carried out with a Monte-Carlo-type integration. In such type of integration, the phase-space integral is carried out by summing samples of the integrand taken at different phase-space positions. In our proposed method, this phase-space integral is replaced by quadratures over an Eulerian grid in the $(s, \theta^\star, v_\perp, \alpha)$ directions and by integrating analytically in the $v_\parallel$ direction, having used a local Maxwellian distribution function for the background. These quadratures are adapted to the resolution of the grid on which the field is represented in order to resolve the short scales provided by this grid. Moreover, in this new ORB5 solver the field is solved for the poloidal and toroidal discrete Fourier representation of its finite-element coefficients. This discrete Fourier representation significantly reduces the size of the corresponding matrix system [McMillan et al., 2010]. A Padé version of the solver has also been implemented and is compared to the integral solver results. Comparison of results obtained using such a Padé approximation with results considering a generalized solver was originally done in reference [Lin and Lee, 1995], where a generalized electrostatic field solver was also presented.

The remainder of this chapter is organized as follows. In section 4.2, the quasi-neutrality equation and the different electron and ion models implemented are introduced. In section 4.3, the version of the quasi-neutrality equation discretized with finite elements and its weak formulation are introduced. In section 4.4, the new field solver implementation valid for arbitrary geometry is introduced. Finally, in section 4.7, a linear benchmark is carried out with ORB5 against the global version of the gyrokinetic code GENE [Jenko et al., 2000, Görler et al., 2011] in global realistic MHD geometry considering the three electron models: adiabatic, hybrid, and kinetic.

4.2 Quasi-neutrality equation

The self-consistent field quasi-neutrality equation (QNE) can be obtained from a variational approach when considering the variation of the particle-field Lagrangian with respect to the perturbation field $\delta\phi$, see references [Dubin et al., 1983, Sugama, 2000, Brizard, 2000]. The QNE reads $\sum_\sigma q_\sigma N_\sigma(\mathbf{x}; t) = 0$ with q_σ the electric charge of species σ, and N_σ the density is obtained from the gyrokinetic description [Hahm et al., 1999]

$$N_\sigma(\mathbf{x}; t) = \int d\mathbf{Z}\ \delta(\mathbf{X} + \boldsymbol{\rho} - \mathbf{x}) \left(f_\sigma + \frac{q_\sigma}{B_0} \delta\tilde{\phi} \frac{\partial f_\sigma}{\partial \mu} + \frac{m_\sigma}{q_\sigma B_0^2} \nabla \delta\tilde{\Phi} \times \mathbf{b} \cdot \frac{\partial f_\sigma}{\partial \mathbf{X}} \right), \qquad (4.1)$$

where the deviation from quasi-neutrality is neglected and neither the strong flows or magnetic perturbations are considered in this work. In the following, the quasi-neutrality equation will be linearized, and the contribution coming from the term proportional to $\nabla\delta\tilde{\Phi} \times \mathbf{b} \cdot \partial_{\mathbf{X}} f_\sigma$ will be neglected invoking the fact that both terms $\delta\tilde{\Phi} = \int^\alpha d\alpha \delta\tilde{\phi}$

and $\partial_{\mathbf{X}} f_\sigma$ are small. In equation (4.1), one has $f_\sigma(\mathbf{X}, v_\perp, \mu; t)$ the particle distribution function in gyrocenter variables which is evolved according to the gyrokinetic equation [Brizard and Hahm, 2007], $\mathbf{X}$ the guiding center, $\boldsymbol{\rho} = \boldsymbol{\rho}(\mathbf{X}, \mu, \alpha)$ the Larmor vector, α the gyro-angle, $\mu = m_\sigma v_\perp^2 / 2B_0$ the magnetic moment, $v_\perp$ the magnitude of the particle velocity component perpendicular to the magnetic field, $v_\parallel$ the magnitude of the velocity component parallel to the magnetic field, $d\mathbf{Z} = d\mathbf{X} dv_\parallel d\mu d\alpha (B^\star_{0\parallel}/m_\sigma)$ the infinitesimal phase-space volume in guiding-center coordinates $(\mathbf{X}, v_\parallel, \mu, \alpha)$, $B^\star_{0\parallel} = B_0 + (m_\sigma/q_\sigma) v_\parallel \mathbf{b} \cdot \nabla \times \mathbf{b}$, B_0 the equilibrium magnetic field amplitude, $\mathbf{b} = \mathbf{B}_0/B_0$, and $\delta(\mathbf{X} + \boldsymbol{\rho} - \mathbf{x})$ the Dirac delta function. The polarization term is explicitly function of the electrostatic field $\delta\phi$ through the term $\delta\tilde{\phi}(\mathbf{X}, \mu, \alpha) = \delta\phi(\mathbf{X} + \boldsymbol{\rho}) - \langle \delta\phi \rangle_\alpha(\mathbf{X}, \mu)$ with

$$\langle \delta\phi \rangle_\alpha(\mathbf{X}, \mu) = \oint \frac{d\alpha}{2\pi} \delta\phi(\mathbf{X} + \boldsymbol{\rho}), \tag{4.2}$$

standing for the gyro-averaged field. Note that the norm of the Larmor vector is $\rho_\sigma(\mathbf{X}, \mu) = v_\perp / \Omega_{\sigma 0}(\mathbf{X})$ with $\Omega_{\sigma 0}(\mathbf{X}) = q_\sigma B_0(\mathbf{X})/m_\sigma$ the cyclotron frequency and m_σ the species mass. Moreover, the species thermal Larmor radius is defined by $\rho_{\mathrm{th,j}}(\mathbf{x}) = v_{\mathrm{th},j}(\mathbf{x})/\Omega_{\sigma 0}(\mathbf{x})$ with $v_{\mathrm{th},j}(\mathbf{x}) = \sqrt{T_{\sigma 0}(\mathbf{x})/m_\sigma}$ the thermal velocity, and $T_{\sigma 0}(\mathbf{x})$ the species background temperature. The ion sound Larmor radius is $\rho_s(\mathbf{x}) = c_s(\mathbf{x})/\Omega_{i0}(\mathbf{x})$ with $c_{\mathrm{s}} = \sqrt{N_e T_e / \sum_\sigma m_\sigma N_\sigma}$ the sound speed approximated by $c_{\mathrm{s}}(\mathbf{x}) \simeq \sqrt{Z_i T_{e0}(\mathbf{x})/m_i}$ where i labels the main ion species with ionization degree Z_i.

As the background plasma is assumed neutral, $\sum_\sigma q_\sigma N_{\sigma 0}(\mathbf{x}) = 0$, the quasi-neutrality equation can then be rewritten by keeping only the perturbation terms $\sum_\sigma q_\sigma \delta N_\sigma(\mathbf{x}; t) = 0$, where the particle distribution function f_σ is split into a time-independent background, $f_{\sigma 0}$, and a time-dependent perturbation, δf_σ, such that $f_\sigma(\mathbf{X}, v_\parallel, \mu; t) = f_{\sigma 0}(\mathbf{X}, v_\parallel, \mu) + \delta f_\sigma(\mathbf{X}, v_\parallel, \mu; t)$. From equation (4.1), the background density is

$$N_{\sigma 0}(\mathbf{x}) = \int d\mathbf{Z}\, \delta(\mathbf{X} + \boldsymbol{\rho} - \mathbf{x}) f_{\sigma 0}(\mathbf{X}, v_\parallel, \mu), \tag{4.3}$$

and the perturbation density is composed of two terms: the gyro-density contribution

$$\delta N_\sigma^{\mathrm{gy}}(\mathbf{x}; t) = \int d\mathbf{Z}\, \delta(\mathbf{X} + \boldsymbol{\rho} - \mathbf{x}) \delta f_\sigma(\mathbf{X}, v_\parallel, \mu; t), \tag{4.4}$$

and the linearized polarization-drift contribution

$$\delta N_\sigma^{\mathrm{pol}}(\mathbf{x}; t) = \int d\mathbf{Z}\, \delta(\mathbf{X} + \boldsymbol{\rho} - \mathbf{x}) \frac{q_\sigma}{B_0(\mathbf{X})} \delta\tilde{\phi}(\mathbf{X}, \mu; t) \frac{\partial f_{\sigma 0}(\mathbf{X}, v_\parallel, \mu)}{\partial \mu}, \tag{4.5}$$

such that $\delta N_\sigma = \delta N_\sigma^{gy} + \delta N_\sigma^{pol}$ and having neglected the nonlinear contribution to the polarization density. Nonlinear polarization drift contribution to the QNE has been considered in references [Mishchenko et al., 2005, Idomura, 2012].

In the present work, different approximations and models are considered for the perturbation density, which we will briefly list here. For *ion species* and for sufficiently long wavelengths with respect to the ion Larmor radius, $k_\perp \rho_i \ll 1$, with $k_\perp$ the perturbation wavenumber in the direction perpendicular to the magnetic field, the so-called long-wavelength approximation may be considered for estimating

$$\delta N_i^{\mathrm{pol}}(\mathbf{x};t) \simeq \frac{q_i}{m_i} \nabla_\perp \cdot \frac{N_{i0}(\mathbf{x})}{\Omega_{i0}^2(\mathbf{x})} \nabla_\perp \delta\phi(\mathbf{x};t), \tag{4.6}$$

with $q_i = eZ_i$ the ion charge and e the elementary electric charge. This approximation was made in the previous versions of the gyrokinetic code ORB5 [Tran et al., 1999, Jolliet et al., 2007, Bottino et al., 2010]. For the present work, a new field solver is implemented in the ORB5 code, for which the linear polarization contribution to the perturbed density is computed from the integral form as described in equation (4.5). Note that, as an improvement over the long-wavelength approximation equation (4.6), a Padé approximation version of this integral solver has been implemented as well, for which the ion polarization drift term is estimated using the relation

$$\delta N_i^{\mathrm{pol}}(\mathbf{x};t) \simeq \left[1 - \nabla_\perp \cdot \rho_i^2(\mathbf{x}) \nabla_\perp\right]^{-1} \left[\frac{eZ_i}{m_i} \nabla_\perp \cdot \frac{N_{i0}(\mathbf{x})}{\Omega_{i0}^2(\mathbf{x})} \nabla_\perp \delta\phi(\mathbf{x};t)\right]. \tag{4.7}$$

This approximation is based on the expression of the polarization drift term in Fourier space for a homogeneous plasma [Lebrun and Tajima, 1995, Lin and Lee, 1995] $\delta \hat{N}_i^{\mathrm{pol}}(\mathbf{k}) = (qN_{i0}/T_{i0}) \left[1 - \Lambda_0(k_\perp^2 \rho_{th,i}^2)\right] \delta\hat{\phi}(\mathbf{k})$ and on the Padé approximation of the scaled modified Bessel function of order zero $\Lambda_0(\xi) = e^{-\xi} I_0(\xi) \simeq 1/(1+\xi)$. In practice, the operator $[1 - \nabla_\perp \cdot \rho_i^2 \nabla_\perp]$ is applied to all terms of the QNE effectively canceling the operator $[1 - \nabla_\perp \cdot \rho_i^2 \nabla_\perp]^{-1}$ in equation (4.7). For *electrons* and for small wavelengths with respect to the ion Larmor radius, $k_\perp \rho_i \gtrsim 1$, but still sufficiently long with respect to the electron Larmor radius, $k_\perp \rho_e \ll 1$, the drift-kinetic approximation can be made. It consists in neglecting the electron polarization term, equation (4.5), thus reducing the electron perturbed density to its gyro-density in which the Larmor radius is taken to be zero

$$\delta N_e(\mathbf{x};t) \simeq \delta N_e^{\mathrm{gy}}(\mathbf{x};t) \simeq \int d\mathbf{Z}\, \delta f_e(\mathbf{x}, \mu, v_\parallel; t). \tag{4.8}$$

For certain types of fluctuations the electron response can also be computed from the adiabatic (Boltzmann) approximation [Horton, 1999]

$$\delta N_e^{\mathrm{ad}}(\mathbf{x};t) = \frac{eN_{0e}}{T_{0e}} \left[\delta\phi(\mathbf{x};t) - \langle \delta\phi \rangle_{FS}(s;t)\right], \tag{4.9}$$

where $\langle \delta\phi \rangle_{FS}$ the flux-surface averaged potential reads

$$\langle \delta\phi \rangle_{FS} = \frac{1}{\oint d\varphi \oint d\theta^\star \mathcal{J}} \oint d\varphi \oint d\theta^\star \mathcal{J}\, \delta\phi,$$

in magnetic coordinates $(s, \theta^\star, \varphi)$ with s the flux-surface label, $\theta^\star$ the straight-field-line poloidal angle, φ the toroidal angle, and $\mathcal{J}$ the associated Jacobian. Finally, a hybrid model can also be considered, in which the trapped electrons are described kinetically and the passing electrons are described adiabatically $\delta N_e^{\text{hyb}}(\mathbf{x}) = \delta N_{e,\text{trp}}^{\text{kin}}(\mathbf{x}) + \delta N_{e,\text{pas}}^{\text{ad}}(\mathbf{x})$. More details concerning these electron models are given in references [Jolliet, 2010, Dominski et al., 2015].

Considering the different possible electron models and approximations, the most general form of the quasi-neutrality equation can be written

$$-\sum_{\sigma\in\{\text{kin}\}} \int d\mathbf{Z}\delta(\mathbf{X}+\boldsymbol{\rho}-\mathbf{x})\delta\tilde{\phi}\frac{q_\sigma^2}{B_0}\frac{\partial f_{\sigma 0}}{\partial \mu} + \sum_{\sigma\in\{\text{ad}\}} N_{\sigma 0}\frac{q_\sigma^2(\delta\phi - \langle\delta\phi\rangle_{FS})}{T_{\sigma 0}} = \sum_{\sigma\in\{\text{kin}|\text{dk}\}} q_\sigma \delta N_\sigma^{\text{gy}}, \tag{4.10}$$

where one uses the sets {kin}, {ad}, and {kin|dk} to denote the (subgroup) species which are modeled kinetically, adiabatically, and either kinetically or drift-kinetically, respectively.

4.3 Discretized QNE with finite elements

In this section, the Ritz-Galerkin method is used to project the quasi-neutrality equation (QNE) on a set of finite-elements $\{\Lambda_\nu(\mathbf{x})\}$. Solving the QNE using the Ritz-Galerkin method is equivalent to consider the weak variational [Sugama, 2000, Brizard, 2000] form of the QNE

$$\int d\mathbf{x}\delta\Psi(\mathbf{x}) \left[\sum_\sigma q_\sigma \int d\mathbf{Z}\delta(\mathbf{X}+\boldsymbol{\rho}-\mathbf{x})\left(f_\sigma + \frac{q_\sigma}{B_0}\delta\tilde{\phi}\frac{\partial f_{\sigma 0}}{\partial\mu}\right)\right] = 0, \tag{4.11}$$

where the test function $\delta\Psi(\mathbf{x})$ can be any of the finite-elements $\Lambda_\nu(\mathbf{x})$. The continuous integral equation is thus transformed into a system of linear equations [Fivaz et al., 1998, Tran et al., 1999]

$$\sum_{\nu'} L_{\nu\nu'}\,\delta\phi_{\nu'} = S_\nu, \tag{4.12}$$

where $L_{\nu\nu'}\,\delta\phi_{\nu'}$ and S_ν are, respectively, the Galerkin projections, $\int d\mathbf{x}\Lambda_\nu(\mathbf{x})...$, of the left and right hand sides of equation (4.10). The unknown terms $\delta\phi_{\nu'}$ in this system of linear equations are the coefficients of the finite element representation of the electrostatic field

$$\delta\phi(\mathbf{x}) = \sum_{\nu'} \delta\phi_{\nu'}\,\Lambda_{\nu'}(\mathbf{x}). \tag{4.13}$$

The source term S_ν is the projection of the gyro-density

$$S_\nu = 2\pi \sum_{\sigma\in\{\mathrm{kin}|\mathrm{dk}\}} q_\sigma \int d\mathbf{X} dv_\| d\mu \, \frac{B^\star_{0\|}}{m_\sigma} \langle\Lambda_\nu\rangle_\alpha(\mathbf{X},\mu)\, \delta f_\sigma(\mathbf{X},\mu,v_\|), \tag{4.14}$$

where one performed the simplification $\int d\mathbf{x}\Lambda_\nu(\mathbf{x})\delta(\mathbf{X}+\boldsymbol{\rho}-\mathbf{x}) \equiv \Lambda_\nu(\mathbf{X}+\boldsymbol{\rho})$. In PIC representation, as considered in the ORB5 code [Tran et al., 1999], this source term is computed from the marker particles

$$S_\nu = \sum_p q_p w_p \,\langle\Lambda_\nu\rangle_\alpha(\mathbf{X}_p,\mu_p), \tag{4.15}$$

with p the subscript labeling the particle quantities and w_p the particle weight. Finally, the matrix $L_{\nu\nu'}$ is composed of the linearized polarization-drift contribution(s), $L^{\mathrm{pol}}_{\nu\nu'}$, as well as of the possibly adiabatic electron response, $L^{\mathrm{ad}}_{\nu\nu'}$, with $L_{\nu\nu'} = L^{\mathrm{pol}}_{\nu\nu'} + L^{\mathrm{ad}}_{\nu\nu'}$.

The *adiabatic response* matrix reads

$$L^{\mathrm{ad}}_{\nu\nu'} = -\sum_{\sigma\in\{\mathrm{ad}\}} q_\sigma^2 \int d\mathbf{x} \frac{N_{\sigma 0}(\mathbf{x})}{T_{\sigma 0}(\mathbf{x})} \Lambda_\nu(\mathbf{x}) \left[\Lambda_{\nu'}(\mathbf{x}) - \langle\Lambda_{\nu'}\rangle_{FS}(s)\right], \tag{4.16}$$

with {ad} the set of species sub-groups which are modeled adiabatically, see equation (4.10).

The *arbitrary-wavelength* polarization matrix, weak formulation of equation (4.5), reads

$$L^{\mathrm{pol}}_{\nu\nu'} = 2\pi \sum_{\sigma\in\{\mathrm{kin}\}} q_\sigma \int d\mathbf{X} dv_\| d\mu \, \frac{B^\star_{0\|}}{m_\sigma} \frac{q_\sigma}{B_0} \left(-\frac{\partial f_{\sigma 0}}{\partial\mu}\right) \left[\langle\Lambda_\nu\Lambda_{\nu'}\rangle_\alpha - \langle\Lambda_\nu\rangle_\alpha\langle\Lambda_{\nu'}\rangle_\alpha\right], \tag{4.17}$$

where $\langle\Lambda_\nu\rangle_\alpha = \langle\Lambda_\nu\rangle_\alpha(\mathbf{X},\mu)$. This latter matrix is symmetric and positive definite because it is the positively weighted $(-\partial f_{\sigma 0}/\partial\mu > 0)$ sum of the symmetric and positive definite sub-matrices $P_{\nu\nu'} = \langle\Lambda_\nu\Lambda_{\nu'}\rangle_\alpha - \langle\Lambda_\nu\rangle_\alpha\langle\Lambda_{\nu'}\rangle_\alpha$ ($P = P^t$ and $\langle\phi^2\rangle_\alpha \geq \langle\phi\rangle_\alpha^2$ for all ϕ).

The *long-wavelength* polarization matrix, defined by equation (4.6), reads

$$L^{\mathrm{pol}}_{\nu\nu'} = \sum_{\sigma\in\{\mathrm{kin}\}} \frac{q_\sigma^2}{m_\sigma} \int d\mathbf{x} \frac{N_{\sigma 0}(\mathbf{x})}{\Omega^2_{\sigma 0}(\mathbf{x})} \nabla_\perp\Lambda_\nu(\mathbf{x})\nabla_\perp\Lambda_{\nu'}(\mathbf{x}), \tag{4.18}$$

where one has performed an integration by parts of the form

$$\int_\Omega d\mathbf{x}\Lambda_\nu(\nabla_\perp F\nabla_\perp\delta\phi) = \int_{\partial\Omega} \Lambda_\nu F\nabla_\perp\delta\phi\cdot d\mathbf{S} - \int_\Omega d\mathbf{x}\nabla_\perp\Lambda_\nu \; F\nabla_\perp\delta\phi,$$

and the boundary term, $\int_{\partial\Omega}...$, is replaced by imposing Dirichlet boundary conditions to the solution.

In case of the *Padé approximation*, the operator $(1-\nabla_\perp\cdot\rho_i^2\nabla_\perp)$ is applied on both sides of the QNE. For a two-species plasma with drift-kinetic electrons, this Padé version of the discretized QNE reads

$$-\frac{q_i^2}{m_i}\nabla_\perp\cdot\frac{N_{i0}}{\Omega_{i0}^2}\nabla_\perp\phi=(1-\nabla_\perp\cdot\rho_i^2\nabla_\perp)\sum_{\sigma=\{i,e\}}q_\sigma\int d\mathbf{Z}\,\delta(\mathbf{X}+\boldsymbol{\rho}_\sigma-\mathbf{x})\,\delta f_\sigma, \tag{4.19}$$

where $|\boldsymbol{\rho}_e|=0$ and $q_e=-e$. Compared to the long wavelength version of the solver, the difference is the presence of the operator $(1-\nabla_\perp\cdot\rho_i^2\nabla_\perp)$ on the RHS of equation (4.19). This operator effectively necessitates the computation of an additional source term on the RHS of equation (4.12), which now reads $\sum_{\nu'}L^{\mathrm{pol}}_{\nu\nu'}\delta\phi_{\nu'}=S_\nu+S_\nu^{\mathrm{corr}}$ with $S_\nu^{\mathrm{corr}}=\sum_{\nu'}L^{\mathrm{corr}}_{\nu\nu'}s_{\nu'}$ and

$$L^{\mathrm{corr}}_{\nu\nu'}=-\sum_{\nu'}\int d\mathbf{x}\,\rho^2_{\mathrm{th,i}}(\mathbf{x})\nabla_\perp\Lambda_\nu(\mathbf{x})\nabla_\perp\Lambda_{\nu'}(\mathbf{x}), \tag{4.20}$$

where an integration by parts and Dirichlet boundary conditions have been used, and the s_ν stand for the coefficients of the decomposition into finite elements of the total gyro-density: $\sum_{\nu'}s_{\nu'}\Lambda_{\nu'}(\mathbf{x})=\sum_s q_s\int d\mathbf{Z}\,\delta(\mathbf{X}+\boldsymbol{\rho}_s-\mathbf{x})\,\delta f_s$. The above relation can be inverted for s_ν by projection onto the basis elements $\Lambda_\nu(\mathbf{x})$ and making use of the definition (4.14) of S_ν, leading to

$$s_{\nu'}=\sum_\nu M^{-1}_{\nu'\nu}S_\nu, \tag{4.21}$$

where $M_{\nu\nu'}=\int d\mathbf{x}\,\Lambda_\nu(\mathbf{x})\Lambda_{\nu'}(\mathbf{x})$ is the mass matrix. In this Padé version of the solver, the weak formulation of the QNE is thus $L^{\mathrm{pol}}_{\nu\nu'}\delta\phi_{\nu'}=S_\nu^{\mathrm{Pade}}$, where $L^{\mathrm{pol}}_{\nu\nu'}$ is given by equation (4.18) and $S_\nu^{\mathrm{Pade}}=S_\nu+S_\nu^{\mathrm{corr}}=(1+\sum_{\nu'}L^{\mathrm{corr}}_{\nu\nu'}\sum_\nu M^{-1}_{\nu'\nu})S_\nu$.

The main advantages of the Padé version of the solver is that the additional Padé matrices are smaller and easier to converge than the ion polarization drift matrix of the arbitrary wavelength solver. The matrix accounting for the ion polarization drift computed in its integral form is numerically very demanding as we will discuss in the following section.

4.4 Matrix assembly in discrete Fourier representation

In ORB5, the field quantities are represented in magnetic coordinates $(s,\theta^\star,\varphi)$ where $s=\sqrt{\psi/\psi_{edge}}$, ψ is the poloidal magnetic flux and ψ_{edge} its value at the edge, $\theta^\star$ is the straight-field-line poloidal angle, and φ is the periodic toroidal angle. The $3D$ finite elements $\Lambda_\nu(\mathbf{x})$ introduced in section 4.3 are chosen to be tensor products of $1D$ basis functions

$$\Lambda_\nu(\mathbf{x})=\Lambda_i(s)\Lambda_j(\theta^\star)\Lambda_l(\varphi),$$

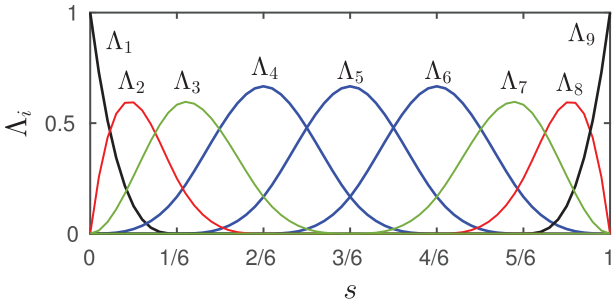

Figure 4.1 – Cubic ($d = 3$) BSpline [de Boor, 1978] basis functions, $\Lambda_i(s)$, such as used in ORB5 for the radial direction. These basis functions are arbitrarily labeled with $i = 1..9$. The radial direction is split into 6 regular intervals.

where $\Lambda_i(s)$, $\Lambda_j(\theta^\star)$, and $\Lambda_l(\varphi)$ are Bspline [de Boor, 1978] finite elements of degree d in the radial, poloidal, and toroidal directions, respectively, and the index ν corresponds to the triple index (i, j, l). Each one of these finite elements is defined on a regular grid composed of n_s, n_θ, and n_φ intervals in the radial, poloidal, and toroidal directions, respectively. The toroidal grid on which the toroidal finite elements, $\Lambda_l(\varphi)$, are defined being regular, it permits to preserve discrete translational symmetry, *i.e.*, $\Lambda_l(\varphi) = \Lambda_0(\varphi - 2\pi l/n_\varphi)$. A similar comment can be made in the poloidal direction. In the radial direction, $n_s + d$ Bspline basis functions are defined with the DeBoor algorithm [de Boor, 1978] and only one finite element is non-zero at each boundary, see figure 4.1. In this finite element representation, the field perturbation reads

$$\delta\phi(s, \theta^\star, \varphi) = \sum_{i,j,l} \delta\phi_{ijl}\, \Lambda_i(s)\Lambda_j(\theta^\star)\Lambda_l(\varphi),$$

and the discretized QNE (4.12) reads

$$\sum_{i',j',l'} L_{(ijl)(i'j'l')}\delta\phi_{i'j'l'} = S_{ijl}. \tag{4.22}$$

The value of the matrix elements $L_{(ijl)(i'j'l')}$ with respect to l and l' in fact depends only on the difference $l - l'$, because of the symmetry of the background quantities with respect to φ. One thus defines $L^{(l-l')}_{(ij)(i'j')} = L_{(ijl)(i'j'l')}$. The sum over l' on the LHS of equation (4.22) thus corresponds to a discrete convolution

$$\sum_{l'} \sum_{i',j'} L^{(l-l')}_{(ij)(i'j')}\, \delta\phi_{i'j'l'} = S_{ijl},$$

which takes an algebraic form in Fourier representation. A discrete Fourier transform (DFT) is thus applied on both the matrix coefficients and the finite-element coefficients used for representing the fields

$$\begin{cases} \delta\hat{\phi}_{ij}^{(n)} = n_\varphi^{-1} \sum_{l=0}^{n_\varphi-1} \delta\phi_{ijl}\, e^{-\imath 2\pi\, nl/n_\varphi}, \\ \hat{S}_{ij}^{(n)} = n_\varphi^{-1} \sum_{l=0}^{n_\varphi-1} S_{ijl}\, e^{-\imath 2\pi\, nl/n_\varphi}, \\ \hat{L}_{(ij)(i'j')}^{(n)} = n_\varphi^{-1} \sum_{\Delta l=0}^{n_\varphi-1} L_{(ij)(i'j')}^{(\Delta l)}\, e^{-\imath 2\pi\, n\Delta l/n_\varphi}, \end{cases} \tag{4.23}$$

with $\Delta l = l - l'$, in order to obtain a system of decoupled equations [Tran et al., 1999]

$$n_\varphi \sum_{i',j'} \hat{L}_{(ij)(i'j')}^{(n)}\, \delta\hat{\phi}_{i'j'}^{(n)} = \hat{S}_{ij}^{(n)}.$$

In ORB5, the electrostatic perturbation is furthermore represented by the poloidal DFT of its finite-element coefficients [McMillan et al., 2010]

$$\hat{\hat{\phi}}_{im}^{(n)} = n_\theta^{-1} \sum_{j=0}^{n_\theta-1} \delta\hat{\phi}_{ij}^{(n)}\, e^{-\imath 2\pi mj/n_\theta}. \tag{4.24}$$

The core electrostatic turbulence has a small parallel wave number $k_\parallel \simeq (nq_s - m)/Rq_s \ll 1$ and its spectrum is dominated by contributions of modes which are such that $m \simeq nq_s$. Therefore, as already done in the previous version of the long-wavelength field-aligned solver [McMillan et al., 2010], the turbulence can be accurately represented by the set of poloidal mode numbers K_i^n which contains the mode numbers $m \in [nq_s(s_i) - \Delta m, ..., nq_s(s_i) + \Delta m]$ with $\Delta m \ll n_\theta/2$ typically. This set of poloidal mode numbers is adjusted radially as a result of the radial variation of the safety factor $q_s = q_s(s)$. With this representation, the system of equations used to discretized the QNE becomes

$$n_\varphi \sum_{i'=1}^{n_s+d} \sum_{m' \in K_{i'}^n} \hat{\hat{L}}_{(im)(i'm')}^{(n)}\, \delta\hat{\hat{\phi}}_{i'm'}^{(n)} = \hat{\hat{S}}_{im}^{(n)}, \tag{4.25}$$

for all $m \in K_i^n$. Compared to $\hat{L}_{(ij)(i'j')}^{(n)}$ with $j = 1..n_\theta$ and $j' = 1..n_\theta$, the matrix $\hat{\hat{L}}_{(im)(i'm')}^{(n)}$ with $m \in K_i^n$ and $m' \in K_{i'}^n$ has the advantage of requiring a much smaller amount of memory because a limited set of coefficients are stored, given that $\Delta m \ll n_\theta/2$. These smaller matrices are also faster to assemble, in particular for the arbitrary wavelength solver.

In the considered discrete Fourier representation, the matrix $L_{\nu\nu'}^{\mathrm{pol}}$ in equation (4.17) becomes

$$\hat{\hat{L}}_{(im)(i'm')}^{\mathrm{pol\,(n)}} = n_\theta M^{(n)} \sum_{\sigma \in \mathrm{kin}} q_\sigma^2 \int ds d\theta^\star \mathcal{J} \int dv_\perp v_\perp \frac{N_{\sigma,\mathrm{eq}}(s,\theta^\star)}{T_{\sigma 0}^2(s,\theta^\star)} \exp\left[-\frac{m_\sigma v_\perp^2}{2T_{\sigma 0}(s,\theta^\star)}\right]$$
$$\times \left[\langle \Lambda_i \hat{\Lambda}_m \Lambda_{i'} \hat{\Lambda}_{m'}^* \rangle_\alpha(s,\theta^\star,v_\perp) - \langle \Lambda_i \hat{\Lambda}_m \rangle_\alpha(s,\theta^\star,v_\perp) \langle \Lambda_{i'} \hat{\Lambda}_{m'}^* \rangle_\alpha(s,\theta^\star,v_\perp)\right], \tag{4.26}$$

where one introduced the notations $\hat{\Lambda}_m(\theta^\star) = n_\theta^{-1}\sum_{j=0}^{n_\theta-1} e^{-\imath 2\pi\, jm/n_\theta}\Lambda_j(\theta^\star)$ and $\hat{\Lambda}_m^*$ is the complex conjugate of $\hat{\Lambda}_m$, and the background distribution function is assumed to be a local Maxwellian

$$f_{\sigma 0} = \frac{N_{\sigma,\mathrm{eq}}}{(2\pi T_{\sigma 0}/m_\sigma)^{3/2}} \exp\left(-\frac{m_\sigma v_\parallel^2/2 + \mu B_0}{T_{\sigma 0}}\right), \tag{4.27}$$

the density field $N_{\sigma,\mathrm{eq}}$ is chosen such as to ensure quasi-neutrality of the background (see reference [Angelino et al., 2006]), $\mathcal{J}$ is the Jacobian in $(s,\theta^\star,\varphi)$ coordinates, the integral in the $v_\parallel$ direction has been carried out analytically, the gyroaveraging is computed in the approximation $\boldsymbol{\rho}\cdot\nabla\varphi = 0$ such that the toroidal integral simplifies into the toroidal mass matrix [Tran et al., 1999]

$$M^{(n)} = n_\varphi^{-1}\sum_{\Delta l=0}^{n_\varphi-1} e^{-\imath 2\pi\, n\Delta l/n_\varphi}\int_0^{2\pi} d\varphi\, \Lambda_{\Delta l}(\varphi)\Lambda_0(\varphi).$$

In equation (4.26), one has kept the poloidal dependency of the density and temperature fields in the equations, *i.e.*, $N = N(s,\theta^\star)$ and $T = T(s,\theta^\star)$, to account for the effect of strong flows as presented in references [Collier, 2015, Collier et al., 2016]. This is a further generalization to the field solver implementation described in reference [McMillan et al., 2008], more details are given in appendix A. Note that this upgrade has been consistently carried out for all the solver matrices. For example the long-wavelength ion polarization drift matrix, equation (4.18), in its discrete Fourier representation is assembled from

$$\begin{aligned}\hat{\hat{L}}^{\mathrm{pol\,(n)}}_{(im)(i'm')} = n_\theta M^{(n)} \sum_{\sigma\in\mathrm{kin}} \frac{q_\sigma^2}{m_\sigma}\int dsd\theta^\star \mathcal{J}(s,\theta^\star)\frac{N_{\sigma 0}(s,\theta^\star)}{\Omega_{\sigma 0}^2(s,\theta^\star)}& \\ \times \nabla_{\mathrm{pol}}\Lambda_i(s)\hat{\Lambda}_m(\theta^\star)\cdot\nabla_{\mathrm{pol}}\Lambda_{i'}(s)\hat{\Lambda}_{m'}^*(\theta^\star),&\end{aligned} \tag{4.28}$$

where one uses the approximation $\nabla_\perp \simeq \nabla_{\mathrm{pol}} = \nabla s\partial_s + \nabla\theta^\star\partial_{\theta^\star}$.

To assemble the arbitrary wavelength matrix, the integrals in *configuration space* with respect to the radial and poloidal directions are handled in a different manner for the integral operator, equation (4.26), than for the differential operator, equation (4.28). The rationale is that, in the integral operator, the integrand is composed of gyroaveraged quantities such as, for example,

$$\langle\Lambda_i\hat{\Lambda}_m\rangle_\alpha(\mathbf{X},v_\perp) = \int d\alpha\,\Lambda_i\Big(s(\mathbf{X}+\boldsymbol{\rho}(\alpha))\Big)\,\hat{\Lambda}_m\Big(\theta^\star(\mathbf{X}+\boldsymbol{\rho}(\alpha))\Big),$$

which is not the case of the differential operator. In the integrand of the integral operator equation (4.26), the finite elements are thus estimated at guiding-center positions shifted by the Larmor vector, so that these shifted finite-elements are not systematically piecewise continuous per radial or poloidal intervals of the grid (except in the particular case that

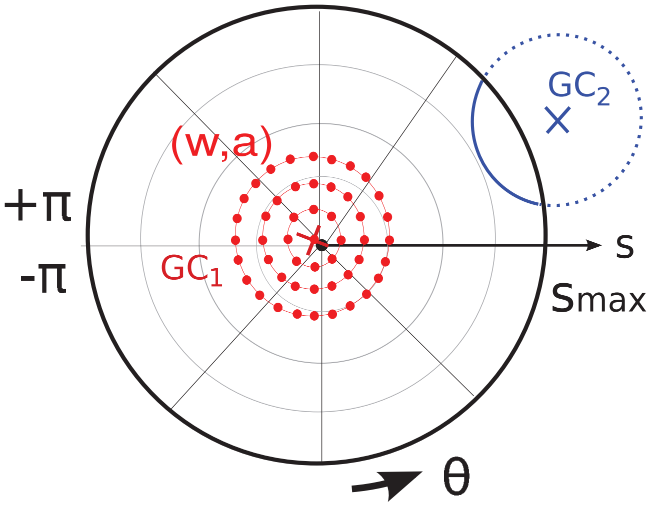

Figure 4.2 – Sketch of the gyropoints used to compute velocity quadrature of the arbitrary wavelength polarization matrix (4.26). Local grid of gyropoints (red dot markers), $\{\mathbf{X}+\boldsymbol{\rho}(v_\perp^{(w)},\alpha^{(a)})\}$, associated with a guiding center GC_1 (red cross) located near the magnetic axis (black dot marker). Also shown is a guiding-center GC_2 located outside the simulation domain (blue cross) with its associated gyroring crossing the simulation domain (full blue line).

$\boldsymbol{\rho}=0$ for example). Therefore, there is no advantage to use Gauss points over the radial and poloidal intervals for carrying out these radial and poloidal integrals accurately. We thus decided to use equidistant points in these directions. Moreover, as a second consequence of having shifted finite-elements in the integrand of equation (4.26), the integral in the radial direction is carried out over a radial domain larger than the simulation domain, because we account for guiding centers, $\mathbf{X}$, which are outside the simulation volume if a fraction of their gyroring, $\mathbf{X}+\boldsymbol{\rho}(\alpha)$, is inside this simulation volume. See the guiding-center and gyroring plotted in blue in figure 4.2. This volume of guiding-centers which are outside the simulation domain represents a small volume of a few local thermal Larmor radii in the radial direction, because the quadrature over the perpendicular velocity is typically carried out from 0 to $v_{\perp,max}$ with $v_{\perp,max}=5v_{\mathrm{th}}$. The background values $N_{\sigma0}$ and $T_{\sigma0}$ are extrapolated to be constant outside ($s>1$).

To assemble the polarization drift matrix of the arbitrary wavelength solver, equation (4.26), the integrals in *velocity space* are carried out with quadrature points adapted to the $(s,\theta^\star)$ grid resolution, because we intend to resolve the physics at all scales provided by this grid. This grid of quadrature points $(v_{\perp,w},\alpha_a)$ indexed by w and a integers is chosen to be regular: $v_{\perp,w}=w\,v_{\perp,max}(\mathbf{X})/n_\perp$ with $w=0..n_\perp-1$ and $v_{\perp,max}\simeq 5v_{\mathrm{th}}(\mathbf{X})$ typically, and $\alpha_a=a\,2\pi/n_\alpha$ with $a=0..n_\alpha-1$ and $n_\alpha=n_\alpha(\mathbf{X},v_\perp)$ is adapted in order to keep the length of arc $\Delta\rho_\alpha=2\pi v_{\perp,w}/n_\alpha\Omega_0(\mathbf{X})$ essentially constant. Note that the solution converges with $\mathcal{O}(1/n_\perp^4)$ when using a regular grid in $v_\perp$, instead of converging with $\mathcal{O}(1/n_\perp^2)$ when using a regular grid in μ. The density of quadrature points determined by $\Delta\rho_\alpha$ and $n_\perp$ is now discussed. From a geometric point of view, this $2D$ grid of velocity quadrature points, $(v_{\perp,w}, \alpha_a)$, corresponds to a $2D$ grid of gyropoints, $\{\mathbf{X}+\boldsymbol{\rho}_{\text{pol}}(v_{\perp,w}, \alpha_a)\}$ with $\mathbf{X} = \mathbf{X}(s, \theta^\star)$ a given guiding-center, see the cartoon in figure 4.2. The density of quadrature points is thus chosen such as to have a 2D grid of gyropoints significantly denser than the resolution of the $(s, \theta^\star)$ grid. Such criteria might be too constraining near axis where the poloidal resolution of the grid, $\Delta\theta^\star = 2\pi/n_\theta$, includes arbitrarily short scales as a result of having $s\Delta\theta^\star \to 0$ when $s \to 0$. Indeed, for a given guiding-center and for a given $v_\perp$, the gyroring representing the gyroaveraging path might lies on several grid cells. Resolving the shortest poloidal length might require near axis to use $n_\alpha > n_\theta$ with $n_\theta \gtrsim 1000$ typically. Nonetheless, when assembling the matrix $\hat{\hat{L}}^{(n)}_{(im)(i'm')}$, the shortest poloidal scales provided by the grid are filtered out by the field-aligned filter, in particular near axis. The field-aligned filter thus permits to gyroaverage near axis with a reasonable amount of gyroppoints, *i.e.*, $n_\alpha < n_\theta$. No filter is applied in the radial direction, and when using a regular grid in $s = \sqrt{\psi/\psi_{edge}}$, the radial resolution of this grid is, in general, the highest near the axis. Note that in the present work, we study ITG or TEM regimes in which cases the turbulence has a wavenumber $k_\theta\rho_i \lesssim 2$ typically, but we also account for the fine radial structures due to the non-adiabatic response of passing electrons near mode rational surfaces which requires a significantly higher resolution in the radial direction, with $k_r\rho_i \lesssim 20$ typically. We thus use grids for which one typically has a higher radial resolution than poloidal resolution, and, in this case, we adapt the density of quadrature points to the radial resolution.

Boundary conditions

The ORB5 simulation volume has the topology of a torus with either the full domain $s \in [0, s_{max}]$ or an annulus with $s \in [s_{min}, s_{max}]$ and $0 < s_{min} < s_{max} \leq 1$. In case of an annulus, both edges are handled in the same way.

In case of simulating a full domain the field is regularized at the magnetic axis by imposing unicity to the solution [Tran et al., 1999], $\delta\phi(s = 0, \theta^\star) = \langle\delta\phi\rangle_\theta(s = 0)$, for all $\theta^\star$. Imposing this condition is trivial because only the first radial basis function, $\Lambda_1(s)$, is non-zero on axis, see figure 4.1. Therefore, one sets to zero all the $m \neq 0$ Fourier coefficients of the perturbation field at the axis position $s = 0$, by imposing that $\forall$ n and $\forall$ $m \neq 0$ then $\delta\hat{\hat{\phi}}^{(n)}_{1m} = 0$.

The boundary condition on the edge is handled in a different manner for the arbitrary wavelength solver than for the other solver versions. Instead of imposing Dirichlet boundary conditions to the solution as it is done for the long wavelength and Padé versions of the solver, in case of the arbitrary wavelength solver, the solution is let free to obey natural boundary conditions of the weak QNE. As we will illustrate in a simple example, these natural boundary conditions depend on the family of functions chosen for the finite-element basis function. In the poloidal direction, the choice of using translational invariant basis function is natural, but in the radial direction different basis functions could be used. Let us consider the case of a plasma composed of gyro-kinetic ions and drift-kinetic electrons, in which case the self-consistent field $\delta\phi$ is computed from the linear system of equation (4.25) where the matrix $\hat{\hat{L}}^{(n)}_{(im)(i'm')}$ is only composed of the ion polarization drift contribution matrix $\hat{\hat{L}}^{\mathrm{pol(n)}}_{(im)(i'm')}$ equation (4.26). In this linear system of equations, the weak formulation of the polarization drift contribution, equation (4.26), is of the form

$$P = \int dsd\theta^\star \mathcal{J} \int d\mu' e^{-\mu'} \frac{N_{\sigma 0}}{T_{\sigma 0}} \left(\langle \delta\Psi\delta\phi \rangle_\alpha - \langle \delta\Psi \rangle_\alpha \langle \delta\phi \rangle_\alpha \right), \tag{4.29}$$

where $\mu' = \mu B_0 / T_{\sigma 0}$ and $\delta\Psi$ is the test function. This integral equation can be formulated in an integro-differential form by Taylor expanding the gyroaveraging operation using

$$\int d\alpha \delta(\mathbf{X} + \boldsymbol{\rho} - \mathbf{x}) \equiv \int d\alpha \exp(\boldsymbol{\rho} \cdot \nabla_\perp) = \int d\alpha \sum_{n=0}^{+\infty} \frac{1}{n!} (\boldsymbol{\rho} \cdot \nabla_\perp)^n, \tag{4.30}$$

which leads to

$$P = \left[\sum_{\gamma,\sigma \geq 0} b_{\gamma\sigma} \frac{\partial^\gamma \delta\Psi}{\partial s^\gamma} \frac{\partial^\sigma \delta\phi}{\partial s^\sigma} \right]_{\partial\Omega} + \int_\Omega dsd\theta^\star \mathcal{J}\, \delta\Psi \int d\mu' e^{-\mu'} \frac{N_{\sigma 0}}{T_{\sigma 0}} \left(\sum_{\gamma,\sigma \geq 0} c_{\gamma\sigma} \frac{\partial^\gamma}{\partial s^\gamma} \frac{\partial^\sigma}{\partial \theta^{\star\,\sigma}} \right) \delta\phi, \tag{4.31}$$

having assumed unicity of the solution on edge for simplicity of the discussion, and where $b_{\gamma\sigma}$ and $c_{\gamma\sigma}$ are real coefficients. For natural boundary conditions, the boundary term in square brackets is equal to zero. For example, in the typical long wavelength approximation this boundary term, for which $b_{01} = 1$ else $b_{\gamma\sigma} = 0$, reads

$$0 = \left[\delta\Psi \frac{\partial\delta\phi}{\partial s} \right]_{\partial\Omega},$$

and corresponds to the condition

$$0 = \left[\Lambda_{n_s+d}(s) \frac{\partial\delta\phi}{\partial s} \right]_{\partial\Omega},$$

because the last finite element $\Lambda_{n_s+d}(s)$ is the only test function which is non-zero at the edge, see figure 4.1. This equation, which corresponds to the Neuman boundary condition $\partial\delta\phi/\partial s|_{edge} = 0$, is usually replaced by the Dirichlet boundary condition $\delta\phi|_{edge} = 0$. Now considering the general case, equation (4.31), the general natural boundary condition on $\delta\phi$

$$0 = \left[\sum_{\gamma,\sigma \geq 0} b_{\gamma\sigma} \frac{\partial^\gamma \delta\Psi}{\partial s^\gamma} \frac{\partial^\sigma \delta\phi}{\partial s^\sigma} \right]_{\partial\Omega} ,$$

depends on the value of the terms $b_{\gamma\sigma}$ and on the value of the derivatives $\partial^\gamma \delta\Psi / \partial s^\gamma$. The values of these terms depend on the choice made for the finite element basis function $\{\Lambda_i(s)\}$. *First*, it is obvious that if $\delta\Psi$ corresponds to any basis function $\Lambda_i(s)$ then the values of $\partial^\gamma \delta\Psi / \partial s^\gamma$ depends on the choice made for defining the $\Lambda_i(s)$ basis functions. In our case, only one radial basis function is non-zero on edge, but several ones have derivatives which are non-zero on edge, see figure 4.1. Therefore, the general natural boundary condition can be written as the system of equations

$$0 = \left[\sum_{i'} \delta\phi_{i'} \sum_{\gamma,\sigma \geq 0} b_{\gamma\sigma} \frac{\partial^\gamma \Lambda_i}{\partial s^\gamma} \frac{\partial^\sigma \Lambda_{i'}}{\partial s^\sigma} \right]_{\partial\Omega} ,$$

where one has one equation per index i for which there exists an integer value of $\gamma \geq 0$ such that $\partial^\gamma \Lambda_i / \partial s^\gamma \neq 0$ at the edge, and having used the finite element representation of the field $\delta\phi(s) = \sum_{i'} \delta\phi_{i'} \Lambda_{i'}(s)$. Moreover, the set of finite elements with at least one non-zero derivative at the edge and the value of these derivatives depend on the order of the finite elements, such that this system of equations determining the natural boundary condition of the weak QNE varies with the order of the BSpline finite element basis functions. *Second*, the choice made of defining the finite element only inside the simulation volume ($s \leq 1$) influences the value of the gyroaveraged quantities in the vicinity of the edge where a fraction of gyroring might be outside the simulation volume. Indeed, the fact that no finite element is defined outside $s > 1$ corresponds to the fact that $\delta\phi = 0$ outside, because no contribution can come from the fraction of gyroring outside where $\delta\phi$ is not represented. This feature influences the nature of the kernel of the integral equation (4.26) which is of the form of equation (4.29), and in terms of equation (4.31) this feature influences the values of the coefficients $b_{\gamma\sigma}$ and $c_{\gamma\sigma}$. *Finally*, it turns out that the arbitrary wavelength solver such as presented in this chapter does not respect the Dirichlet boundary conditions. Nonetheless, the solution obtained with this new solver tends to these Dirichlet boundary conditions when the plasma conditions are brought toward long wavelength conditions. In general, the amplitude of $|\delta\phi|$ at the edge is small compared to its typical value inside the simulation volume where the physics of interest is studied.

4.5 Gyroaveraging in magnetic coordinates

For all operations associated with gyro-averaging, the plane of the gyro-motion, which is in fact perpendicular to the magnetic field, is approximated to the poloidal plane $\varphi = const$, for practical purposes. This approximation is justified in a tokamak of sufficiently large aspect ratio. In particular, the operator $\nabla_\perp$ appearing in the equations of section 4.3 is approximated by $\nabla_\perp \simeq \nabla_{\mathrm{pol}} = \nabla s \partial_s + \nabla\theta^\star \partial_{\theta^\star}$ expressed in magnetic coordinates.

For computing gyro-averages appearing in equations (4.14) and (4.17), the gyropoints, *i.e.* the particle positions along the gyroring are parametrized by the gyro-angle α

$$\mathbf{x}(\alpha) = \mathbf{X} + \boldsymbol{\rho}(\alpha) = \mathbf{X} + \rho\frac{\nabla s}{|\nabla s|}\cos\alpha + \rho\frac{\mathbf{b}\times\nabla s}{|\mathbf{b}\times\nabla s|}\sin\alpha, \tag{4.32}$$

where $\rho = \rho(\mathbf{X}, \mu)$ and having dropped the index σ for species dependence to lighten notation. The $(s, \theta^\star)$ coordinates of the gyropoints can be estimated by linearizing the metric around the guiding-center position. However, such a linearization of the metric is problematic when considering the polar-like coordinate system $(s, \theta^\star)$ which presents a singularity at $s = 0$ (magnetic axis). Indeed, when approaching this point the metric starts to vary significantly over the scale of the Larmor radius. To avoid this problem one considers the pseudo-Cartesian coordinate system $(\xi, \eta) = (s\cos\theta^\star, s\sin\theta^\star)$ which is absent of any singular point. The radial variable s must be defined so as to be proportional to the geometrical minor radius r near the magnetic axis, *e.g.*, $s \propto \sqrt{\psi}$. The estimation of the $(s, \theta^\star)$ coordinates of points along the gyro-ring is now carried out by performing an analytical mapping in between the two sets of variables $(s, \theta^\star) \leftrightarrow (\xi, \eta)$ and by linearizing the metric around the guiding-center position in the (ξ, η) coordinates, which leads to [Lapillonne, 2010]

$$\begin{cases} s(\mathbf{X}+\boldsymbol{\rho}) = \sqrt{[s(\mathbf{X}) + \boldsymbol{\rho}(\alpha)\cdot\nabla s(\mathbf{X})]^2 + s^2(\mathbf{X})\,[\boldsymbol{\rho}(\alpha)\cdot\nabla\theta^\star(\mathbf{X})]^2}, \\ \theta^\star(\mathbf{X}+\boldsymbol{\rho}) = \theta^\star(\mathbf{X}) + \mathrm{arctan2}\Big[\frac{s(\mathbf{X})\,\boldsymbol{\rho}(\alpha)\cdot\nabla\theta^\star(\mathbf{X})}{s(\mathbf{X})+\boldsymbol{\rho}(\alpha)\cdot\nabla s(\mathbf{X})}\Big]. \end{cases} \tag{4.33}$$

4.6 Structure of the polarization matrix

The polarization matrix $L^{\mathrm{pol\,(n)}}_{kk'}$, equation (4.26), can be seen as a weighted integral of spline factors

$$P^{(n)}_{kk'}(s, \theta^\star, v_\perp) = \langle\hat\Lambda_k\hat\Lambda^*_{k'}\rangle_\alpha - \langle\hat\Lambda_k\rangle_\alpha\langle\hat\Lambda^*_{k'}\rangle_\alpha, \tag{4.34}$$

where the gyroaveraged operation $\langle\ \rangle_\alpha = \langle\ \rangle_\alpha(s, \theta^\star, \rho)$ is computed with equation (4.32), the double index $k = (i, m)$ is defined by $k = 1 + m - nq_s(s_i) + (1 + 2\Delta m)(i - 1)$ with $m \in K^n_i$, and $\hat\Lambda_k(s, \theta^\star) = \Lambda_i(s)\hat\Lambda_m(\theta^\star)$.

The matrix $L^{\mathrm{pol\,(n)}}_{kk'}$ is stored in an upper triangular band matrix. Keeping only its upper part ensures hermicity of the matrix, and storing only a limited number of bands reduces its size. This matrix is thus composed of the elements for which $k \leq k' \leq k + n_{bands}$ with n_{bands} an integer.

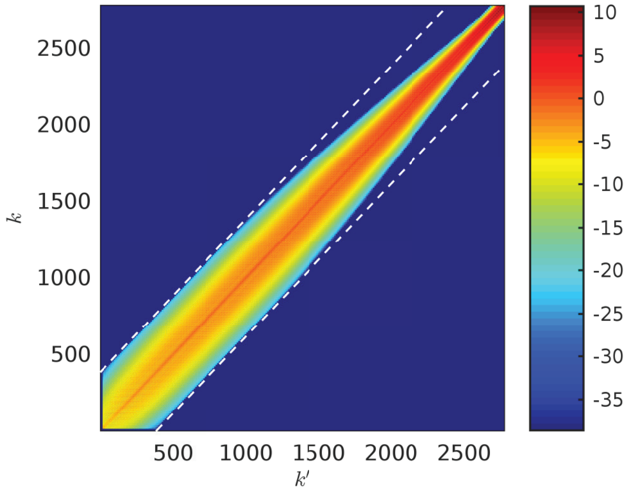

Figure 4.3 – Arbitrary wavelength solver matrix of a $n = 0$ toroidal mode number. Plotted is the log of the absolute value of its elements, $\log |L_{kk'}^{(n=0)}|$. TCV test case, see section 5, with kinetic electrons (no adiabatic matrix). In this figure, we choose the particular parameters $s \in [0, 1]$, $n_s = 250$, $n_m = 11$, and $v_{\perp,max} = 7v_{th}$. The lines and columns are indexed with the $2D$ index $k = m + (1 + 2\Delta m)(i - 1)$ where m is the poloidal mode number and i the radial spline index ($nq_s = 0$ here). White dashed lines delimit the bands which have non-null elements.

Looking at the spline factor, equation (4.34), its second term $\langle\hat{\Lambda}_k\rangle_\alpha\langle\hat{\Lambda}^*_{k'}\rangle_\alpha$ might couple very distant positions, *i.e.* twice the largest value of the Larmor radius used for gyroaveraging. This coupling between distant positions is described by elements of the polarization matrix far from the diagonal. Compared to the long-wavelength solver, the arbitrary wavelength solver bandwidth is thus, generally, broader. As an illustration, an arbitrary wavelength matrix $L_{kk'}^{\mathrm{pol}\,(\mathrm{n}=0)}$ is plotted in figure 4.3.

This matrix is assembled for conditions relevant to the TCV tokamak with the same ideal MHD equilibrium than the one used at end of this chapter, and when using the parameters $n = 0$, $s \in [0, 1]$, $n_s = 250$, $\Delta m = 5$, and $v_{\perp,max} = 7v_{\mathrm{th}}$.

For given values of i and i', the $P_{kk'}^{(n)}$ elements are organized in the matrix as blocks of poloidal Fourier coefficients, as a consequence of the definition of the double index k. The size of these blocks is determined by the field-aligned filter width $1 + 2\Delta m$. Therefore, n_{bands} must be a multiple of $1 + 2\Delta m$.

For given values of m and m', the $P_{kk'}^{(n)}$ elements are sparse in the matrix. They are located on bands identified by the index $\Delta k = k' - k$ which are associated to radial bands identified by $\Delta i = i' - i$. The bandwidth of the matrix is $n_{bands} = 1 + \max \Delta k$ which is related to the max of Δi by the relation $n_{bands} = (1+2\Delta m)(1+\max \Delta i)$. This bandwidth depends on the Larmor radius used for gyroaveraging and on the resolution of the s grid. Indeed, the first term of equation (4.34) couples radial finite elements $\Lambda_i(s)$ with their $1+2d$ neighbors, but the second term of this equation couples radial finite elements distant of each other by a distance which is at maximum equal to $2\rho_{\max} = 2\,v_{\perp,\max}/\Omega_0$, thus leading to

$$\max \Delta i = 1 + 2d + \max_{s,\theta^\star}\left[ceil\frac{2v_{\perp,\max}(s,\theta^\star)}{\Omega_0(s,\theta^\star)\Delta r_s(s,\theta^\star)}\right],$$

where $\Delta r_s = \Delta s/|\nabla s|$ is the local radial resolution of the grid. From this expression one deduces the matrix bandwidth

$$n_{bands} = (1+2\Delta m)\left\{2 + 2d + \max_{s,\theta^\star}\left[ceil\frac{2v_{\perp,\max}(s,\theta^\star)}{\Omega_0(s,\theta^\star)\Delta r_s(s,\theta^\star)}\right]\right\}.$$

This estimate is not exact because $|\nabla s|$ is not radially constant and there are positions for which $|\nabla s(\mathbf{X})| \neq |\nabla s(\mathbf{X} + 2\boldsymbol{\rho}_{\max})|$.

The coupling between distant elements is weak because of the presence of a Maxwellian weight, $\exp\left(-\rho_\perp^2/2\rho_{\rm th}^2\right)$, in equation (4.26). Indeed, in figure 4.3, one can see that elements on the diagonal are of bigger amplitude than elements far from it. One could thus be tempted to further truncate this matrix by keeping a number of matrix bands smaller than n_{bands} (but still multiple of $1+2\Delta m$), because it consists in ignoring terms of small amplitude. Nonetheless, the importance of keeping all the non-null radial bands of the matrix is illustrated in a Rosenbluth-Hinton test [Rosenbluth and Hinton, 1998]. For this verification, a plasma regime is chosen for which the long wavelength approximation is a good approximation. This choice is made in order to compare the results with one of the long wavelength solver and to verify the convergence of their solutions, see figure 4.4. In subplot (a), one shows that the results obtained with the arbitrary wavelength solver are clearly sensitive to the number of radial bands. Indeed, in case that all the (27 for this case) radials bands required for representing the arbitrary wavelength matrix are kept, both the long wavelength solver and the arbitrary wavelength solver are in a very good agreement. On the contrary, when one truncates the matrix the arbitrary wavelength solver provides a solution which significantly diverge from the expected solution. In subplot (b), the relative differences between a theoretical estimate and the simulation results using the arbitrary wavelength solver is plotted with respect to the parameter $v_{\perp,\max}$ used for assembling the polarization matrix. For $v_{\perp,max} \geq 5v_{\rm th}$ the simulation results obtained with both the arbitrary wavelength solver and the long wavelength solver are in good quantitative agreement. In both cases there are reasonable differences of 3% and 7% between the numerical results and the theoretical predictions for the residual $res = 1/(1+1.6q_s^2\sqrt{a/R})$ and frequency $\omega_G = (v_{\rm th,i}/R)\sqrt{1+1/2q_s^2}$, respectively.

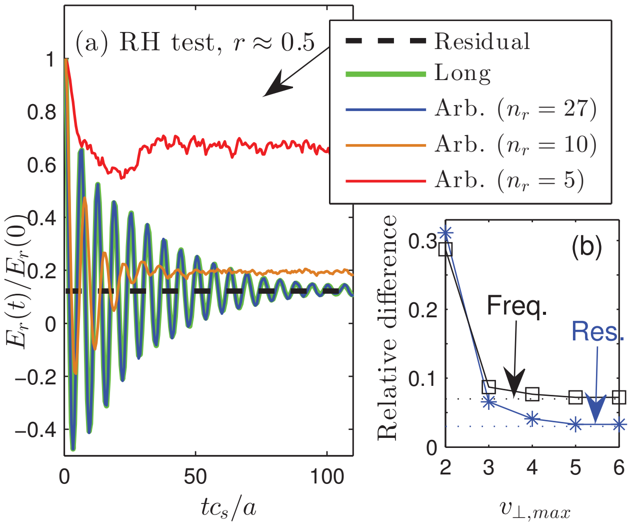

Figure 4.4 – Rosenbluth-Hinton test in CBC geometry with zero density and temperature gradients, $\rho^\star = 1/180$, $n_s = 360$, $n_{p,\mathrm{tot}} = 16$M marker particles, adiabatic electrons, and the results are taken at radial position $r \approx 0.5$. Plotted is the radial electric field E_r in arbitrary units. Subplot (a), comparison between the long wavelength solver and the arbitrary wavelength solver. The matrix of the arbitrary wavelength solver is composed of $n_r = 27$ (blue), 10 (orange), and 5 (red) radial bands for representing the solver matrix. The total number of bands of the matrix is $(1 + 2\Delta m)\, n_r$. Subplot (b), convergence study with respect to $v_{\perp,max}$ used for assembling the arbitrary wavelength solver. Plotted are the relative differences of the simulation results for the GAM frequency (Freq.) and residual (Res.) with the theoretical estimates: $res = 1/(1 + 1.6q_s^2\sqrt{a/R})$ and $\omega_G = (v_{\mathrm{th,i}}/R)\sqrt{1 + 1/2q_s^2}$. The dotted lines, in subplot (b), stand for the long wavelength results.

4.7 Linear benchmark ORB5 versus GENE

To verify the new solver, a benchmark has been carried out between ORB5 and the global version of the gyrokinetic code GENE [Jenko et al., 2000, Görler et al., 2011]. The gyrokinetic code GENE already has an arbitrary wavelength solver and therefore provides appropriate reference in this case. For this benchmarking, two realistic magnetohydrodynamic (MHD) equilibria from reference [Burckel et al., 2010] were used: *Geometry V* which is the simplest one with nearly circular concentric magnetic surfaces, and *Geometry I*, which is the most complicated one with finite Shafranov shift, elongation, triangularity, and up/down asymmetry. When using Geometry 5, three electron models (adiabatic, hybrid, and kinetic) were used, as well as the three solver versions: long wavelength, Padé, and arbitrary wavelength. When using Geometry 1, one used the adiabatic electron model for both the long wavelength and the arbitrary wavelength solvers.

The considered plasma is a two-species plasma with hydrogen ions ($q_i = -q_e = e$), heavy electrons ($m_i/m_e = 400$), and $T_{i0} = T_{e0}$. The background gradient profiles are chosen to be peaked, such as to radially localize the source of instability and to avoid the presence of modes with similar growth rates at different radial locations. Both density and temperature profiles are thus defined by

$$\frac{d\ln N,T}{d\rho_{\mathrm{vol}}} = -\frac{\kappa_{N,T}}{2}\left[\tanh\left(\frac{\rho_{\mathrm{vol}}-\rho_{\mathrm{vol},0}+\Delta\rho_{\mathrm{vol}}}{\Delta_{N,T}}\right)-\tanh\left(\frac{\rho_{\mathrm{vol}}-\rho_{\mathrm{vol},0}-\Delta\rho_{\mathrm{vol}}}{\Delta_{N,T}}\right)\right], \tag{4.35}$$

with $\rho_{\mathrm{vol}} = \sqrt{V/V_{\mathrm{edge}}}$ the normalized radial variable, $V = V(\psi)$ the volume contained within the flux surface ψ, $\kappa_{N,T} = a/L_{N,T}$, a the minor radius, and $L_{N,T} = -\nabla\ln(N_0, T_0)$. In this benchmark exercise one takes $\kappa_N = 0.78$, $\kappa_T = 2.47$, $\Delta_N = \Delta_T = 0.02$, $\rho_{\mathrm{vol},0} = 0.5$, and $\Delta\rho_{\mathrm{vol}} = 0.075$ for both ion and electron species. The number of markers, the time step, and the numerical resolution of the grid are adapted for each toroidal mode number n in order to converge the results.

In figure 4.5, using the fully shaped MHD equilibrium Geometry 1, the dispersion relations obtained from simulations carried out with GENE and ORB5 are in good agreement when using the new arbitrary wavelength solver. This validates the fact that the new arbitrary wavelength solver handles accurately the complex ideal MHD geometries. This ITG type mode is unstable in the range $0 < k_\theta\rho_s \lesssim 1.2$, where $k_\theta\rho_s$ is an average of the normalized poloidal wave number. Note that at shorter scales, $k_\theta\rho_s \gtrsim 1$, the long-wavelength solver starts to deviates from the arbitrary wavelength solution.

In figure 4.6, using the simplest MHD equilibrium Geometry 5, it is shown that the long-wavelength solver fails at correctly reproducing the growth rate γ for the the short wavenumbers, $k_\theta\rho_s \gtrsim 1$, of the TEM branch, when using either the hybrid or the fully

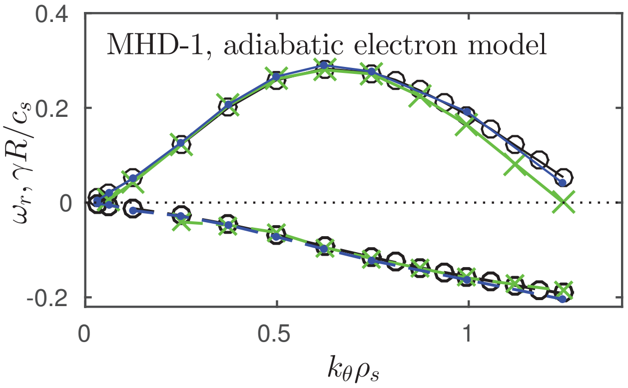

Figure 4.5 – Dispersion relation for the Geometry 1 case. Results have been obtained with the GENE code (black lines with circle markers), as well as the ORB5 code considering either the long wavelength solver (green crosses) or arbitrary wavelength solver (blue line with dot markers). The adiabatic electron model was considered for all cases. Growth rate γ in full line and real frequency ω_r in dashed line. The normalized poloidal wavenumber is estimated from $k_\theta \rho_s = n\, q_s \rho_s / a$ with $q_s \rho_s / a$ estimated at the radial position $\rho_{\mathrm{vol},0}$ where the gradient profile is peaked.

kinetic electron models. On the contrary, the new arbitrary wavelength solver successfully solves these short scale modes with both the hybrid and kinetic electron models and is in very good quantitative agreement with GENE. Finally, the Padé version of the solver also shows a very good agreement with GENE and thus with the new integral solver.

In figure 4.7 subplots (a) and (b), it is shown that the radial envelopes of the eigenmode $n = 24$ ($k_\theta \rho_s \simeq 0.37$) obtained with the fully-kinetic electron model are in very good agreement between GENE and ORB5 when using the arbitrary wavelength solver. Note also agreement in this case with ORB5 results considering the the Padé solver. Moreover, the systematic presence of fine radial structures due to the non-adiabatic response of passing electrons near low order MRSs [Dominski et al., 2015] is confirmed, and the agreement of the radial width of these fine structures obtained with GENE and ORB5 reflects convergence down to these short scales. It should be pointed that the Padé approximation version of the solver provides a very good approximation for resolving such short scale. The full width at half maximum (FWHM) of the fine structure of non-adiabatic passing electron response measure $\delta r \approx 0.3 \rho_i$ which corresponds roughly to $k_r \rho_i \approx 20$. The intermediate range of scales at which the Padé approximation might not be a good approximation are not present. Note also that there is good agreement between GENE and ORB5 despite the fact that the former code considers the drift-kinetic model for electrons while the latter considers the gyrokinetic model for evolving electrons. On the other hand, it is shown that the long wavelength solver fails at solving these fine radial structures. Note that fine structures of similar short scales are present on the QNE source term, $\delta N_i^{\mathrm{gy}} - \delta N_e^{\mathrm{gy}}$, when using either the long or arbitrary wavelength solver,

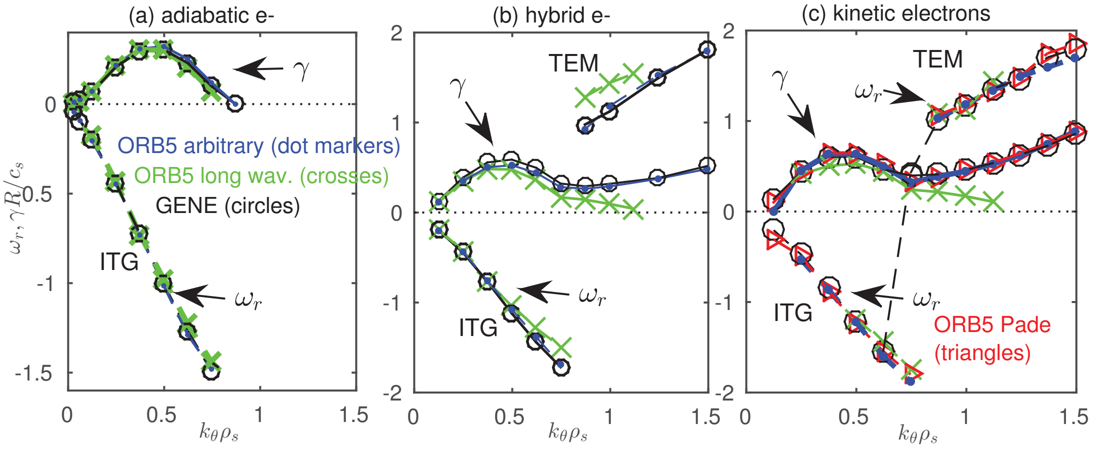

Figure 4.6 – Dispersion relation for the Geometry 5 case, results have been obtained with GENE (black circles), ORB5 and long wavelength solver (green crosses) or arbitrary wavelength solver (blue dots), when using the (a) adiabatic, (b) hybrid, and (c) kinetic electron models. The ORB5 results obtained with the Padé approximation solver (red triangles) and kinetic electrons are also presented in subplot (c). Growth-rate in full-line and real frequency in dashed line.

see subplots (c) and (d). Therefore, the fact that such fine structures are missing on the envelope of the potential computed with the long wavelength solver compared to the envelope of the potential obtained with the arbitrary wavelength solver, see subplots (a) and (b), is only a consequence of the long wavelength approximation made when computing the self consistent field.

For the results obtained when using the arbitrary wavelength solver, the fact that the growth rate is larger when using the fully-kinetic electron model than when using the hybrid electron model (see figure 4.6 subplots (b) and (c)) shows that the non-adiabatic passing electron response is not only corrugating the eigenmode radial structure but further reinforces the destabilization mechanism. For example, for the wave number $k_\theta \rho_s \approx 1.2$ of the TEM branch, the growth rate is $\gamma \simeq 0.38$ with the hybrid electron model and $\gamma \approx 0.64$ with the fully kinetic electron model.

4.8 Conclusion

A *new arbitrary wavelength field solver* has been implemented in the ORB5 code which enables the study of quasi-neutral micro-turbulence at arbitrarily short scales in $k_\perp \rho_i$. The linearized polarization drift contribution to the quasi-neutrality equation is now accounted for in its integral form. The new solver implementation has been described in detail and the particular requirements to converge the electrostatic field solution on axis and near the edge have been discussed. The behavior of the solution at the boundary has also been discussed for the integral operator. The option of using the Padé approximation

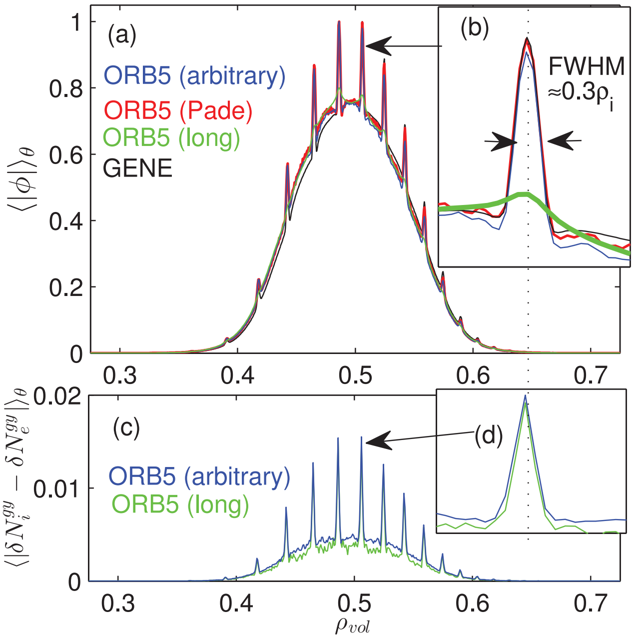

Figure 4.7 – Eigenmode of an ITG mode for toroidal mode number $n = 24$ ($k_\theta \rho_s \simeq 0.37$). Radial structure (poloidal-average of the absolute value) of the electrostatic field in subplots (a,b), and of the gyrodensity in subplots (c,d). Results have been obtained with GENE (black), ORB5 with long wavelength solver (green), ORB5 with arbitrary wavelength solver (blue), and ORB5 with Padé approximation solver (red). Very high radial resolutions: 800 and 1000 radial points on the plotted radial interval have been considered for ORB5 and GENE, respectively.

for computing the ion polarization drift contribution to the quasi-neutrality equation is also available when running simulations with the fully kinetic electron model.

A *benchmark of the gyrokinetic code ORB5* with this new solver has been carried out against the global version of the gyrokinetic code GENE, in realistic ideal MHD toroidal geometry. This benchmark was conducted in the ITG to TEM part of the instability spectra ($0 < k_\theta \rho_s < 1.5$). The three different electron models, *i.e.* adiabatic, hybrid, and kinetic, have been used to study the short scale physics of the non-adiabatic responses of either the trapped electrons or the passing electrons. In each case a very good quantitative agreement has been found between GENE and ORB5 when using the new arbitrary wavelength solver. A good quantitative agreement has also been found with the Padé version of the solver which is implemented for the kinetic electron model only. As expected, the long wavelength version of the solver totally fails at resolving the short scale physics due to the non-adiabatic response of both trapped electrons and passing electrons. In this benchmark, it was also shown that the TEM branch is more unstable when using the fully-kinetic electron model than when using the hybrid model. This increase of the destabilization is due to the fact that a large fraction of the passing electron population has a non-adiabatic response to the perturbation. This reduction of the global adiabatic response of the passing electrons has a destabilizing effect, qualitatively confirming results obtained in chapter 3 and in reference [Dominski et al., 2015].

Nonlinear simulations using this new arbitrary wavelength solver are carried out in conditions relevant for the TCV tokamaks, in the next chapter.

5 The passing electron channel of turbulent transport in global gyrokinetic simulations relevant for TCV

5.1 Introduction

In this chapter, nonlinear simulations of a two-species plasma, *i.e.*, kinetic ions and electrons, are carried out in conditions relevant for TCV [Hofmann et al., 1994], shot number #45353. The magnetic geometry is shaped with elongation, triangularity, small up-down asymmetry, and Shafranov shift, see figure 5.1. This TCV shot was initially used in references [Vernay, 2013, de Meijere et al., 2014] where nonlinear simulations were carried out with ORB5 using a simpler model for the plasma, *i.e.* the hybrid electron model, the long-wavelength solver, and a lower radial resolution ($n_s = 128$), thus missing the physics of non-adiabatic passing-electron dynamics near mode rational surfaces.

In section 5.3, results obtained with the integral solver are compared to the Padé approximation version, when using the heavy electron mass ratio ($m_i/m_e = 400$). In section 5.4, full-torus and half-torus simulations carried out with heavy kinetic electrons are carried out. In section 5.5, half-torus simulations are carried out with the physical deuterium to electron mass ratio ($m_i/m_e = 3672$) and compared to heavy electron simulations. The differing contributions of sub- and suprathermal particle species to the fluxes, and the radial organization of these quantities in the vicinity of mode rational surfaces, are studied in detail; we also consider how the zonal flow structures interact with the structures near MRSs.

ORB5 moments and fluxes diagnostics are discussed in references [Jolliet, 2010, Vernay, 2013] and in appendix B. Let us just mention that diffusivities are expressed in gyro-Bohm units $D_{GB} = \chi_{GB} = \rho_{s0}^2 c_{s0}/a$ with $c_{s0} = \sqrt{T_{e0}(s_{peak})/m_i}$, $\rho_{s0} = mc_{s0}/qB_{\text{axis}}$, and $s_{peak} = 0.6$ in this TCV case.

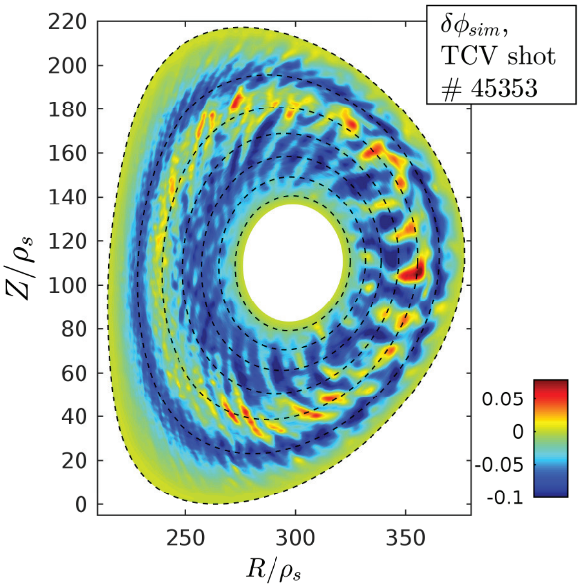

Figure 5.1 – Electrostatic field in the poloidal plane, snapshot taken during the turbulent saturated time window. TCV full-torus simulation test case.

5.2 Test case description

The *half-torus* case consists of carrying out a simulation assuming periodicity over half the toroidal domain. Practically, it is obtained by dropping every second toroidal mode number n, *i.e.*. We use $n \in [0, 2, 4, \cdots, 42, 44]$, with $n_{\mathrm{p,tot}} = 10^9$ marker particles for both the ion and electron species. The *full-torus* case is carried out by using the full toroidal mode spectrum $n \in [0, 1, 2, \cdots, 43, 44]$ and keeping the same number of marker particles per toroidal mode number, *i.e.* $n_{\mathrm{p,tot}} \simeq 2 \times 10^9$ for ions and electrons. The number of gyropoints used for gyroaveraging is $n_\alpha = 18$ for an ion with a thermal Larmor radius and is scaled linearly with the Larmor radius of each oin.

The configuration space grid resolution is $n_s \times n_\theta \times n_\varphi = 360 \times 1024 \times 512$ with $s \in [0.35, 1.0]$ and $\rho^\star = \rho_s/a = 1/81$ at the position of reference $s_{\mathrm{peak}} = 0.6$ ($\rho_{\mathrm{vol}} \approx 0.48$). The temperature ratio is equal to $T_{i0}/T_{e0} = 0.267$, note that $\rho_i/a \approx 1/157$ at s_{peak} and the chosen radial simulation domain represents more than 100 ion Larmor radii. In linear simulations, we verified that the chosen radial resolution provides converged values (within a few percent error) of the growth rates for the most unstable toroidal mode numbers, and, in nonlinear simulations, we verified that the same level of turbulent fluxes ($\lesssim 10\%$ difference) are obtained for a nonlinear simulation carried out with a lower radial resolution and with less toroidal mode numbers, *i.e.*, $n_s = 250$ and $0 \leq n \leq 32$.

Two physical aspects have been considered when choosing the radial resolution of these simulations carried out with the kinetic electron model: the radial width of the fine structures of non-adiabatic passing-electron response and the radial distribution of MRSs. In reference [Dominski et al., 2015] which results have been presented in chapter 3, it was shown that these fine structures are broadened in nonlinear simulations and that their width varies with the density of MRSs, see figure 3.11. (The distance between mode rational surfaces is $L_{MRS} = 1/\hat{s}k_y$ and $k_y \equiv nq_0/r_0$.) Choosing a radial grid significantly denser than the distribution of MRSs appears as a reasonable choice for studying the non-adiabatic passing electron dynamics in nonlinear simulations. The rational numbers being dense with respect to the real numbers, an infinity of MRSs are present in a tokamak. Nonetheless, the turbulence is resolved only for its mode numbers $0 \leq n \leq 44$, and the resonant MRSs associated to the mode number $n = 44$ are located at radial positions where the safety factor is $q_s = m/44$ with m integer. In order to study the influence of each MRS on the turbulent flux spectra of particle and heat, we thus choose a radial grid denser than the distribution of these MRSs over essentially all the radial domain ($s \lesssim 0.9$). The resolution of the MRSs is addressed in more detail at the end of the chapter, see figure 5.15 (g,h). Note that in chapter 3, we also showed that the level of turbulent transport requires the use of a very high radial resolution for reaching convergence, because this high radial resolution permits to resolve the fine structures on the profile of $\omega_{E\times B}$ which furthermore saturate the turbulence.

A typical field-aligned filter [Jolliet et al., 2007, McMillan et al., 2010] is used such that for a given toroidal mode number n only the poloidal modes contained in the local interval $m \in [nq_s - 5, nq_s + 5]$ are solved.

A modified Krook operator [McMillan et al., 2008] is used for controlling the noise by setting the parameter $\gamma_k a/c_s = 0.027$ (heavy electrons) and 0.024 (Deuterium/electron mass ratio) which roughly corresponds to a tenth of the respective maximum linear growth rates. This operator does not introduce sources of particles or parallel momentum and conserves the residual ZFs phase space structure. On the other hand, its effect is to keep the species temperature profiles close to their initial values. The associated effective heat source is a smooth radial function corresponding consistently to a source near the core and a sink near the edge. The radial density profile can relax during the simulation and the time-averaged (over the turbulent saturated regime) profile shows a significant deviation from the initial input, by up to 20%. This loss of density is caused by a strong burst of particle flux when the system state enters in the nonlinear saturated regime, after which there is a remaining particle flux of decreasing amplitude during the simulation so that the density continues to relax. This relaxation of the density profile is currently not taken into account by the assembly of the solver. This would require implementing the nonlinear polarization drift contribution to the QNE, which is left for future works. A shielding of the electric field [Jolliet, 2010] is used at the edge of the simulation domain, to avoid the presence of non-physical electric field caused by secular accumulation of charge losses near the boundary.

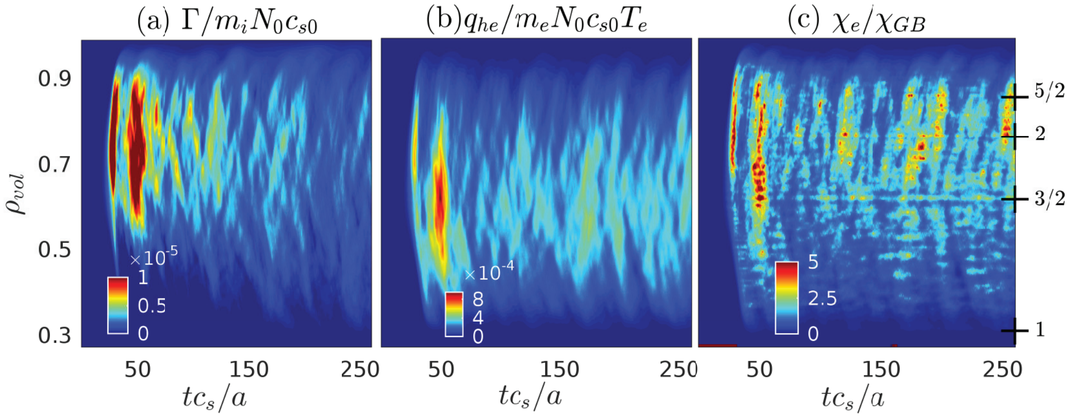

Figure 5.2 – Particle flux (a), electron heat flux (b), and electron heat diffusivity (c) with respect to the time, tc_s/a, and radial position, ρ_{vol}. Global simulation of TCV #45353 using the arbitrary wavelength solver, the kinetic electrons, the heavy electron mass ratio $m_i/m_e = 400$, in a half torus.

5.3 Arbitrary wavelength and Padé solvers in the *half-torus* test case with heavy electrons

The time-dependent radial profile of particle flux, $\Gamma(\rho_{vol}, t) = \Gamma_e(\rho_{vol}, t) = \Gamma_i(\rho_{vol}, t)$, electron heat flux, $q_{H,e}(\rho_{vol}, t)$, and electron heat diffusivity, $\chi_e(\rho_{vol}, t)$, are plotted in figure 5.2 for heavy electrons ($m_i/m_e = 400$) in a half-torus. The simulation time window covers several flux bursts during the turbulent saturated regime, thus ensuring reasonably good statistics. Subplots (a) and (b) of figure 5.3 show the radial profile of the time-averaged heat diffusivity of the ions $\langle\chi_i\rangle_t(s)$ and electrons $\langle\chi_e\rangle_t(s)$, respectively. For simulations carried out with both the Padé solver and the arbitrary wavelength solver, the ratio of ion to electron diffusivity is higher near the core than in the edge. Each species heat diffusivity is found to be in good quantitative agreement between simulations carried out with either the Padé solver or the arbitrary solver. There is only 6% of relative difference between their time- and radial-averaged amplitudes, see the dotted lines in figure 5.3. Moreover, $\langle\chi_i\rangle_t$ and $\langle\chi_e\rangle_t$ are of similar level, but having a constant background temperature ratio $T_{e0}/T_{i0} = \nabla T_{e0}/\nabla T_{i0} \simeq 3.75$ the total heat flux, roughly $q_h \simeq \langle\chi_i\rangle_t N|\nabla T_{i0}| + \langle\chi_e\rangle_t N|\nabla T_{e0}|$, is essentially dominated by the electron contribution. This observation will be confirmed in results shown in figure 5.7.

In simulations carried out with either the arbitrary solver or the Padé solver, both the time-dependent and time-averaged radial profiles of electron heat diffusivity, respectively plotted in figures 5.2(c) and 5.3(b), show the systematic presence of fine radial structures near low order MRSs which are due to the non-adiabatic response of passing electrons [Waltz et al., 2006, Chowdhury et al., 2008, Dominski et al., 2015]. These corrugations are clearly more pronounced at the surfaces of safety factor $q_s = 3/2$, 2,

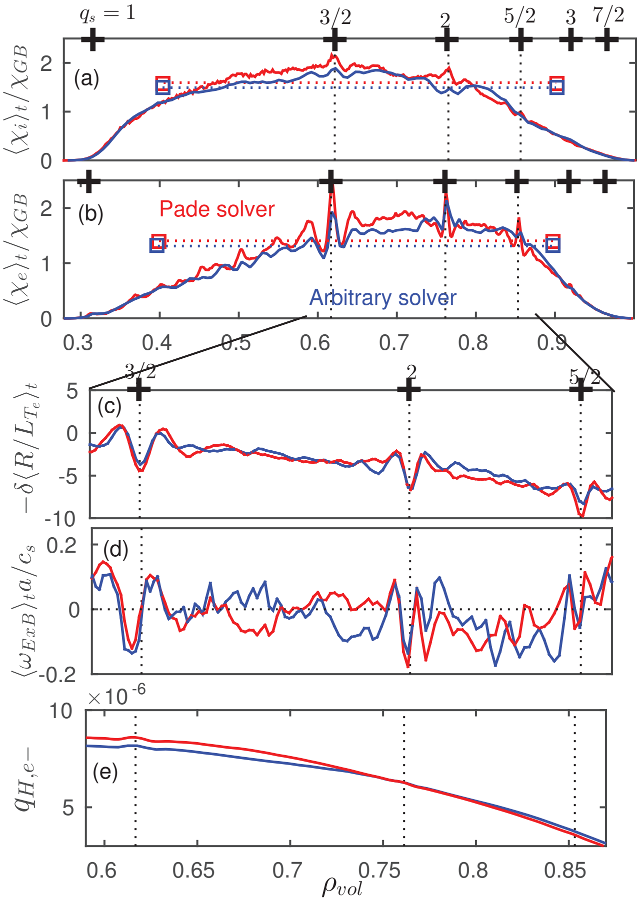

Figure 5.3 – Time-averaged radial profile of the heat diffusivity of (a) the ions and (b) the electrons, for the simulation of figure 5.2. Time-averaged radial profiles of (c) the electron temperature gradient perturbation, (d) the $E \times B$ shearing rate, and the electron turbulent heat flux. Padé solver (red) and arbitrary wavelength solver (blue) test cases. Time averaged quantities, $\langle \cdot \rangle_t$, are obtained over the turbulent saturated regime for $tc_s/a > 75$. Position of the lowest order mode rational surfaces are pointed out with black crosses and safety factor value given on top of subplots (a) and (c).

5/2 compared to other rational surfaces, because these rational surfaces are of lowest order in the case of a half-torus simulation. The electron heat flux, $q_{h,e}$, being smooth in the radial direction, see figure 5.2(b), the presence on $\chi_e \propto q_{h,e}/|\nabla_\psi T_e|$, where $|\nabla_\psi T_e| = \langle (dT_e/d\psi)\,|\nabla\psi|^2\rangle_{FS}$, of these fine radial structures near MRSs is the result of the presence of similar fine structures on the perturbation of the temperature gradient

$$\delta R/L_{T_e} = \left\langle \frac{R}{T_e}\frac{d\delta T_e}{d\psi}|\nabla\psi|^2 \right\rangle_{FS},$$

with δT_e the electron temperature perturbation and $T_e = T_{e0} + \delta T_e$. In figure 5.3(d), the $E \times B$ shearing rate associated to the ZFs, defined by (see references [Hahm, 1994, Villard et al., 2002])

$$\omega_{E\times B} = \frac{s}{2\psi_e q}\frac{d}{ds}\left(\frac{1}{s}\frac{d\langle\delta\phi\rangle_{FS}}{ds}\right), \tag{5.1}$$

is zero at lowest order MRSs where the electron temperature gradient perturbation has a local minimum and the electron diffusivity has a local maximum in agreement with reference [Dominski et al., 2015] which results are presented in chapter 3. We have checked, by varying the value of the Krook parameter, that the observed corrugations are not due to an artifact of the associated heating source.

The time-dependent radial profile of the $E \times B$ shearing rate associated to the ZFs is plotted in figure 5.4. This field is computed from the finite-element representation of $\delta\phi$ and thus provide an insight into the numerical resolution which is achieved by the field solver. The $E \times B$ shearing rate associated to the ZFs being essentially a second order radial derivative of the electrostatic field, the short scale noise is much more visible than on the potential $\delta\phi$. Notice that the low level of noise reached in these simulations is a result of the use of a high number of particles ($n_{p,tot} = 10^9$) and of a high number of gyropoints (18 for thermal ion Larmor radius) for computing the RHS of the QNE (gyrodensity).

Figure 5.5 shows the time-dependent radially-averaged amplitude of the $E \times B$ shearing rate associated to ZFs $\langle|\omega_{E\times B}|\rangle_s(t)$ in subplot (a), and the time-window averaged $E \times B$ shearing rate, $\omega_{eff}(t_w) = \langle|\langle\omega_{E\times B}\rangle_{t_\mathrm{w}}|\rangle_{st}$, in subplot (b), which is given by

$$\omega_{eff}(t_w) = \int_{s_\mathrm{min}}^{s_\mathrm{max}} \frac{ds}{s_\mathrm{min} - s_\mathrm{max}} \int_{t_1}^{t_\mathrm{end}} \frac{dt}{t_\mathrm{end} - t_1} \left| \int_t^{t+t_w} \frac{dt'}{t_\mathrm{w}} \omega_{E\times B}(s,t') \right|, \tag{5.2}$$

with $t_1 = 75a/c_s$ identified in our case as the start of the fully saturated turbulent regime, see reference [Dominski et al., 2015] for more details. It is clearly shown in subplot (b) of figure 5.5 that the Padé solver and the arbitrary wavelength solver have the same ω_eff at all t_w and thus the same temporal spectra for $\omega_{E\times B}$.

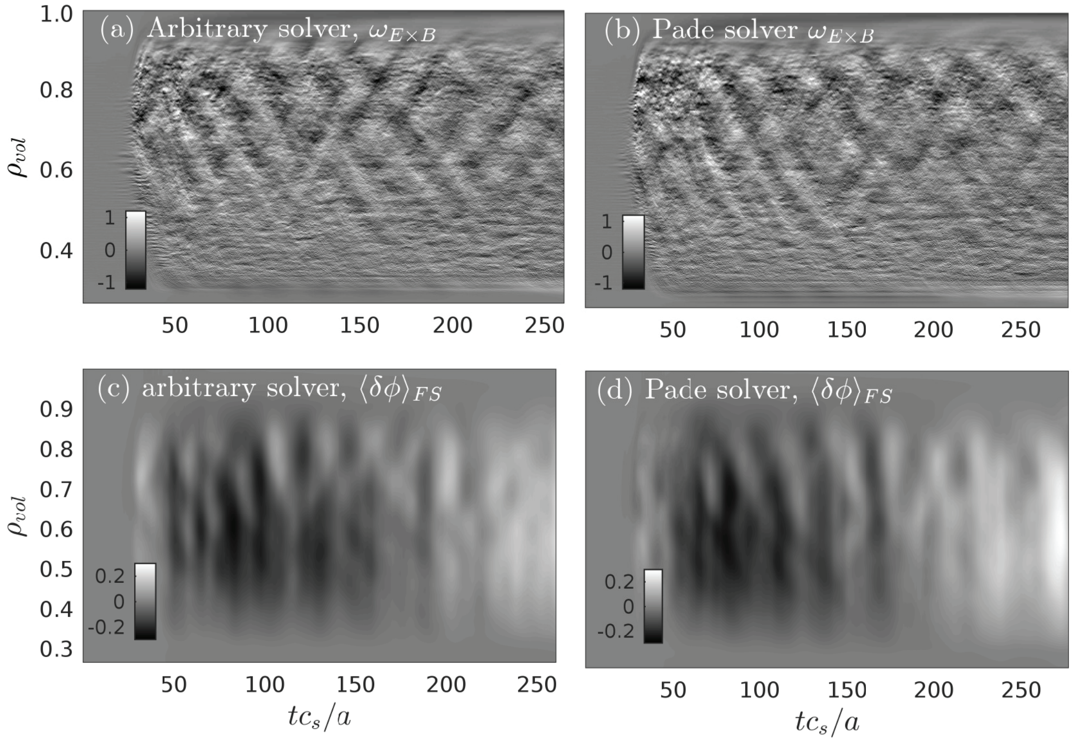

Figure 5.4 – $E \times B$ shearing rate associated to the ZFs as a function of time and radial position: (a) arbitrary solver, (b) Padé solver. $\langle\delta\phi\rangle_{FS}$ as a function of time and radial position: (c) arbitrary solver, (d) Padé solver. For the parameters of figure 5.3.

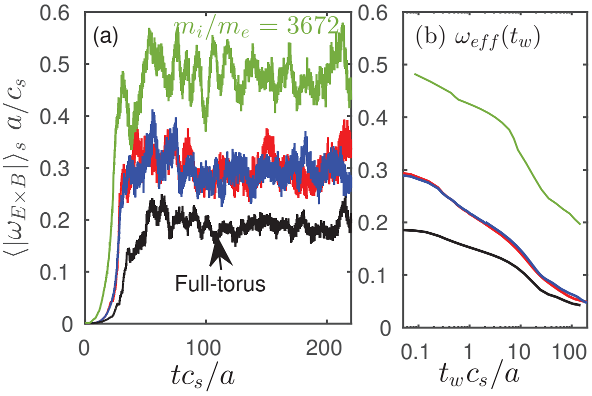

Figure 5.5 – Radially averaged (a) $E \times B$ shearing rate associated to the ZFs versus time and (b) time-windowed averaged $E \times B$ shearing rate versus size of the window t_w, $\omega_{eff}(t_w) = \langle|\langle\omega_{E\times B}\rangle_{t_\mathrm{w}}|\rangle_{st}$, see Eq. (5.2). In subplot (a), the time traces are computed with a time window averaging essentially equal to the sampling period, *i.e.* $t_w \lesssim 0.1a/c_s$. Color code: blue for the half-torus case with arbitrary wavelength solver and heavy electrons, red for the half-torus case with Padé solver and heavy electrons, black for the full-torus with arbitrary wavelength solver and heavy electrons, green for the half-torus with arbitrary wavelength solver and physical electron mass ($m_i/m_e = 3672$).

5.4 Full-torus versus half-torus simulations

Figure 5.6 compares results of the previous half-torus simulation with a full-torus simulation, both carried out with heavy electrons($m_i/m_e = 400$). This figure shows the time-averaged radial profiles of the ion heat diffusivity $\chi_i(\rho_{vol})$, the electron heat diffusivity $\chi_e(\rho_{vol})$, the electron temperature logarithmic gradient perturbation $\langle\delta\, R/L_{T_e}\rangle_t(\rho_{vol})$, and the $E \times B$ shearing rate associated to the ZFs $\omega_{E\times B}(\rho_{vol})$. The major difference between these radial profiles obtained in the half-torus and full-torus cases is the presence, in the half-torus test case, of fine structures of big amplitude near non-integer rational surfaces, see figure 5.6 near $q_s = 3/2$ for example. In a full-torus simulation, all the required toroidal mode numbers n are accounted for, and solely the magnetic surfaces of integer safety factor, $q_s = m/1$ with m an integer, are of lowest order. As a consequence, the magnetic surfaces of rational safety factor $q_s = p + 1/2$ with p an integer are, in reality, not of lowest order. Only the mode of toroidal numbers $n = 2p'$ (half of the spectrum) can be exactly field aligned at these surfaces where $q_s = p + 1/2 = m'/2p'$ with p' and m' integers and m' is obviously an odd number. By carrying out a half-torus simulation, one artificially increases the fraction of simulated modes to which the passing electron respond non-adiabatically. For example, in figure 5.6 (b), the fine structures at the magnetic surfaces of safety factor $q_s = 3/2$ and $5/2$ have very significantly reduced in the full-torus simulation results. This is also clearly visible on the electron temperature gradient perturbation, see subplot (c). We conclude that, in order to properly simulate the physics of kinetic electrons near MRSs, realistic nonlinear simulations including the

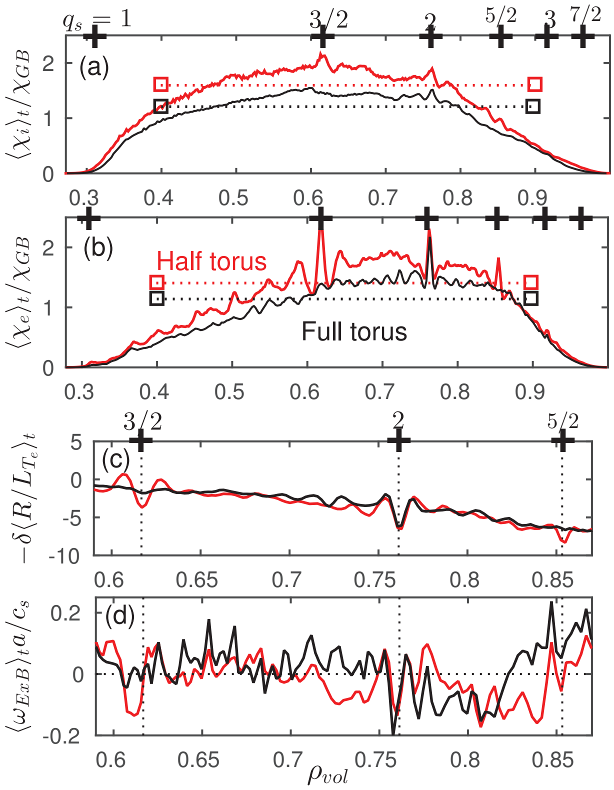

Figure 5.6 – Time-averaged radial profile of (a) the heat diffusivity of the ions, (b) the heat diffusivity of the electrons, (c) the electron temperature gradient perturbation, and (d) the $E \times B$ shearing rate associated to the ZFs. Half-torus (red) and full-torus (black) test cases with heavy electrons ($m_i/m_e = 400$).

physics of kinetic electrons must resolve the whole toroidal mode spectrum.

The radially averaged $E \times B$ shearing rate, $\langle|\omega_{E\times B}|\rangle_s$, is decreased by 34% in the full-torus case compared to the half-torus case, see figure 5.5(a). This decrease of the $E \times B$ shearing occurs over all time scales, see figure 5.5(b). We also observe a 24% and 19% relative decrease of, respectively, the ion and the electron heat diffusivity in the full-torus simulation compared to the half-torus case. Remark that not enough statistics is used for computing the time-averaged $E \times B$ shearing rate associated to the ZFs, so that its fine structures located near MRSs are almost drown in the fluctuations, see figure 5.6. In the flux tube simulation of reference [Dominski et al., 2015] these long time-averaged fine structures were of the same amplitude as the fluctuations, such that less statistics were necessary for showing their presence. We shall see in Sec. 5.5.6 that this low level of corrugations on the time-averaged $\omega_{E\times B}$ is essentially due to the choice of using heavy electrons for this test case. Indeed, in figure 5.5 one observes a strong increase of the time-averaged $E \times B$ shearing rate when using $m_i/m_e = 3672$ (green curve) instead of $m_i/m_e = 400$.

5.5 Half-torus simulation with the physical Deuterium to electron mass ratio

In this section, we present the results of a fully kinetic simulation carried out with the deuterium to electron mass ratio $m_i/m_e = 3672$. In this case, the annular width has been slightly reduced in order to decrease the numerical cost of the simulation. It is a half-torus simulation with $s \in [0.5, 1.0]$ and $n_s \times n_\theta \times n_\varphi = 360 \times 1024 \times 512$, $n \in [0, 2, 4, \cdots, 42, 44]$. The Krook parameter is set to $\gamma_k a/c_s = 0.027$ corresponding to 10% of the linear growth rate.

The results of this test case carried out with the physical mass ratio differ significantly from the previous simulation carried out with the heavy electrons. We thus re-run an heavy electron simulation using the same narrow torus configuration than the one used for the $m_i/m_e = 3672$ simulation, in order to better isolate the electron mass influence.

In figure 5.7, the simulation carried out with $m_i/m_e = 400$ clearly has higher transport levels in spite of lower gradient drives, compared to the simulation carried out with $m_i/m_e = 3672$. This increase of the transport is due to nonlinear effects as the linear growth rate are roughly 10% smaller for heavy electron simulations when using the initial density and temperature profiles. Note that, the linear growth-rates are not significantly different when using the time-averaged (over the turbulent saturated regime) relaxed profiles of density and species temperature taken from nonlinear simulations as backgrounds instead of the initial ones. Before discussing this reduction of the turbulence, the linear regime is studied in more details.

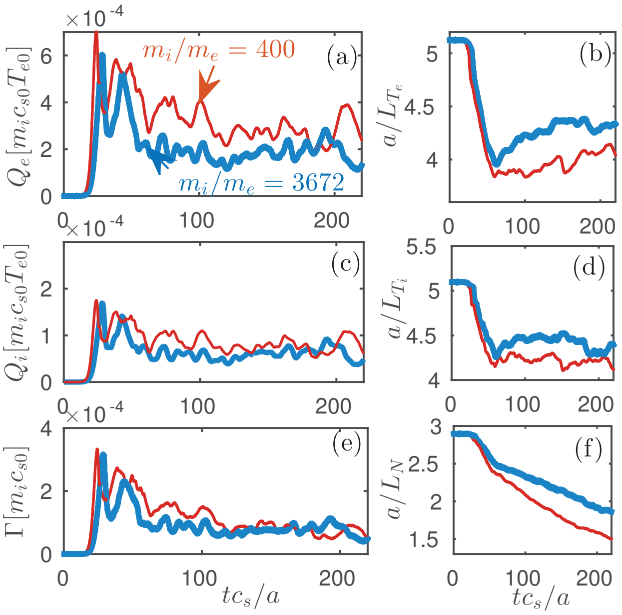

Figure 5.7 – Nonlinear simulation results of TCV carried out with heavy electrons (red) and physical D/e^- mass ratio (blue thick line). Radial transport of (a) electron heat, (c) ion heat, and (e) particles. Radially averaged inverse gradient lengths of (b) the electron temperature profile, (d) the ion temperature profile, and (f) the particle density. Results show a higher level of transport associated with a lower gradient when using the heavy electrons $m_i/m_e = 400$ instead of the D/e^- mass ratio $m_i/m_e = 3672$. The density profile continuously relaxes because no particle source is considered in these nonlinear simulations.

5.5.1 Linear destabilization

An alternative to estimating the growth rate γ of instabilities in a linear system by simply evaluating the exponential growth of the electrostatic field is provided by the following energy based relation (see references [Fivaz et al., 1998, Fivaz, 1997])

$$\gamma_{\mathcal{E}} = \frac{1}{2\mathcal{E}_{\text{field}}} \frac{d\mathcal{E}_{\text{field}}}{dt}, \tag{5.3}$$

with

$$\mathcal{E}_{\text{field}} := (q_i/2) \int d\mathbf{x} \delta N^{\text{pol}}(\mathbf{x}) \delta\phi(\mathbf{x}), \tag{5.4}$$

and

$$\frac{d\mathcal{E}_{\text{field}}}{dt} = -\sum_{\sigma} q_\sigma \int d\mathbf{X} d\mathbf{v}\, \delta f_\sigma\, \dot{\mathbf{X}} \cdot \langle \mathbf{E} \rangle_\alpha, \tag{5.5}$$

where the approximation $-\nabla \langle \phi \rangle_\alpha \simeq \langle \mathbf{E} \rangle_\alpha$ made in ORB5 has been employed. This relation allows us to separate the relative contributions to the instability mechanism from different particle species and particle subgroups (*i.e.* trapped versus passing particles). Furthermore, by decomposing $\dot{\mathbf{X}} = v_\parallel \mathbf{b} + \mathbf{v}_{\nabla B} + \mathbf{v}_{\text{curv}}$ into its different velocity terms, one can identify, thanks to equation (5.5), corresponding contributions to the instability drive.

In this TCV test case, the plasma is destabilized by a mixed ion temperature gradient (ITG) and trapped electron mode (TEM) regime. The instability is driven by the electrons at low n and by the ions at higher n, up to $n \simeq 32$ which corresponds roughly to $k_\theta \rho_i \simeq 0.6$ or $k_\theta \rho_s \simeq 1.2$. The species contributions to the destabilization are split into their different drift contributions in figure 5.8. In the electron case, the parallel damping is essentially due to the passing electrons and the grad-B and curvature drift destabilizing influence is essentially due to the trapped electrons. In the ion case, the passing and trapped particles are both contributing to the different drift terms in a more complex manner.

Numerical comment: In ORB5, the field is represented with finite elements, and the particles with markers by using the low noise delta-f PIC representation [Tran et al., 1999, Jolliet et al., 2007]. These simulations must be carried out with a high enough radial resolution and a high enough number of particles to properly simulate the particle-field interactions, due to the fact that fine radial structures are present on both the electrostatic field and on the perturbation density. To converge the numerical estimate of $\gamma_{\mathcal{E}}$, in simulations carried out with $m_i/m_e = 3672$, it appeared that it was necessary to use a higher radial resolution, when keeping a constant density of markers per radial interval, than in simulations carried out with $m_i/m_e = 400$, in order to converge $\gamma_{\mathcal{E}}$. Indeed in figure 5.9, the contributions to $\gamma_{\mathcal{E}}$ from the different groups of particles are plotted

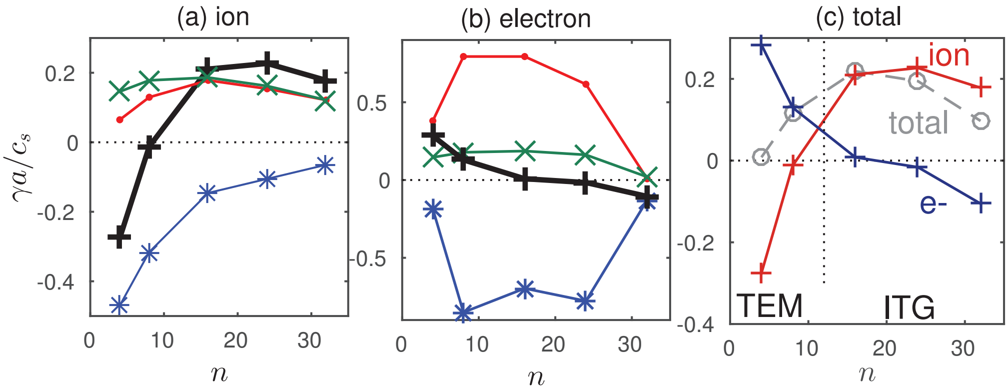

Figure 5.8 – Species contribution to the linear growth rate $\gamma_{\mathcal{E}}$ (black +), Eq. (5.3), is decomposed into the drift contributions $\gamma_{\|}$ (blue $*$), $\gamma_{\nabla B}$ (red $\bullet$), γ_{curv} (green $\times$). Subplot (c) recall the ion (red) and electron (blue) contributions to the growth rate as well as their sum (grey), to highlight the TEM and ITG dominated part of the spectra.

with respect to the radial position s. One can clearly appreciate that the destabilization drive is finely corrugated near MRSs illustrating that one needs a sufficiently high radial resolution for converging this local contribution to the instability dynamics.

5.5.2 Non-adiabatic electron responses

The non-adiabatic electron response turns out to be different for the subthermal ($E_{\text{kin}} = m_e v_\|^2/2 + \mu B_0 < T_e(\mathbf{X})$) and suprathermal ($E_{\text{kin}} < T_e(\mathbf{X})$) electrons. Characterizing these non-adiabatic responses permits to predict their respective contributions to the electron particle flux

$$\Gamma_e \simeq \int d\mathcal{S} \cdot \mathbf{v}_{E\times B}\, \delta N_e. \tag{5.6}$$

As we will see, the subthermal and suprathermal electrons contribute to the flux in opposite direction because their non-adiabatic density perturbations, respectively, $\delta N^{n.a.}_{e,E>T_e}$ and $\delta N^{n.a.}_{e,E<T_e}$, are essentially of opposite signs, at each position.

In figure 5.10 subplots (a-d), the electron density perturbation is split into the four following subgroups: subthermal passing electrons, suprathermal passing electrons, subthermal trapped electrons , and suprathermal trapped electrons.

In this figure, the density perturbation contribution of passing electrons shown in subplot (a) for $E_{\text{kin}} < T$ and (b) for $E_{\text{kin}} > T$ are both composed of adiabatic and non-adiabatic components. The adiabatic component corresponds to the large structures comparable to the ones observed on $\delta\phi$ in subplot (f). The non-adiabatic passing-electron component is radially localized on the different MRSs of this $n = 16$ eigenmode. The MRSs can

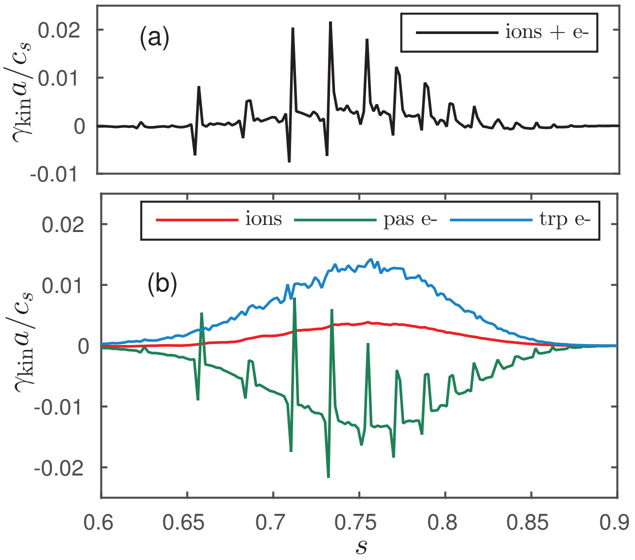

Figure 5.9 – Linear simulation, TCV test case, $n = 16$ mode, $m_i/m_e = 3672$. Radial contribution from the different species and subgroups to the growth rate $\gamma_{\mathcal{E}}$. Subplot (a) sum of all species contribution, subplot (b) the contribution of the ions, passing electrons, and trapped electrons are decomposed. Note that the effective mode growth-rate $\gamma_{\mathcal{E}}$ is obtained by integrating radially the curve of subplot (a).

be easily localized by identifying the layer of parallel current $\delta u_{\|,e}$ in subplot (e). It is noticeable that the poloidal shift of the non-adiabatic passing-electron contribution to δN_e with respect to the adiabatic contribution is counter-clockwise for $E_{\rm kin} < T_e(\mathbf{X})$, (a), and clockwise for $E_{\rm kin} > T_e(\mathbf{X})$, (b). In turn, the total passing electron density perturbation, which is the sum of these subthermal and suprathermal contributions, is almost vanishing at MRSs.

In comparison, the trapped electron population is also split into the same subthermal and suprathermal subgroups. It clearly appears in subplots (c) and (d) that the density perturbation related to these two subgroups of trapped electrons are out of phase by π, and presenting a de-phase of approx $\pm\pi/2$ with respect to $\delta\phi$. Moreover, the trapped electron subthermal group density perturbation is localized at a more inward radial position than the density perturbation of the suprathermal group kinetic response.

It is of interest to look at the cause for having different phase-shift signs, *i.e.*,

$$sign\left[arg\left(\frac{\delta N^{non-adiab.}_{e,E_{kin<T}}}{\delta\phi}\right)\right] = -sign\left[arg\left(\frac{\delta N^{non-adiab.}_{e,E_{kin>T}}}{\delta\phi}\right)\right],$$

for this particular case, because it predicts that the respective subthermal and suprathermal electron contributions to the particle flux will be in opposite directions, as we will

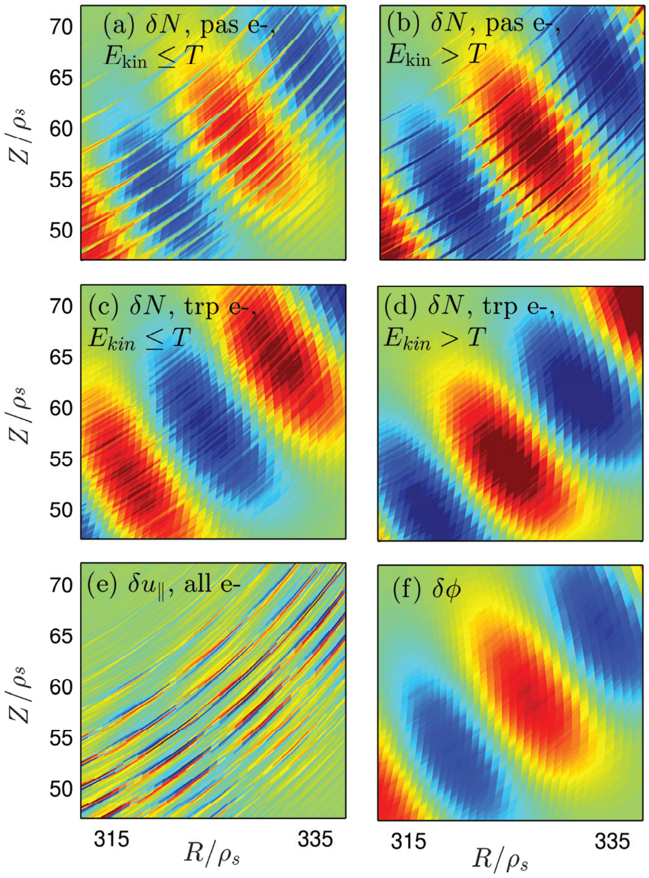

Figure 5.10 – Linear TCV simulation physical mass ratio $m_i/m_e = 3672$, and $n = 16$. Electron density perturbation split into four subgroups: (a) passing electrons with $E_{\text{kin}} < T_e$, (b) passing electrons with $E_{\text{kin}} > T_e$, (c) trapped electrons with $E_{\text{kin}} < T_e$, (d) trapped electrons with $E_{\text{kin}} > T_e$. Subplot (e) electron parallel current $\delta u_{\|}$. Subplot (f) $\delta\phi$. These results provide insight into the “smoothness” of each subgroup contributions to the charge assignment when computing the self consistent electrostatic field $\delta\phi$ (f).

confirm later in nonlinear simulations.

5.5.3 Local flux estimate

We are now interested to look at the rationale explaining why the subthermal and suprathermal electrons respond differently to the electrostatic perturbation. This study is conducted when considering the local estimate of the particle flux

$$\hat{\Gamma}^{\rm loc} \simeq \Re\left(\frac{\imath\, k_\theta}{B}\delta\hat{\phi}^*\delta\hat{N}\right) = -\frac{k_\theta|\delta\hat{\phi}|^2}{B}\,\Im\left(\frac{\delta\hat{N}}{\delta\hat{\phi}}\right), \tag{5.7}$$

where $\Re$ stands for the real part and $\Im$ for the imaginary part of complex number, and the Fourier representation of the fields, *i.e.*, $\delta\hat{N}$ and $\delta\hat{\phi}$, have been employed. Note that when $0 < arg(\delta\hat{N}/\delta\hat{\phi}) < \pi$ the radial flux is inward and when $-\pi < arg(\delta\hat{N}/\delta\hat{\phi}) < 0$ the radial flux is outward. The normalized density perturbation $\delta\hat{N}/\delta\hat{\phi}$ is computed with the local dispersion relation already introduced in subsection 3.3.3 and which equation (3.9) is recalled here

$$\begin{aligned} 0 \;&=\; \frac{ZT_{e0}}{T_{i0}} + 1 - \frac{ZT_{e0}}{T_{i0}}\int d^3v\, J_0^2(k_\perp\rho_i)\frac{\omega-\omega_i^\star}{\omega - k_\parallel v_\parallel - \omega_{Di}}\frac{f_{i0}}{N_{i0}} \\ &+\; \left(1-\frac{\omega_e^\star}{\omega}\right)\left[\alpha_t z_{be}^2 W(z_{be})\right] \\ &+\; \left(1-\frac{\omega_e^\star}{\omega}\right)\left[-1+\alpha_t + W(z_e) - \alpha_t W\left(\frac{z_e}{\alpha_t}\right)\right], \end{aligned} \tag{5.8}$$

in its form which includes fully kinetic species responses. In this equation α_t is the fraction of trapped electrons, $\omega_{Di} = -k_\perp(v_\parallel^2 + v_\perp^2/2)/\Omega_0 R$ is the drift frequency of ions related to curvature and gradient of the magnetic field, $z_{be} = \text{sgn}(\omega_{\varphi e})\sqrt{2\omega/\omega_{\varphi e}}$, $\omega_{\varphi e} \simeq \omega_{Ne}L_N/R$, $z_e = \omega/k_\parallel v_{the}$, and $W(z)$ is the dispersion function. The *non-adiabatic response of the passing electrons*, *i.e.* the term on the third line of equation. (5.8), was obtained from the non-adiabatic electron distribution response

$$\delta\hat{g}_e(\vec{v}, R/L_{T_e}) = -N_{e0}\frac{e\delta\hat{\phi}}{T_{e0}}\frac{\omega-\omega_e^\star}{\omega-k_\parallel v_\parallel}\frac{f_{e0}}{N_{e0}}, \tag{5.9}$$

where the explicit electron temperature gradient dependency is contained in the diamagnetic drift

$$\omega_e^\star = \omega_{Ne}[1+\eta_e(\tilde{E}-3/2)],$$

$\omega_{Ne} = T_{e0}k_\perp/eB_0L_N$, $\eta_e = L_N/L_{T_e}$, $\tilde{E} = mv^2/2T$, and $v = \sqrt{v_\perp^2 + v_\parallel^2}$. At MRSs, where $k_\parallel = 0$, we observe that this local non-adiabatic response does not depend on the pitch

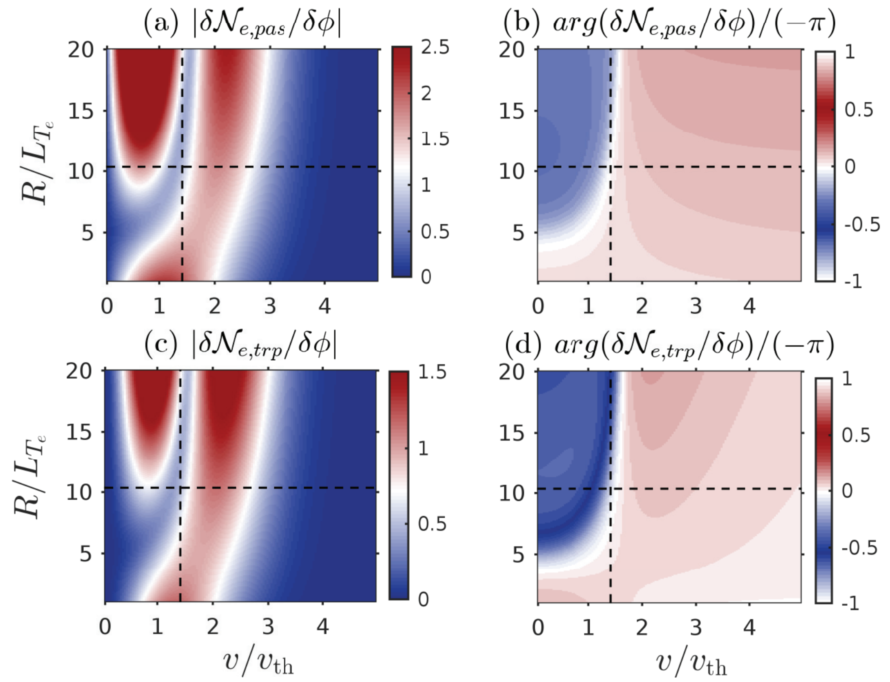

Figure 5.11 – Amplitude (a,c) and phase (b,d) of the non-adiabatic electron response of passing electrons $\delta N_{e,pas}/\delta\phi$ (a,b) and trapped electrons $\delta N_{e,trp}/\delta\phi$ (c,d). Results obtained with a local dispersion relation analysis at the radial position $q_s = 1.5$ where $k_\parallel Rq_s = 0$. The horizontal line indicates the value of the TCV electron temperature gradient taken at $q_s = 3/2$ from CHEASE input file. The vertical line indicates the position at which $v = \sqrt{2T/m}$ which is the boundary we have chosen for further dissociating the subthermal and suprathermal subgroups of electrons. Parameters: $R/L_N = 5.0$, $R/L_{T_e} = 11.7$, $R/L_{T_i} = 11.7$, $T_e/T_i = 3.75$, $m_i/m_e = 3672$, $r/R = 0.2$, $\hat{s} = 1.1$, $k_\parallel = 0$, $k_y\rho_i = 0.5$.

angle so that one defines the quantity

$$\frac{\delta\hat{\mathcal{N}}_{e,pas}(v,R/L_{T_e})}{\delta\hat{\phi}} = -(1-\alpha_t)\frac{e}{T_{e0}}4\pi v^2\frac{\omega-\omega_e^{\star}}{\omega}f_{e0}(v). \tag{5.10}$$

The *non-adiabatic response of the trapped electrons*, *i.e.* the second line of Eq. (3.9), was obtained from the non-adiabatic bounce-averaged trapped electron response which is here taken in its form independent of the pitch angle

$$\frac{\delta\hat{\mathcal{N}}_{e,trp}(v,R/L_{T_e})}{\delta\hat{\phi}} = -\alpha_t\frac{e}{T_{e0}}4\pi v^2\frac{\omega-\omega_e^{\star}}{\omega-n\langle\dot{\varphi}\rangle}f_{e0}(v), \tag{5.11}$$

see reference [Dominski et al., 2015] and references therein for details. From these velocity-dependent contributions to the electron density perturbation, one can recover the local electron density perturbation with the equation $\delta\hat{N}_e = (eN_{e0}\delta\hat{\phi}/T_{e0}) + \int dv\,\delta\hat{\mathcal{N}}_{e,trp} + \int dv\,\delta\hat{\mathcal{N}}_{e,pas}$.

For simplicity, we conduct the local study with this local dispersion relation at the outer mid-plane on the magnetic surface $q_s = 3/2$, for a resonant mode ($k_\parallel = 0$) such that both the trapped and passing electrons contribute to the turbulent flux. According to equation (5.7), a value of the velocity for which the imaginary part of $\delta\hat{\mathcal{N}}_e/\delta\hat{\phi}$ is non zero, *i.e.*, $arg(\delta\hat{\mathcal{N}}_e/\delta\hat{\phi}) \neq 0$ or π, will contribute to the radial transport. In figure 5.11, the velocity-dependent responses $\delta\hat{\mathcal{N}}_{e,trp}$ and $\delta\hat{\mathcal{N}}_{e,pas}$ are plotted with respect to the gradient R/L_{T_e}, for physical parameters taken at low order MRS $q_s = 3/2$. For each electron temperature gradient value, the complex frequency ω is first solved using equations (5.8) and then injected in equation (5.10) and (5.11) for obtaining the non-adiabatic responses of the passing and trapped electrons with respect to v. Represented are the absolute value $|\delta\hat{\mathcal{N}}_e/\delta\hat{\phi}|$ and the phase shift $arg(\delta\hat{\mathcal{N}}_e/\delta\hat{\phi}|)$ of these non-adiabatic responses. The choice for representing this non-adiabatic response with respect to v and R/L_{T_e} is made for showing that the non-adiabatic responses of subthermal and suprathermal electrons are differing for certain value of R/L_{T_e}. A transition occurs near the critical gradient $R/L_{T_e,c} \simeq 6$. For the temperature gradient of reference $R/L_{T_e} = 11.7$ (horizontal dotted line) which value is bigger than the critical one, there are two local maxima of $|\delta\hat{\mathcal{N}}_e/\delta\hat{\phi}|$: one located in the subthermal part and one in the suprathermal part of the direction v. Moreover, these two subgroups have phase shifts $arg(\delta\hat{\mathcal{N}}_e/\delta\hat{\phi})$ of opposite signs. From this observation these two subgroups might contribute to the flux in opposite directions thus potentially canceling each other. For values of the gradient smaller than $R/L_{T_e} \simeq 6$, the non-adiabatic electron response is essentially homogeneous in the v direction: there is only one maximum on $|\delta\hat{\mathcal{N}}_e/\delta\hat{\phi}|$ and the phase shift $arg(\delta\hat{\mathcal{N}}_e/\delta\hat{\phi})$ is nearly constant. The rationale for the presence of two energetic subgroups which contribute to the quasi-linear flux in opposite directions for big values of R/L_{T_e} is due to the physics described by the diamagnetic drift which is velocity- and gradient-dependent. Indeed, in our TCV test case, $R/L_{T_e} = 11.7$ and $\eta_e \simeq 2$ so that $\omega_e^{*} \simeq 2\omega_{Ne}(\tilde{E}-1)$ is of opposite sign for suprathermal and subthermal electrons.

5.5.4 Particle electron flux in the linear growing phase of the nonlinear simulation

For electrons, the turbulent particle flux, equation. (B.4) with $\mathcal{A}=1$, can be approximated by $\Gamma_e \simeq \langle \delta N_e \, (-\nabla\phi \times \mathbf{B}/B^2)\cdot\nabla s/|\nabla s|\rangle_{\mathcal{S}}$ with $\langle\cdot\rangle_{\mathcal{S}}$ the surface average, see equation (B.5), and using the approximations $B_\parallel^\star \simeq B$ and $\langle\phi\rangle_\alpha \simeq \phi$. The electron turbulent fluxes are then decomposed into their subthermal and suprathermal subgroup contributions.

The predictions made in the previous quasi-linear analysis, that subthermal and suprathermal subgroups of electrons contribute to the particle flux in opposite directions, are confirmed in global ORB5 nonlinear simulations when looking at the instantaneous turbulent flux, taken at $tc_s/a \simeq 17$, *i.e.* during the regime of "linear growth", see figure 5.12 (a). The subthermal particles have an inward flux and the suprathermal ones have an outward flux. This is true for both trapped and passing electrons. For passing electrons, these thermal subgroup contributions to the particle flux essentially cancel each other, so that the total passing electron particle flux is negligible. For trapped electrons, the particle flux is dominated by the suprathermal trapped electron contribution, which is outward.

These subgroup contributions to the particle flux are also split in their toroidal-spectral components, in figure 5.12 subplots (b-e). Each subplot is a mixed representation: direct in the radial direction and discrete Fourier in the toroidal direction. This spectral-radial representation, $\tilde{\Gamma}_e(s,n)$, is computed from equation

$$\Gamma_e(s) \;=\; \frac{1}{\mathcal{S}}\oint d\theta^\star d\varphi \mathcal{J}\,\delta N(s,\theta^\star,\varphi)\frac{-\nabla\delta\phi(s,\theta^\star,\varphi)\times\mathbf{B}}{B^2}\cdot\nabla s \;=\; \underbrace{\sum_n \tilde{\Gamma}_e(s,n)}_{Parseval},$$

with

$$\tilde{\Gamma}_e(s,n) = \frac{1}{\mathcal{S}}\oint d\theta^\star \mathcal{J}\,\delta\hat{N}^*(s,\theta^\star,n)\frac{-\nabla\delta\hat{\phi}(s,\theta^\star,n)\times\mathbf{B}}{B^2}\cdot\nabla s,$$

where Parseval theorem has been employed to replace the integral over the toroidal direction with the sum over the toroidal mode number n. Note that $\tilde{\Gamma}_e(s,n)$ is a discrete spectral representation computed over the regular toroidal grid[1].

---

[1] Going from the DFT of the finite-element coefficients, $\delta\hat{\phi}_n(s,\theta^\star)$, toward the DFT of the field represented on a grid, $\delta\hat{\phi}(s,\theta^\star,n)$, is trivially carried out by doing

$$\delta\hat{\phi}(s,\theta^\star,n) = \hat{\Lambda}_n^*(\varphi=0)\,\delta\hat{\phi}_n(s,\theta^\star),$$

which is valid because the toroidal grid is regular and the finite-element are translational invariant.

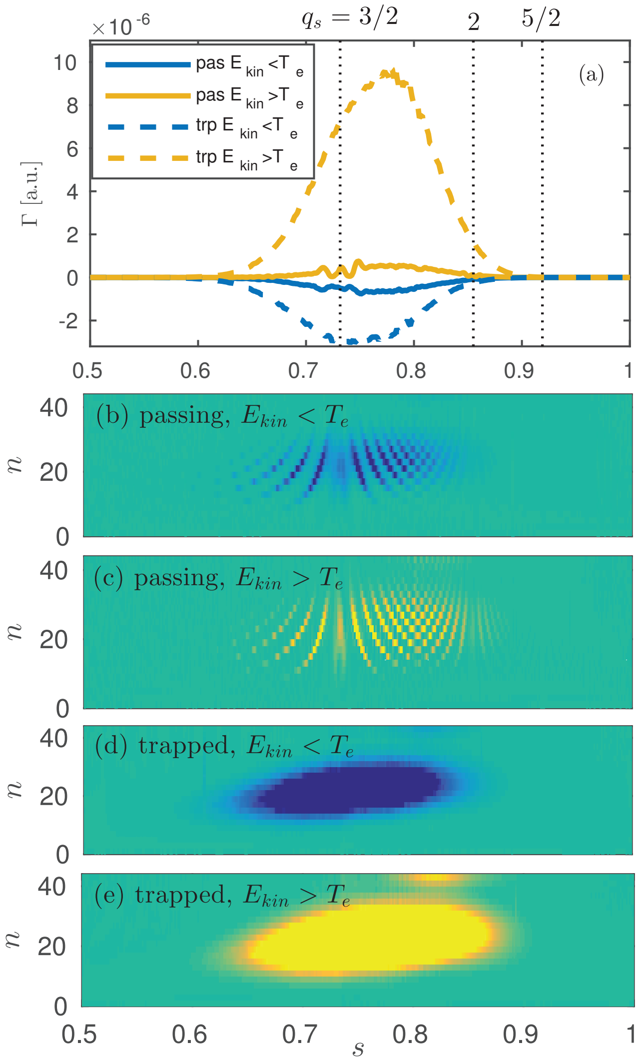

Figure 5.12 – Turbulent particle transport during the linear regime, $tc_s/a \simeq 17$, of the nonlinear simulation of TCV carried out with the D/e^- mass ratio. Subplot (a) is the time-averaged turbulent particle flux contributions from the different subgroup of electrons: passing with $E_{\text{kin}} \leq T_e$, passing with $E_{\text{kin}} > T_e$, trapped with $E_{\text{kin}} \leq T_e$, and trapped with $E_{\text{kin}} > T_e$. The time-averaged toroidal spectra are plotted at each radial position for these same subgroups in subplot (b), (c), (d), and (e), respectively. Color code: blue for inward flux, yellow for outward flux, and green for zero flux. The amplitude (colorbar) has been chosen such as to reveal the radial structures.

It is remarkable that the passing electron contribution to the particle flux is solely localized near the MRSs of each toroidal mode number n. This obviously results from the fact that only the non-adiabatic response can contribute to the fluxes, which for a given toroidal mode number n is non-zero only in the vicinity of corresponding MRSs. As a result, for bigger n there are more surfaces for which the passing electrons contribute to the turbulent transport. This flux of passing electrons is thus organized in a structured manner strongly linked to the safety factor profile q_s. Note that the radial width of the fine structures near MRSs are thinner in the case of suprathermal particles because these fast particles are more akin to respond adiabatically.

An important remark is that the passing electron flux is sustained by radially localized contributions coming from the different mode numbers n, but that the sum of these "discrete" contributions has a remarkably smooth radial profile, see figure 5.12 subplot (a). This smoothness of the overall passing electron profile of turbulent flux indicates the existence of a strong interplay between the different toroidal modes composing the spectra. This interplay reflects the fact that this early phase of the simulation which we refer to as the regime of linear growth of the modes is actually not strictly a linear regime. It could be interesting to compare the evolution of each mode during this early phase of the simulation, with their respective evolution computed from purely linear simulations. The trapped electron contribution to the turbulent flux is not showing such a clear organization near the lowest order MRSs.

5.5.5 Particle and heat electron fluxes in the turbulent saturated regime

The particle flux spectra in the turbulent saturated regime (figure 5.13) are following the same organization as in the linear regime (figure 5.12). The subthermal electrons carry an inward flux and the suprathermal electrons carry an outward flux. The subthermal and suprathermal passing electron contributions to the particle flux further cancel each other, and the trapped suprathermal electron contribution dominates the particle transport with a resulting outward flux. The radial spectra show that the passing electron channel of transport has the same organization: both thermal subgroups of passing electrons have a radially smooth profile of turbulent transport $\Gamma_e(s)$, but at each radial position s only the locally resonant toroidal mode numbers n contribute to this transport. For example, in this half torus simulation all the toroidal modes n can carry a turbulent flux at the lowest order MRSs $q_s = 3/2$, 2, 5/2, 3, and 7/2, the contributions from each mode are consequently relatively low, but at the second order MRSs, for example $q_s = 3/4$, only half of the spectra can carry a turbulent transport, so that the contributions from the modes which are resonant at this point is relatively large.

The influence on turbulence of the value of the electron mass is studied in some details, by comparing results of a simulation carried out with the deuterium/electron mass ratio ($m_i/m_e = 3672$) with the ones of a simulation carried out with the heavy electron mass ratio ($m_i/m_e = 400$). In figure 5.14, it is shown that when increasing the electron mass, the electron subgroup contributions to the particle flux are significantly increased: subthermal passing electron +300%, suprathermal passing electron +350%, subthermal trapped electron +190%, and suprathermal trapped electron +25% (at $s \simeq 0.84$). This increase of the transport seems to be due to an increase of the non-adiabatic response of the electrons. For the passing electrons, the increase of the non-adiabatic response due to the use of heavy electron mass is clearly visible through the enlargement of the fine structures near MRSs, in subplots (b) and (c) of figure 5.14. For the trapped electrons, there is no similar direct observation of the electron mass influence. Nonetheless, in their rapid motion along the field line, these trapped electrons are essentially similar to the passing electrons. They might thus be influenced by MRSs, but in a weaker manner. Indeed, in nonlinear GENE flux tube simulations of chapter 3, there were fine structures near MRSs even when using the hybrid electron model. The main difference is that for the hybrid electron model, these fine structures are of very little amplitude.

Coming back to the *passing electron* channel of turbulent transport, heavy electrons being $\simeq 9$ times heavier than real ones, their thermal speed is $\simeq 3$ times slower and the radial width of the fine structures of non-adiabatic passing electron response are $\simeq 3$ times larger. As a consequence, one can roughly estimate that a given toroidal mode number n will be "turbulence conducting" over a radial region roughly $\simeq 3$ times larger when using the heavy electrons. This local influence of the mass ratio over the radial profile of passing electron turbulence transport is illustrated in figure 5.14 subplot (b) and (c), where the radial profile of turbulent particle flux is plotted for each mode n composing the

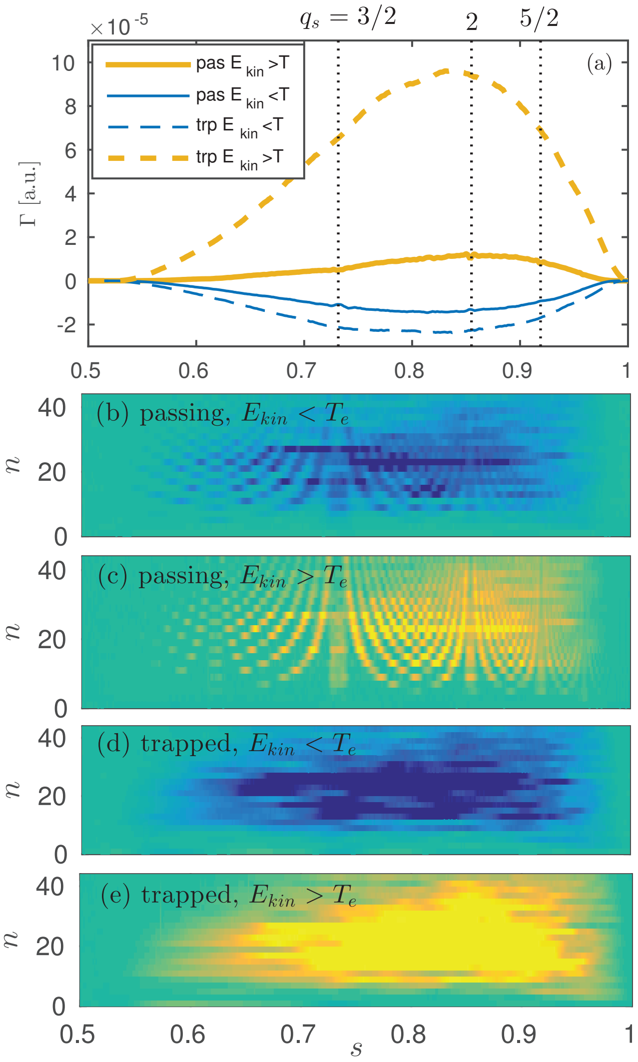

Figure 5.13 – Turbulent particle transport time-averaged over the turbulent saturated regime, $0 < tc_s/a > 220$ from the same simulation as in figure 5.12 and same subplots and color codes: *Subplot (a) is the time-averaged turbulent particle flux contributions from the different subgroups of electrons: passing with* $E_{\text{kin}} \leq T_e$*, passing with* $E_{\text{kin}} > T_e$*, trapped with* $E_{\text{kin}} \leq T_e$*, and trapped with* $E_{\text{kin}} > T_e$*. The time-averaged toroidal spectra are plotted at each radial position for these same subgroups in subplot (b), (c), (d), and (e), respectively. Color code: blue for inward flux, yellow for outward flux, and green for zero flux. The amplitude (colorbar) has been chosen such as to reveal the radial structures.*

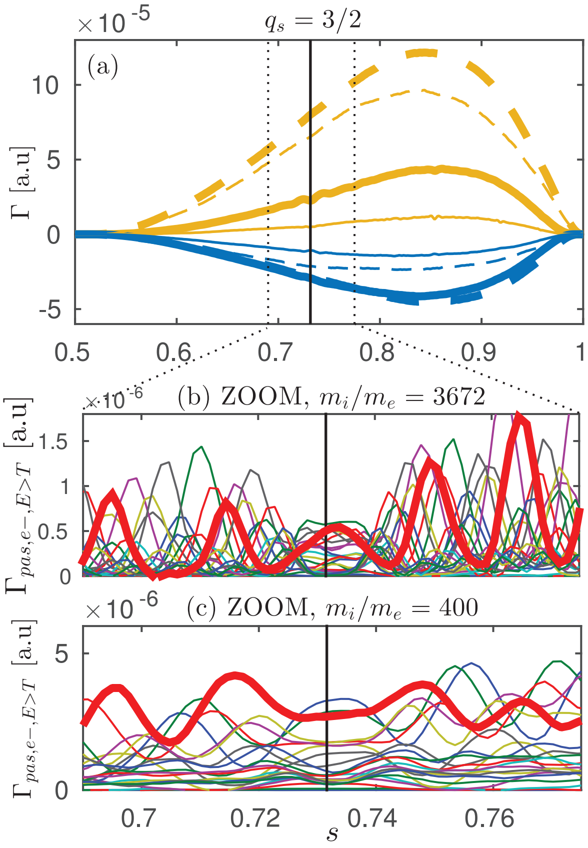

Figure 5.14 – Comparison of the turbulent electron particle flux between nonlinear simulations carried out with heavy electrons $m_i/m_e = 400$ (thick line in subplot (a)) and the Deuterium/electron mass ratio $m_i/m_e = 3672$ (thin lines in subplot (a)). Same color code in subplot (a) than in subplot (a) of figure 5.12. The radial profile of each toroidal mode number n contribution to the suprathermal passing electron, *i.e.* $\tilde{\Gamma}_{pas,e-,E>T}(s,n)$ is plotted in subplot (b) for the D/e- physical mass ratio and in subplot (c) for the heavy electron mass ratio. In subplot (b) and (c) the colors are not labeled, except for the toroidal mode number $n = 12$ which contribution is represented with a red thick line.

simulation spectra. It appears, in particular for the mode number $n = 12$ highlighted with red thick lines, that the turbulent flux contribution of each mode number n composing the turbulence spectra are localized near the lowest order MRSs proper to each mode number. A significant difference when using the heavy electrons is that the radial width of these “fine” structures of non-adiabatic passing electron response are larger than the distance between their respective lowest order MRSs. In comparison, for the real electron mass, the fine structures present on the simulated modes ($n \leq 44$) are always thinner than the distance between consecutive MRSs (except for biggest values of n in the region of high shear). When summing these mode number contributions to the passing-electron turbulent flux, the resulting particle flux is radially smooth (a) despite the fact that the density of modes to which the passing electrons respond non-adiabatically is varying radially. Finally, one can assume that the local turbulence diffusivity D_{turb} is proportional to the density of resonant mode number n which can carry turbulence. As a consequence this turbulence diffusivity is radially more corrugated in case of D/e- mass ratio because in this case the non-adiabatic structures are thinner and thus radially more sparse, see figure 5.15 (a). If the flux, Γ, is radially smooth but the turbulence diffusivity, D_{turb}, is radially corrugated, then the radial profile of gradient, $d \ln N/ds$, compensates these corrugations so that $\Gamma = D_{\text{turb}}(-d \ln N/ds)$ is smooth. A direct observation of such a property of the gradients can be made when looking at the density and temperature gradients in figure 5.15 subplots (c) and (d).

For the considered physical scenario, the total passing electron contribution to the turbulent **particle** flux is essentially negligible, see figure 5.16 (a). The subthermal and suprathermal passing-electron contributions to the particle flux cancel each other. The turbulent flux is thus dominated by the trapped electron contribution. This trapped electron contribution is weakly affected by the mass ratio, as the increase of the subthermal and suprathermal trapped electron contributions essentially cancel each other.

The passing electron **heat** flux, on the other hand, is non negligible. The suprathermal passing electron flux being systematically outward and the subthermal one being systematically inward, their sum will result in an outward heat flux. The passing electrons contribute to $\simeq 11\%$ (resp. 27%) of the total electron turbulence heat flux for $m_i/m_e = 3672$ (resp. 400), see figure 5.16 (b). In absolute value the passing electron heat flux is $\simeq 3$ times bigger with the heavy electrons than with physical electrons, and the trapped electron contribution is only $\simeq 10\%$ bigger. The passing electrons thus contribute significantly to the overestimate of the turbulence heat flux measured in simulation carried out with heavy electrons. This increase of the turbulence transport in spite of equivalent linear drive ($\lesssim 10\%$ lower linear growth rates in case of heavy electrons) is obviously due to a nonlinear effect. Regarding the radial spectra in subplot (c) and (d), it appears than there is a strong interplay between the modes for ensuring continuity of the passing-electron heat flux. With physical electrons ($m_i/m_e = 3672$), the fine structures are much finer and the interplay between the n modes involve a broader band of modes compared to the spectra obtained with heavy electrons. The fact that the spectrum is

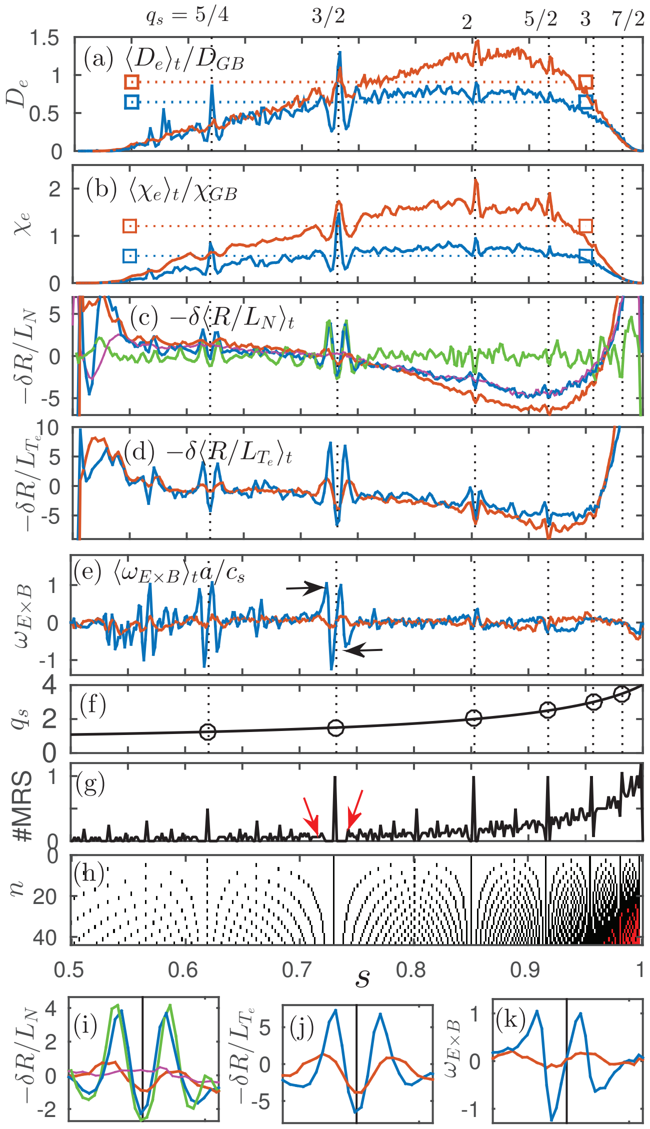

Figure 5.15 – Nonlinear simulation of half-torus with physical D/e$^-$ mass ratio (blue) and heavy electrons (red). Subplots time-averaged of the (a) electron particle diffusivity, (b) electron heat diffusivity, (c) perturbed particle density gradient (green: contribution of the ion polarization and magenta: contribution from the ion gyrodensity for simulation with $m_i/m_e = 3672$), (d) perturbed electron temperature gradient, (e) $E \times B$ shearing rate associated to the ZFs. Subplot (f) safety factor. Subplot (g) the number of MRSs per radial interval $[s, s + \Delta s]$ divided by the number of simulated toroidal mode numbers. In subplot (h), plotted is the contribution from each simulated mode number n decomposition to the subplot (g), color code: white 0, black for 1, and red for 2 and more. Half torus simulations. Subplots (i), (j), and (k) are zooms on the $q_s = 3/2$ surface of the subplots (c), (d), and (e), respectively.

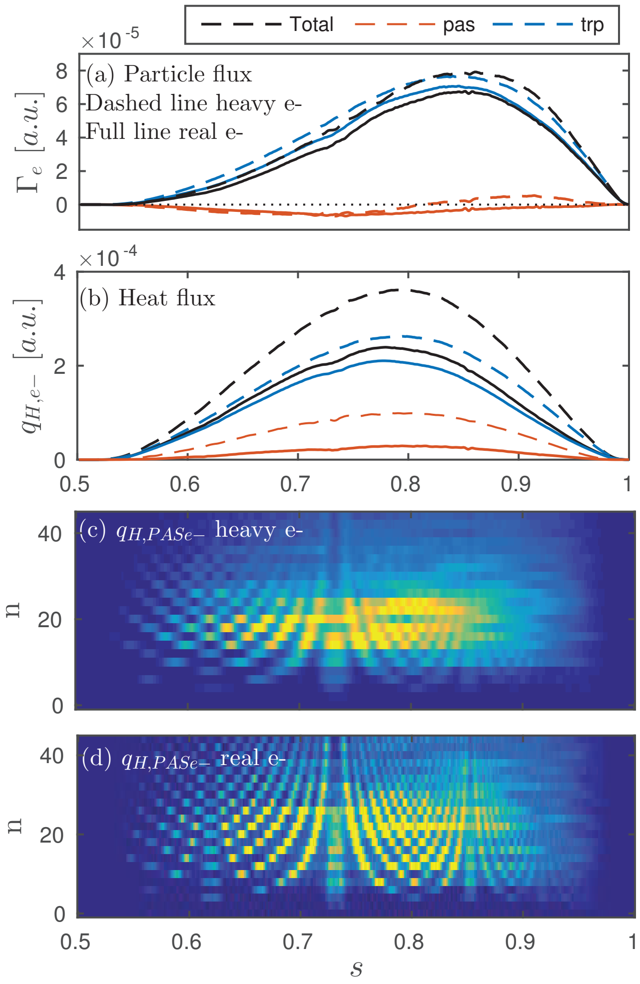

Figure 5.16 – Turbulent electron fluxes in simulations carried out with heavy electrons $m_i/m_e = 400$ and physical electrons $m_i/m_e = 3672$. Subplot (a,b): radial profile of turbulent electron flux of (a) particles and (b) heat. Color code: total fluxes (black), trapped electrons (blue), passing electrons (red). Mass ratio $m_i/m_e = 3672$ (full line) and $m_i/m_e = 400$ (dashed line). Subplot (c,d): radial spectra of the passing electron contribution to the heat flux for (c) $m_i/m_e = 400$ and (d) $m_i/m_e = 3672$.

broader for $m_i/m_e = 3672$ means that the weakly unstable modes contribute to the flux at a similar level than the most unstable modes. It might thus explain why the level of transport is thus smaller when $m_i/m_e = 3672$. As observed for the particle flux, a steepening of the gradients appears to be necessary for ensuring continuity of the flow in radial regions where only a few weakly unstable modes can carry transport.

5.5.6 Organization of zonal flows

It has been observed that particle and heat flux spectra of the passing electrons are not radially homogenous. This radial variation of the turbulent flux spectra reflects the radial variation of the associated turbulence diffusivity. Consequently, radial corrugations of the density and species temperature gradients are thus necessary for ensuring smooth radial profiles of turbulent fluxes.

In figure 5.15, the time-averaged radial profiles of the electron particle diffusivity (a), the electron heat diffusivity (b), the density gradient perturbation (c), the electron temperature gradient perturbation (d), the $E \times B$ shearing rate associated to the ZFs (e), the safety factor (f), the MRSs density (g), and the MRSs density per mode number (h) are plotted. Two simulations with physical electron mass (blue curves) and heavy electron mass (red curves) are presented.

It is remarkable in subplots (c,d,e) of this figure, that the time-averaged radial profiles of the electron temperature gradient perturbation, $\langle \delta R/L_{T_e} \rangle_t$, density gradient perturbation, $\langle \delta R/L_N \rangle_t$, and $E \times B$ zonal flow (ZF) shearing rate, $\langle \omega_{E\times B} \rangle_t$, show the same organization near lowest order MRSs, $q_s = 5/4$, $3/2$, and 2, as already shown in flux-tube geometry [Dominski et al., 2012, Dominski et al., 2015]: a steepening-flattening-steepening of the gradients and the $E \times B$ shearing rate which is zero at MRS and extremum just before and after. See the zooms in subplots (i), (j), and (k). The presence of these fine structures highlights the importance of using the new arbitrary wavelength solver. For example, the fine structure on the radial profile of the ion polarization density $\delta R/L_{N,pol}$ (green curve), which is located near the $q_s = 3/2$ surface is of about $\simeq 2\rho_i$. This estimate is made by measuring the distance between the local maxima which are located just before and after the $q_s = 3/2$ surface.

When analyzing the passing electron turbulent particle flux, in the previous section, we did not use the ZF saturation mechanism argument for explaining the reduction of turbulent transport. We rather showed that this reduction of passing electron turbulent transport is related to a rarefaction of the radial region of non-adiabatic passing electron response, *i.e.*, the regions where the different spectral modes can sustain a turbulent transport. It turns out that fine zonal flow structures are present near low order MRSs. The reduction of passing electron turbulence diffusivity causes a local steepening of the plasma kinetic profiles on either side of the low order MRSs, which can be sustained thanks to a reinforced ZF shearing rate there. This can be seen as a nonlinear feedback potentially reducing the turbulence transport. In an opposite manner, at the low order MRSs, heat diffusivity is enhanced, which causes a flattening of the profiles, noting that the ZF shearing rate is vanishing there, see figure 5.15(k).

Comparing the simulation results obtained with the two different mass ratios, it appears that these ZFs and gradient structures located near low order MRSs have a $\simeq 3$ times bigger amplitude when using the real electron mass, see figure 5.15 (c,d,e) in particular near $q_s = 3/2$ and $5/4$. In this simulation carried out with the real electron mass compared to the one carried out with heavy electrons, the time- and radial-averaged $E \times B$ zonal flow amplitude $\langle\langle|\omega_{E\times B}|\rangle_s\rangle_t$ is increased by $\simeq 25\%$, and the radial averaged amplitude of the long-time-averaged $E \times B$ zonal flow $\langle|\langle\omega_{E\times B}\rangle_t|\rangle_s$ is increased by a factor $\gtrsim 2$.

Despite the fact that these fine ZFs structures have a different amplitude when modifying the electron mass, their radial width remains essentially the same, see the black arrows in figure 5.15 subplot (e). Moreover, in the region of low shear, these ZFs radial widths are typically larger in nonlinear simulations than in linear simulations, as already observed in reference [Dominski et al., 2015]. It is rather interesting to point out that these fine structure widths seem to be related to the topology of the magnetic field and in particular to the local density of MRSs. It appears that these ZFs structures fit in a radial gap surrounding the low order MRS where no other MRS is simulated. The gap associated with the MRS $q_s = 3/2$ is identified with red arrows in subplot (g). A similar observation can be made for surfaces $q_s = 5/4,\ 2,\ 5/2$, in simulations carried out with either the physical mass ratio or heavy electrons. This gap between MRSs is also clearly illustrated in subplot (h) for each toroidal mode number n. When such a gap exists, the destabilizing influence of the low order MRS on the passing electron dynamics seems more significant.

5.6 Conclusion

Nonlinear electrostatic simulations for conditions relevant to TCV have been carried out with the heavy electrons, $m_i/m_e = 400$, the new solver, and the kinetic model for both ions and electrons. It was shown that using the Padé solver is essentially equivalent to using the arbitrary wavelength solver for the considered test case, and that to correctly simulate the physics of passing electrons near mode-rational surfaces, one must account for the whole set of mode numbers composing the toroidal spectra. The rationale is that the density of mode rational surfaces is different in a full torus than in a half torus. As a consequence, in a half torus simulation, the non-adiabatic passing electron response is not properly modeled, in particular for comparison with experiments.

Physical deuterium to electron mass ratio ($m_i/m_e = 3672$) simulations of this TCV relevant test case have been carried out with the fully kinetic model and the arbitrary wavelength solver. The particular radial organization of the passing electron turbulent flux spectrum and its strong ties with the radial profile of safety factor are revealed. Each toroidal mode number n contributes to the passing electron turbulent flux only near its associated lowest order MRSs, *i.e.* where the passing electron respond non-adiabatically. The whole turbulent flux spectrum is organized in such a way as to ensure a radially smooth profile of passing electron turbulent flux, despite the radial sparsity of each mode contribution to the flux. At lowest order MRSs the turbulence diffusivity, D_{turb}, is maximum because all the modes composing the spectrum can be non-adiabatic and thus "conduct" turbulence, whereas at highest order MRSs (for example just before and after the lowest order MRSs) the turbulence diffusivity is minimum because only a few toroidal mode numbers can be non-adiabatic and thus "conduct" turbulence. To ensure a smooth radial profile of turbulent transport, the gradients which drive this turbulent flux are corrugated so that $\Gamma = -(\delta R/L_N)\, D_{\text{turb}}$ is smooth. The organization is actually a bit more complex because the turbulence diffusivity will be locally increased or decreased, by the local steepening or flattening of the gradient, respectively. The fine zonal flows structures due to the non-adiabatic passing electron response near MRSs are strongly amplified in nonlinear simulation carried out with the realistic mass ratio compared to simulations carried out with heavy electrons. A decrease of the level of turbulence is also observed in these physical mass ratio simulations: the level of electron turbulent heat flux is decreased by a factor $\simeq 2$, and, even if the time-averaged turbulent particle flux $\langle\Gamma\rangle_t$ is not significantly increased ($\simeq 10\%$), its associated turbulent diffusivity is, by $\simeq 30-40\%$, as a consequence of profile relaxation. It is thus necessary to use the physical mass ratio for correctly simulating the turbulence and its associated transport level.

The *differing contributions of subthermal and suprathermal* particles to the turbulent transport has been shown, by means of quasi-linear flux estimates, which predictions are qualitatively confirmed in nonlinear global ORB5 simulations. In the considered conditions relevant for TCV, the passing and trapped electrons are organized in two subgroups: the subthermal and the suprathermal electrons. The particularity of this organization is that the two subgroups contribute to the flux in opposite directions, potentially canceling each other. This feature is common to the trapped and passing electrons and appears to be a consequence of the diamagnetic drift which differs significantly for these two subgroups, in the considered plasma. In *nonlinear global simulations* carried out with ORB5, the passing electron turbulent flux was found to be essentially zero. Nonetheless, the particle flux contributions from the subthermal and suprathermal passing electrons represent each a significant fraction of the total turbulent transport. These fluxes, of opposite directions, trigger radial corrugations near low order MRSs in order to ensure a smooth radial profile of particle flux. If the particle fluxes of both these subgroups was zero, no radial corrugations on the profiles would have been necessary for ensuring a smooth radial flux, thus potentially canceling the existence of the ZFs structures. Finally it was shown that the passing electron contribution to the turbulence heat flux represents up to 30% of the total electron heat flux.

6 Conclusion and outlook

This thesis work has dealt with the study of electrostatic microturbulence and more particularly the non-adiabatic response of passing electrons near mode rational surfaces and its effects on turbulent transport. This study has been carried out with the flux-tube version of the gyrokinetic code GENE and with the global gyrokinetic code ORB5. The physical plasma models which are implemented by these codes have been introduced in chapter 2.

The physical study has thus been initiated with the gyrokinetic Eulerian code GENE in its flux-tube version using the circular ad-hoc geometry, see chapter 3. The non-adiabatic response of passing electrons has been thoroughly studied in linear simulations of ITG and TEM instablities, showing the systematic presence near mode rational surfaces of fine radial structures on the perturbation fields. In nonlinear simulations, it was shown that this non-adiabatic response strongly influences the level of turbulent transport of particles and heat. For example, in the ITG regime, up to 75% of the turbulent particle transport is due to the passing electron channel. Moreover, the passing electron dynamics strongly affects the zonal flow organization of turbulence, as well as the $E \times B$ saturation of turbulence, because of the presence of these fine radial layers of non-adiabatic response near mode rational surfaces.

Chapter 4 and 5 address the follow-up of this study of the non-adiabatic response of passing electrons near mode rational surfaces with the global gyrokinetic Particle-In-Cell code ORB5.

This study carried out with the gyrokinetic code ORB5 has necessitated the development of a new field solver in order to overcome the former long-wavelenth approximation made for self-consistently solving the electrostatic field, see chapter 4. The new arbitrary wavelength solver, implemented in the frame of this thesis work, is thus able to account for the ion polarization drift contribution to the quasi-neutrality equation to arbitrary order in $k_\perp \rho_i$. In this new solver, the ion polarization-drift contribution is accounted for in its integral form as described by gyrokinetic theory. Compared to the differential form implemented for the long wavelength approximation version of the solver, the integral form of the generalized field equation has required significant numerical efforts. Note that a Padé approximation version of the solver has also been implemented. Both the integral form and the Padé solver implementation have been succesfully confronted to the global version of the GENE code in a benchmark effort. Indeed, the Eulerian gyrokinetic code already provides an arbitrary wavelength version of the field equation. This benchmark has been carried out using realistic magnetic configurations obtained from an ideal MHD equilibrium code (CHEASE), because the new integral solver is valid for arbitrary geometries. In the frame of the study of the electron dynamics, this benchmark has been conducted for the three different electron models: adiabatic, hybrid (trapped are kinetic and passing are adiabatic), and kinetic.

The study of the non-adiabatic response of passing electrons has thus been pursued with the global ORB5 code in global ideal MHD equilibrium geometry for a case relevant to the TCV tokamak, see chapter 5. This study has been carried out with the physical deuterium to electron mass ratio m_i/m_e, which was a numerical challenge because of the wide time scale separation of the light electrons and heavy ions. The physics of passing and trapped particles, as well as the physics of sub- and suprathermal populations, has been studied. The radial organization of the passing-electron channel of turbulent transport has been studied. In particular, it was shown that the passing electron channel of transport is radially homogeneous despite the fact that the non-adiatic response of passing electrons is located near low-order mode rational surfaces essentially. It was also shown that subthermal and suprathermal particles can contribute to the particle turbulent flux in opposite directions thus partly cancelling each other. The formation of fine ZFs structures near MRSs has been observed, thus confirming nonlinear flux-tube results of chapter 3. The presence of these fine structures is shown to be a cause of the interplay between modes for ensuring a smooth radial profile of passing-electron turbulent flux. The strong coupling between the safety factor profile and the passing electron turbulent fluxes was also shown.

Outlook

Ongoing solver implementation

The Padé version of the field solver has been implemented for the kinetic electron model only and has to be extended to the adiabatic and hybrid electron models. The main advantage of this version of the solver compared to the arbitrary wavelength solver is that its matrix is smaller (necessitates less bands) and is much faster to assemble. The implementation of this minor upgrade consists in adding a correction term to the adiabatic electron contribution to the quasi-neutrality equation. A collaboration with Emmanuel Lanti has been initiated and first results have been presented at the Varenna 2016 conference.

Implementation of higher order terms in the QNE

Near mode rational surfaces, fine structures develop on various perturbation fields such as the species density, species temperature, and the electrostatic potential. Their respective gradients might thus become big enough so that the gyrokinetic term

$$\delta N_\sigma^{\mathbf{X}} = \int d\mathbf{Z}\, \delta(\mathbf{X} + \rho - \mathbf{x})\, \frac{m_\sigma}{q_\sigma B_0^2} \nabla\tilde{\Phi} \times \mathbf{b} \cdot \nabla f_\sigma$$

cannot be neglected from the quasi-neutrality equation, see equation (4.1). Note that if one considers adding the nonlinear contribution $\int d\mathbf{Z}\, \delta(\mathbf{X} + \rho - \mathbf{x}) \nabla\tilde{\Phi} \times \mathbf{b} \cdot \nabla \delta f_\sigma$, one should also consider adding the nonlinear term

$$\delta N_\sigma^{\mu\,(NL)} = \int d\mathbf{Z}\, \delta(\mathbf{X} + \rho - \mathbf{x})\, \frac{q_\sigma}{B_0} \widetilde{\delta\phi} \frac{\partial \delta f_\sigma}{\partial \mu}.$$

The amplitudes of $\nabla \delta f_\sigma$ and $\partial \delta f_\sigma / \partial \mu$ should be compared, in particular near mode rational surfaces, to see if there is an evidence that one of these nonlinear terms dominates.

Interplay between short ion scales and fine structure of non-adiabatic passing electron response

During this thesis work, the formation of fine structures due to the non-adiabatic response of passing electrons near mode rational surfaces has been studied. It has been shown, in chapter 3, that these fine structures shape is influenced by many parameters, such as the magnetic shear, the temperature ratio, the mass ratio, the safety factor, and the wavenumber in the binormal direction k_y. It was also shown that these fine structures survive in nonlinear simulations somewhat broadened, and influence the level of turbulent transport. In global nonlinear simulations, chapter 5, it was also shown that the formation of these fine structures is associated to ion polarization effects, in particular near low order mode rational surfaces where fine zonal flow structures are present.

The interplay between the fine structures of non-adiabatic passing electron response and the short-scale ion polarization effects should be studied in more details. Modifying T_i influences the ion thermal Larmor radius and potentially the ion polarization effects. Modifying T_e influences the radial width of the fine structures of non-adiabatic passing electron response (at least in linear simulations). Modifying these temperatures and thus the temperature ratio might affect the nonlinear dynamics and in particular the influence of passing electrons on the zonal flow and $E \times B$ shearing rate organization. This influence of the temperature ratio could be furthermore studied. For example, in chapter 3, we did not study in details why, for the TEM test case, the turbulence is saturated by $E \times B$ shearing rate when choosing a temperature ratio $T_e/T_i = 1$ but not for $T_e/T_i = 3$, as already observed in [Lang et al., 2008].

Influence of the magnetic shear on the turbulence organization

In chapter 5, it was shown that the radial organization of the passing electron contribution to the turbulent particle flux is strongly influenced by the safety factor profile and associated distribution of mode rational surfaces. It is thus of interest to study the influence of the magnetic shear on the turbulent organization in nonlinear simulations. In appendix C, preliminary results of nonlinear simulations carried out with the flux-tube version of GENE show an influence of the shear on the radial organization of the passing-electron turbulent spectra. Further studies, including reversed shear cases, could be carried out in the future with global gyrokinetic simulations.

Non-adiabatic response of passing electrons in high-β electromagnetic simulations

In the present thesis, the non-adiabatic response of passing electrons near mode rational surfaces has been studied in the electrostatic limit. It is of interest to pursue this study in the electromagnetic cas for increasing values of β. For example, in reference [Falchetto et al., 2003], the presence of fine corrugations near low order mode rational surfaces on the perturbation potential $\delta\phi$ has been observed in electromagnetic gyrokinetic simulations with the code GLOGYSTO, which code has been introduced in [Brunner, 1997, Brunner et al., 1998]. The importance of the electromagnetic turbulence on the level of turbulent transport has been, for example, discussed in [Guttenfelder et al., 2011]. In this reference, the necessity to finely resolve the radial distribution of mode rational surfaces is also discussed in the context of electromagnetic micro-turbulence.

Current sheet layer and discontinuity of magnetic field safety factor near low order mode rational surfaces

In recent publications [Loizu et al., 2015, Loizu et al., 2016], a new class of ideal MHD equilibria is introduced. The particularity of these equilibria is that singular layers of currents cause jumps of the safety factor profile. Consequently, these new ideal MHD equilibria do not have lowest order mode rational surfaces. It could be interesting to see if the non-adiabatic response of passing electrons could be involved in the generation of these layers of current leading to jumps in the safety factor. In turn, the jumps of safety factor could result in a reduced non-adiabatic passing electron response.

A Matrix assembly in discrete Fourier representation

Adiabatic electron matrix

The adiabatic response matrix, Eq. (4.16), is decomposed into two sub matrices, such that $L^{\mathrm{ad}}_{kk'} = L^{\mathrm{noFS}}_{kk'} + L^{\mathrm{FS}}_{kk'}$ where $k = (i, m, n)$ is the triplet index. The matrices are

$$\begin{aligned} L^{\mathrm{noFS}}_{kk'} &= n_\theta M^{(n)} \sum_{\sigma \in \{\mathrm{ad}\}} q_\sigma^2 \sum_{I=1}^{n_s} \sum_{Q} w_Q \Lambda_i(s_I + s_Q) \Lambda_{i'}(s_I + s_Q) \\ &\times \sum_q w_q \hat{\Lambda}_m(\theta^\star_q) \hat{\Lambda}^*_{m'}(\theta^\star_q) \hat{C}_{\sigma, m-m'}(s_I + s_Q, \theta^\star_q), \end{aligned} \tag{A.1}$$

and

$$\begin{aligned} L^{\mathrm{FS}}_{kk'} &= -n_\theta M^{(n)} \sum_{\sigma \in \{\mathrm{ad}\}} q_\sigma^2 \sum_{I=1}^{n_s} \sum_{Q} w_Q \frac{\Lambda_i(s_I + s_Q) \Lambda_{i'}(s_I + s_Q)}{2\pi \langle \mathcal{J} \rangle_{\theta^\star}(s_I + s_Q)} \\ &\times \sum_q w_q \hat{\Lambda}_m(\theta^\star_q) \hat{C}_{\sigma, m}(s_I + s_Q, \theta^\star_q) \\ &\times \sum_{q'} w_{q'} \hat{\Lambda}^*_{m'}(\theta^\star_q) \hat{\mathcal{J}}^*_{m'}(s_I + s_Q, \theta^\star_{q'}), \end{aligned} \tag{A.2}$$

where $\theta^\star_J = 2\pi J / n_\theta$, $\theta^\star_q = 2\pi q / (n_\theta \, n_q)$, I indexes the grid intervals associated with the regular knot sequence $s_I = (I - 1)/n_s$, s_Q are quadrature points over the interval $[0, 1/n_s]$, w_Q the associated quadrature weights, $\hat{C}_{\sigma,m}(s, \theta^\star) = \sum_{J=1}^{n_\theta} C_\sigma(s, \theta^\star + \theta^\star_J) \exp\left(-\imath m \theta^\star_J\right)$ with $C_\sigma(s, \theta^\star) = \mathcal{J}(s, \theta^\star) N_{\sigma 0}(s, \theta^\star) / T_{\sigma 0}(s, \theta^\star)$, $\hat{\mathcal{J}}_m(s, \theta^\star) = \sum_{J=1}^{n_\theta} \mathcal{J}(s, \theta^\star + \theta^\star_J) \exp\left(-i m \theta^\star_J\right)$, and $2\pi \langle \mathcal{J} \rangle_{\theta^\star}(s) = 2\pi \oint d\theta^\star \mathcal{J}(s, \theta^\star)$. For this matrix $\Delta\varphi = 0$ so that $C^{(n)}(\Delta\varphi = 0) = M^{(n)}$ without approximation.

Ion polarization drift matrix and Padé correction matrix

The long-wavelength polarization matrix, Eq. (4.18), as well as the Padé correction matrix, Eq. (4.20), are assembled with

$$\begin{aligned} L_{kk'} &= n_\theta M^{(n)} \sum_{\sigma\in\{\mathrm{kin}\}} \sum_{\{\alpha\beta\}} \sum_{I=1}^{n_s} \sum_{Q,q} w_Q w_q \\ &\times \partial_\alpha[\Lambda_i(s_I+s_Q)\hat{\Lambda}_m(\theta^\star_q)] \\ &\times \partial_\beta[\Lambda_{i'}(s_I+s_Q)\hat{\Lambda}^*_{m'}(\theta^\star_q)]\, \hat{G}^{\alpha\beta}_{\sigma,m-m'}(s_I+s_Q,\theta^\star_q), \end{aligned} \tag{A.3}$$

where $\hat{G}^{\alpha\beta}_{\sigma,m}(s,\theta^\star) = \sum_{J=1}^{n_\theta} G^{\alpha\beta}_\sigma(s,\theta^\star_J+\theta^\star)e^{-\imath m\theta^\star_J}$ with $G^{\alpha\beta}_\sigma = m_\sigma g^{\alpha\beta}\mathcal{J}N_{\sigma0}/B_0^2$ for the long-wavelength polarization matrix and $G^{\alpha\beta}_\sigma = (m_\sigma/q_\sigma^2)g^{\alpha\beta}\mathcal{J}T_{\sigma0}/B_0^2$ for the Padé correction matrix. In Eq. (A.3), one used the approximation $\nabla_\perp \simeq \nabla_{\mathrm{pol}} = \nabla s\partial_s + \nabla\theta^\star\partial_{\theta^\star}$, the sum over $\{\alpha\beta\}$ is done for $\alpha\beta \in \{ss, s\theta, \theta s, \theta\theta\}$ with $g^{\alpha\beta} = \nabla\alpha\cdot\nabla\beta$. The approximations $\Delta\varphi \simeq 0$ and $C^{(n)} \simeq M^{(n)}$ are made.

Arbitrary-wavelength polarization drift matrix

The arbitrary-wavelength polarization drift matrix, Eq. (4.17), is assembled by assuming a local Maxwellian for the background distribution function

$$f_{\sigma0}(\mathbf{x}) = \frac{N_{\sigma,\mathrm{eq}}(\mathbf{x})}{[2\pi T_{\sigma0}(\mathbf{x})/m_\sigma]^{3/2}} \exp\left[-\frac{m_\sigma v_\parallel^2/2 + \mu B_0(\mathbf{x})}{T_{\sigma0}(\mathbf{x})}\right]. \tag{A.4}$$

The polarization-drift matrix then reads

$$\begin{aligned} \hat{L}^{\mathrm{pol}}_{kk'} &= n_\theta \sum_{\sigma\in\mathrm{kin}} q_\sigma^2 \sum_{I,Q,J,q} w_Q w_q \mathcal{J}(s_I+s_Q,\theta^\star_J+\theta^\star_q)\frac{N_{\sigma,\mathrm{eq}}(s_I+s_Q,\theta^\star_J+\theta^\star_q)}{T_{\sigma0}(s_I+s_Q,\theta^\star_J+\theta^\star_q)} \\ &\times \sum_{w=0}^{n_w-1} \Delta\tilde{v}_\perp\ \tilde{v}_{\perp,w} \exp\left(-\tilde{v}^2_{\perp,w}/2\right) \\ &\times \left[\frac{1}{n_a}\sum_{a=1}^{n_a} M^{(n)}\Lambda_i(s_a)\hat{\Lambda}_m(\theta^\star_a)\Lambda_{i'}(s_a)\hat{\Lambda}^*_{m'}(\theta^\star_a)\right. \\ &- \left.\frac{1}{n_a^2}\sum_{a=1}^{n_a}\Lambda_i(s_a)\hat{\Lambda}^*_m(\theta^\star_a)\sum_{a'=1}^{n_a} C^{(n)}(\varphi_a-\varphi_{a'})\Lambda_{i'}(s_{a'})\hat{\Lambda}^*_{m'}(\theta^\star_{a'})\right], \end{aligned} \tag{A.5}$$

with a and a' the gyroaveraging quadrature points, n_a the number of these quadrature points which varies proportionally to $\tilde{v}_{\perp,w}$, $\tilde{v}_{\perp,w} = w\Delta\tilde{v}_\perp$, $n_w = \tilde{v}_{\perp,\mathrm{max}}/\Delta\tilde{v}_\perp$ an input parameter of the simulation, and $\tilde{v}_\perp = v_\perp/v_{\mathrm{th}}(s_I+s_Q,\theta^\star_J+\theta^\star_q)$. The quadrature over the perpendicular velocity is thus carried-out over a velocity grid which is systematically adapted to the local thermal velocity. To lighten the notation, the gyropoints coordinates have been noted $(s_a, \theta^\star_a, \varphi_a)$ when in fact they are functions of other guiding-centre coordinates: $s_a = s(s_I + s_Q, \theta^\star_J + \theta^\star_q, \tilde{v}_{\perp,w}, \alpha_a)$, $\theta^\star_a = \theta^\star(s_I + s_Q, \theta^\star_J + \theta^\star_q, \tilde{v}_{\perp,w}, \alpha_a)$, and in case of the toroidal angle only the difference $\varphi_a - \varphi_{a'} = \Delta\varphi(s_I + s_Q, \theta^\star_J + \theta^\star_q, \tilde{v}_{\perp,w}, \alpha_a, \alpha_{a'})$ is necessary for computing the integral. This difference is actually zero in our case, because we assemble the matrix in the approximation $\boldsymbol{\rho} \cdot \nabla\varphi = 0$. The term $C^{(n)}(\varphi_a - \varphi_{a'})$ is thus approximated by $C^{(n)}(\varphi_a - \varphi_{a'}) \simeq C^{(n)}(0) = M^{(n)}$, where the function $C^{(n)}(\Delta\varphi)$ reads

$$\begin{aligned}
C^{(n)}(\Delta\varphi) &= n_\varphi^{-1} \sum_{l,l'} e^{-\imath 2\pi n l/n_\varphi} \oint d\varphi \Lambda_l(\varphi)\Lambda_{l'}(\varphi + \Delta\varphi) e^{\imath 2\pi n' l'/n_\varphi} \\
&= n_\varphi^{-1} \sum_{l,l'} e^{-\imath 2\pi (nl - n'l')/n_\varphi} \oint d\varphi\, \Lambda_l(\varphi)\Lambda_{l'}(\varphi + \Delta\varphi) \\
&= n_\varphi^{-1} \sum_{L=0}^{n_\varphi - 1} \int_0^{2\pi/n_\varphi} d\varphi\, \hat{\Lambda}_n(\varphi + \varphi_L)\hat{\Lambda}^*_{n'}(\varphi + \varphi_L + \Delta\varphi) \\
&= n_\varphi^{-1} \sum_{L=0}^{n_\varphi - 1} \int_0^{2\pi/n_\varphi} d\varphi\, e^{\imath 2\pi L(n-n')/n_\varphi} \hat{\Lambda}_n(\varphi)\hat{\Lambda}^*_{n'}(\varphi + \Delta\varphi) \\
&= \int_0^{2\pi/n_\varphi} d\varphi\, \hat{\Lambda}_n(\varphi)\hat{\Lambda}^*_n(\varphi + \Delta\varphi).
\end{aligned} \tag{A.6}$$

Finally, the computation of the gyropoints coordinates, in this approximation $\boldsymbol{\rho} \cdot \nabla\varphi = 0$, is described in Eq. (4.33).

B ORB5 moments and fluxes diagnostics

A new 3D diagnostic feature is implemented in the ORB5 code. The aim is to compute moments of the perturbed species distribution function using a finite-element representation. For example, one obtains the coefficients $(\delta N)_k$ for the density which perturbed field is computed with

$$\delta N(s, \theta, \varphi) = \sum_k (\delta N)_k \, \hat{\Lambda}_k(s, \theta^\star, \varphi).$$

In these new diagnostics, the moments of the particle perturbation distribution function, δf, are computed by doing a Galerkin projection of the marker weights, which are furthermore weighted by 1 for density and $mv^2/2$ for kinetic energy, on the same DFT-finite-element representation as the one used for the perturbed electrostatic potential $\delta\phi$. In addition, this projected quantity is multiplied by the inverse mass matrix such as to obtain the DFT-finite-element coefficients of the expected physical quantity. The computation of these moments is comparable to the coefficients of the source term in Eq. (4.21). For example, the DFT finite-element coefficients of the perturbation gyrodensity are computed from

$$(\delta N_\sigma)_{k'} = \hat{\hat{\mathcal{M}}}{}^{-1}_{kk'} \sum_p w_p \; 1 \; \langle \hat{\Lambda}_k \rangle_\alpha(\mathbf{X}_p, \mu_p), \tag{B.1}$$

with the mass matrix $\hat{\hat{\mathcal{M}}}_{kk'}$ defined by

$$\begin{aligned} \hat{\hat{\mathcal{M}}}_{kk'} &= n_\theta^{-1} \sum_{j=0}^{n_\theta - 1} \sum_{j'=0}^{n_\theta - 1} e^{-\imath 2\pi (mj - m'j')/n_\theta} \; \hat{\mathcal{M}}^{(n)}_{(ij)(i'j')} \\ &= n_\theta^{-1} \sum_{j=0}^{n_\theta - 1} \sum_{j'=0}^{n_\theta - 1} e^{-\imath 2\pi (mj - m'j')/n_\theta} \left(n_\varphi^{-1} \sum_{\Delta l = 0}^{n_\varphi - 1} \mathcal{M}^{(\Delta l)}_{(ij)(i'j')} e^{-\imath 2\pi n \Delta l / n_\varphi} \right) \end{aligned} \tag{B.2}$$

where $\Delta l = l - l'$, $\mathcal{M}^{(l-l')}_{(ij)(i'j')} = \mathcal{M}_{(ijl)(i'j'l')}$ and

$$\mathcal{M}_{(ijl)(i'j'l')} = \int dsd\theta^\star d\varphi \Lambda_i(s)\Lambda_j(\theta^\star)\Lambda_l(\varphi)\Lambda_{i'}(s)\Lambda_{j'}(\theta^\star)\Lambda_{l'}(\varphi).$$

We can also define a partition of velocity phase space and split each moments in subgroups of particle of the same species. For example, the DFT finite-element coefficients of the perturbation gyrodensity subgroups, g, are computed from

$$(\delta N_{\sigma,g})_{k'} = \mathcal{M}^{-1}_{kk'} \sum_p w_p \; 1 \; \left(|\tilde{E}_g \leq \tilde{E}_p < \tilde{E}_{g+1}| \times |\lambda_g \leq \lambda_p < \lambda_{g+1}| \right) \; \langle \hat{\Lambda}_k \rangle_\alpha (\mathbf{X}_p, \mu_p), \tag{B.3}$$

where the value of an inequality is one or zero. These subgroups are flexibly determined by any 2D grid over the normalized kinetic energy $\tilde{E} = mv^2/T_\sigma(\mathbf{X})$ and the signed pitch angle $\tilde{\lambda} = sign(v_\parallel)\lambda/\lambda_c$ with $\lambda = |\arctan{(v_\perp/v_\parallel)}|$ and $\lambda_c = \arccos \alpha_{\text{trap}}(\mathbf{X})$.

In ORB5, the gyrocenter fluxes are computed from equation [Vernay, 2013]

$$\bar{\mathcal{F}}_\sigma[\mathcal{A}] = \left\langle \frac{\nabla\psi}{|\nabla\psi|} \cdot 2\pi \int_0^{+\infty} d\mu \int_{-\infty}^{+\infty} dv_\parallel \frac{B^\star_{0\parallel}}{m_\sigma} \mathcal{A} \, f_\sigma \dot{\mathbf{X}} \right\rangle_{\mathcal{S}}, \tag{B.4}$$

where $\dot{\mathbf{X}}$ is the guiding-center drift and $\mathcal{A}$ is a function of position and velocity $\mathcal{A} = \mathcal{A}(\mathbf{X}, \mu, v_\parallel)$ such that the particle, kinetic energy, potential energy, and heat fluxes are then, respectively, given by $\bar{\Gamma}_\sigma = \bar{\mathcal{F}}_\sigma[1]$, $\bar{Q}_{\text{kin},\sigma} = \bar{\mathcal{F}}_\sigma[mv^2/2]$, $\bar{Q}_{\text{pot},\sigma} = \bar{\mathcal{F}}_\sigma[q\phi]$, $\bar{q}_{\text{h},\sigma} = \bar{\mathcal{F}}_\sigma[m(v^2 - 5v^2_{\text{th},\sigma})/2 + q\phi] = \bar{Q}_{\text{kin},\sigma} + \bar{Q}_{\text{pot},\sigma} - (5/2)T_\sigma\Gamma_\sigma$. In Eq. (B.4), the brackets $\langle \; \rangle_S$ denote the surface average

$$\langle \mathcal{A} \rangle_{\mathcal{S}}(\psi, t) = \frac{1}{\mathcal{S}} \int_{\mathcal{S}(\psi)} d\mathcal{S} \; \mathcal{A}, \tag{B.5}$$

with $\mathcal{S} = \int d\mathcal{S}$ the surface, $d\mathcal{S} = d\varphi d\theta^\star \mathcal{J} |\nabla\psi|$ the surface element and

$$\int_{\mathcal{S}(\psi)} d\mathcal{S} \, \mathcal{A} = \oint d\varphi \oint d\theta^\star \mathcal{J}(\psi, \theta) |\nabla\psi(\psi, \theta^\star)| \, \mathcal{A}(\psi, \theta^\star).$$

In terms of the flux-surface average operation, the surface average reads $\langle \mathcal{A} \rangle_{\mathcal{S}} = \langle |\nabla\psi| \mathcal{A} \rangle_{FS} / \langle |\nabla\psi| \rangle_{FS}$. Numerically the flux-surface averaged fluxes are computed from the volume averaged operation

$$\langle \mathcal{A} \rangle_{\Delta V} = \frac{1}{\Delta V} \int_{\Delta v} d^3 V \mathcal{A},$$

with ΔV the small volume delimited by the surfaces ψ and $\psi + \Delta\psi$.

For electrons, the particle fluxes can be approximated by the corresponding gyrocenter fluxes as a result of the small electron mass. For ions, $\boldsymbol{\rho}_i \neq 0$ and one needs to account for the polarization and magnetization correction terms [Brizard, 2008, Brizard, 2009]. The relation between the particle current Γ_σ and the gyro-center current $\bar{\Gamma}_\sigma$ for a given species σ is

$$\boldsymbol{\Gamma}_\sigma = \bar{\boldsymbol{\Gamma}}_\sigma + \partial \mathbf{P}_\sigma / \partial t + \nabla \times \mathbf{M}_\sigma,$$

where $\partial \mathbf{P}_\sigma / \partial t$ is a polarization current contribution to the particle flux and $\nabla \times \mathbf{M}_\sigma$ is a magnetization current contribution to the particle flux [Brizard, 2008, Brizard, 2009]. In a quasi-steady state, the surface- and time-averaged fluxes of particle, denoted Γ_σ, and gyrocenters are essentially equivalent $\Gamma_\sigma(s) = \langle \langle \boldsymbol{\Gamma}_\sigma \rangle_{\mathcal{S}} \rangle_t \simeq \left\langle \langle \bar{\boldsymbol{\Gamma}}_\sigma \rangle_{\mathcal{S}} \right\rangle_t$, indeed $\langle \nabla \times \mathbf{M}_\sigma \rangle_{\mathcal{S}} = 0$ and $\langle \partial \mathbf{P}_\sigma / \partial t \rangle_{\mathcal{S}} = 0$. The magnetization current contribution goes to zero when averaging over a closed toroidal surface. From now on, no more distinction will therefore be made between the gyrocenter fluxes and the particle fluxes.

The particle diffusivity and the heat diffusivity are defined by

$$D_\sigma = \Gamma_\sigma / \left\langle -\frac{\nabla \psi}{|\nabla \psi|} \cdot \nabla N_\sigma \right\rangle_{\mathcal{S}} \simeq \frac{\Gamma_\sigma \, \langle |\nabla \psi| \rangle_{FS}}{(-dN_\sigma / d\psi) \, \langle |\nabla \psi|^2 \rangle_{FS}}, \tag{B.6}$$

and

$$\chi_\sigma = q_{\sigma,H} / \left\langle -\frac{\nabla \psi}{|\nabla \psi|} \cdot N_\sigma \nabla T_\sigma \right\rangle_{\mathcal{S}} \simeq \frac{q_{h,\sigma} \, \langle |\nabla \psi| \rangle_{FS}}{N_\sigma(-dT_\sigma / d\psi) \, \langle |\nabla \psi|^2 \rangle_{FS}}, \tag{B.7}$$

where one assumes that the effective profiles of $N_\sigma = N_\sigma(\psi)$ and $T_\sigma = T_\sigma(\psi)$ are flux-surface functions. These quantities are expressed in gyro-Bohm units $D_{GB} = \chi_{GB} = \rho_{s0}^2 c_{s0} / a$ with $c_{s0} = \sqrt{T_{e0}(s_{peak}) / m_i}$ and $\rho_{s0} = m c_{s0} / q B_{\text{axis}}$.

C Influence of the magnetic shear on the turbulence organization

In chapter 5, it was shown that the radial organization of the passing electron contribution to the turbulent particle flux is strongly influenced by the safety factor profile and associated distribution of mode rational surfaces. It is thus of interest to study the influence of the magnetic shear on the turbulent organization.

In figure C.1, preliminary results of nonlinear simulations carried out with the flux-tube version of GENE show the influence of the shear on the radial organization of the passing-electron turbulent spectra. The fact that the radial organization of the passing-electron turbulent particle flux spectra is coupled to the distribution of mode rational surfaces is in qualitative agreement with TCV simulation results shown in chapter 5. One difference between the TCV turbulent regime and this ITG turbulent regime is that in this ITG test case, the electron temperature gradient is such that there is no distinction in the behavior of sub- and supra-thermal electrons. Coming back to the radial organization of this spectra, it is clearly shown that each k_y mode contributes to the flux where the passing electron response to this k_y mode is non-adiabatic. The turbulent particle flux contribution of a given k_y mode exhibits peaks of transport localized near associated low order mode rational surfaces. For example, the mode of wave number $k_y\rho_i = k_{y,min}$ contributes to $\langle\Gamma_{e,pas}\rangle_{zt}$ near all mode rational surfaces of lowest order, *i.e.*, $x = p\,L_{MRS}$ with p integer; and the mode number of wave number $k_y\rho_i = 2k_{y,min}$ contributes to $\langle\Gamma_{e,pas}\rangle_{zt}$ near all mode rational surfaces of lowest order and of second order, *i.e.*, $x = (p/2)\,L_{MRS}$ with p integer. Comparing the results obtained with the two values of the shear, one observes that, as expected, a decrease of the magnetic shear results in a decrease of the density of low order mode rational surfaces and thus in a decrease of the number of these fine structures. It also appears in these simulation results that the fine structures near the mode rational surfaces are larger in simulations carried out with $\hat{s} = 0.4$ than with $\hat{s} = 0.8$. Note that, as discussed in chapter 5 for TCV simulations, the overall passing-electron contribution to the turbulent particle flux, $\langle\Gamma_{e,pas}\rangle_{zt}(x) = \sum_{k_y}\langle\hat{\Gamma}_{e,pas}\rangle_{zt}(x, k_y)$ is radially homogeneous. It is of interest to study in more details the mechanisms which permit the turbulent flux spectra to adapt radially and thus ensure continuity of the turbulent flux.

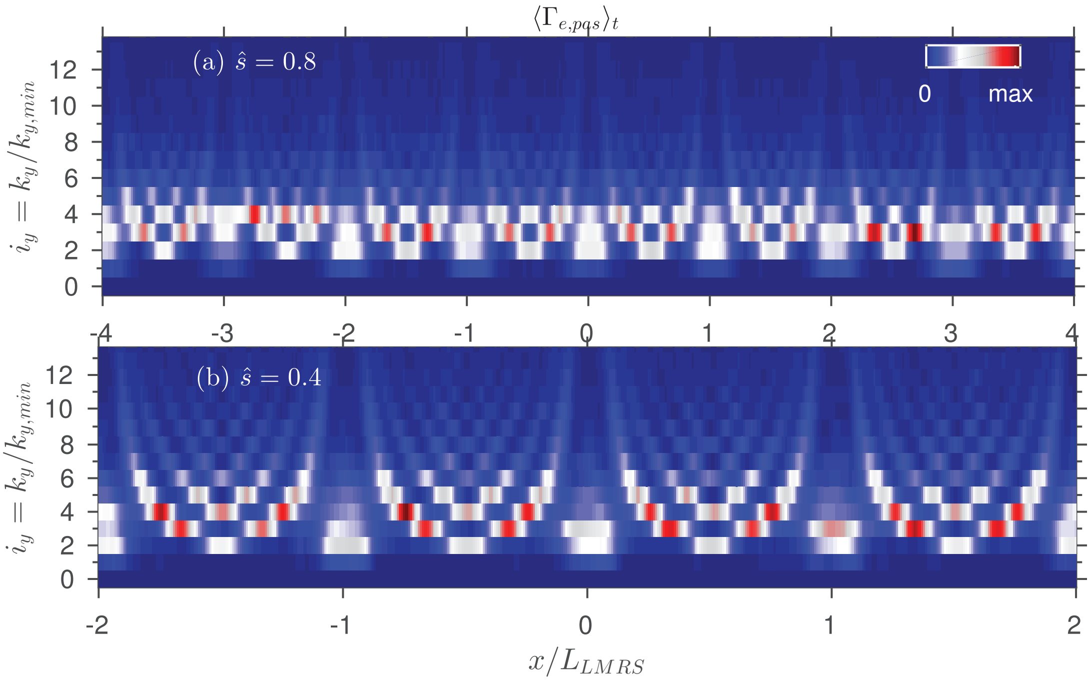

Figure C.1 – Time-averaged passing-electron contribution to the turbulent particle flux in the same ITG flux-tube case as in chapter 3 except for the magnetic shear equal to (a) $\hat{s} = 0.8$ and (b) $\hat{s} = 0.4$. The simulation boxes have the same size, $L_{box} = n_{x,box}/\hat{s}k_{y,min} = n_{x,box}L_{LMRS}$, which is kept constant by adapting $n_{x,box}$ to the value of the magnetic shear. Only a fraction of the k_y spectra is shown. Parameters: $k_{y,min}\rho_i = 0.07$, $n_{k_y} = 64$, and $n_x = 512$.

In linear simulations of chapter 3 it was shown how the variation of the shear influences the non-adiabatic response of passing electrons and thus the width the fine structures. But, in nonlinear simulations, the same explanation does not hold because these structures are much broader than predicted. It could thus be interesting to study in more details the physics which determine the width of the fine structures in nonlinear simulations. In the nonlinear simulation preliminary results shown here, the fine structures present near mode rational surfaces on the time-averaged density and species temperature perturbation gradient profiles and the $E \times B$ zonal structures have a radial width which varies with the value of the magnetic shear: their width increases when the magnetic shear decreases, see figure C.2 and datatips on subplots (d,e,f). A case with $\hat{s} = 1.4$ has been added in this latter figure to enforce the claim. Now regarding these fine structures amplitude, the perturbation of the electron temperature gradient is 45% bigger at lowest order mode rational surfaces when $\hat{s} = 0.4$ than when $\hat{s} = 0.8$. This increase of the gradient could be necessary for compensating the lower density of mode rational surfaces when $\hat{s} = 0.4$ than when $\hat{s} = 0.8$, thus ensuring a constant turbulent flux $\Gamma_{e,pas} \simeq D_{e,pas}\nabla T_e$. In chapter 5, where a similar comment was made, the passing electron turbulent diffusivity $D_{e,pas}$ was found to be in relation with the density of mode rational surfaces. It could be of interest

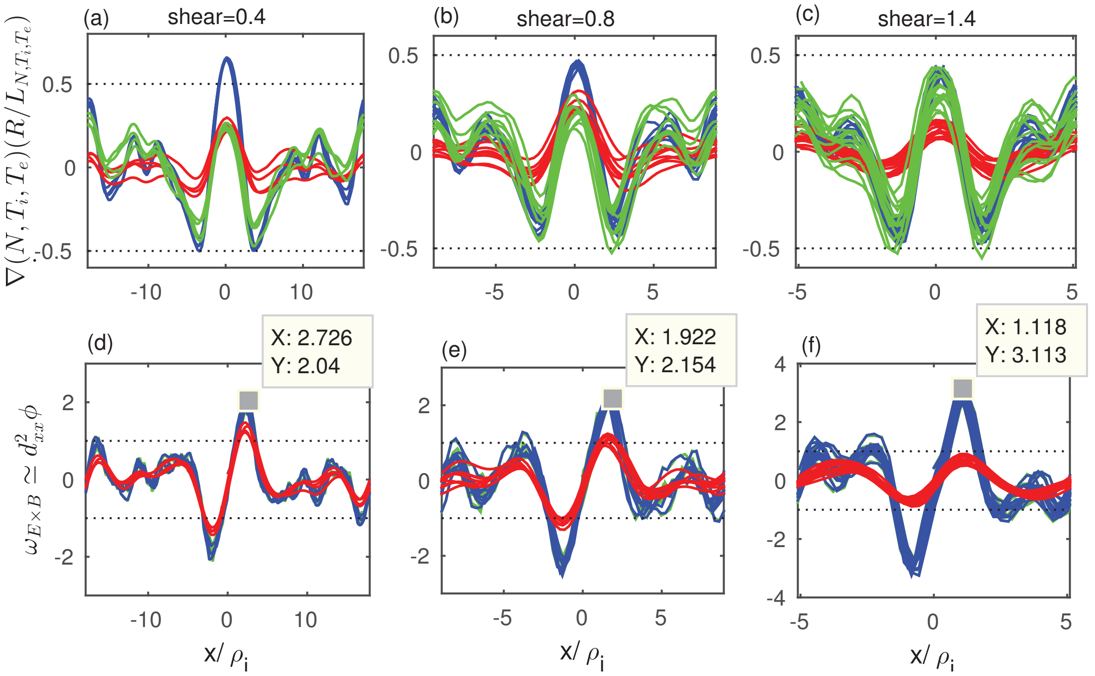

Figure C.2 – Subplots (a-c) Radial gradient $\nabla_x\langle\delta\mathcal{A}\rangle_{yzt}$ of the time- and flux-surface- averaged fluctuations for different field quantities $\mathcal{A}$ normalized with respect to corresponding background gradients $|\nabla_x\mathcal{A}_0| = \mathcal{A}_0/L_{\mathcal{A}}$: density $\mathcal{A} = N$ (green), electron temperature $\mathcal{A} = T_{e0}$ (blue), and ion temperature $\mathcal{A} = T_{i0}$ (red). Profile sections of length L_{LMRS} have been superimposed (with lowest order MRSs at $x = 0$). Subplots (d-f) Time-averaged shearing rate $\langle\omega_{E\times B}\rangle_t$ estimated with $E = -\nabla_x\langle\phi\rangle_{yz}$ (green) and effective shearing rate $\langle\omega^{i,e}_{E\times B}\rangle_t$ felt by the ions and electrons estimated with gyroaveraged $\bar{E} = -\nabla_x\langle\bar{\phi}\rangle_{yz}$ (red and blue respectively). Same simulations than in figure C.1.

to study in more details the correlation between the amplitude and width of these fine structures with the radial distribution of mode rational surfaces.

The time-averaged particle flux, including contributions from trapped and passing particles, decreases by 30% for $\hat{s} = 0.4$ instead of $\hat{s} = 0.8$. This decrease is only due to a 50% decrease of the passing electron contribution to this turbulent flux. The spectra of the trapped and passing electron contributions to the particle flux are plotted in figure C.3 for $\hat{s} = 0.4$ (blue) and 0.8 (red). In these plots, the trapped-electron turbulent particle flux spectra does not depend on the value of the magnetic shear. On the other hand, both k_x and k_y spectra of passing-electron turbulent particle flux vary with the magnetic shear. Regarding the k_y-spectrum in subplot (b), it clearly appears that solely the long wavelength part of the k_y-spectra, $0 < k_y\rho_i \leq 0.28$, is affected by the change of magnetic shear. It is interesting to point that the radial organization of this same long-wavelength part of the k_y-spectra is significantly affected by the radial distribution of mode rational surfaces shown in figure C.1. Regarding the k_x-spectra in subplot (a), these passing-

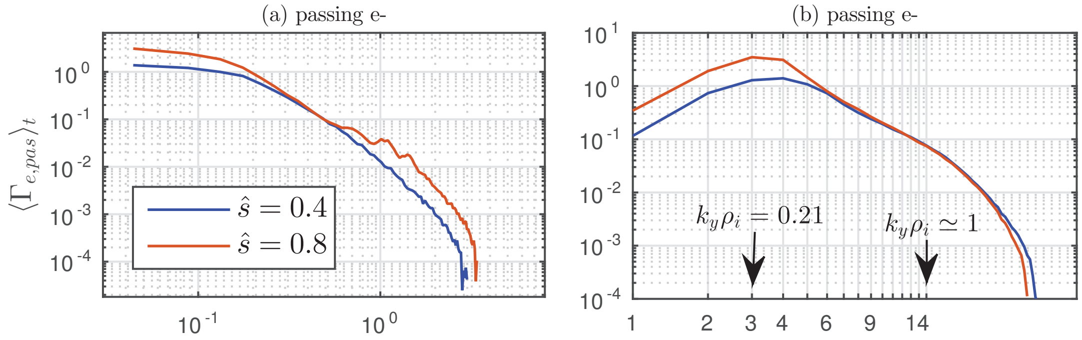

(a) passing e-

(b) passing e-

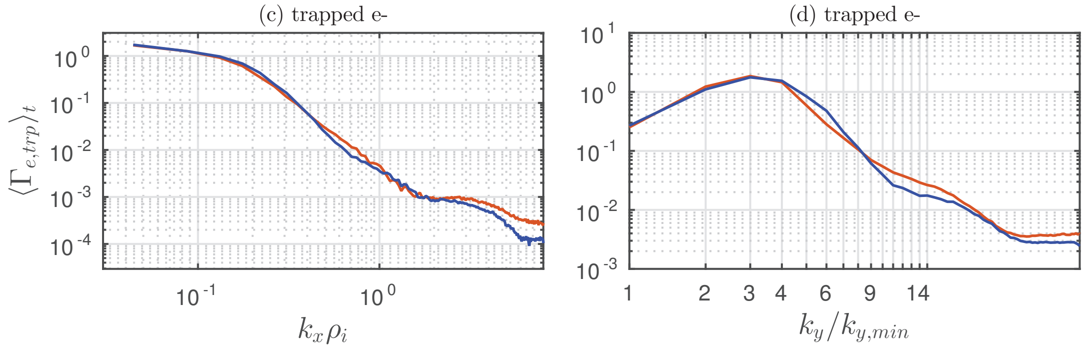

(c) trapped e-

(d) trapped e-

Figure C.3 – Time-averaged spectra of the passing-electron contribution to the turbulent particle flux in the same ITG flux-tube simulation as in chapter 3. Magnetic shear equal to $\hat{s} = 0.4$ (blue) and $\hat{s} = 0.8$ (red). Left column: fluxes spectra as a function of radial mode number. Right column: fluxes spectra as a function of binormal mode number. Same simulations than as figure C.1.

electron spectra carried out with $\hat{s} = 0.8$ and 0.4 are shown to be significantly different at long wavelengths. Moreover, the k_x-spectra obtained from the $\hat{s} = 0.8$ simulation shows the presence of peaks near $k_x\rho_i \simeq 1$. These peaks were already observed in chapter 3 and are due to the magnetic shear: after a poloidal turn a k_x mode is sheared and couples to the mode $k_x + 2\pi\hat{s}k_y$. For the smaller values of the magnetic shear the spectral spreading $\Delta k_x = 2\pi\hat{s}k_y$ is smaller and its small amplitude peaked contributions near $k_x\rho_i \simeq 0.5$ are drawn in the spectra. It could be interesting to study this magnetic shear influence in more detail.

Bibliography

[Abel et al., 2013] Abel, I. G., Plunk, G. G., Wang, E., Barnes, M., Cowley, S. C., Dorland, W., and Schekochihin, A. A. (2013). Multiscale gyrokinetics for rotating tokamak plasmas: fluctuations, transport and energy flows. *Reports on Progress in Physics*, 76(11):116201.

[Angelino et al., 2006] Angelino, P., Bottino, A., Hatzky, R., Jolliet, S., Sauter, O., Tran, T. M., and Villard, L. (2006). On the definition of a kinetic equilibrium in global gyrokinetic simulations. *Physics of Plasmas*, 13(5).

[Angioni et al., 2007] Angioni, C., Dux, R., Fable, E., Peeters, A. G., and the ASDEX Upgrade Team (2007). Non-adiabatic passing electron response and outward impurity convection in gyrokinetic calculations of impurity transport in asdex upgrade plasmas. *Plasma Physics and Controlled Fusion*, 49(12):2027.

[Beer et al., 1995] Beer, M. A., Cowley, S. C., and Hammett, G. W. (1995). Field aligned coordinates for nonlinear simulations of tokamak turbulence. *Physics of Plasmas (1994-present)*, 2(7):2687–2700.

[Biancalani et al., 2016] Biancalani, A., Bottino, A., Briguglio, S., Könies, A., Lauber, P., Mishchenko, A., Poli, E., Scott, B. D., and Zonca, F. (2016). Linear gyrokinetic particle-in-cell simulations of alfvén instabilities in tokamaks. *Physics of Plasmas*, 23(1).

[Bottino et al., 2010] Bottino, A., Scott, B., Brunner, S., McMillan, B., Tran, T., Vernay, T., Villard, L., Jolliet, S., Hatzky, R., and Peeters, A. (2010). Global nonlinear electromagnetic simulations of tokamak turbulence. *Plasma Science, IEEE Transactions on*, 38(9):2129–2135.

[Brizard, 2000] Brizard, A. J. (2000). Variational principle for nonlinear gyrokinetic vlasov–maxwell equations. *Physics of Plasmas*, 7(12):4816–4822.

[Brizard, 2008] Brizard, A. J. (2008). On the dynamical reduction of the vlasov equation. *Communications in Nonlinear Science and Numerical Simulation*, 13(1):24 – 33. Vlasovia 2006: The Second International Workshop on the Theory and Applications of the Vlasov Equation.

[Brizard, 2009] Brizard, A. J. (2009). Variational principles for reduced plasma physics. *Journal of Physics: Conference Series*, 169(1):012003.

[Brizard and Hahm, 2007] Brizard, A. J. and Hahm, T. S. (2007). Foundations of nonlinear gyrokinetic theory. *Rev. Mod. Phys.*, 79:421–468.

[Brunner, 1997] Brunner, S. (1997). *Global approach to the spectral problem of microinstabilities in tokamak plasmas using a gyrokinetic model.* PhD thesis, Ecole Polytechnique Fédérale de Lausanne, Switzerland. Thesis number 1701.

[Brunner et al., 1998] Brunner, S., Fivaz, M., Tran, T. M., and Vaclavik, J. (1998). Global approach to the spectral problem of microinstabilities in tokamak plasmas using a gyrokinetic model. *Physics of Plasmas*, 5(11):3929–3949.

[Burckel et al., 2010] Burckel, A., Sauter, O., Angioni, C., Candy, J., Fable, E., and Lapillonne, X. (2010). On the effects of the equilibrium model in gyrokinetic simulations: from s-alpha to diverted mhd equilibrium. *Journal of Physics: Conference Series*, 260(1):012006.

[Candy, 2005] Candy, J. (2005). Beta scaling of transport in microturbulence simulations. *Physics of Plasmas*, 12(7):–.

[Cary and Brizard, 2009] Cary, J. R. and Brizard, A. J. (2009). Hamiltonian theory of guiding-center motion. *Rev. Mod. Phys.*, 81:693–738.

[Catto, 1978] Catto, P. (1978). Linearized gyro-kinetics. *Plasma Physics*, 20:719–722.

[Chowdhury et al., 2008] Chowdhury, J., Ganesh, R., Angelino, P., Vaclavik, J., Villard, L., and Brunner, S. (2008). Role of nonadiabatic untrapped electrons in global electrostatic ion temperature gradient driven modes in a tokamak. *Physics of Plasmas*, 15(7):072117.

[Collier, 2015] Collier, J. (2015). PhD thesis, University of Warwick, United Kingdoms.

[Collier et al., 2016] Collier, J. D., McMillan, B. F., and Robinson, J. R. (2016). Global gyrokinetic simulations with strong flows. *Physics of Plasmas*, 23(11).

[Connor et al., 1978] Connor, J. W., Hastie, R. J., and Taylor, J. B. (1978). Shear, periodicity, and plasma ballooning modes. *Phys. Rev. Lett.*, 40:396–399.

[de Boor, 1978] de Boor, C. (1978). A practical guide to splines.

[de Meijere et al., 2014] de Meijere, C. A., Coda, S., Huang, Z., Vermare, L., Vernay, T., Vuille, V., Brunner, S., Dominski, J., Hennequin, P., Krämer-Flecken, A., Merlo, G., Porte, L., and Villard, L. (2014). Complete multi-field characterization of the geodesic acoustic mode in the tcv tokamak. *Plasma Physics and Controlled Fusion*, 56(7):072001.

[D'haeseleer et al., 1991] D'haeseleer, W., Hitchon, W., Callen, J., and Shohet, J. (1991). *Flux Coordinates and Magnetic Field Structure*. Springer.

[Diamond et al., 2005] Diamond, P. H., Itoh, S.-I., Itoh, K., and Hahm, T. S. (2005). Zonal flows in plasma—a review. *Plasma Physics and Controlled Fusion*, 47(5):R35.

[Dimits et al., 1992] Dimits, A. M., LoDestro, L. L., and Dubin, D. H. E. (1992). Gyroaveraged equations for both the gyrokinetic and drift kinetic regimes. *Physics of Fluids B*, 4(1):274–277.

[Dominski et al., 2012] Dominski, J., Brunner, S., Aghdam., S. K., Görler, T., Jenko, F., and Told, D. (2012). Identifying the role of non-adiabatic passing electrons in itg/tem microturbulence by comparing fully kinetic and hybrid electron simulations. *J.Phys:Conf.Ser.*, 401.

[Dominski et al., 2015] Dominski, J., Brunner, S., Görler, T., Jenko, F., Told, D., and Villard, L. (2015). How non-adiabatic passing electron layers of linear microinstabilities affect turbulent transport. *Physics of Plasmas*, 22(6).

[Dubin et al., 1983] Dubin, D., Krommes, J., Oberman, C., and Lee, W. (1983). *Phys. Fluids*, 26:3524.

[Falchetto et al., 2003] Falchetto, G. L., Vaclavik, J., and Villard, L. (2003). Global-gyrokinetic study of finite β effects on linear microinstabilities. *Physics of Plasmas*, 10(5):1424–1436.

[Fivaz, 1997] Fivaz, M. (1997). PhD thesis, École Polytechnique Fédérale de Lausanne, Switzerland. Thesis number 1692.

[Fivaz et al., 1998] Fivaz, M., Brunner, S., de Ridder, G., Sauter, O., Tran, T., Vaclavik, J., Villard, L., and Appert, K. (1998). Finite element approach to global gyrokinetic particle-in-cell simulations using magnetic coordinates. *Computer Physics Communications*, 111(1–3):27 – 47.

[Garbet et al., 2010] Garbet, X., Idomura, Y., Villard, L., and Watanabe, T. (2010). Gyrokinetic simulations of turbulent transport. *Nuclear Fusion*, 50(4):043002.

[Görler, 2009] Görler, T. (2009). *Multiscale effects in plasma turbulence*. PhD thesis, University of Ulm, Germany.

[Görler et al., 2011] Görler, T., Lapillonne, X., Brunner, S., Dannert, T., Jenko, F., Merz, F., and Told, D. (2011). The global version of the gyrokinetic turbulence code gene. *Journal of Computational Physics*, 230(18):7053 – 7071.

[Grandgirard et al., 2007] Grandgirard, V., Sarazin, Y., Angelino, P., Bottino, A., Crouseilles, N., Darmet, G., Dif-Pradalier, G., Garbet, X., Ghendrih, P., Jolliet, S., Latu, G., Sonnendrücker, E., and Villard, L. (2007). Global full- f gyrokinetic simulations of plasma turbulence. *Plasma Physics and Controlled Fusion*, 49(12B):B173.

[Guttenfelder et al., 2011] Guttenfelder, W., Candy, J., Kaye, S. M., Nevins, W. M., Wang, E., Bell, R. E., Hammett, G. W., LeBlanc, B. P., Mikkelsen, D. R., and Yuh, H. (2011). Electromagnetic transport from microtearing mode turbulence. *Phys. Rev. Lett.*, 106:155004.

[Hahm, 1988] Hahm, T. S. (1988). Nonlinear gyrokinetic equations for tokamak microturbulence. *Physics of Fluids*, 31(9).

[Hahm, 1994] Hahm, T. S. (1994). Rotation shear induced fluctuation decorrelation in a toroidal plasma. *Physics of Plasmas*, 1(9):2940–2944.

[Hahm et al., 1999] Hahm, T. S., Beer, M. A., Lin, Z., Hammett, G. W., Lee, W. W., and Tang, W. M. (1999). Shearing rate of time-dependent e x b flow. *Physics of Plasmas*, 6(3):922–926.

[Hallatschek and Dorland, 2005] Hallatschek, K. and Dorland, W. (2005). Giant electron tails and passing electron pinch effects in tokamak-core turbulence. *Phys. Rev. Lett.*, 95:055002.

[Hatch et al., 2013] Hatch, D. R., Jenko, F., Bañón Navarro, A., and Bratanov, V. (2013). Transition between saturation regimes of gyrokinetic turbulence. *Phys. Rev. Lett.*, 111:175001.

[Hazeltine and Newcomb, 1990] Hazeltine, R. D. and Newcomb, W. A. (1990). Inversion of the ballooning transformation. *Physics of Fluids B: Plasma Physics (1989-1993)*, 2(1):7–10.

[Helander et al., 2012] Helander, P., Beidler, C. D., Bird, T. M., Drevlak, M., Feng, Y., Hatzky, R., Jenko, F., Kleiber, R., Proll, J. H. E., Turkin, Y., and Xanthopoulos, P. (2012). Stellarator and tokamak plasmas: a comparison. *Plasma Physics and Controlled Fusion*, 54(12):124009.

[Hinton and Hazeltine, 1976] Hinton, F. L. and Hazeltine, R. D. (1976). Theory of plasma transport in toroidal confinement systems. *Rev. Mod. Phys.*, 48:239–308.

[Hofmann et al., 1994] Hofmann, F., Lister, J. B., Anton, W., Barry, S., Behn, R., Bernel, S., Besson, G., Buhlmann, F., Chavan, R., Corboz, M., Dutch, M. J., Duval, B. P., Fasel, D., Favre, A., Franke, S., Heym, A., Hirt, A., Hollenstein, C., Isoz, P., Joye, B., Llobet, X., Magnin, J. C., Marletaz, B., Marmillod, P., Martin, Y., Mayor, J. M., Moret, J. M., Nieswand, C., Paris, P. J., Perez, A., Pietrzyk, Z. A., Pitts, R. A., Pochelon, A., Rage, R., Sauter, O., Tonetti, G., Tran, M. Q., Troyon, F., Ward, D. J., and Weisen, H. (1994). Creation and control of variably shaped plasmas in tcv. *Plasma Physics and Controlled Fusion*, 36(12B):B277.

[Horton, 1999] Horton, W. (1999). Drift waves and transport. *Rev. Mod. Phys.*, 71:735–778.

[Howard et al., 2016] Howard, N., Holland, C., White, A., Greenwald, M., and Candy, J. (2016). Multi-scale gyrokinetic simulation of tokamak plasmas: enhanced heat loss due to cross-scale coupling of plasma turbulence. *Nuclear Fusion*, 56(1):014004.

[Howard et al., 2014] Howard, N. T., Holland, C., White, A. E., Greenwald, M., and Candy, J. (2014). Synergistic cross-scale coupling of turbulence in a tokamak plasma. *Physics of Plasmas*, 21(11).

[Idomura, 2012] Idomura, Y. (2012). Accuracy of momentum transport calculations in full-f gyrokinetic simulations. *Computational Science and Discovery*, 5(1):014018.

[Idomura et al., 2008] Idomura, Y., Ida, M., Kano, T., Aiba, N., and Tokuda, S. (2008). Conservative global gyrokinetic toroidal full-f five-dimensional vlasov simulation. *Computer Physics Communications*, 179(6):391 – 403.

[Itoh et al., 2006] Itoh, K., Itoh, S.-I., Diamond, P. H., Hahm, T. S., Fuj isawa, A., Tynan, G. R., Yagi, M., and Nagashima, Y. (2006). Physics of zonal flowsa). *Physics of Plasmas*, 13(5):–.

[Jenko et al., 2000] Jenko, F., Dorland, W., Kotschenreuther, M., and Rogers, B. N. (2000). Electron temperature gradient driven turbulence. *Physics of Plasmas*, 7(5):1904–1910.

[Jolliet, 2010] Jolliet, S. (2010). *Gyrokinetic Particle-In-Cell Global Simulations of Ion-Temperature-Gradient and Collisionless-Trapped-Electron-Mode Turbulence in tokamaks.* PhD thesis, Ecole Polytechnique Fédérale de Lausanne, Switzerland. Thesis number 4684.

[Jolliet et al., 2007] Jolliet, S., Bottino, A., Angelino, P., Hatzky, R., Tran, T., Mcmillan, B., Sauter, O., Appert, K., Idomura, Y., and Villard, L. (2007). A global collisionless {PIC} code in magnetic coordinates. *Computer Physics Communications*, 177(5):409 – 425.

[Jolliet et al., 2009] Jolliet, S., McMillan, B. F., Vernay, T., Villard, L., Hatzky, R., Bottino, A., and Angelino, P. (2009). Influence of the parallel nonlinearity on zonal flows and heat transport in global gyrokinetic particle-in-cell simulations. *Physics of Plasmas*, 16(7).

[Kammerer et al., 2008] Kammerer, M., Merz, F., and Jenko, F. (2008). Exceptional points in linear gyrokinetics. *Physics of Plasmas (1994-present)*, 15(5):–.

[Lang et al., 2008] Lang, J., Parker, S. E., and Chen, Y. (2008). Nonlinear saturation of collisionless trapped electron mode turbulence: Zonal flows and zonal densitya). *Physics of Plasmas*, 15(5):–.

[Lapillonne, 2010] Lapillonne, X. (2010). *Local and Global Eulerian Gyrokinetic Simulations of Microturbulence in Realistic Geometry with Applications to the TCV Tokamak.*

PhD thesis, École Polytechnique Fédérale de Lausanne, Switzerland. Thesis number 4684.

[Lawson, 1957] Lawson, J. (1957). Some criteria for a power producing thermonuclear reactor. *Proceedings of the Physical Society. Section B*, 70(1):6.

[Lebrun and Tajima, 1995] Lebrun, M. and Tajima, T. (1995). *Bull. Am. Phys. Soc.*, 39:1533.

[Lin et al., 1998] Lin, Z., Hahm, T. S., Lee, W. W., Tang, W. M., and White, R. B. (1998). Turbulent transport reduction by zonal flows: Massively parallel simulations. *Science*, 281(5384):1835–1837.

[Lin and Lee, 1995] Lin, Z. and Lee, W. W. (1995). Method for solving the gyrokinetic poisson equation in general geometry. *Phys. Rev. E*, 52:5646–5652.

[Lister, 2011] Lister, J. (2011). *Plasma Physics III, Vol. 1.*

[Littlejohn, 1983] Littlejohn, R. (1983). *Journal of Plasma Physics*, 29(1):111–125.

[Loizu et al., 2015] Loizu, J., Hudson, S. R., Bhattacharjee, A., Lazerson, S., and Helander, P. (2015). Existence of three-dimensional ideal-magnetohydrodynamic equilibria with current sheets. *Physics of Plasmas*, 22(9).

[Loizu et al., 2016] Loizu, J., Hudson, S. R., Helander, P., Lazerson, S. A., and Bhattacharjee, A. (2016). Pressure-driven amplification and penetration of resonant magnetic perturbations. *Physics of Plasmas*, 23(5).

[Lütjens et al., 1996] Lütjens, H., Bondeson, A., and Sauter, O. (1996). The chease code for toroidal mhd equilibria. *Computer Physics Communications*, 97(3):219 – 260.

[Maeyama et al., 2015] Maeyama, S., Idomura, Y., Watanabe, T.-H., Nakata, M., Yagi, M., Miyato, N., Ishizawa, A., and Nunami, M. (2015). Cross-scale interactions between electron and ion scale turbulence in a tokamak plasma. *Phys. Rev. Lett.*, 114:255002.

[McMillan et al., 2010] McMillan, B., Jolliet, S., Bottino, A., Angelino, P., Tran, T., and Villard, L. (2010). Rapid fourier space solution of linear partial integro-differential equations in toroidal magnetic confinement geometries. *Computer Physics Communications*, 181(4):715 – 719.

[McMillan et al., 2008] McMillan, B. F., Jolliet, S., Tran, T. M., Villard, L., Bottino, A., and Angelino, P. (2008). Long global gyrokinetic simulations: Source terms and particle noise control. *Physics of Plasmas*, 15(5).

[Merz, 2009] Merz, F. (2009). *Gyrokinetic simulation of multimode plasma turbulence.* PhD thesis, Universität Münster, Germany.

[Merz and Jenko, 2008] Merz, F. and Jenko, F. (2008). Nonlinear saturation of trapped electron modes via perpendicular particle diffusion. *Phys. Rev. Lett.*, 100:035005.

[Merz et al., 2012] Merz, F., Kowitz, C., Romero, E., Roman, J., and Jenko, F. (2012). Multi-dimensional gyrokinetic parameter studies based on eigenvalue computations. *Computer Physics Communications*, 183(4):922 – 930.

[Mishchenko et al., 2005] Mishchenko, A., Könies, A., and Hatzky, R. (2005). Particle simulations with a generalized gyrokinetic solver. *Physics of Plasmas*, 12(6).

[Pueschel et al., 2010] Pueschel, M., Dannert, T., and Jenko, F. (2010). On the role of numerical dissipation in gyrokinetic vlasov simulations of plasma microturbulence. *Computer Physics Communications*, 181(8):1428 – 1437.

[Roman et al., 2010] Roman, J. E., Kammerer, M., Merz, F., and Jenko, F. (2010). Fast eigenvalue calculations in a massively parallel plasma turbulence code. *Parallel Computing*, 36(5–6):339 – 358. Parallel Matrix Algorithms and Applications.

[Romanelli and Briguglio, 1990] Romanelli, F. and Briguglio, S. (1990). Toroidal semi-collisional microinstabilities and anomalous electron and ion transport. *Physics of Fluids B: Plasma Physics*, 2(4):754–763.

[Rosenbluth and Hinton, 1998] Rosenbluth, M. N. and Hinton, F. L. (1998). Poloidal flow driven by ion-temperature-gradient turbulence in tokamaks. *Phys. Rev. Lett.*, 80:724–727.

[Sauter and Medvedev, 2013] Sauter, O. and Medvedev, S. (2013). Tokamak coordinate conventions:. *Computer Physics Communications*, 184(2):293 – 302.

[Scott, 1998] Scott, B. (1998). Global consistency for thin flux tube treatments of toroidal geometry. *Physics of Plasmas (1994-present)*, 5(6):2334–2339.

[Scott, 2006] Scott, B. D. (2006). Computation of turbulence in magnetically confined plasmas. *Plasma Physics and Controlled Fusion*, 48(12B):B277.

[Spitzer, 1951] Spitzer, L. (1951). *Project Matterhorn Report*, PM-S1 NYO-993, Princeton University.

[Sugama, 2000] Sugama, H. (2000). Gyrokinetic field theory. *Physics of Plasmas*, 7(2).

[Told, 2012] Told, D. (2012). *Gyrokinetic Microturbulence in Transport Barriers*. PhD thesis, Universität Ulm.

[Tran et al., 1999] Tran, T., Appert, K., Fivaz, M., Jost, G., Vaclavik, J., and Villard, L. (1999). Global gyrokinetic simulation of ion-temperature-gradient-driven instabilities using particles. *Theory of Fusion Plasmas, Int. Workshop (Bologna Editrice Compositori,Società Italiana di Fisica)*, page 45.

[Vernay, 2013] Vernay, T. (2013). PhD thesis, École Polytechnique Fédérale de Lausanne, Switzerland. Thesis number 5638.

[Vernay et al., 2010] Vernay, T., Brunner, S., Villard, L., McMillan, B. F., Jolliet, S., Tran, T. M., Bottino, A., and Graves, J. P. (2010). Neoclassical equilibria as starting point for global gyrokinetic microturbulence simulations. *Physics of Plasmas*, 17(12).

[Villard et al., 2002] Villard, L., Bottino, A., Sauter, O., and Vaclavik, J. (2002). Radial electric fields and global electrostatic microinstabilities in tokamaks and stellarators. *Physics of Plasmas*, 9(6):2684–2691.

[Waltz et al., 2005] Waltz, R., Candy, J., Hinton, F., Estrada-Mila, C., and Kinsey, J. (2005). Advances in comprehensive gyrokinetic simulations of transport in tokamaks. *Nuclear Fusion*, 45(7):741.

[Waltz et al., 2006] Waltz, R. E., Austin, M. E., Burrell, K. H., and Candy, J. (2006). Gyrokinetic simulations of off-axis minimum-q profile corrugations. *Physics of Plasmas*, 13(5):052301.

Acknowledgments

My Ph.D. diploma is the fruit of a long adventure starting when I decided to go back to university for studying physics, after five years of work in the financial sector as a software engineer. This would have not been possible without the help, encouragement, criticism, and support of many people. I attend here to thanks them.

I would like to start thanking my wife Andrea who has been a great contributor in the achievement of this thesis work and previous studies through her constant support. Thanks my dear. Thanks also to my daughter Estelle, who is born during my PhD and who reminded me every day that playing puzzle and reading stories together were a much more important activity than doing physics or writing a thesis. I would also like to thank my parents and family for their support.

I would like to thank the physics department of Nice who made me love physics when I was student. Particular thanks to Fabrice Mortessagne, Olivier Legrand, Olivier Alibart, and Eric Aristidi... to whom I had great pleasure learning from.

I would like to thank my Ph.D. colleagues. First of all, many thanks David for showing me your beautiful country “Le Valais” and its beautiful mountains. Then, I would like to thank Jonathan with whom we shared many discussions and our common interest in good food and good beers. I would also like to thank my two office mates Annamaria and Paola for the discussions. There comes the long list of people with whom we shared more than just a coffee: Alex, Antoine, Claudio, Falk, Hamish, Joaquim, Karim, Emmanuel, Gabriele, Himank, Samuel, Thibaut, Umar, Zhouzi... and many others who I forgot.

I would like to thank many scientists for their teaching in the field of plasma physics. First, thanks to Ambrogio Fasoli for his great course on plasma physics. I would also like to thank Tony Cooper and Jonathan Graves for their respective courses on MHD, as well as Stephan Brunner for his great course on advanced theory of plasmas. Thanks as well to Joaquim Loizu and Paolo Ricci with whom I carried out my first project on plasma physics during my master studies at EPFL. Thanks all of you for sharing your time and knowledge.

A particular thank to the people I met during conferences or workshop. First of all I would like to thank the Professor Sanatae Itoh for the discussion at my poster presentation at the EPS 2012. Receiving the High commendation from the jury at the Itoh prize was very stimulating. I would also like to thank Professor Yasuhiro Idomura for his interest and for discussions when we met during conferences. I would like to thank Professor Alain Brizard for discussions and for sharing his lecture notes, which notes were a formidable tool for studying gyrokinetic theory at the end of my thesis.

This Ph.D. work was also the result of scientific collaborations. I would like to thank Ben McMillan. It was a privilege working with you, every discussions were fruitful and your opinion is always more than valuable. Thanks a lot! I would also like to thank Frank Jenko, Tobias Goerler, and Daniel Told for the collaboration when studying physics with the code GENE. Finally, thanks to Emmanuel Lanti and Gabriele Merlo for the collaboration on gyrokinetic codes at SPC.

I would like to thank the members of the thesis jury Ben, Joan, and Yann for reading the manuscript with such attention and consideration.

Last but not least, I would like to thank my supervisors Laurent Villard and Stephan Brunner who gave me the grest opportunity to accomplish this PhD thesis in their group. First, thanks to Laurent for the position in the ORB5 group and for sharing with me the pleasure of successfully running this challenging code ORB5. Finally, I would like to give particular thanks to Stephan, as we started working together during my master thesis. You helped me transforming many ideas into scientific results. It has always been a privilege discussing physics, numerics, and any scientific topics with you. Thanks for your time and for your generosity.

Many thanks to all of you again,

Lausanne, 07 November June 2016 J. D.

Julien Dominski – Résumé

julien.dominski@gmail.com

Education

2010-2012	M.Sc. Physics - École Polytechnique Fédérale de Lausanne, Switzerland
2009-2010	B.Sc. Physics (3rd year) - University of Nice, France
2001-2004	M.Sc. (Titre d'ingénieur) in Computer Science - Polytech'Nice, France
1999-2001	DEUG in Math and Physics (1st and 2nd years of B.Sc.) - University of Nice, France

Employment History

Aug 2012 - Oct 2016 EPFL, Swiss Plasma Center
Doctoral assistant

"Development and application of Eulerian and PIC gyrokinetic codes to study the effect of the non-adiabatic dynamics of passing electrons on microturbulence"

- Study of plasma turbulence with the gyrokinetic codes GENE and ORB5
- Implementation of a new electrostatic field solver with finite-elements
- *Technologies:* Fortran, MPI, Matlab, high performance computing.

Main assistant, courses of numerical physics (teaching duties)

- Preparation of exercices and C++ programs for 2nd year bachelor in physics.
- *Technologies:* C++, Matlab.

Sep 2004 - Aug 2009 Credit Agricole Asset Management (partly as an external consultant)
Software developper / Technical team lead / Project follow-up

Software development for financial applications: asset management, trading, risk

- Team leader of a group of five people during two years
- Experience at London's front office with portfolio managers, traders, and risk
- *Technologies:*: Java, VBA, STP (automatic trade processing), Database.

Publications

- **J Dominski**, BF McMillan, S Brunner, G Merlo, L Villard *"An arbitrary wavelength solver for global gyrokinetic simulations. Application to the study of fine radial structures on microturbulence due to non-adiabatic passing electron dynamics"* (to be submited in Physics of Plasmas)
- **J Dominski**, S Brunner, T Görler, F Jenko, D Told, L Villard *"How non-adiabatic passing electron layers of linear microinstabilities affect turbulent transport"*, Physics of Plasmas 22 (6), 062303 (2015)
- L Villard, BF McMillan, O Sauter, F Hariri, **J Dominski**, G Merlo, S Brunner, TM Tran *"Turbulence and zonal flow structures in the core and L-mode pedestal of tokamak plasmas"*, Journal of Physics: Conference Series 561 (1), 12022-12034, (2014)
- CA de Meijere, S Coda, Z Huang, L Vermare, T Vernay, V Vuille, S Brunner, **J Dominski**, P Hennequin, G Merlo, L Porte, L Villard *"Complete multi-field characterization of the geodesic acoustic mode in the TCV tokamak"*, Plasma Physics and Controlled Fusion 56 (7), 072001 (2013)
- J Loizu, **J Dominski**, P Ricci, C Theiler *"Potential of a plasma bound between two biased walls"* Physics of Plasmas 19 (8), 083507 (2012)

Proceeding with referee

- **J Dominski**, S Brunner, SK Aghdam, T Görler, F Jenko, D Told, *“Identifying the role of non-adiabatic passing electrons in ITG/TEM microturbulence by comparing fully kinetic and hybrid electron simulations”*, Journal of Physics: Conference Series 401 (1), 012006 (2012)

Conference posters (as first author)

- **J Dominski**, S Brunner, BF McMillan, TM Tran, L Villard *“Kinetic electron dynamics and short scales in gyrokinetic simulations”*, Bulletin of the American Physical Society 60, (2015)
- **J Dominski**, S Brunner, BF McMillan, TM Tran, L Villard *“An arbitrary wavelength solver for the gyrokinetic quasi-neutrality equation”* 19th Joint EU-US Transport Task Force Meeting Culham, September 8-11, (2014)
- **J Dominski**, S. Brunner, T-M. Tran, L. Villard *“Electrostatic field solver based on an integral form of the quasi-neutrality equation in B-Spline representation”*, PASC conference Zurich, (2014)
- **J Dominski**, S Brunner, TM Tran and L. Villard *“Simulating the effect of fine radial structures resulting from non-adiabatic passing electrons on turbulent transport in the ITG and TEM regimes”* 40th EPS conference on Plasma Physics, Espoo Finland (2013)

Talks and invited

- **J Dominski**, S Brunner, TM Tran, L Villard *“Simulating the effect of fine radial structures resulting from non-adiabatic passing electrons on turbulent transport in the ITG and TEM regimes”* Joint annual meeting of the APS and SPS, Linz Austria (2013)
- **J Dominski**, S Brunner, BF McMillan, G Merlo, L Villard *“Global benchmark of realistic plasma geometries when including short scales effect due to kinetic electrons dynamics”* NumKin 26 - 30 October 2015, IPP Garching, Germany (Invited)

Seminar

- **J Dominski** *“The non-adiabatic response of passing electrons near mode rational surfaces in strongly magnetized plasmas of tokamak fusion reactor”*, University of Nice LPMC laboratory, 17 December 2015
- **J Dominski** *“Effect of nonadiabatic passing electron dynamics near mode rational surfaces on turbulent transport using gyrokinetic simulations”*, Princeton Plasma Physics Laboratory (PPPL) Princeton University, 23 November 2015
- **J Dominski** *“Passing electron dynamics and file radial structures in ITG and TEM regimes of tokamak plasma”*, Warwick University, 7 April 2014

Prizes

- High commendations from the judges at the 2013 Itoh Prize in Plasma Turbulence, for a poster presentation at the 40th EPS conference on plasma physics, Espoo Finland (2013)
- Teaching assistantship award, Faculty of Basic Sciences, EPFL, (2012)